

**INVESTIGATION OF STRUCTURAL, OPTICAL AND ELECTRICAL PROPERTIES
AND
VALENCE BAND SPLITTING IN Cu-In-Se COMPOUNDS.**

A thesis
submitted for the award of the degree of
Doctor of Philosophy
in the Faculty of Science

by

Rachel Reena Philip



**Department of Physics
Cochin University of Science and Technology
Kochi - 682 022, India.**

December 2004

Department of Physics
Cochin University of Science and Technology
Kochi-682 022
India

Certificate

Certified that the work presented in this thesis entitled “**Investigation of structural, optical and electrical properties and valence band splitting in Cu-In-Se compounds**” is based on the research work carried out by **Rachel Reena Philip** under my guidance in the Department of Physics, Cochin University of Science and Technology and no part of this has been presented by her for the award of any other degree.

Kochi-22

23rd December 2004

Dr.B.Pradeep
Reader
(Supervising guide)

DECLARATION

I hereby declare that the work reported in this thesis entitled **“Investigation of structural, optical and electrical properties and valence band splitting in Cu-In-Se compounds”** is original and has been carried out by me independently under the supervision of Dr.B.Pradeep, Reader, Department of Physics, Cochin University of Science and Technology, Kochi, Kerala. I further declare that this work has not been included in any other thesis submitted previously for the award of any degree, diploma or fellowship of any university or institution.

Kochi-22

23rd December 2004


Rachel Reena Philip

Acknowledgements

It is with deep felt thanks in my heart to God Almighty, who equipped me to finish this tiny task that I move on to express my thanks to all who have in one way or another helped me in accomplishing the same.

With a profound sense of gratitude, first of all I wish to thank my research supervisor Dr.B.Pradeep, for his gentle and inspiring guidance, invaluable suggestions, understanding nature and constant support that has been the main contributory factor for the successful completion of this work. I am indebted to the former as well as the present Heads of the department of physics- Prof.M.Sabir, Dr.Elizabeth Mathai, Prof.K.P.Vijayakumar and Dr.V.C.Kuriakose for allowing me to use the experimental facilities in the department and for providing constant encouragement. I am grateful to Prof.K.P.Rajappan Nair, Dr.M.R.AnanthaRaman, Dr.C.Sudha Kartha, Dr.S.JayaLakshmi, Dr.T.Ramesh Babu, Dr.M.K.Jayaraj, Sharangadharan sir and all other faculty members in the dept. for their advices and guidance. Also my sincere thanks to all the non-teaching staff in the department for their help in various ways. I'm indebted to Dr.Vijayakumar, for the courtesy in granting permission to use the photoluminescence facility in his lab.

I recall with deep gratitude the encouragement and counsel given by Dr.V.P.N.Nampoori and Dr.C.P.Girjavallabhan, ISP, CUSAT, during the course of this work. For the courtesy in granting permission to use the XRR facilities at IUC Indore, I'm greatly indebted to Dr.Ajay Gupta and to Dr.T.Shripati for letting me take ESCA, to Dr.G.S.Okram for helping with low temperature dark conductivity measurements and to Dr.V.Ganesan for taking AFM of my samples. I would always cherish with gratitude the pleasant experience I had in discussing the experiments and receiving counsel from them. The help rendered by Uday Deshpande, S.C Das and Ajoy of IUC, Dr.Sam Philip, Resmi and Manju of IISC are also remembered with deep felt thanks. Special thanks to Jayakrishnan for helping with PL measurements.

With a great sense of gratitude I remember my colleagues at U.C. College especially the teachers in the dept. of physics whose inspiration and encouragement are remarkable in taking up this research work. Special thanks to Shenoji sir for his

inclination to discuss and help with some mathematical evaluations done in this work. Thanks are also due to Prof. Joy George for giving me good counsel in the beginning stages of this work.

To my lab mates, past and present-Binoy sir, Ampili, Santhosh, Saji Augustine and Reena Rajan, lots of thanks for making the lab work a joint venture to perform and for sharing the sorrows and joys in the course of the work. For helps in various ways and in most needed moments, special thanks are due to my friends Teny, Shaji, Joseph, Sajeev, Deepthi, Malini, Viji, Syamala teacher, Rupa, Swapna, Saravanan, Paul, Kishore, Bindu, Anila, Manoj, Nisha and all other research scholars in the department of physics. I thank all the M.Sc and M.Phil students who joined our lab from time to time, for their kind acts of love.

My family deserves the ultimate gratitude for their selfless support, encouragement and patience. It is only with tears that I can recall all the wise counsels of my beloved mother who departed from me in the 2nd year of this research course. A Pillar of love and support, she had always enthused me to take up all challenges in life with a positive attitude and never to stoop to disappointments in life. It is actually her attitude to life that instilled in me the motivation to embark upon this research carrier. How can I thank her but she never opted for that...! I know there is no need to express my overwhelming sense of gratitude to my dear father for his constant encouragement, wise counsel, support and guidance, since the completion of this work itself will be taken as the most rewarding expression of my love and gratitude to him. Words are not enough to express my deep felt thanks to my dear mother-in-law for taking charge of my home whenever I needed her so that I could work on my experiments. Special thanks to my brothers and their families especially to my elder brother for various timely help. I ought to acknowledge many more of my relatives, aunts and in-laws for their support in various ways. I cannot leave out thanking my little kids- Tara, Tarun and Arun for being always there to cheer me up and to help me with minor details especially while doing the synopsis seminar preparations and thesis work. Last but not the least, I wish to express my deep felt thanks to my dear husband for constantly encouraging me, for not counting the sacrifices he made for me and for helping me with many details I

needed during the course of this work. I acknowledge that without his selfless support this venture would not have come to its completion.

With thanks to all my well-wishers all whose names I can't mention here for limitation of space, I dedicate this Thesis to the loving memory of my beloved mother ...!

...In loving memory of my beloved mother

Contents

Preface	v
Publications	ix
1 An Overview of Chalcopyrites and the Experimental Techniques used for the preparation and characterization of Cu-In-Se compounds.	
1.1 Introduction.....	1
1.2 The Chalcopyrites: An Overview	2
1.2.1 The I-III-VI ₂ Semiconductors.....	2
1.2.2 Motivation for the present work.....	6
1.3 Experimental Techniques.....	7
1.3.1 Preparation techniques.....	7
1.3.1.1 Methods of thin film deposition.....	8
1.3.1.2 Gunther's Three Temperature method- modified.....	9
1.3.1.3 Selection of substrates and substrate cleaning.....	9
1.3.1.4 Cleaning the evaporators.....	10
1.3.1.5 Vacuum coating system.....	10
1.3.1.6 Deposition of film.....	11
1.3.2 Structural characterization techniques.....	13
1.3.2.1 X-ray diffraction.....	13
1.3.2.2 X-ray photoelectron spectroscopy.....	14
1.3.3 Compositional and morphological characterization techniques.....	15
1.3.3.1 Energy dispersive analysis of X-rays.....	15
1.3.3.2 Scanning electron microscopy.....	15
1.3.3.3 Atomic force microscopy.....	16
1.3.3.4 Thickness measurement.....	18
1.3.4 Optical measurements.....	19
1.3.4.1 Measurement of optical constants.....	19
1.3.4.2 Photoconductivity set up.....	22
1.3.4.3 Photoluminescence measurements.....	24
1.3.5 Electrical measurements.....	24

1.3.5.1	Conductivity measurements.....	24
1.3.5.2	Hall coefficient measurements.....	25
1.4	Conclusion.....	26
	References.....	27
2	Preparation and structural characterization of CuInSe₂ thin films	
2.1	Introduction.....	30
2.2	Three Source Vacuum Evaporation.....	30
	(Gunther's 3-temperature method-a modified form).	
2.3	Preparation of CuInSe ₂ Thin films.....	31
2.4	Compositional analysis.....	32
2.4.1	Energy dispersive analysis of X-rays.....	32
2.5	Morphological Characterization.....	35
2.5.1	Scanning electron microscopic studies.....	36
2.5.2	Atomic Force Microscopy.....	38
2.5.3	Thickness measurement.....	41
2.6	Structural characterization.....	42
2.6.1	X-ray diffraction.....	42
2.6.2	Lattice parameters.....	44
2.6.2.1	Lattice equations and Nelson Riley Taylor Sinclair function.....	44
2.6.2.2	Grain size and strain in the films.....	48
2.6.2.3	Tetragonal deformation, non-ideal anion displacement and bond lengths.....	49
2.7	X-ray photoelectron spectroscopy.....	54
2.8	X-ray Reflectivity.....	59
2.9	Conclusion.....	61
	References.....	62
3	Optical studies on CuInSe₂	
3.1	Introduction.....	64
3.2	Optical transmission and absorption studies.....	64
3.2.1	Absorption spectra and Energy band gap.....	64

3.2.2	Transmission spectra and refractive index.....	68
3.3	Photo conductivity studies in CuInSe ₂ film.....	71
3.3.1	Transient photoconductivity.....	71
3.3.2	Steady state photoconductivity.....	76
3.3.3	Spectral response in CuInSe ₂	81
3.4	Conclusion.....	83
	References.....	84
4	Electrical characterization of CuInSe₂	
4.1	Introduction.....	85
4.2	Electrical conductivity in CuInSe ₂ films.....	85
4.2.1	Conductivity type.....	86
4.2.2	Electrical conductivity of CIS films.....	86
4.2.2.1	Electrical conductivity in Cu-rich CIS films.....	87
4.2.2.2	Electrical conductivity in In-rich CIS films.....	90
4.3	Hall measurements.....	96
4.4	Conclusion.....	97
	References.....	99
5	Preparation and Structural characterization of OVC's	
5.1	Introduction.....	101
5.2	Preparation of thin films of CuIn ₅ Se ₈ , CuIn ₃ Se ₅ and CuIn ₇ Se ₁₂	103
5.3	Compositional analysis and Morphological Characterization.....	103
5.3.1	EDAX spectra.....	104
5.3.2	Scanning Electron Micrographs.....	106
5.3.3	Atomic Force Microscopy.....	107
5.4	Structural characterization.....	115
5.4.1	X-ray diffraction.....	115
5.4.2	Lattice parameters.....	120
5.4.3	Grain size and strain in the films.....	121
5.4.4	Tetragonal deformation, non-ideal anion displacement and bond lengths.....	123

5.5	X-ray photoelectron spectroscopy.....	125
5.6	X-ray Reflectivity.....	128
5.7	Conclusion.....	131
	References.....	132
6 Optical studies on the OVC films		
6.1	Introduction.....	134
6.2	Optical absorption studies.....	134
6.3	Photoconductivity studies in OVC films.....	140
	6.3.1 Transient photoconductivity.....	141
	6.3.2 Steady State Photoconductivity.....	147
	6.3.3 Spectral Response Studies.....	155
6.4	Photoluminescence studies on the OVC's.....	160
6.5	Conclusion.....	164
	References.....	165
7 Electrical characterization of the OVC's.		
7.1	Introduction.....	166
7.2	Electrical conductivity in the OVC's.....	166
7.3	Hall measurements.....	175
7.4	Conclusion.....	176
	References.....	178
8 Valence band splitting in Cu-In-Se compounds		
8.1	Introduction.....	179
8.2	A brief review of investigations on valence band splitting in chalcopyrites.....	180
8.3	Investigations on Valence band Splitting in thin films of CuInSe ₂ and the OVC's CuIn ₃ Se ₅ , CuIn ₅ Se ₈ and CuIn ₇ Se ₁₂	182
8.3	Conclusion.....	197
	References.....	198
Scope for future research		199

Preface

Growing concern over the world's ever-increasing energy needs and the prospect of rapidly dwindling natural reserves of energy such as oil, natural gas, uranium fuel etc. have prompted efforts to develop viable alternative energy sources. Many countries have initiated programs to develop renewable energy technologies that would enable them to reduce fossil-fuel consumption and its attendant problems. Some technologies that are being actively pursued are fusion devices, techniques designed to make wider and more efficient use of the energy in sunlight, wind, moving water, terrestrial heat etc. The amount of energy in such renewable and virtually pollution-free sources is large in relation to world energy needs, yet at the present time only a small portion of it can be converted to electric power at reasonable cost. A variety of devices and systems has been created to better tap the energy in sunlight. Among the most efficient are photovoltaic systems that transform radiant energy from the Sun directly into electricity by means of solar cells. Because they have no moving parts that could require service or fuels that would require replenishment, solar cells are ideal for providing power in space, to provide electric power in many remote terrestrial locations, to convert the energy in sunlight into electrical energy for distribution to industrial, commercial and residential users. Another growing application of solar cells is in consumer products, such as electronic toys, hand-held calculators, and portable radios. Solar cells used in devices of this kind may utilize indoor artificial light (e.g., from incandescent and fluorescent lamps) as well as natural light from the Sun in converting radiant energy into electricity.

The search for low cost, high efficiency junction layers for solar cells has created renewed interest in investigation of the ternary chalcopyrite CuInSe_2 which is recognized as a highly efficient, low cost, radiation resistant and stable absorber layer in solar cell fabrication. With the realization of the peculiar property of existence of a number of stable non-stoichiometric ordered vacancy compounds related to CuInSe_2 , which could form junctions with p-type CuInSe_2 , increasing the efficiency of solar cells, the investigation of the properties of the different OVC's that could give an

insight into the defect physics and chemistry of these semiconducting materials is also being pursued widely. Investigation on preparation and systematic characterization of the ternary chalcopyrite CuInSe_2 and three related ordered vacancy compounds CuIn_3Se_5 , CuIn_5Se_8 and $\text{CuIn}_7\text{Se}_{12}$ forms the main body of this thesis.

This thesis is organized in to eight chapters of which the introductory chapter gives a brief overview of the chalcopyrite compounds and the experimental techniques employed for the preparation and characterization of the compounds studied. A glance at the various properties of the chalcopyrites in general and CuInSe_2 in particular in connection with reports available in literature is also included in this introductory chapter.

The preparation of thin films of CuInSe_2 and their structural, compositional and morphological characterization are detailed in chapter 2. A modified form of Gunther's Three Temperature method has been used for the preparation of all the Cu-In-Se compounds. Depending on composition, the CuInSe_2 films have been classified as Cu-rich and In rich for getting a better perspective of the variation in properties with stoichiometry of the films. The use of X-ray diffraction data for phase identification, evaluation of lattice parameters, tetragonal distortion, anion displacement and bond length evaluation is elaborated. Binding energy studies using ESCA and mass density determination using X-ray reflectivity are also outlined in this chapter.

The optical studies that help in accurate determination of band gap in CuInSe_2 of In-rich and Cu-rich compositions are elaborated in the third chapter. The photoconducting properties of the material have been dealt with. Etching techniques have been used to get an understanding of the negative photoconducting phenomena observed in Cu-rich CuInSe_2 . The optical constants' evaluation is also included. P-d interaction effects on the band gap variation of CuInSe_2 with variation in stoichiometry are studied. The possibility of tailoring the band gap of CuInSe_2 for applications in solar cell fabrication by systematically controlling the composition is explored in this chapter.

Chapter 4 highlights the importance of composition control pertaining to defect formations that intrinsically dope CuInSe_2 films n-type or p-type and influence their resistivity. The metallic behaviour of the Cu-rich films due to segregation of

copper selenide phase on surface is investigated through etching studies. The conducting process of p-type Cu-rich films and n-type In rich films in different temperature ranges observed experimentally are explained through adoption of different models like Arrhenius, Seto's and Mott's. Room temperature Hall studies have been used to gather information regarding concentration and type of carriers, mobility of carriers, resistivity, sheet resistance, Hall coefficient etc.

In chapter 5, the preparation and structural characterization of the OVC compounds CuIn_3Se_5 , CuIn_5Se_8 and $\text{CuIn}_7\text{Se}_{12}$ is elaborated. The compositional characterization using EDAX and morphological characterization employing SEM and AFM are used to demarcate the different OVC compounds, which are then structurally characterized using XRD. The lattice parameter and bond length evaluation of the three OVC's is also included in this chapter. The absence of any binary phases in the films is regarded on the basis of binding energy studies using ESCA.

Chapter 6 gives insight into the increased band gap of the OVC's in comparison with that of CuInSe_2 . Reduction in p-d repulsion due to decreased Cu-content in the OVC's is correlated with the increased band gap in these compounds. Photoconducting properties of the OVC films are investigated. Defect studies in the OVC's done through spectral response and photoluminescence measurements also form a part of this chapter.

Chapter 7 elaborates upon the electrical properties of the OVC films, which are all, determined to be n-type by Hot- probe method and Hall measurements. Using different models, the electrical behaviour of the films in different temperature ranges is explained. The opto-electronic studies of the compound $\text{CuIn}_7\text{Se}_{12}$ are done for the first time to the best of our knowledge.

Chapter 8 is a treatise on the valence band splitting observed in these compounds due to the simultaneous effect of non-cubic crystalline field and spin-orbit interaction. The presence of metal d-orbital in the valence bands of the compounds is found to influence the p-d hybridization and the spin-orbital splitting in the compounds. The splitting parameters ΔCF and ΔSO are evaluated in the compound using Hopfield's model and correlated with the structural properties, the mode of construction of the films, stoichiometry etc.

A comprehensive summary of the investigations done on these samples is included at the end with the scope for future studies in these materials.

Publications

The following is the list of publications resulting from this thesis:

Article in book:

Valence band splitting in CuInSe_2 and the related ordered vacancy compounds CuIn_3Se_5 , CuIn_5Se_8 and $\text{CuIn}_7\text{Se}_{12}$, **Rachel Reena Philip**, B.Pradeep and T.Shripathi, **Trends in Semiconductor research**, Leach J.M (ed.), Nova Publishers, New York (in press).

Journal Papers:

1. Crystal- field and spin-orbit interactions in the valence band of the ordered vacancy compound CuIn_4Se_7 , **Rachel Reena Philip** and B.Pradeep, *Semicond.Sci.Technol.* **17** (2002) 1157-1161.
2. Structural analysis and optical and electrical characterization of the ordered defect compound CuIn_5Se_8 , **Rachel Reena Philip** and B.Pradeep, *Semicond.Sci.Technol.* **18** (2003) 768-773.
3. Non-ideal anion displacement, band gap variation and valence band splitting in Cu-In-Se compounds, **Rachel Reena Philip** and B.Pradeep, *Thin Solid Films*, **472**. 1-2 (2004) 136-143.
4. Investigations of the electrical properties in CuInSe_2 and the related ordered vacancy compounds. **Rachel Reena Philip**, B.Pradeep, G.S.Okram and V.Ganesan, *Semicond. Sci.Technol.* **19** (2004) 1-8.
5. Spin orbit and tetragonal crystalline field interaction in the valence band of CuInSe_2 related ordered vacancy compound $\text{CuIn}_7\text{Se}_{12}$, **Rachel Reena Philip**, B.Pradeep and T.Shripathi, *Physica Status Solidi (b)* (in press).

6. Photoconductivity in the ordered vacancy compound CuIn_5Se_8 , **Rachel Reena Philip**, B.Pradeep and T.Shripathi, Applied Surface Science (communicated).

7. Photoconductivity and photoluminescence in the ordered vacancy compounds CuIn_3Se_5 and $\text{CuIn}_7\text{Se}_{12}$, **Rachel Reena Philip** and B.Pradeep (communicated).

8. Defect studies in Cu-In-Se compounds, **Rachel Reena Philip** and B.Pradeep (communicated).

Chapter 1

An overview of Chalcopyrites and the experimental techniques used for the preparation and characterization of Cu-In-Se compounds.

1.1 Introduction

Investigations on thin films that started decades back due to scientific curiosity in the properties of a two-dimensional solid, has developed into a leading research field in recent years due to the ever expanding applications of the thin films in the form of a variety of active and passive microminiaturized components and devices, solar cells, radiation sources and detectors, magnetic memory devices, interference filters, reflection and antireflection coatings etc. [1]. The recent environment and energy resource concerns have aroused an enormous interest in the study of materials in thin film form suitable for renewable energy sources such as photovoltaic devices. Recognition of the immense potential applications of the chalcopyrites that can form homojunctions or heterojunctions for solar cell fabrication has attracted many researchers to extensive and intense research on them.

In this thesis, we have started with studies performed on CuInSe_2 thin films, a technologically well recognized compound belonging to the I-III-VI family of semiconductors and have riveted on investigations on the preparation and characterization of compounds CuIn_3Se_5 , CuIn_5Se_8 and $\text{CuIn}_7\text{Se}_{12}$, an interesting group of compounds related to CuInSe_2 called Ordered Vacancy Compounds, having promising applications in photovoltaic devices. A pioneering work attempted on preparing and characterizing the compound $\text{CuIn}_7\text{Se}_{12}$ is detailed in the chapters on OVC's. Investigation on valence band splitting in OVC's have also been attempted for the first time and included as the last chapter in the thesis. Some of the salient features of the chalcopyrite compounds are given in the next section of this introductory chapter.

1.2 The Chalcopyrites: An Overview

The ternary semiconductors $A^I B^{III} C_2^{VI}$ and $A^{II} B^{IV} C_2^V$ form a group of nearly 40 different species commonly referred to as chalcopyrites and span a wide range of structural, chemical, electrical and optical properties [2-4]. Of these the II-IV- V_2 compounds are the simplest structural analogues of III-V zincblende compounds where as the ternary I-III-VI ABC_2 compounds ($A=Cu$ and Ag , $B=Al$, Ga and In and $C=S$, Se and Te) are the structural analogues of II-VI binary compounds [5].

1.2.1 The I-III- VI_2 Semiconductors

The I-III-VI chalcopyrites upon which the present investigation has been done have an energy band structure and overall structure similar to that of their II-VI binary analogues, where as the band gaps of the former are substantially smaller than the latter [6]. It is the strong red shift of the ternary band gap that makes some of the ABC_2 compounds strong absorbers of sunlight, a property that makes these materials promising candidates for photovoltaic solar- energy applications [7,8].

In addition to this electronic anomaly, ternary chalcopyrites also have some interesting structural anomalies relative to their binary analogues. First, rather than have a single cation, the ternary chalcopyrites have two cations; starting from the A atom and translating in the vertical direction through intervals of $c/2$, following the sequence ABAB... whereas translating horizontally with an interval of a , the sequence AAA... is followed. These crystals often show a tetragonal distortion where the ratio between the lattice parameters $\eta = c/2a$ differ from 1. Also, the anions in these compounds are displaced from their zinc-blende sites. In short, while in binary AC zinc-blende compounds each cation A has four anions C as nearest neighbours and vice versa, in a ternary chalcopyrite ABC_2 each cation A and B has four anions C as nearest neighbours and each anion has two A and two B cations as nearest neighbours. As a result, the anion C usually adopts an equilibrium position closer to one pair of cations than to the other, that is, unequal bond lengths $R_{AC} \neq R_{BC}$ in these chalcopyrites [6].

Shay and Kasper [9] observed that the down shift of band gap in the ternary chalcopyrites when compared to that in the binary analogues could be correlated with the observed d character in the upper half of the valence band found in the ternaries, but not in the binaries. That is the proximity of noble metal d-levels in the valence band of

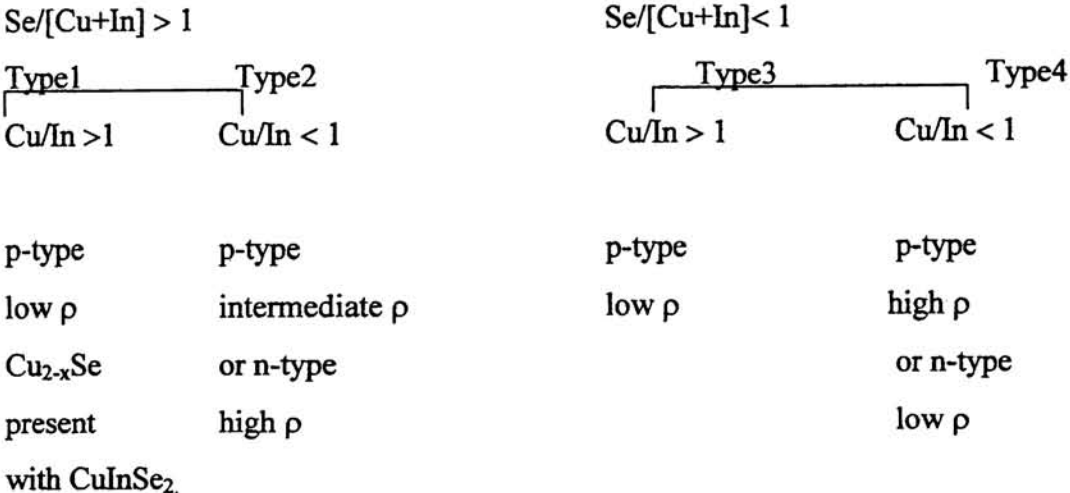
the ternaries exerts a profound influence on the energy band gaps. The electroreflectance measurements performed by Shay et al [10] confirmed the presence of the noble metal d-levels in the valence band of I-III-VI compounds directly. J.E.Jaffe and A.Zunger [11] succeeded in correlating the band gap anomaly in ternaries with (1) a structural source due to the existence of a non-ideal anion displacement $u \neq \frac{1}{4}$ which is dictated by the mismatch in the classical atomic radii, and (2) an electronic source due to the p-d level repulsion associated with the noble atom d-orbitals. They identified the simple structural factor u as sensitively controlling the optical band gap of the chalcopyrite materials and established a unique relationship between the structural and optical properties of ternary chalcopyrite semiconductors [11]. In ternaries, the $\Gamma_{15}(p)$ state of the anion interact with the $\Gamma_{15}(d)$ state of the cation having the same symmetry forming a lower bonding state weighted more by the lower energy $\Gamma_{15}(d)$ state and an upper antibonding state weighted more by a higher energy $\Gamma_{15}(p)$ state, where due to p-d repulsion the upper state is pushed up resulting in band gap reduction. In the present investigation, the same reason that is p-d interaction effect is used in explaining the increase in band gap in the OVC's.

Another very interesting property exhibited by the chalcopyrites is the valence band splitting in them due to the combined effect of the non-cubic crystalline field and the spin orbit interaction in them, which is also related to the structure of the crystals. The presence of noble metal d-levels in the valence band of the chalcopyrites are found to produce not only the band gap variation but also an anomalous reduction in the spin-orbit splitting of the valence-band maximum [2].

The chalcopyrites especially the II-IV-V₂ ternaries have been studied for their potential as non-linear optical material for frequency conversion applications in the near and mid- infrared region. The compound ZnGeP₂ is an established NLO material. The I-III-VI₂ family of materials with direct band gap also exhibits non-linear properties [12-13].

Erwin and Zutie examined theoretically the prospects for ferromagnetism within the class of all possible II-IV-V₂ chalcopyrites and identified two small sets of chalcopyrites that showed excellent prospects for stable ferromagnetism under realistic and attainable experimental conditions [14]. The ferromagnetic properties of I-III-VI

compounds are yet to be studied. The electrical properties of the compounds are dependent to a large extent on stoichiometry [15]. Noufi et al studied the resistivity dependence on composition in CuInSe_2 , a typical I-III-VI₂ compound and gave the following classification.



This property of the chalcopyrites, that is the ability to dope them p-or n-type by native defects on variation of stoichiometry has interesting applications in photovoltaic devices [16]. The role of defects in determining the electrical type and other properties of the materials that has been the basis of many electrical, photoluminescence, photoconductivity etc investigations has helped in elucidation of the dependence of the former on stoichiometry [17-20]. Some chalcopyrites exhibit persistent photoconductivity properties [21]

The unusual defect physics of this class of materials has been a matter of investigation for many [22,23]. The structural tolerance of chalcopyrites to large off-stoichiometry, the ability to dope the chalcopyrites via native defects making them p-type or n-type as mentioned earlier and the electrically benign nature of the structural defects due to electronic passivation of the defects are three unusual phenomena that have made the chalcopyrites technologically very important. Unlike in many groups of semiconductors like III-V compounds where defects are highly detrimental to the performance of optoelectronic devices, in chalcopyrites the defects often lead to the formation of stable n and p-type semiconductors which can form homojunctions in the

fabrication of photovoltaic solar cells [24,25]. The fact that the three unusual phenomena or puzzling effects regarding the defect structure are technologically beneficial has led to attempts to understand these phenomena. Thus extensive efforts have been taken at characterizing the defect levels in these compounds via electrical measurements [26,27], absorption [28], luminescence [29], deep level transient spectroscopy [30] but very little evidence existed as to the chemical and structural identification of the defect centers producing those levels. To remove the discrepancies associated with characterization of defect levels Zhang et al [22] calculated the formation energies and electrical transition levels of point defects and defect pairs and arrays in a prototype member of the family ie. CuInSe_2 , which is the compound of our interest, using the first principles self-consistent electronic structure theory and obtained the following order of formation energies.

$$V_{\text{Cu}} < \text{Cu}_{\text{In}} < V_{\text{In}} < \text{Cu}_i < \text{In}_{\text{Cu}} \quad (\text{Cu rich; In rich; n type}),$$

$$V_{\text{Cu}} < \text{Cu}_{\text{In}} < \text{In}_{\text{Cu}} < \text{Cu}_i < V_{\text{In}} \quad (\text{Cu rich; In rich; p type}),$$

$$V_{\text{Cu}} < V_{\text{In}} < \text{In}_{\text{Cu}} < \text{Cu}_{\text{In}} < \text{Cu}_{\text{In}} \quad (\text{Cu poor; In rich; n type}),$$

$$V_{\text{Cu}} < \text{In}_{\text{Cu}} < V_{\text{In}} < \text{Cu}_{\text{In}} < \text{Cu}_i \quad (\text{Cu poor; In rich; p type}),$$

$$\text{Cu}_{\text{In}} < V_{\text{In}} < V_{\text{Cu}} < \text{Cu}_i < \text{In}_{\text{Cu}} \quad (\text{Cu rich; In poor; n type}),$$

$$\text{Cu}_{\text{In}} < V_{\text{Cu}} < V_{\text{In}} < \text{Cu}_i < \text{In}_{\text{Cu}} \quad (\text{Cu rich; In poor; p type}),$$

Where as the order of formation energies earlier developed by Neumann et al [26] was

$$\text{In}_{\text{Cu}} < \text{Cu}_{\text{In}} < V_{\text{Se}} < V_{\text{Cu}} < V_{\text{In}} < \text{Cu}_i.$$

The above results are made use of in later chapters in explaining the photoconductivity, photoluminescence etc. spectra experimentally obtained in the present study.

CuInSe_2 , the compound of our interest, a prototype member of the I-III-VI family of chalcopyrites, tolerates a large range of anion -to- cation off stoichiometry, and the extreme limit of 'off- stoichiometry' is manifested by the existence of a series of compounds with different Cu/In/Se ratios like CuIn_5Se_8 , CuIn_3Se_5 , $\text{Cu}_3\text{In}_5\text{Se}_9$ etc. These compounds are generally known as Ordered Vacancy Compounds (OVC) assuming that the defects in them are ordered throughout the crystal. Different researchers have given different structural formulas to the OVC's [31-38]. Of all the explanations for the structural stability of the OVC's the most widely accepted is the one given by Zhang et al [22] where they explained the existence of OVC's CuIn_5Se_8 ,

CuIn_3Se_5 , $\text{Cu}_2\text{In}_4\text{Se}_7$ and $\text{Cu}_3\text{In}_5\text{Se}_9$ as a repeat of a single unit of $(2V_{\text{Cu}}^- + \text{In}_{\text{Cu}}^{2+})$ pairs for each $n=4, 5, 7$ and 9 units, respectively of CuInSe_2 and rationalize the stabilities of the three observed off-tie-line compounds $\text{CuIn}_7\text{Se}_{12}$, $\text{CuIn}_9\text{Se}_{16}$ and $\text{Cu}_3\text{In}_6\text{Se}_{11}$ as emerging from the creation of 2,1 and 1 neutral Cu vacancies per molecule in the on-tie-line compounds $\text{Cu}_3\text{In}_7\text{Se}_{12}$ ($n=6, m=1$), $\text{Cu}_5\text{In}_9\text{Se}_{16}$ ($n=8, m=1$) and $\text{Cu}_4\text{In}_6\text{Se}_{11}$ ($n=11, m=1$) respectively. As we mentioned in the introduction, the investigations on the structural and optoelectronic properties of the OVC's are still in the initial stages and the scope of these technologically important compounds in the field of photovoltaic applications is attracting many researchers to investigate on them.

Before winding up this brief overview on some properties of the chalcopyrites that have been investigated by different researchers, some combinations of these thin films in solar cell fabrication is mentioned. Shukni et al [39] developed Au/CIS/CdS/ZnO solar cells with 5% efficiency while there are reports of Mo/CIS/CdS/ZnO solar cells with efficiency ranging from 8.5% to 13.7% by different researchers [40-43]. Device structures with combinations like Mo/CIS/CdS/ZnO:Al with efficiencies 6.9% to 11.3% respectively have been developed by Okano et al and Nakada et al [44,45]. Schmid et al constructed and analyzed solar cells forming heterojunctions between CIS and OVC CuIn_3Se_5 , ie. of CIS/OVC/CdS/ZnO structure and concluded that OVC's form a very efficient part of the heterojunction and hence further analysis of these compounds can give worthy out puts [46].

1.2.2 Motivation for the present work

The brief review presented on CIS and the related OVC's in the preceding section highlights the importance of these compounds with versatile structural, opto-electronic, non-linear properties in the field of renewable energy sources. Although much investigations have been done on CuInSe_2 , very few reports are available on a systematic study of the electrical and photoconductivity properties of these materials with change in composition from Cu-rich to In-rich in thin film form and relating them to defects or binary phases formed in the materials. This issue is addressed in the present investigation, through etching studies and observance of reversal of effects from negatively photoconducting to positively photoconducting with etching of samples in Cu-rich compounds as well as through spectral response studies. For this,

good quality films deposited by co-evaporation techniques and characterized by XRD, EDAX, XPS, SEM and AFM are made use of. Though valence band splitting property of this compound has been addressed by many as mentioned in the brief review above, no reports are available, to the best of our knowledge, on valence band studies in thin films of the OVC's. An attempt to evaluate the splitting parameters and correlate them with structural make up of the thin films is made in the last chapter of the thesis. Moreover, an examination of literature shows that the preparation and characterization of the OVC $\text{CuIn}_7\text{Se}_{12}$ has not been attempted by any researchers so far and that study on CuIn_5Se_8 with chalcopyrite tetragonal structure is very few. Hence in this thesis, investigation of the structural, electrical and optical properties of $\text{CuIn}_7\text{Se}_{12}$ thin films as well as tetragonal CuIn_5Se_8 deposited by multisource co-evaporation is undertaken in detail. In addition to the above-mentioned pioneering fields of investigations, in the current study we have attempted to report the structural, morphological, compositional, optical and electrical properties of the compounds in a systematic way, trying to correlate the properties with each other at appropriate points, so that it would be useful for researches in future.

A brief description of the experimental techniques used for the preparation, structural, optical and electrical characterization of the thin films is given in the succeeding section.

1.3 Experimental Techniques

The experimental techniques include the set up that has been used for the deposition as well as for the characterization of the different types of films reported in this thesis.

1.3.1 Preparation Techniques

Thin film properties are strongly dependent on the methods of deposition, the substrate materials, the substrate temperature, cleanliness of the substrates, the rate of deposition and the back ground pressure. A multitude of techniques have been developed to prepare polycrystalline and nearly single –crystal films of all types of materials and deposition rates range from a fraction of an angstrom to thousands of angstroms per second [1]. In the following section, an account of the deposition technology used for

preparing thin films for the present investigation is given after briefing upon some of the methods of thin film deposition.

1.3.1.1 Methods of thin film deposition

Various methods such as Thermal evaporation, Sputtering, Chemical deposition etc. are used for preparation of the chalcopyrites in thin film form [1]. In thermal evaporation, the solid materials vaporize when heated to sufficiently high temperatures. The condensation of the vapour onto a cooler substrate yields thin solid films. The deposition by thermal evaporation is simple and very convenient but the rate of deposition of the vapour on a substrate depends on the source geometry, its position relative to the substrate and the condensation coefficient. Resistive heating, flash evaporation, arc evaporation, laser evaporation etc. are some thermal evaporation methods commonly used.

The ejection of atoms from the surface of a material by bombardment with energetic particles is called sputtering. If ejection is due to positive ion bombardment, it is referred to as 'cathodic sputtering'. The ejected or sputtered atoms can be condensed on a substrate to form a thin film. There are different methods of sputtering like glow-discharge sputtering, RF sputtering, reactive sputtering etc. An important advantage of the sputtering process is that the composition of a sputtered film is same as that of the cathode provided that (1) the cathode temperature is not too high for the rapid compensation of the higher- sputtering- yield material at the surface by volume diffusion from the bulk (2) the cathode does not decompose (3) the cathode surface does not alter chemically and (4) the sticking coefficients for the components on the substrate are the same.

Chemical methods may be broadly classified into two categories (1) electroplating and (2) chemical vapour deposition (CVD). The different electrodeposition processes are electrolytic deposition, electroless deposition, anodic deposition etc. and the different CVD process are pyrolysis, Hydrogen reduction, Polymerization etc. In CVD, when a volatile compound of the substance to be deposited is vaporized, and the vapour is thermally decomposed or reacted with other gases, vapours or liquids at the substrate, to yield nonvolatile reaction products, which deposit atomistically on the substrate, the process is called chemical vapour deposition.

Since a large variety of chemical reactions are available, CVD is a versatile and flexible technique in producing deposits of pure metals, semiconductors and insulators.

1.3.1.2. Gunther's Three Temperature method- modified

The method used in preparing the thin films in the present investigation is 3-source vacuum co-evaporation, which is a variable form of "Gunther's three temperature method". According to Gunther's method, the continuous condensation of a given vapour on a substrate is possible only if critical supersaturation is exceeded. That is, continuous condensation of a particular vapour at a given deposition rate is possible only if the temperature of the substrate drops below a critical temperature or if a critical super cooling is reached. Since these critical values are a function of the interfacial energies, they should differ in magnitude for different kinds of vapour and surface conditions. Furthermore, if different vapours are present in the vapour phase, they may interact with each other and thus influence considerably the above-mentioned critical values of supersaturation or super cooling. But at a particular substrate temperature and at a critical value of incident fluxes, sufficient molecules of the compound are formed on the substrate and nucleation and progressive condensation of the compound occurs. It has been observed in many binary systems [47] that the deposition of stoichiometric compound layers by simultaneous evaporation of the individual components is possible by selecting a suitable substrate temperature and adequate incident rates for the components. For the formation of the stoichiometric binary compound, generally three temperatures, that is substrate temperature and the two-evaporator temperatures are to be fixed and hence the process is called "3-temperature method". In its modified form for the deposition of a ternary compound, three separate evaporators are used instead of two for elemental evaporation.

1.3.1.3. Selection of substrates and Substrate cleaning

The nature and surface finish of the substrates are extremely important because they greatly influence the properties of films deposited on to them. Glass, quartz and ceramic substrates are commonly used for polycrystalline films. MgO, Si, Ge etc. are used for epitaxial growth [48]. The most commonly used glass slides as substrates are of pyrex, sodalime glass, coming glass etc. Properties such as stability at high temperatures, chemical and thermal stability are some of the qualities required for the

substrates. The quality of the surface is the most important property of a substrate since it is here that film-substrate interaction occurs.

The procedure of cleaning of the substrates is important, as it is one of the factors determining the composition and quality of the films. Different methods such as solvent cleaning, electron and ion bombardment of the surface, fire polishing etc. are adopted for cleaning of the substrates depending on the nature of the substrates and type of contaminants [48]. Since hot detergent solution may produce non-uniform etching of soda lime glass substrates, the initial cleaning of the substrates is done by first applying an industrial detergent and thoroughly cleaning in clear running water. After this the glass slides are rinsed in distilled water a number of times. The slides are then arranged in a specially made holder immersed in doubly distilled water and are subjected to cleaning by ultrasonic agitation. This gives a scrubbing effect on the substrates and removes the dust that has still been adhering to the surface. The slides are then dried with a hot air blower and are loaded into the vacuum chamber. Inside the vacuum system, they are further cleaned by ionic bombardment, prior to deposition of films.

1.3.1.4 Cleaning the evaporators

The cleanliness of the evaporators is very important since contamination of the films is sure to happen if the sources used are not clean. The molybdenum boats are initially dipped in nitric acid for removal of contaminants. Then they are thoroughly washed in clean running water and in distilled water. They are dried by blowing hot air and are then connected between the electrodes connected to the high current power supply in the vacuum chamber. After creation of vacuum, a suitable current is passed for 'baking' the boats at the temperature at which they would be used. The boats are kept at this temperature for about 10min. to 15min. and then cooled in vacuum. Now the boats are ready for use as evaporators.

1.3.1.5 Vacuum Coating system

The performance of a vacuum system with a chamber or bell jar is the single most important consideration for vacuum deposition techniques. The structure and properties of the film, depending on the material, may be influenced profoundly by the ultimate vacuum and residual gases and their partial pressures. The schematic representation of

diffusion – pump bell jar system such as the one used for the preparation of the films in the present study is given in Fig.1.1.

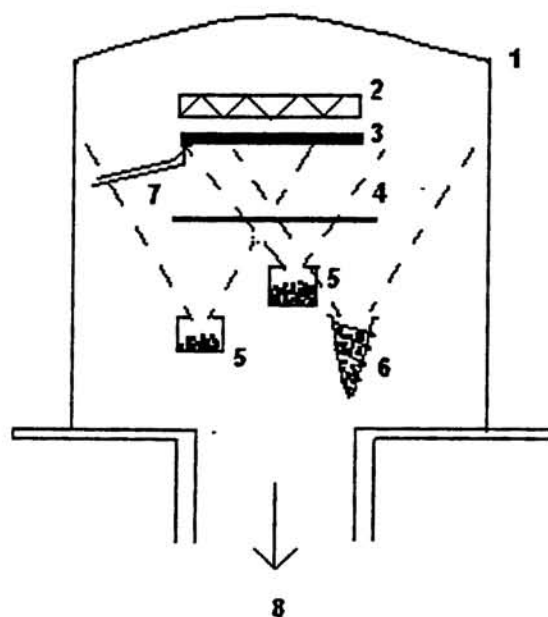
Two molybdenum boats and one glass crucible kept in a molybdenum basket are used for the evaporation of elements in the present study and they are connected between electrodes at fixed, pre-determined distance from the substrates. Three high current sources (100A, 10V) supply the current to the evaporators. A movable shutter is provided to shut off any unintentional deposition of elements on the substrate. The evacuation of the chamber has been achieved by working a 4-inch oil diffusion pump backed by a rotary pump with a pumping speed of 200 liters/minute. The pressure that is attained inside the chamber while the rotary pump is worked is measured using a pirani gauge while the high vacuum obtained after pumping with the diffusion pump is measured employing a penning gauge. There are provisions for ion-bombardment cleaning and substrate heating. The substrate temperature is measured using a fine-wire chromel- alumel thermo couple.

1.3.1.6 Deposition of film

After loading the substrates and elements for evaporation, the chamber is evacuated initially by working the rotary pump. When the pressure has come down to 0.5Torr, high tension is given for cleaning by ion bombardment. As the vacuum increases, the high-tension glow subsides and it is switched off. When the vacuum reaches about 0.001Torr, the evacuation using diffusion pump is started. After ensuring that the pressure is steadily going down the substrate heating is begun. Passing a small current through the heater initially does the heating very slowly. The substrate is given the full current to heat it up to the required temperature 350K only after the pressure has gone down to 10^{-5} Torr. When the stability of substrate temperature is attained at the lowest pressure attainable in the system (10^{-5} Torr) under the present conditions, the source supplies are switched on ensuring that the shutter is in the closed position. The Se source is then switched on and the current is adjusted to a value pre-calibrated through different trials for obtaining a certain incident flux. When sufficient Se atmosphere has been achieved in the chamber, the metal sources are switched on and the current through them adjusted to a pre-determined value to obtain the required incident flux. The shutter is then opened, so that the vapours of the individual elements meet at the

substrate surface and react to form the compound film on the substrate surface. The unreacted elemental atoms or molecules will re-evaporate from the substrate surface due to elevated temperature. Care is taken to keep the substrate and source temperatures stable through out the time of deposition. When the deposition is completed, the shutter is immediately closed and the source currents are adjusted back to zero. The films are slowly cooled back to room temperature in vacuum and then the pumps are shut down stage by stage.

The chamber is opened only after the films are cooled down to room temperature. The films so obtained are handled with care for avoiding contamination and are stored in desiccators for characterizations.



1. Bell jar. 2. Substrate heater. 3. Substrates. 4. Shutter. 5. Boats for Cu and In. 6. Se crucible.

7. Thermocouple. 8. To pump.

Fig.1.1 Vacuum coating unit set up for film deposition.

1.3.2 Structural characterization techniques.

For the structural characterization of the films different methods such as X-ray diffraction (XRD) and X-ray photoelectron spectroscopy (XPS) have been used.

1.3.2.1 X-ray diffraction.

XRD is one of the most powerful and non-destructive tool for the structural analysis of the thin films. By using X-rays of known wavelength λ and measuring θ , the spacing d of various planes in a crystalline sample can be measured.

In the present analysis, the Bragg-Brentano geometry is used for diffraction studies, according to which, the X-ray beam falling with a glancing angle θ on the film is detected by a detector at an angle 2θ with the incident direction of X-rays. The specimen and the detector are rotated at angular velocities ω and 2ω , to get the various diffracting planes. In this geometry when thin films are used, the effective thickness of the films to the incident radiation varies as $t/\sin\theta$, where t is the thickness of the film and θ is the glancing angle of the X-ray beam. This must be taken into account when comparing the experimental intensities with standard data. By noting the positions of the peaks in the XRD profile and comparing with JCPDS data, the different phases formed in the film can be identified.

In addition to phase identification, using the hkl values and the corresponding d -values of the peaks in the XRD pattern, the lattice parameters can be calculated. This enables one to determine the distortion if any, of the crystal lattice, the structure factors as well as the cation-anion bond lengths in the crystal. Thus a complete elucidation of the crystal structure is possible through XRD analysis. The broadening of the peaks is measured to estimate the strain in the films and the grain size of the crystalline / polycrystalline samples [49]. Such an analysis of crystal structure of CuInSe_2 and the related OVC's CuIn_3Se_5 , CuIn_5Se_8 and $\text{CuIn}_7\text{Se}_{12}$ from XRD data that has been obtained when monochromatic $\text{Cu } k\alpha$ radiations are used as source radiation and the X-ray gun has been operated with a 30KV accelerating voltage and 20mA tube current is given in chapters 2 and 5.

1.3.2.2 X-ray photoelectron spectroscopy

XPS has its origin in the investigations of the photo-electric effect in which X-rays were used as the exciting photon source. Using this method, electron binding energies in atoms can be accurately measured from the positions of the peaks and the atomic structure studies can be done [50]. The measurement of chemical shift effect on core level binding energies has enabled in studying the chemical environment of elements in different compounds. If it is assumed that the photoemission process is elastic, X-rays give rise to photo-electron emission according to the equation

$$E_k = h\nu - E_B - \phi \quad 1.1$$

where E_k is the measured electron kinetic energy, $h\nu$ the energy of the exciting radiation, E_B the binding energy of the electron in the solid and ϕ the 'work function'.

An ESCA machine of VSW scientific instruments make with a Mg and Al twin anode X-ray gun as the source has been used for recording the XPS spectra of the samples under study. For obtaining the spectra, the samples for analysis are first loaded into the scraping chamber at atmospheric pressure and the turbo is switched on. When the chamber pressure has come to $\sim 10^{-7}$ Torr, the samples are transferred to sample preparation chamber, in which the base pressure is maintained below 10^{-8} Torr. The argon sputtering on repeated analysis is also given in this chamber after the initial recording of the spectra in the sample analyzing chamber. The analysis is done inside the sample- analyzing chamber by working the X-ray gun at 20A filament current, 10KV high-tension voltage. Recording of the survey scan is carried out setting the multiplier voltage at 2100V. The full scan on the samples are done in the binding energy range 0-10,000 eV with a step width of 1 eV. A band pass energy of 44 eV is used through out the experiments. The detailed scans are recorded with a step size of 0.023 eV in the following binding energy ranges.

$$\text{Cu } 2p \rightarrow 925 \text{ to } 960 \text{ eV}$$

$$\text{In } 3d \rightarrow 438 \text{ to } 460 \text{ eV}$$

$\text{Se } 3d \rightarrow 48 \text{ to } 59 \text{ eV}$. After the initial recording of the spectra on the unetched samples, the samples are again transferred to the sample preparation chamber and Ar etching is done. For this a beam of Ar gas is directed at the surface of the

samples. As a result of the exchange of energy in the surface and subsurface regions, some atoms or clusters of atoms at the surface are given enough kinetic energy to leave the surface and be lost from it. In other words the surface is eroded. The process of erosion of the surface is called sputtering and the source of ions is called an ion gun.

The spectra obtained before and after etching on CIS and OVC's as well as the detailed scans taken on them after etching are analysed in chapters 2 and 5 to get an understanding of the chemical environment of the elements in the compounds.

1.3.3 Compositional and morphological characterization techniques

Since deviations from stoichiometry of the CIS compounds are found to produce changes in the optoelectronic properties of the samples, knowledge of the sample composition is essential to evaluate the performance of the films of different compositions when used in device fabrication. In the present investigations, the compositional analysis has been done using EDAX. For morphological studies, atomic force microscopy (AFM) as well as scanning electron microscopy (SEM) has been used.

1.3.3.1 Energy dispersive analysis of X-rays.

In EDAX the samples are bombarded with electrons accelerated from an electron gun, so that X-rays characteristic of the atoms in the samples are emitted from the irradiated area and are detected and analysed. In the present investigations using EDAX machine of Cambridge instruments model no: LINK 10,000, which uses K-ray for Cu and L-rays for In and Se as standards, the compositional analysis has been done with an error less than 2%. The EDAX spectra obtained on the samples and further discussions are given in chapters 2 and 5.

1.3.3.2 Scanning electron microscopy

The technique is a useful tool for studying the surface features of the films, as the micrographs obtained will be a faithful reproduction of the surface features of the films. The secondary electrons emitted on bombardment of the sample surface with accelerated electrons from an electron gun are collected by appropriate detectors and the output is used to modulate the brightness of a cathode ray tube (CRT) whose x-y inputs are driven synchronously with the x-y voltages rastering the electron beam. Thus

the image produced on CRT is mapped directly to the corresponding point on the sample. The image magnification is given by the ratio of the display tube dimension to the distance the beam is scanned on the specimen [51]. The samples used for scanning by this method ought to be vacuum compatible as well as conducting. If the samples are highly resistive, there will be charge build up on the sample surface and hence a thin conducting layer of gold or silver has to be deposited on the surface to make the samples conducting . A Cambridge instruments Model no: S-360 machine has been used for taking the micrographs and the scanned micrographs of different samples under study are given in chapters 2 and 5.

1.3.3.3 Atomic force microscopy

Atomic force microscope has the ability to create three-dimensional micrographs with resolution down to nanometer and angstrom scales in applications ranging from semiconductor processing to cell biology. In addition to this topographical imaging, the AFM can also probe nanomechanical and other fundamental properties of sample surfaces, including their local adhesive or elastic properties.

A key element of the AFM is its microscopic force sensor, or cantilever. Mounted on the end of the cantilever is a sharp tip that is used to sense a force between the sample and the tip. The laser-beam is positioned on the back of the cantilever, with a spot visible on the head's filter screen. There are different ways of topographic imaging like 'in contact mode' where the probe tip is brought into continuous or intermittent contact with the sample and raster-scanned over the surface or "tapping mode and non-contact AFM' where oscillating probe systems are used. Fine motion piezoelectric scanners are used to generate topographic images and force measurements. A piezoelectric scanner is a device that moves by a microscopic amount when a voltage is applied across its electrodes. Depending on the AFM design, scanners are used to translate either the sample under the cantilever or the cantilever over the sample. Piezoelectric scanners for AFM's usually can translate in three directions (x,y and z axes) and come in different sizes to allow maximum scan ranges of 0.5 to 125 μ m in the x and y axes and several microns in the vertical axis.

By scanning the AFM cantilever over a sample surface and recording the deflection of the cantilever, the local height of the sample is measured. Three-

dimensional topographical maps of the surface are then constructed by plotting the local sample height versus horizontal probe position. Other imaging techniques are also used including measuring the change in amplitude or phase of an oscillating cantilever, using Tapping Mode. In addition, often the AFM is used to record the amount of force felt by the cantilever as the probe tip is brought close to – and even indented into – a sample surface and then pulled away, which will help in elucidating local chemical and mechanical properties like adhesion and elasticity.

In the present investigation, elaborated in section 2.5.2, the ‘in contact method’ is used for obtaining atomic force micrographs in which the multimode head is fitted with a contact AFM probe tip and the laser beam is positioned on the back of the cantilever, with a spot visible on the head’s filter screen. The adjustment screws are used to adjust the tip’s height just above the sample surface and a magnifier is used to monitor the tip while this is done. The tip should be positioned just high enough to reach the surface when engaged, but not so low as to risk crashing into it. In the current case, silicon nitride cantilevers have been employed for the contact AFM study.

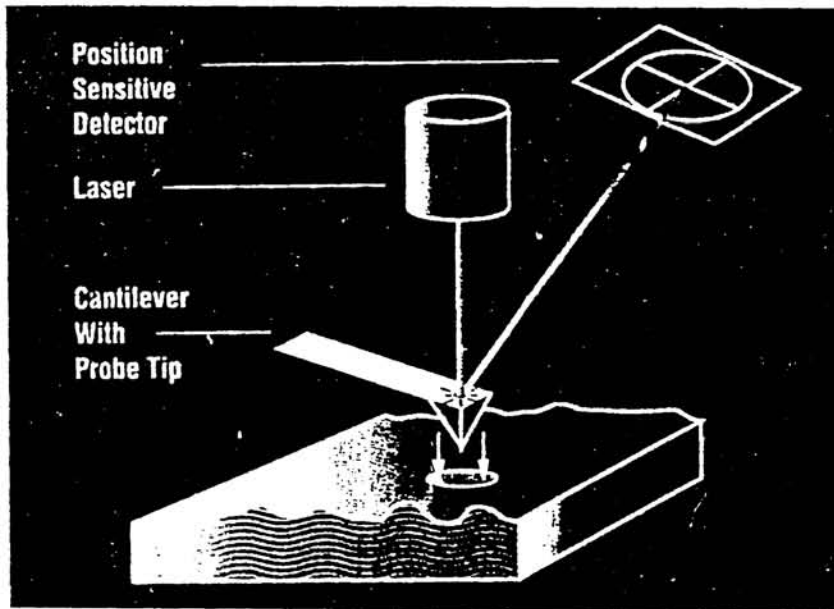


Fig.1.2 Schematic of an AFM showing the force sensing cantilever.

1.3.3.4 Thickness measurement

When two reflecting surfaces are brought into close proximity, interference fringes are produced, the measurement of which makes possible a direct determination of the film thickness and surface topography with high accuracy [1]. Tolansky's interference – fringe methods that is now accepted as one of the absolute standard methods has been employed for thickness measurement in the present investigation.

The Fizeau fringes of equal thickness obtained in an optical arrangement as shown in Fig.1.3 has been utilized for thickness measurement. In this, the interferometer consists of two slightly inclined optical flats, one of them supporting the film, which forms a step on the substrate. When the second optical flat is brought in contact with the film surface, and the interferometer is illuminated with a parallel monochromatic beam at normal incidence and viewed with a low-power microscope, dark fringes can be observed which trace out the points of equal air-gap thickness. The two adjacent fringes are separated by $\lambda/2$. If the surfaces of the optical flats are highly reflecting, with the upper flat possessing an observable transmission, and the relative positions of the flats are adjusted to form a wedge- shaped air gap, the fringes can be made to run in straight lines perpendicular to the steps on the opaque film. This displacement expressed as a fraction of the $\lambda/2$ fringe spacing gives the film thickness and it can be measured to about tenth of a fringe. Thus the thickness of the film

$$t = (d/D)(\lambda/2) \qquad 1.2$$

where D is the fringe spacing, d is the fringe shift and λ the wave length of monochromatic light used. Certain conditions are to be satisfied to obtain sharp interference fringes, ie. it is necessary to coat the film as well as the exposed glass surface uniformly with equal thickness and with the same reflecting layer (of high reflectivity) in order that phase changes on reflection from the two sides of the step will be the same.

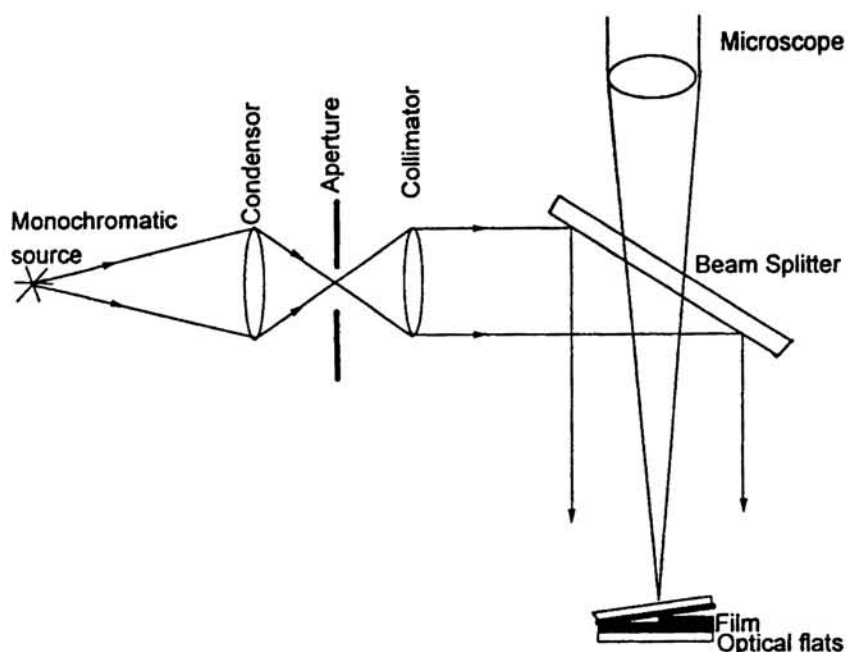


Fig.1.3 Arrangement for thickness measurement.

1.3.4 Optical measurements

1.3.4.1 Measurement of optical constants

Optical constants of any material are characterized by two parameters viz. n and k which form the real and imaginary parts of the complex refractive index $n^* = n - ik$ and the optical absorption coefficient α . There are different methods for determination of optical constants like spectroscopic ellipsometry, simultaneous measurement of transmission and reflection, and measurement of transmission and absorption etc. In the present investigation, the optical constants are calculated from the transmission spectrum using a method developed by Swanepoel [52]. According to this method the transmission spectrum on the thin film of the material under study deposited on a transparent substrate is taken using Hitachi U-3410 UV-Vis- NIR spectrophotometer at room temperature. The system of an absorbing thin film on a transparent substrate is shown in Fig.1.4.

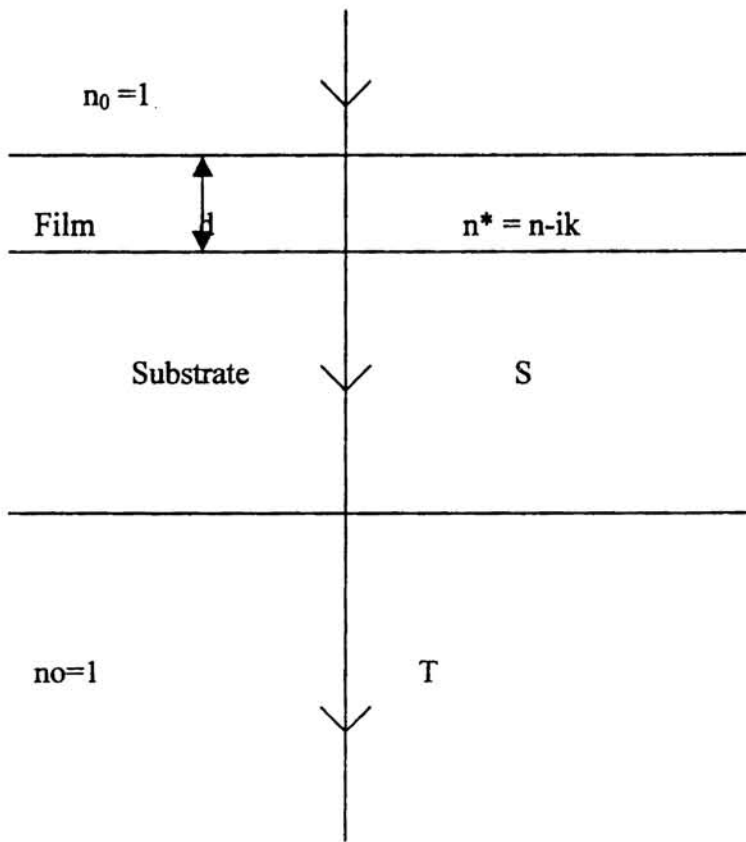


Fig.1.4 System of an absorbing thin film on a thick finite transparent substrate.

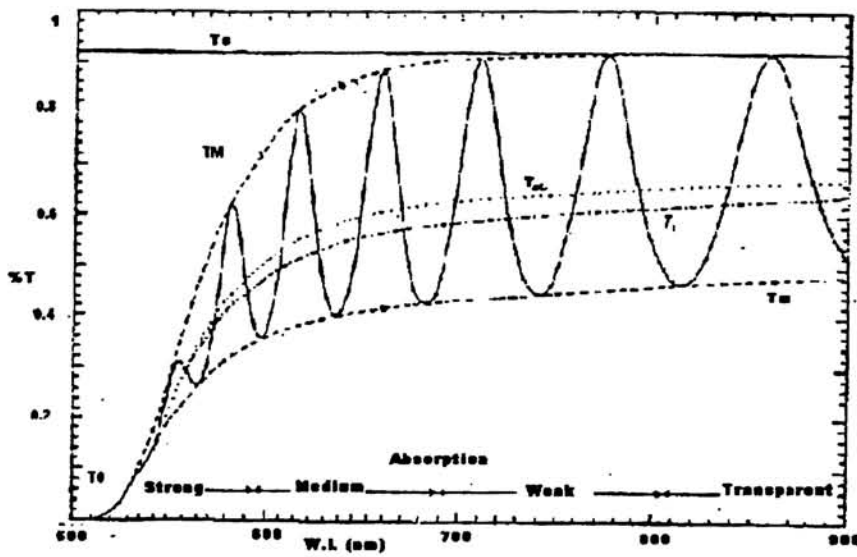


Fig.1.5 Typical transmission spectrum for a thin film of uniform thickness.

Different regions of transmission spectrum are divided into strong, medium, weak and transparent. In the region of weak and medium absorption, the absorption coefficient $\alpha \neq 0$ and the absorbance given by

$$x = \exp(-\alpha d) \quad 1.3$$

is less than 1. If the envelopes of the maxima of the transmission spectrum and minima of the spectrum are drawn and transmission corresponding to a particular wave length λ are taken from these envelopes for maxima and minima as T_M and T_m respectively, then, the refractive index of the film can be determined as

$$n = [N + (N^2 - s^2)^{1/2}]^{1/2} \quad 1.4$$

where

$$N = 2s[(T_M - T_m)/T_M T_m] + [(s^2 + 1)/2] \quad 1.5$$

where s is the refractive index of the substrate which can be evaluated from the transparent region of the spectrum using the equation,

$$T_M = 2s/(s^2 + 1) \quad 1.6$$

Once $n(\lambda)$ is known, the absorbance x can be calculated as

$$x = \{E_M - [E_M^2 - (n^2 - 1)^3(n^2 - s^4)]^{1/2}\} / (n - 1)^3(n - s^2) \quad 1.7$$

where

$$E_M = (8n^2 s / T_M) + (n^2 - 1)(n^2 - s^2) \quad 1.8$$

The absorption coefficient α corresponding to each wavelength can be calculated by substituting the x values in equation 1.3. For this the thickness of the film can be determined by the interferometry technique described in the preceding section or from the value d evaluated by Swanepoel's method where

$$d = \lambda_1 \lambda_2 / [2(\lambda_1 n_2 - \lambda_2 n_1)] \quad 1.9$$

But the value of d determined using eqn.1.9 will not be very accurate and successive iterations are needed.

The extinction coefficient k can be calculated using the values of α corresponding to each λ values employing eqn.1.10

$$K = \alpha \lambda / 4\pi \quad 1.10$$

In the region of strong absorption the interference fringes disappear and values of n can be estimated by extrapolating the values calculated in the other parts of the spectrum. The values of x can then be calculated. For very large α four curves T_M , T_α , T_i and T_m converge to a single curve T_0 . If interference effects are ignored,

$$x = [(n+1)^3 (n+s^2)] T_0 / (16n^2s) \quad 1.11.$$

Thus the method outlined above helps in obtaining the optical constants of the film corresponding to the entire wavelength region.

In addition to the optical constant evaluation, the band gap of the compounds are also determined using optical absorption studies, for which the optical absorbance spectra has been recorded on Hitachi U-3410 UV-Vis- NIR spectrophotometer at room temperature. The determination of band gaps on various compounds is explained in chapters 3 and 6.

1.3.4.2 Photoconductivity set up

The photoconductivity measurements are done by loading the sample in the cryostat and applying silver paste at the two ends of the sample for ohmic contacts. The two-probe technique has been used in the present investigation since the samples being of high resistivity and having a regular shape, the contact resistance can be neglected. The block diagram for the photoconductivity measurement is shown in Fig.1.6.

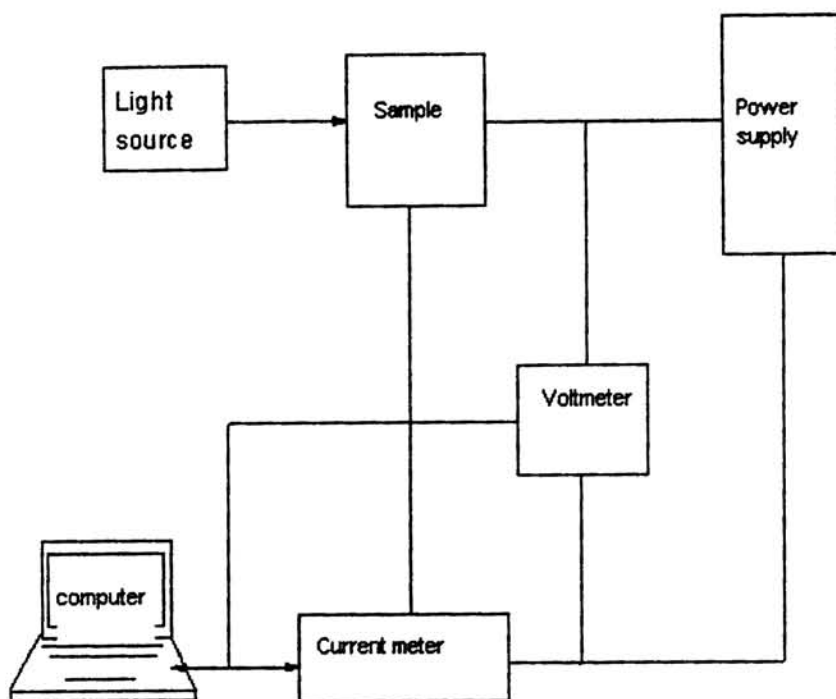


Fig.1.6 Block diagram showing photoconductivity set up.

The liquid He cryostat is switched on only after obtaining sufficient vacuum (10^{-6} Torr) in the chamber by pumping down using a diffusion pump coupled with a rotary pump. A Keithley 236 source measurement unit has been used for voltage supply and for current measurements. The linearity check up for ascertaining the ohmic contact is also done by the Keithley unit. The sample is initially cooled down to 10K and then heated to different temperatures at which measurements are taken using a Lakeshore programmable temperature controller. A 100W Oriel quartz halogen source has been used for the illumination of the samples for steady state and transient photoconductivity. The source has been coupled with an Oriel 7240 grating monochromator for spectral response measurements. The dark current measurement for photosensitivity determination has also been done using the same set up before

illuminating the samples. The experimental results are given in detail in chapters 3 and 6.

1.3.4.3 Photoluminescence measurements

Photoluminescence measurements can provide an excellent means to identify the native defects in the film. In the present set up PL measurements are carried out at room temperature with a Nd-Yag frequency doubled 532nm laser. The analysis of the PL signal has been done using an NIR 512 spectrophotometer Ocean optics and an OOI base 32 soft ware has been used for recording the spectrum.

1.3.5 Electrical measurements

The two standard measurements that are usually taken on semiconductors are the electrical resistivity and the Hall coefficient. The Hall coefficient measurements will enable us to calculate the effective density of charge carriers as well as the carrier type, where as resistivity variation with temperature is suitable for obtaining information regarding the intrinsic band gap, the defect levels present etc. in semiconductors [53].

1.3.5.1 Conductivity measurements

The conductivity at various temperatures is dependent not only on the carrier concentration but also on the mobility of charge carriers. At high temperatures most of the carriers are excited intrinsically but as the temperature is reduced this source of carriers is rapidly removed and the conductivity reduces. This reduction does not continue indefinitely in the same manner as the impurity excitation is still present and this will maintain a certain number of carriers in the conduction band. As the temperature is reduced the mobility of carriers increases and hence there may be a slight increase in conductivity. At low temperatures intrinsic conduction does not occur and the conductivity will be determined by excitation of carriers from defect levels. At very low temperatures, temperature independent hopping conduction mechanisms often sets in.

The conductivity measurements have been done by two probe method where samples of dimension about 4×2 mm have been used with silver paste for ohmic contacts. Low temperature conductivity measurements are done during the heating cycle employing Keithley 617 programmable electrometer for resistance measurement

and Lakeshore DRC-93 CA controller for temperature control. The pressure inside the cryo has been kept of the order of 10^{-6} Torr by working a diffusion pump backed up by a rotary pump. The measurement in Vacuum is always advisable; otherwise the humidity present in the atmosphere may short circuit the specimen giving higher values of conductivity.

1.3.5.2 Hall coefficient measurements

If a current flows along a semiconductor which is in a magnetic field whose direction is perpendicular to the direction of current flow, then an emf, the Hall emf is generated across the specimen in a direction perpendicular to the magnetic field, i.e., the current, the magnetic field and the Hall emf are mutually perpendicular. This phenomenon is called the transverse Hall effect. In general terms it is quite simple. The application of the magnetic field will cause the moving charges to deviate from their motion along the specimen and their paths will curve towards the sides, where a space charge will accumulate. This will produce an electric field, which will eventually be sufficient to counteract the effect of the magnetic field on the other moving charges, and they will then traverse the length of the specimen without deviation. It is this electric field due to the space charge at the sides of the specimen that will give rise to the Hall emf. The sign of Hall constant measured will depend on the sign of charge carrier while the magnitude is inversely proportional to density of charge carriers (n) by the equation $R_H=1/(ne)$.

Hall Van Der Pauw controller together with a programmable power supply and programmable temperature controller have been used for the Hall experiments on the samples. Films of dimension $1\text{cm} \times 1\text{cm}$ have been used for the measurement of Hall voltage when magnetic field and electric field are applied at right angles in a four-probe arrangement, by using silver paste for contacts. A magnetic field $\sim 2000\text{G}$ and current in the range 10^{-6}A to 10^{-11}A are used for the measurement. After the initial linearity check, the magnetic field is applied and readings are taken on mobility and density of carriers, the Hall coefficient, resistivity and sheet resistance of the samples. The type of the carriers is also determined noting the sign of carriers.

1.4 Conclusion

This chapter gives an outline of the investigations done by various researchers on chalcopyrite compounds and presents the motivation behind undertaking the present work. The various experimental techniques adopted in the present investigation are briefed in section.1.3.

References

- [1] K.L.Chopra, *Thin Film Phenomena*, McGraw- Hill, New York (1969) p.1-15.
- [2] J.L.Shay and J.H.Wernick, *Ternary Chalcopyrite Semiconductors: Growth, Electronic properties and applications* (pergamon, Oxford, 1974).
- [3] A.Miller, A.MacKinnon and D.Weaire, in *Solid State Physics*. edited by H.Ehrenreich, F.Seitz and D.Turnbull (Academic, New York, 1981), 36 p.119.
- [4] B.R.Pamplin, *Prog.Crystal Growth Charact.*1(1979)331.
- [5] E.Parthe, *Crystal Chemistry of Tetrahedral Structures* (Gordon and Breach, New York, 1964).
- [6] J.E.Jaffe and A. Zunger, *Phys.Rev.B*, 29 (1984) 1882.
- [7] C.Rincon, J.Gonzalez and G.S.Perez, *Phys.Status Solidi (b)* 108, (1981) K19.
- [8] R.A.Mickelsen and W.S.Chen, in *proceedings of the Fifteenth IEEE photovoltaic Specialists Conference-1981* (IEEE, New York, 1981) p880
- [9] J.L.Shay and H.M.Kasper, *Phys.Rev.Lett.*29 (1972) 1162.
- [10] J.L.Shay, B.Tell, H.M. Kasper and L.M.Schiavone, *Phys.Rev.B*, 5 (1972) 5003.
- [11] J.E.Jaffe and A.Zunger, *Phys.Rev.B*, 27(1983) 5176.
- [12] M.I.Alonso, K.Wakita, J.Pascual, M.Garriga and N.Yamamoto, *Phys.Rev.B*, 63 (2001) 075203-1.
- [13] D.J. Bottomley, A.Mito, S.Niki and A.Yamada, *J.Appl.Phys.*82 (1997) 817.
- [14] S.C.Erwin and I.Zutie, *J. Appl. Phys.* 48 (1977) 1395.
- [15] D.J.Schroeder, J.L.Hernandez, G.D.Berry and A.A. Rockett, *J.Appl.Phys.*83 (1998) 1519.
- [16] C.Guillen and J.Herrero, *J.Appl.Phys.* 71 (1992) 5479.
- [17] C.Rincon, S.M.Wasim, E.Hernandez, M.A.Arsene, F.Voillot, J.P.Peyrade, G.Bacquet and A.Albacete, *J.Phys. Chem.Solids*, 59 (1998) 245.
- [18] G.Masse, *J.Appl.Phys.*68 (1990) 2206.
- [19] J.H.Schon, V.Alberts and E.Bucher, *J.Appl.Phys.*81(1997) 2799.
- [20] P.Lange, H.Neff, M.Fearheiley and K.J. Bachmann, *Phys.Rev.B*, 31 (1985) 4074.

- [21] J.H.Schon and E.Bucher, *J.Phys.D:Appl.Phys.*34 (2001) 25.
- [22] S.B. Zhang; S.H.Wei and A. Zunger. *Phys.Rev.B.* 57 (1998) 9642 .
- [23] J.M.Merino, S.Mahanty, M.Leon, R.Diaz, F. Rueda, J.L.Martin de Vidales, *Thin Solid Films* 361(2000) 70.
- [24] J.Hedstrom, H.J.Olsen, M.Bodegard, A.Kylner, L.Stolt, D.Hariskos, M.Ruekh and H.W.Schock, *The Conference Record of the Twenty-third IEEE photovoltaic Specialists Conference (IEEE, New York,1993).* p.364.
- [25] A.M.Gabor, J.R.Tuttle, D.S.Albin, M.A.Contreras, R.Noufi and A.M.Hermann, *Appl.Phys.Lett.*65, (1994) 198.
- [26] H.Neumann, N.V. Nam, H.Hobler and G. Kuhn, *Solid State Commun.*,25 (1978) 899.
- [27] H.Neumann, R.D.Tomlinson, N.Avgerinos and E.Nowak, *Phys.Status Solidi A* 75 (1983) K199.
- [28] C.Rincon and J.Gonzalez, *Phys.Status Solidi B* 110 (1982) K171
C.Rincon and C.Bellabarba. *Phys.Rev. B* 33 (1986) 7160.
- [29] P.W.Yu, *Solid State commun.*18 (1976)395 C.Rincon, J.Gonzalez and G.S.perez, *J.Appl.Phys.*54 (1983) 6634.
- [30] A.Li and J.Shih, *J.Electron. Mater.* 22 (1993) 195.
- [31] L.S.Palatnik and E.J.Rgacheva, *Dokl. Akad. Nauk SSSR*, 174 (1967) 80.
- [32] W.Honle, G.Kuhn and U.C.Boehnke, *Cryst.Res.Technol.* 23 (1988) 1347.
- [33] S.Normura and S.Endo, *Trans.MRS Jpn* 20 (1996) 755.
- [34] T.Hanada, A.Yamana, Y.Nakamura, O.Nittono and T.Wada, *Jpn.J.Appl.Phys.*36 (1997) L1494.
- [35] C.Manolikas, J.V. Landuyt, R. De Ridder and S.Amelinckx, *Phys. Stat. Sol. (a)* 55 (1979) 709.
- [36] N.Frangis, G.Van Tendeloo, C. Manolikas, J. Van Landuyt and S. Amelinckx,, *Phys. Stat.Sol.* 96 (1986) 53.
- [37] J.C.W. Folmer, J.A.Turner, R.Noufi and D. Cahen, *J.Electrochem.Soc.*132 (1985) 2281.
- [38] B.H.Tseng and C.A Wert, *J.Appl.Phys.* 65 (1989) 2254.
- [39] Z.A.Shukni, *SOLMAT*, 37 (1995) 395.

- [40] R.Schaffler, Mater.Sci. Forum 173-174 (1995) 135.
- [41] R.N.Battacharya, J.Electrochem.Soc. 143 (1996) 854.
- [42] K.Kushiya Japan.J.Appl.Phys.35 (1996) 4383.
- [43] S.Zweigart , J.Crystal growth, 146 (1995) 233.
- [44] Y.Okano SOLMAT,50 (1998)105.
- [45] T.Nakada, Jap.J.of Appl.Phys.34 (1995) 4715.
- [46] D.Schmid, M.Ruekh, F.Grunwald and H.W.Schock, J.Appl.Phys. 73.
- [47] K.G.Gunther, The use of thin films in physical investigations, J.C.Anderson (Ed), Academic press, London,1966; pp.213.
- [48] R.Glang, Hand book of Thin Film Technology, L.I. Maissel and R.Glang (Eds.), Mc Graw Hill, New York, 1970, p.1-81.
- [49] B.D.Cullity, Elements of x-ray diffraction, Addison-Wesley publishing company Inc, U.S.A, 1956.
- [50] D.Briggs and M.P.Seah, Practical surface analysis by auger and X-ray photoelectron spectroscopy, John Wiley and sons, Chichester (1987).
- [51] J.H.Richardson and R.V.Peterson, Systematic Materials Analysis, Vol.2, academic press, New York and London (1974) pp163.
- [52] R.Swanepoel, J.Phys.E.Sci.Instrum. 16 (1983) 1214.
- [53] H.M.Rosenberg, Low temperature solid state physics, OXFORD at Clarendon press (1965) Britain.

Preparation and structural characterization of CuInSe_2 thin films.

2.1 Introduction

CuInSe_2 being a prototype member of the family of I-III-VI chalcopyrite semiconductors is known to resemble the Zinc-blende structure, with two cations A and B co-ordinated tetrahedrally by four anions C. The crystal structure of these compounds (ABC_2) belongs to space group D_{2d}^{12} ($I \bar{4}2d$) with eight atoms per unit cell [1]. The space group symbol [2] represents a body centered tetragonal system having a four fold axes along c, diamond glide plane normal to $[100]$ and $[010]$ and a rotation diad normal to $[110]$ and $[1 \bar{1}0]$. In CuInSe_2 each anion C is coordinated by two A and two B cations where as each cation is tetrahedrally coordinated by four anions. Unlike their binary II-VI analogues, the chalcopyrite having two cation sublattices often has a tetragonally distorted unit cell [3]. The anion is displaced from their ideal tetragonal site and the anion-cation bond lengths are mostly unequal. Many optical, electrical and photoconducting properties shown by these compounds are intrinsically associated with their mode of construction and structural properties. Hence in this chapter, we present a brief description of the preparation technique of the films and a detailed analysis of their structure along with compositional and morphological characterization.

2.2 Three Source Vacuum Evaporation

(Gunther's 3-temperature method-a modified form).

The method used for the preparation of CuInSe_2 films for our studies is 3-source vacuum co-evaporation, which is a modified form of Gunthers's three- temperature method [4]. The details of the method are given in section 1.3.1 of the earlier chapter. In the present case, the temperature of the three boats and the heated substrate is properly controlled throughout the time of deposition, in order to obtain good quality films.

One advantage of this method is that the tedious process of synthesis of the compound from elements prior to deposition is eliminated. Since the elements as such are evaporated, the requirement of high temperature for evaporation of compound and subsequent decomposition often involved with this can be ruled out. One disadvantage of the method is that because of high volatile elemental pressure, some unreacted volatile component is likely to be trapped in the growing film, changing the properties of the film especially at low substrate temperatures. Also determination of the temperatures of the evaporators for achieving control over the incident flux rate that will give rise to a particular composition of the compound can be done only by different trials.

2.3 Preparation of CuInSe₂ Thin films

For the preparation of CuInSe₂, we employed a vacuum coating unit with three separate evaporators for the three elements Cu, In and Se and an arrangement to control and keep constant the substrate temperature. The incident elemental fluxes of the evaporants are independently controlled by separately monitoring the temperatures of two molybdenum boats that are used as the sources for the evaporation of 99.999% pure elemental Cu and In and a glass crucible kept in a molybdenum basket that has been used for evaporating 99.99% pure elemental Se. Constant, pre-determined elemental flux has been maintained through out the deposition for each type of films to prevent any intentional grading of composition through the films. The sources, substrate holder, the shutter are all arranged inside a 12-inch glass bell jar. The detailed description of the vacuum coating unit and deposition technique is given in chapter.1.

With proper control of the source temperatures and maintaining a suitable substrate temperature and high vacuum, the reproducibility and purity of the thin films can be ensured. Since factors such as cleanliness of the substrates, cleanliness of the vacuum coating unit and the sources, the cooling process of the films etc. affect the reproducibility and the quality of the films [5], proper care has been taken in this area also. The details of the preparation of substrates, boats etc prior to deposition of the films are given in chapter.1. In the present work, we have used optically flat soda-lime glass slides as substrates. They are low cost and stable at moderate temperatures. But often, sodium diffusion from the glass substrates to the film has been observed. But

since Na diffusion is found to improve the electrical conductivity of the films, those films are also used for the studies.

The films deposited as described in chapter.1, are labeled and properly stored in desiccators taking care not to contaminate them till further characterizations are done.

2.4 Compositional analysis

In CuInSe_2 , composition determination is of primary importance since this chalcopyrite displays interesting variation in optical and electrical properties with compositional differences. In addition to the fact that CuInSe_2 can be made n-type or p-type by varying the composition that is doping the samples merely by native defects, the compound tolerate a large range of anion to cation off stoichiometry leading to the existence of a number of ordered defect compounds [6]. Hence composition determination of the films is essential to explain many optoelectronic phenomena observed in them.

Here the compositional analysis of the films is made by energy dispersive X-ray analysis (EDAX). Though composition of the films can be determined from X-ray photoelectron spectroscopy also, since Argon sputtering is found to reduce the Se content in the film, we relied on the EDAX data for the composition determination of our films. The films are classified into two categories based on the percentage atomic concentration of Cu to In and studies are made on typical samples from both Cu-rich side and In-rich side. Such a classification is done since many interesting variations in properties are observed with variation in Cu: In ratio keeping the Se percentage a constant.

2.4.1 Energy dispersive analysis of X-rays

The composition determination has been done by an EDAX machine of Cambridge Instruments Model no: LINK 10,000 which uses K-ray for Cu and L-rays for In and Se as standards. The EDAX spectra obtained on four samples of CuInSe_2 with different compositions –two from the Cu-rich side and the other two from the In-rich side are shown in fig.2.1 a –d. The structural determination of the films using XRD shows that when the Cu exceeds often copper selenide phases are present and when In exceeds indium selenide phases co-exist with CuInSe_2 . We refer to the CuInSe_2 samples as

either Cu-rich or In-rich throughout the descriptions since the samples obtained slightly deviated from the Cu: In: Se=25: 25: 50 atomic composition but in all these samples CIS is the dominant or the only phase. The formation of the ordered vacancy compounds with very large variation from stoichiometry is dealt with in Chapter.5. If the $\{[In]/[Cu]}\text{-1}$ lies between 0.2 to 0.5, then the

Samples are said to be In rich and if the value is lesser but positive, then the samples are termed 'slightly In-rich'.

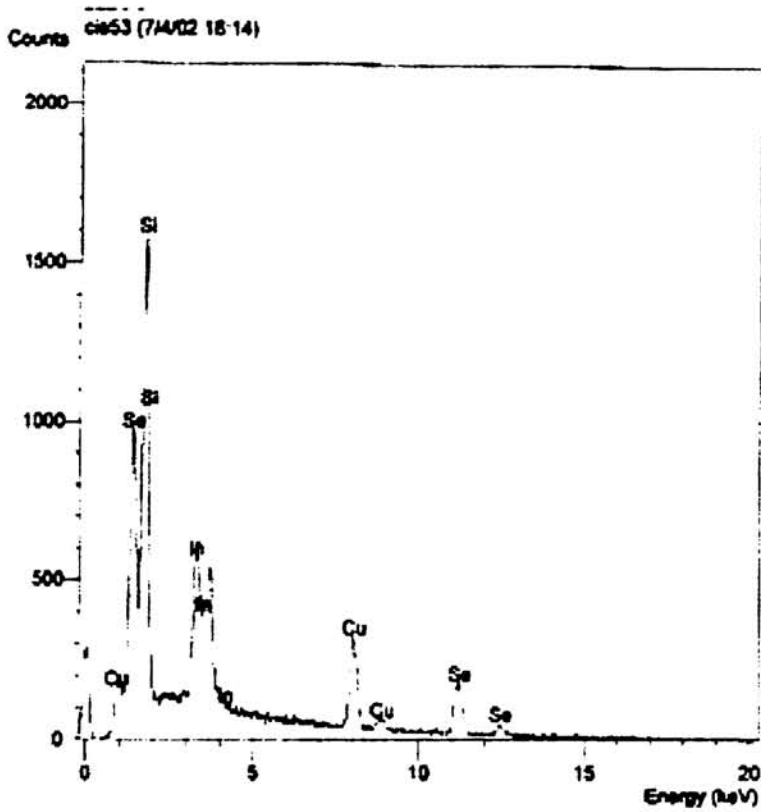


Fig.2.1a EDAX spectra on a Cu rich film with at% Cu: In: Se= 31:20:49

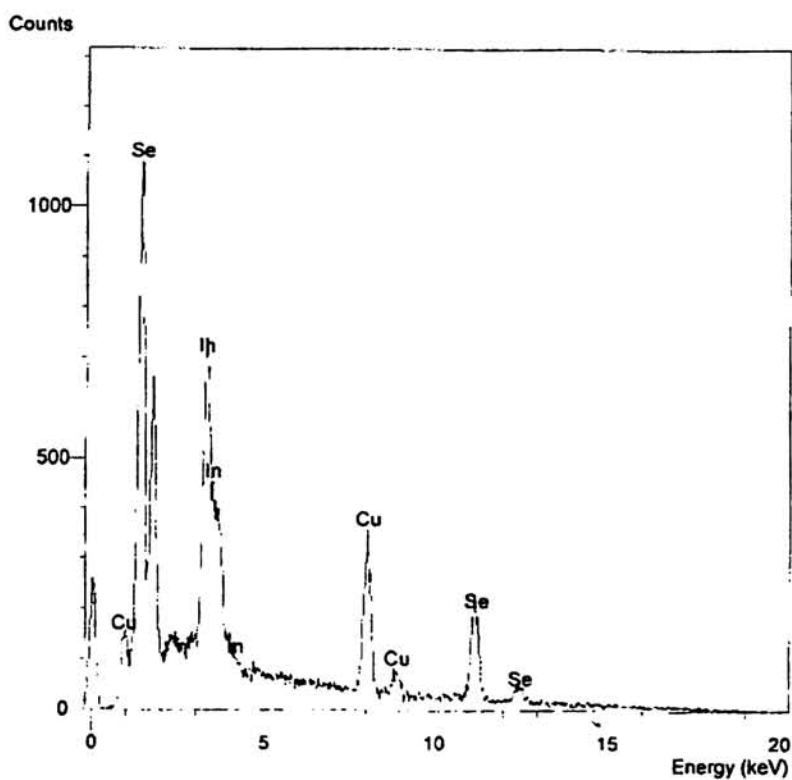


Fig.2.1b EDAX on a slightly Cu rich film with Cu:In:Se= 27:24:49

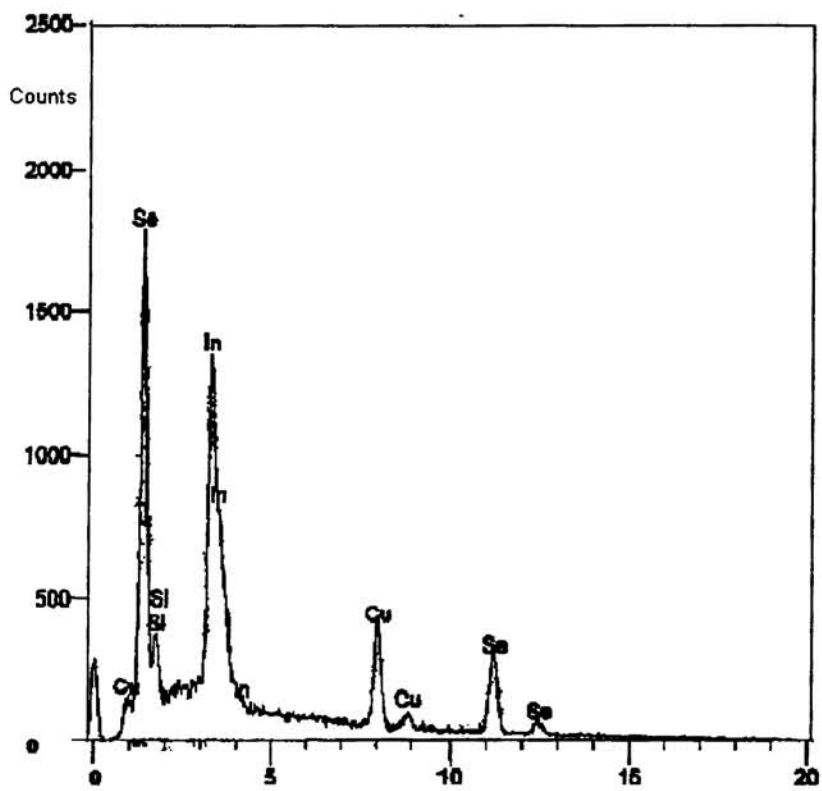


Fig.2.1c EDAX spectra on an In rich film with at% Cu: In: Se= 24:27:49

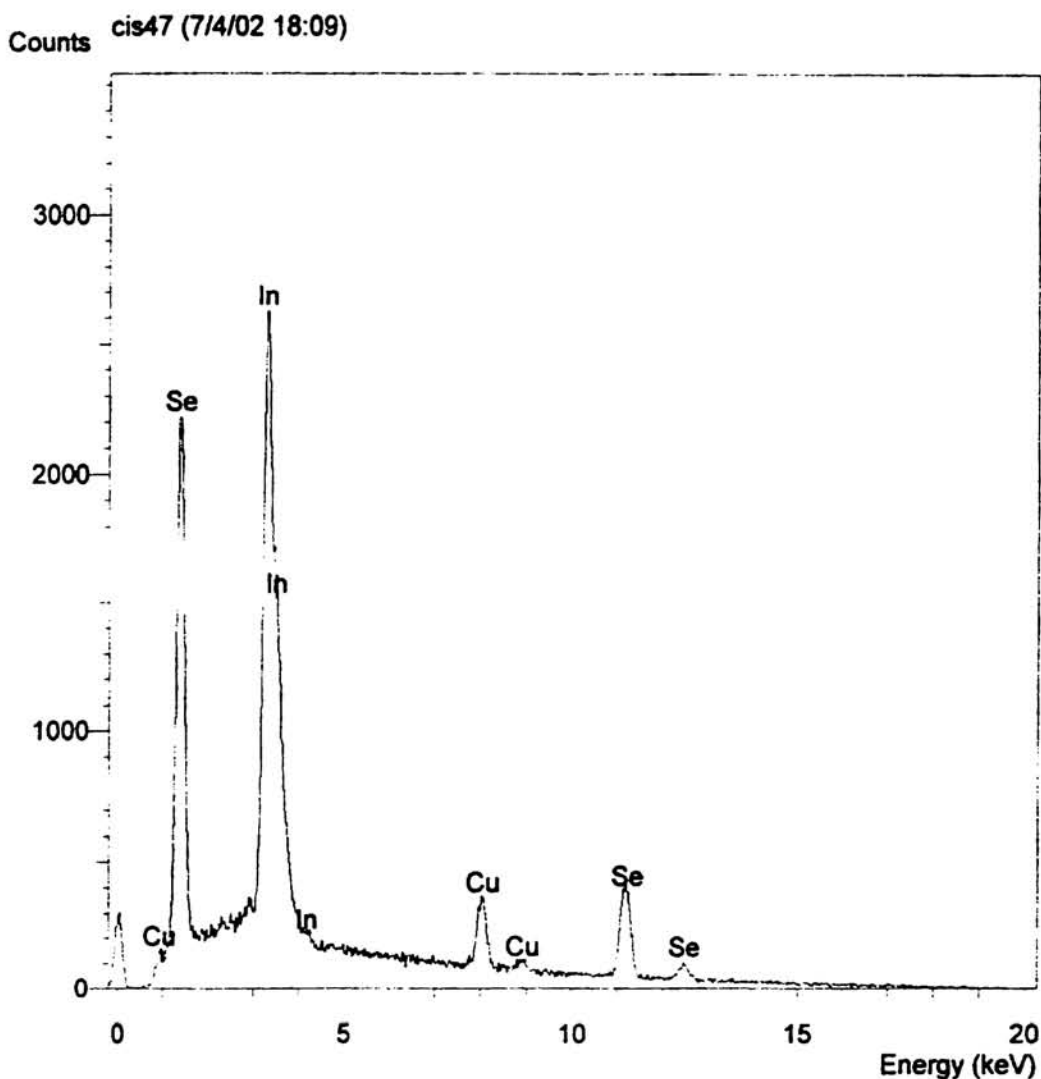


Fig.2.1d EDAX spectra on an In rich film with at% Cu: In: Se= 14:37:49

2.5 Morphological Characterization

The morphological studies are important in the case of thin films for analyzing the grain size, the surface properties etc. that has a profound influence on the transport properties as well as the optical properties of the film, which determines the scope of the films in various device applications. In the present study, the morphological characterization of the films, which to the naked eye appeared to be uniform, is done by atomic force microscopy and scanning electron microscopy.

2.5.1 Scanning electron microscopic studies

In this technique, the secondary electrons are emitted from the surface layer of the films and hence the micrographs obtained will be a faithful reproduction of the surface features of the films.

The scanning electron micrographs of CuInSe_2 with different compositions are shown in the fig.2.2 a and d. The average grain size of CuInSe_2 calculated from SEM in the Cu-rich films is around 0.4 to 0.45 μm which is found to be larger than that measured for In-rich films that is around 0.2 to 0.27 μm . The reduction in grain size with increase in In content is in conformity with the observations made by different investigators on CuInSe_2 [7]. The larger grains appearing in Fig.2.2a are probably that of CuSe_2 grains present in the very Cu rich samples

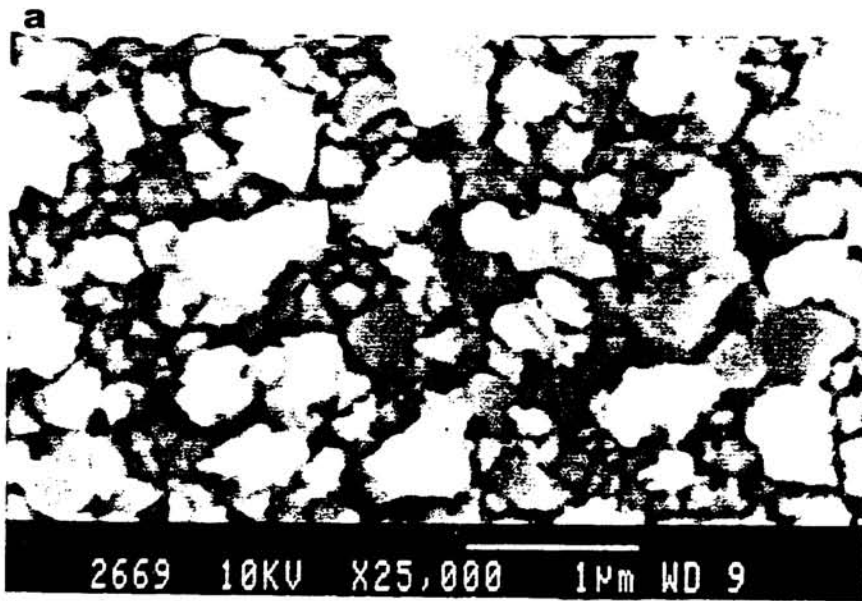


Fig.2.2a SEM on a Cu-rich CuInSe_2 thin film.

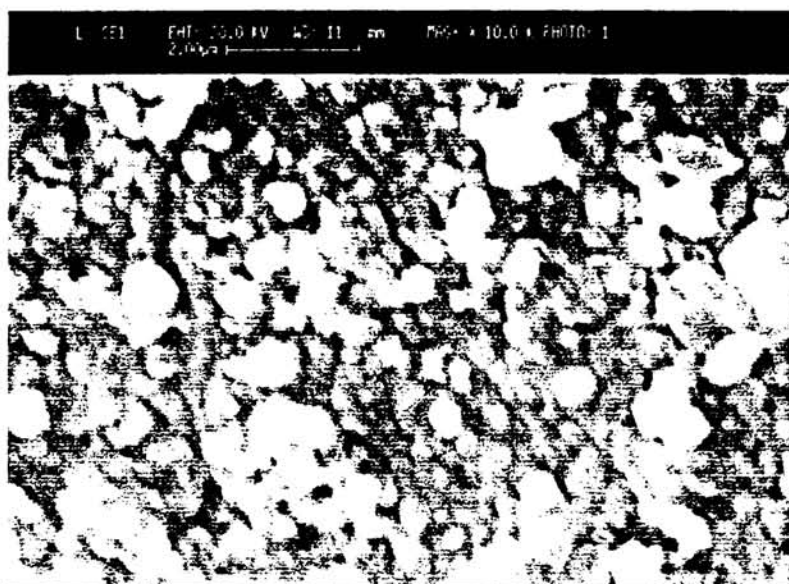


Fig.2.2b SEM on a slightly Cu- rich CuInSe_2 thin film.

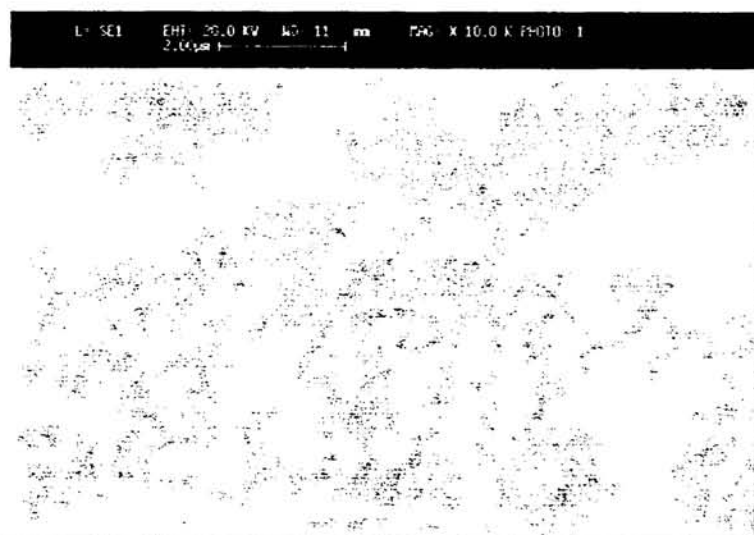


Fig.2.2c SEM on a slightly In-rich CuInSe_2 film.

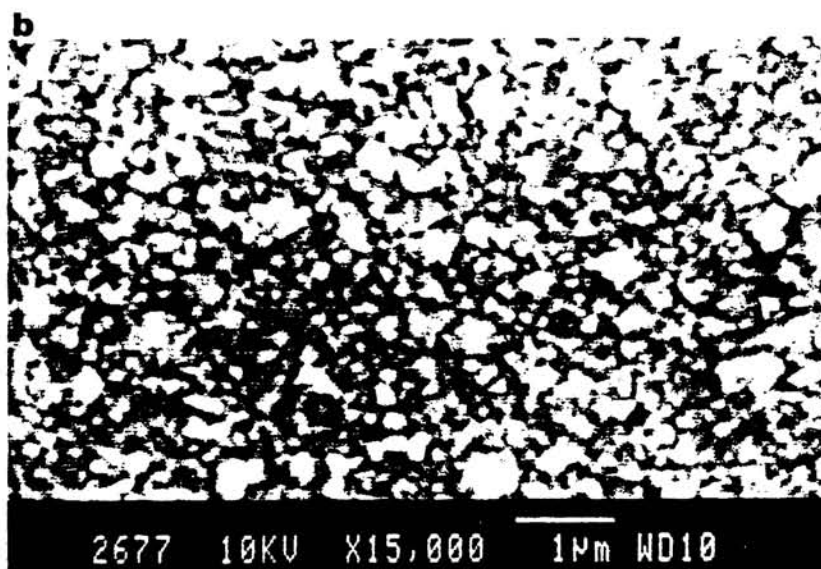


Fig.2.2d SEM on an In-rich CuInSe_2 sample.

2.5.2 Atomic Force Microscopy

The ability of the atomic force microscope to create 3-dimensional micrographs with resolution down to the nanometer and Angstrom scales has made it an essential tool for imaging surfaces. In the present study, we used “in contact mode AFM” where the probe tip is brought in contact with the sample surface as explained in section.1.3.3.3, to image the surface features of the thin film samples. An AFM Nanoscope E, Digital Instruments, with a silicon nitride cantilever has been employed to probe different portions of the film surface. The granular nature of the films is evident from the micrographs. The grain size as well as the root mean square values of the surface roughness of the films from a number of scans from different areas of the films is determined. It is a known fact that surface roughness is an important parameter that affects the light scattering property of the material.

The 3-dimensional images helps in determination of the roughness parameter as well as enables in a comparison of the thickness of the films with the surface roughness. The 2-dimensional images help in visualizing the grain size of the films. The 3-D and 2-D atomic force micrographs taken on CuInSe_2 films with atomic percentage of In concentration to that of Cu concentration ($[\text{In}]/[\text{Cu}] = 0.8$ and 1.1) are shown respectively in Fig.2.3a,b and Fig.2.3c,d. The AFM measurements

showed that as observed from SEM grain size is greater in the case of Cu-rich films than in In-rich films. It is observed to be around $0.33\ \mu\text{m}$ in the slightly Cu-rich film while the measured grain size in In-rich films is about $0.17\ \mu\text{m}$. When the grain size measured from AFM is compared with particle size calculated using XRD, the former is found to be much greater than the latter. It is evident from the 2-D figures that there is agglomeration of the particles in both the films.

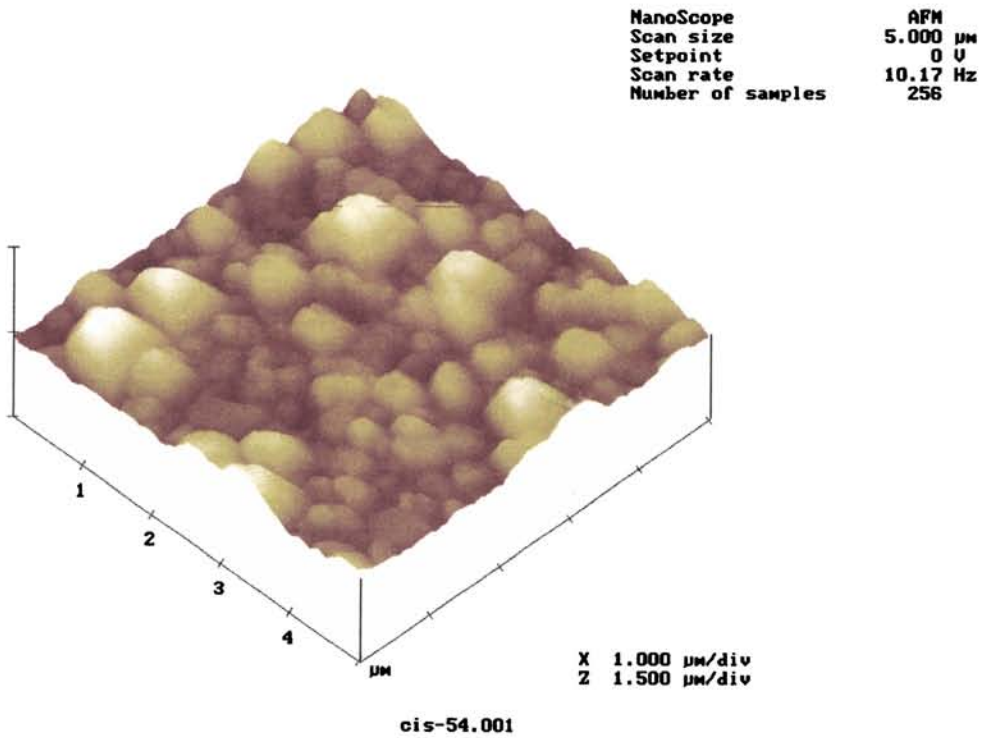


Fig.2.3a Three dimensional AFM on slightly Cu-rich CuInSe_2 .

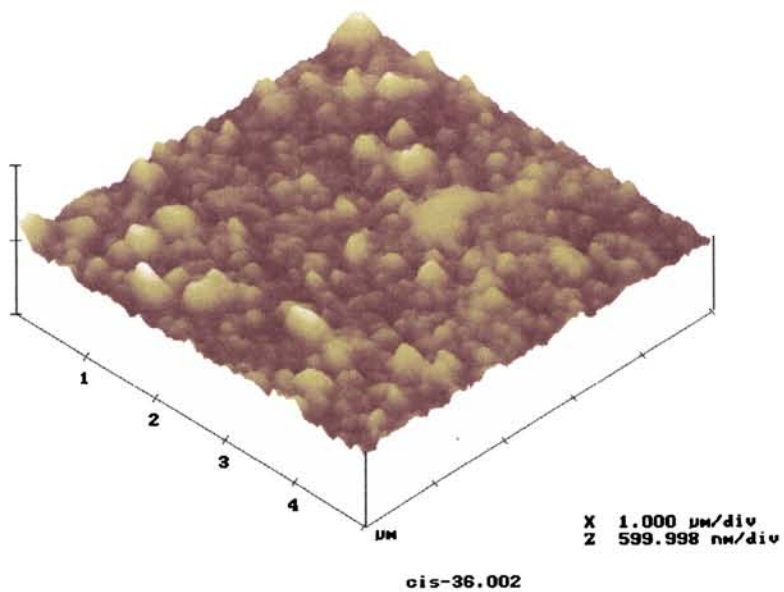


Fig.2.3b *Three dimensional AFM on slightly In-rich CuInSe₂.*

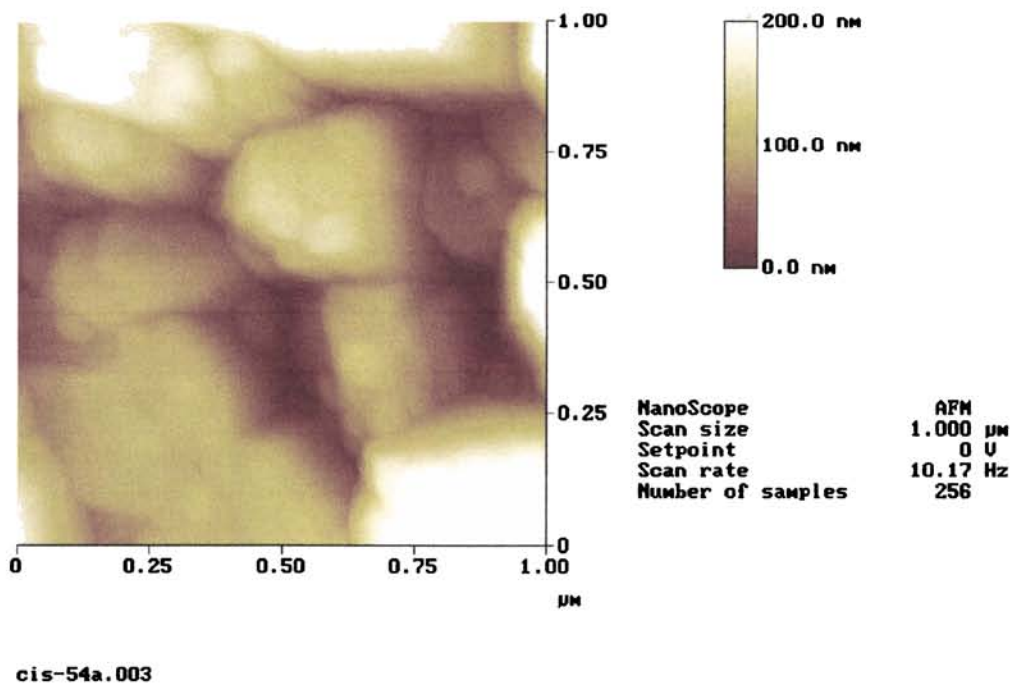


Fig. 2.3 c *Two dimensional AFM on slightly Cu-rich CuInSe₂.*

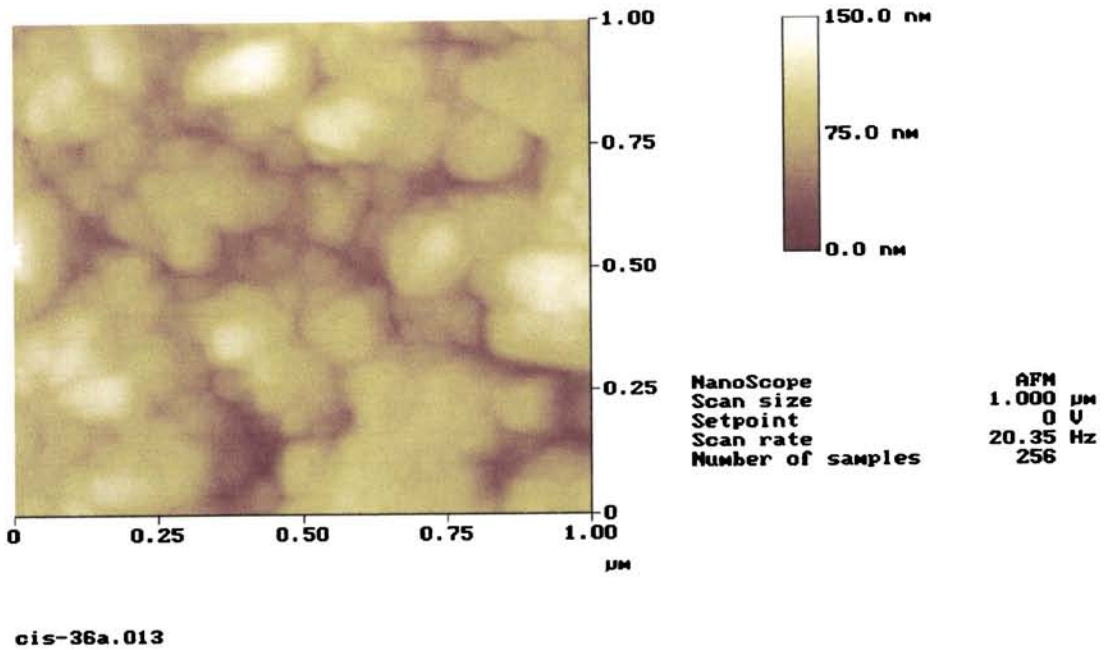


Fig.2.3 d *Two dimensional AFM on slightly In-rich CuInSe₂.*

This might be the reason behind the difference in sizes measured by AFM and SEM from that obtained from XRD since while the calculation of XRD gives the dimension of a single particle, the dimension of each grain formed from the clustering together of particles is often measured from AFM and SEM. The root mean square value of the surface roughness of the Cu-rich films is found to be about 54nm, which is much greater than the 20nm roughness observed in the In-rich films.

2.5.3 Thickness measurement

Thickness of the films is measured by Tolansky's interferometric methods [8]. A sharp and well defined straight edge at the step formed between the substrate and the film is an important requirement in thickness measurement by this technique. For this purpose while the films are deposited, one substrate will be masked to half of its length so that film is deposited only to half of the substrate with a sharp edge at the step. A highly reflective film layer is deposited on the top of the sample (entire portion including the earlier masked region) for study. The thickness measurement is made by placing a semi silvered optically flat film in contact with the film side of the sample to form the

expected interference fringes on incidence of monochromatic light. In the present case mercury green light has been used for getting interference fringes. The thickness of the CuInSe_2 films studied here is found to lie in the range $0.3 \mu\text{m}$ to $0.5 \mu\text{m}$. Tolansky's method is often backed up with the thickness calculated from optical transmission measurements by Swanepoel's method [9].

2.6. Structural characterization

The structural characterization of the films includes the phase determination, the determination of the unit cell dimensions and the bond length calculations. One of the most powerful tool for studying the structure of crystals or films is X-ray diffraction (XRD). In the present study, the XRD data on samples of different composition are used for obtaining the lattice parameters, the bond lengths, the distortion of the unit cell and the non-ideal anion displacement in CuInSe_2 . The strain in the films as well as the particle sizes is also calculated.

2.6.1 X-ray diffraction

A Regaku D MaxC X-ray diffractometer with $\text{CuK}\alpha_1$ as source radiation has been employed in the present X-ray diffraction studies. Three typical XRD patterns on nearly stoichiometric CuInSe_2 films taken at ambient temperature at a scan speed of 1° per minute are shown in Fig.2.4 a -c.

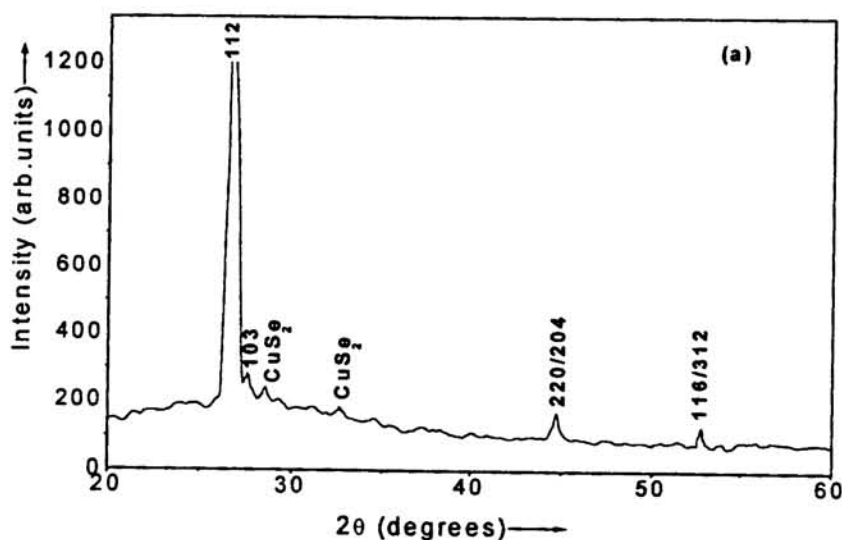


Fig.2.4a XRD profile on Cu-rich CuInSe_2 ($[\text{Cu}/\text{In}]=1.3$)

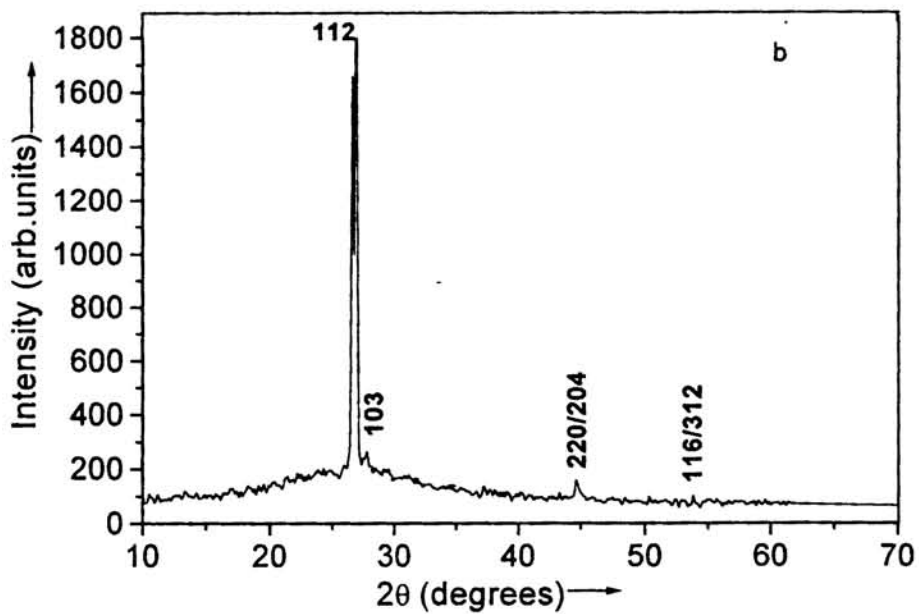


Fig.2.4b XRD on CuInSe_2 sample where binary phases are absent ($[\text{Cu}/\text{In}]=1.1$).

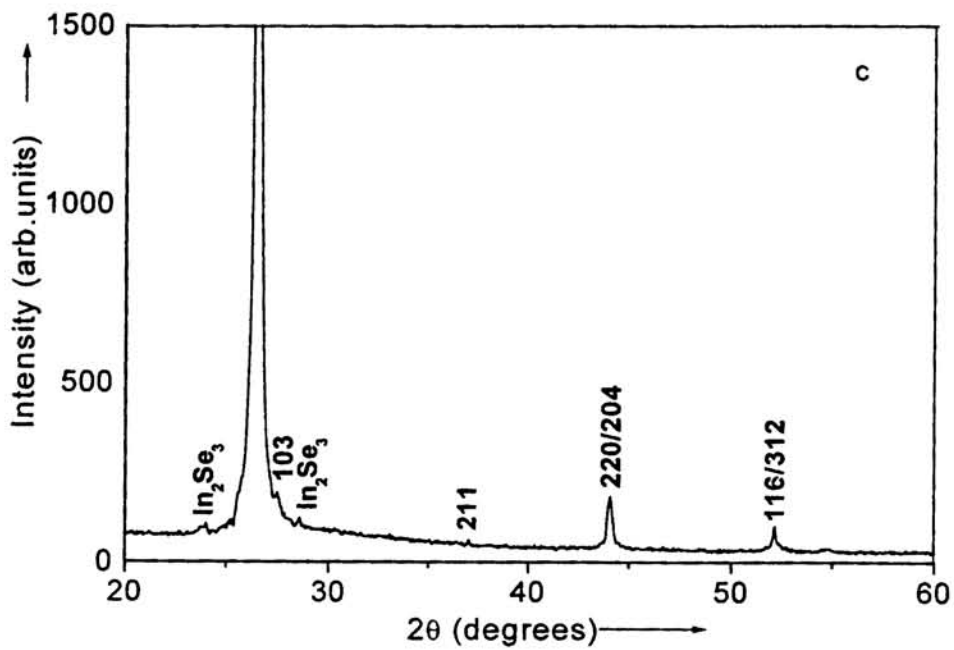


Fig.2.4c XRD profile on In-rich CuInSe_2 ($[\text{Cu}/\text{In}]=0.86$).

A comparison with standard peak positions in JCPDS file shows that the prominent peaks in both correspond to reflections from 112 planes. (Here in the figures, the peaks corresponding to 112 reflection is cut so as to make the other peaks visible.) The other accountable peaks are 220/204 and 116/312 and the chalcopyrite characteristic peak 103. The presence of CuSe₂ in Cu-rich CIS and In₂Se₃ in In-rich CIS are detected from the appearance of some very small peaks corresponding to them in the XRD profile. CuInSe₂ is however the prevalent phase in all the films.

2.6.2 Lattice parameters

We have given special attention to the determination of lattice parameters since these are later used for assessing the bond lengths and the non-ideal anion displacement in the compounds. Lattice parameters can be calculated directly using the basic equations for the unit cell dimensions in a tetragonal lattice, noting the d-spacing of the (hkl) planes from the XRD. But for better accuracy we have adopted the Nelson-Riley method for lattice parameter determination [10].

2.6.2.1 Lattice equations and Nelson Riley Taylor Sinclair function

The process of measuring a lattice parameter is a very indirect one, and is fortunately of such nature that high precision is fairly easily obtainable. The basic equation determining the diffraction from a crystal is given by Bragg's law

$$2d\sin\theta = n\lambda \quad 2.1$$

where d is the spacing of planes from which diffraction occur, n is the order of reflection, θ is the Bragg angle for this set of planes and λ is the wavelength of X-rays. Differentiating Bragg's equation we get

$$\Delta d/d = -\cot\theta \Delta\theta \quad 2.2$$

If for simplicity we consider a cubic system where the lattice parameter

$$a = d(h^2 + k^2 + l^2)^{1/2}$$

Then,

$$(\Delta a/a) = (\Delta d/d) = -\cot\theta \Delta\theta \quad 2.3$$

Since $\cot\theta$ approaches zero as θ approaches 90° , $(\Delta a/a)$, the fractional error in a caused by a given error in θ also approaches zero as θ approaches 90° . Hence one method to

find the true value of a in this case is by plotting the measured values against 2θ and extrapolating to $2\theta = 180^\circ$. Unfortunately, this curve is not linear and the extrapolation of a nonlinear curve is not accurate. However it has been shown that if the measured values of a are plotted against certain functions of θ , rather than against θ or 2θ directly, the resulting curve is a straight line which can be extrapolated with confidence. The function is selected considering the errors in the experiment and the variation of the errors in θ with the angle θ itself.

Some sources of systematic errors are (1) misalignment of the instrument (2) use of flat specimens instead of curved ones (3) absorption in the specimen (4) displacement of the specimen from the diffractometer axis (5) vertical divergence of the beam. No single extrapolation function can be completely satisfactory since it is observed that while $\Delta d/d$ varies as $\cos^2\theta$ for (2) and (3), it varies as $\cos^2\theta / \sin\theta$ for (4). Extrapolation against several functions like θ , $\cos^2\theta$, $\sin^2\theta$ etc. were suggested but it is now generally accepted that an extrapolation against Nelson-Riley function $((\cos^2\theta / \sin\theta) + (\cos^2\theta / \theta))$ which approaches zero as value of θ approaches 90° gives the most accurate values.

In tetragonal crystals,

$$a = (\lambda/2\sin\theta) \{(h^2+k^2) + (l^2/(c/a)^2)\}^{1/2} \quad 2.4$$

and

$$c = (\lambda/2\sin\theta) \{(c/a)^2 (h^2+k^2) + l^2\}^{1/2} \quad 2.5$$

are the basic equations connecting the lattice constants a and c with the Bragg angle θ and the hkl values. The first step is to calculate approximate values, a_1 and c_1 for the lattice parameters from the positions of the two highest angle lines. The approximate axial ratio c_1/a_1 is then calculated and used in Eq.(2.4) to determine an a value for each high-angle line on the pattern. These values of a are then extrapolated against $((\cos^2\theta / \sin\theta) + (\cos^2\theta / \theta))$ to find a more accurate value of a which is then used in the calculation of c using Eq.(2.5). The c values thus obtained can be extrapolated against $((\cos^2\theta / \sin\theta) + (\cos^2\theta / \theta))$ to obtain an accurate value of c . If necessary, the process can

be repeated to yield more accurate values of lattice constants. In the present study, two successive extrapolations are done for obtaining the lattice parameters.

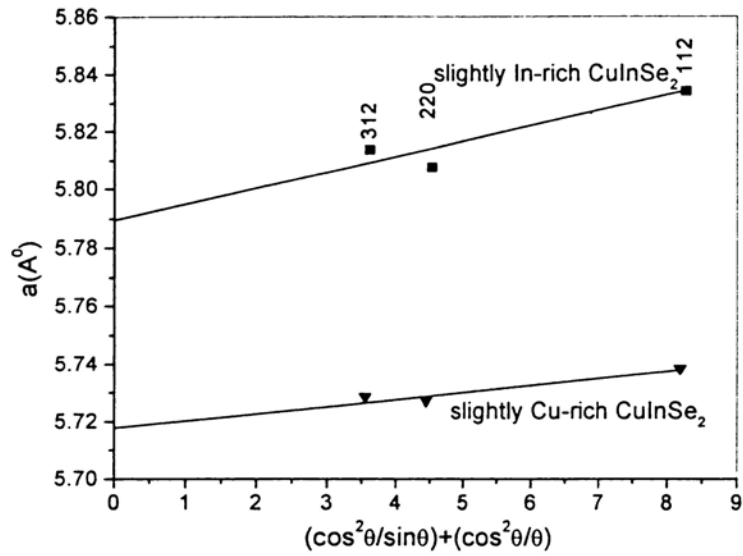


Fig.2.5a Nelson- Riley extrapolation for lattice constant 'a'.

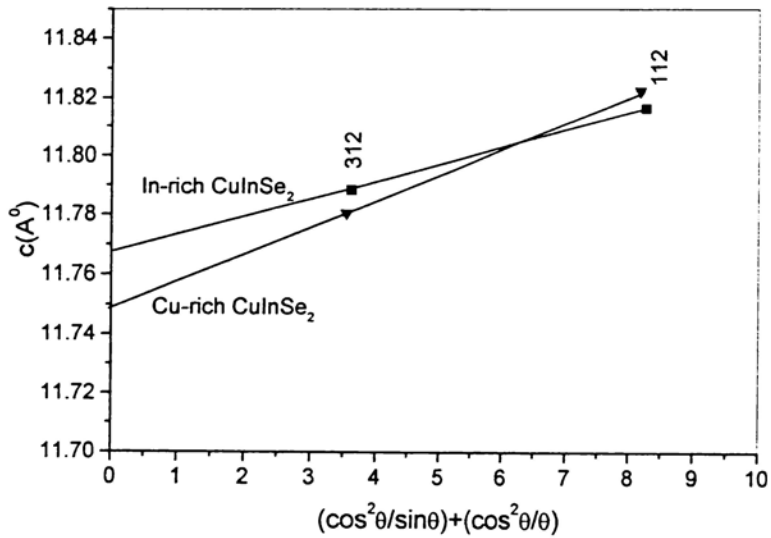


Fig.2.5b Nelson- Riley extrapolation for lattice constant

The lattice constants a_0 and c_0 obtained for two typical CuInSe₂ samples –one from the Cu rich side and the other from the In rich side are given in the table.2.1.

Type of samples	Lattice constant (a_0)	Lattice constant (c_0)
Slightly Cu-rich CuInSe_2	5.717 nm	11.748 nm
Slightly In rich CuInSe_2	5.789 nm	11.768 nm

Table.2.1 *Lattice parameters of CuInSe_2 .*

The small variation in the lattice parameters is found to be linked with various other factors like strain in the films, the composition of the film, the constructional difference etc. The a_0 values are in quite in agreement with the lattice parameters reported for CuInSe_2 in single crystal form and powder form while here the c_0 values are found to be slightly greater, probably due to strain that produced slight lattice dilation along the c-axis. The lattice parameters determined by some other investigators are given below.

Type of CuInSe_2	Lattice constant (a)	Lattice constant (c)	Reference
Powder	5.782 nm	11.62 nm	[11]
Single crystal	5.784 nm	11.62 nm	[12]
Powder	5.784 nm	11.614 nm	[13]
Single crystal	5.781 nm	11.642 nm	[14]
Powder	5.784 nm	11.626 nm	[15]
Single crystal	5.731 nm	11.513 nm	[16]

Table.2.2 *Lattice parameters of CuInSe_2 in powder form and single crystal form.*

An examination of the lattice constants given in Tables.2.1 and 2.2 makes it clear that slight differences in a and c parameters are observed in CuInSe₂ compound as their type and mode of construction vary. In this context, separating out the strain in the films is advantageous to get an insight into many of the characteristic properties exhibited by the compound films.

2.6.2.2 Grain size and strain in the films

It is important to evaluate the strain in the films, which influence the deformation of the grains when we proceed with the bond length calculations. This is done by constructing Williamson-Hall plots taking full-width at half maximum of the XRD peaks $\times \cos\theta$ on the y-axis and $4\sin\theta$ along the x-axis, from which the strain value can be estimated from the slope and the crystallite size from the intercept of the plot.

A uniform strain shifts the peak positions while non-uniform strain broadens peaks. The broadening of the peaks also has another contribution, that is very small crystallite size. Assuming that both contributions are mutually independent and that they linearly combine with a Lorentzian peak profile, one gets the total reflection width

$$\beta_{hkl} = \beta_{\text{size}} + \beta_{\text{strain}} = (0.9\lambda / (D \cos\theta)) + (4\epsilon \tan\theta_{hkl}) \quad 2.6$$

where ϵ is the microstrain in the sample and D is the crystallite size [17]. Fig. 2.6 gives the W.H plots for slightly In-rich and Cu-rich samples.

The microstrain determined for the slightly Cu-rich and In-rich samples from the W.H plots are $\sim 2.03 \times 10^{-3}$ and 1.08×10^{-3} respectively. The particle size determined in the two cases is around 58 nm for Cu-rich films and 50 nm for the In-rich films. The calculation indicates that the particle size decreases with increase in In content. The result is in conformity with the SEM and AFM measurements and with the observation of different investigators. The strain is found to be greater in the Cu-rich film which might be one of the reasons for increase in distortion ($\eta = c/2a$) for the crystallites in the Cu-rich sample.

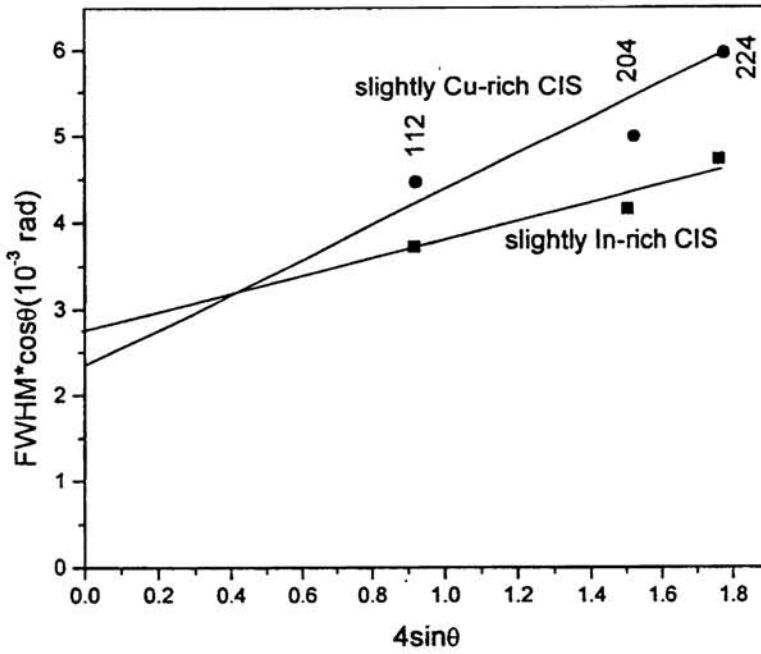


Fig.2.6 *W-H plot for CuInSe₂*

If the strain effects are not considered, the particle size can be calculated using Scherrer formula considering the integral width of the reflection peaks. Accordingly

$$\beta_{hkl} = 0.9\lambda / (D \cos\theta) \quad 2.7$$

where β_{hkl} represents the FWHM in radians of the hkl peaks, λ is the wavelength of the Cu-K α radiation and D is the particle size [10]. The particle size thus determined for Cu-rich CIS films are in the range 35 ± 3 nm and that of In-rich samples are in the range 26 ± 3 nm. Here also the same trend, that is reduction in particle size with increase in In-content, is observed.

2.6.2.3 Tetragonal deformation, non-ideal anion displacement and bond lengths.

The structural difference, especially the anion displacement in the ternary compounds is suggested to contribute largely to the optical band gap reduction in A^IB^{III}C₂^{VI} semi conductors compared to their binary analogues, which in fact makes some of them especially CuInSe₂ among the strongest known absorbers in the solar spectrum. It is

this property of CIS that gives them potential applications in photovoltaic devices. A key issue to be studied is the correlation between the structural and optical properties of these compounds since deviations from stoichiometry in CuInSe₂ produce large variations in their optical properties. In this context, the determination of anion-displacement, anion-cation bond lengths and bond length mismatch of the In-rich and Cu-rich compounds are done.

The crystal structure of this ternary chalcopyrite semi conductor CuInSe₂ is closely related to that of the Zinc-blende binary analogues but with non-ideal tetragonal strain parameter $\eta=c/2a \neq 1$ and anion displacement parameter $u = (1/4) + (\alpha/a^2) \neq 1/4$. Thus the structure reflects the inequality of anion-cation bond lengths R_{AC} and R_{BC} , where the bond length mismatch

$$\alpha = R_{AC}^2 - R_{BC}^2 = (u - 1/4) a^2 \quad 2.8$$

The two cations in the ternary chalcopyrites follows the sequence ABAB... in the vertical direction through intervals of $c/2$ where as we find the sequence AAA ... horizontally with an interval of 'a' [1]. The anion c which has two A and two B cations as nearest neighbours, adopts an equilibrium position closer to one pair of cations than to the other, that is $R_{AC} \neq R_{BC}$ (bond alternation).

There are different methods for the calculation of bond lengths. Here, the bond lengths are initially determined using the method followed by Abrahams and Bernstein [18] where the bond angles at the B atom in the chalcopyrites are considered to have ideal tetrahedral values, which requires that u and η be related by

$$u = u_{tet}(\eta) = (1/2) - ((1/4)(2\eta^2 - 1)^{1/2}) \quad 2.9$$

The nearest neighbour bond lengths are then given by

$$R_{AC}(a, \eta, u) = [u^2 + (1 + \eta^2)/16]^{1/2} a \quad 2.10$$

and

$$R_{BC}(a, \eta, u) = [(u - (1/2))^2 + (1 + \eta^2)/16]^{1/2} a \quad 2.11$$

The values of u and the bond angles so obtained are given in Table.2.3.

Type of film	η	u	$R_{AC} (A^0)$	$R_{BC} (A^0)$	Bond length mismatch
Slightly Cu rich CIS	1.027	0.236	2.457	2.546	-0.445
Slightly In rich CIS	1.016	0.241	2.502	2.559	-0.289

Table.2.3 Anion displacement and bond lengths in $CuInSe_2$ using 'conservation of tetrahedral bond angles' rule .

But since the assumption of "conservation of bond angles" in chalcopyrites as considered above is not always applicable for the ternary chalcopyrites, it is at present replaced by the rule of 'conservation of bond lengths'. This simple rule termed by Jaffe et al [1] as 'CTB plus $\eta = \eta_{\text{expt}}$ ' rule is basically related to Bragg's classical principle of transferability and conservation of elementary bonds in different compounds. In this method, the tetragonal distortion parameter is set as equal to its experimental value and a and u are determined based on the fact that the equations 2.10 and 2.11 and the following eqs.

$$R_{AC}(a, \eta, u) - r_A - r_C = 0 \quad 2.12$$

$$R_{BC}(a, \eta, u) - r_B - r_C = 0 \quad 2.13$$

show only a weak dependence of the bond lengths on η . Pauling's tetrahedral radii of the atoms Cu^{1+} , In^{3+} and Se^{2-} are taken as $r_A(1.35 A^0)$, $r_B(1.44A^0)$ and $r_C(1.14A^0)$.

Defining the bond mismatch parameter as

$$\alpha = R_{AC}^2 - R_{BC}^2 = (r_A + r_C)^2 - (r_B + r_C)^2 \quad 2.14$$

and the mean-square bond as

$$\beta = R_{AC}^2 + R_{BC}^2 = (r_A + r_C)^2 + (r_B + r_C)^2, \quad 2.15$$

the solutions to eqs.2.12 and 2.13 are

$$\alpha^2 = (4\alpha^2) / (\beta - [\beta^2 - (2 + \eta^2) \alpha^2]^{1/2}) \quad 2.16$$

and

$$u = ((\alpha + \beta) - [\beta^2 - (2 + \eta^2) \alpha^2]^{1/2}) / (4\alpha) = (1/4) + (\alpha/\alpha^2). \quad 2.17.$$

The anion displacement and the bond lengths calculated using the method given above, are given in Table.2.4. The tetragonal deformation, anion displacement as well as bond lengths and bond mismatch parameters in the compound determined by different investigators are also given.

As pointed out earlier, the tetragonal deformation seems to be greater in Cu-rich films in the case of samples studied. This might be associated with the greater strain experienced by the Cu-rich films as determined from W.H plots. The Cu-Se bond length is lesser than the In-Se bond length, which means the anion, is slightly displaced towards the cation Cu. But it is seen that though with form of the compound as thin film, single crystal, powder etc. there is slight variation in the bond length values, the bond lengths are almost conserved even with changes in stoichiometry

Type of films	η	u	$R_{AC} (A^0)$	$R_{BC} (A^0)$	Bond length mismatch	Reference
Slightly Cu-rich $CuInSe_2$	1.027	0.2362	2.4708	2.5614	-0.4563	Present work
Slightly In-rich $CuInSe_2$	1.016	0.2363	2.4706	2.5613	-0.4563	Present work
Powder $CuInSe_2$	1.005	0.235	2.484	2.586		[11]
$CuInSe_2$ Single crystal	1.004	0.224	2.424	2.598		[12]
$CuInSe_2$ powder	1.0039	0.2268	2.433	2.588		[13]
$CuInSe_2$ Single crystal	1.0069	0.2260	2.4337	2.5893		[14]
$CuInSe_2$ powder	1.0049 1.005	0.2277 0.2348	2.424 2.458	2.596 2.558		[15]
$CuInSe_2$ Single crystal	1.0044	0.2277	2.4139	2.5611		[16]

Table.2.4 Tetragonal deformation, anion displacement and bond lengths in $CuInSe_2$.

But since even small changes in u can sensitively control the optical band gap as proved by different investigators [1], we should take note of the fact that there is slight variation in u values with changes in composition of the films.

The position of atoms (u_n , v_n and w_n) in CuInSe_2 are given as

n	atom	u_n, v_n, w_n
1	Cu	0, 0, 0
2	Cu	0, $a/2$, $c/4$
3	In	$a/2$, $a/2$, $c/4$
4	In	$a/2$, 0, $c/4$
5	Se	$a((1/4)+u)$, $a/4$, $c/8$
6	Se	$a((3/4)-u)$, $3a/4$, $c/8$
7	Se	$a/4$, $a((3/4)+u)$, $3c/8$
8	Se	$3a/4$, $a((1/4)-u)$, $3c/8$

Table 2.5 Atomic positions of atoms in CuInSe_2 where instead of u and a , the determined experimental values can be substituted to know the actual crystal structure.

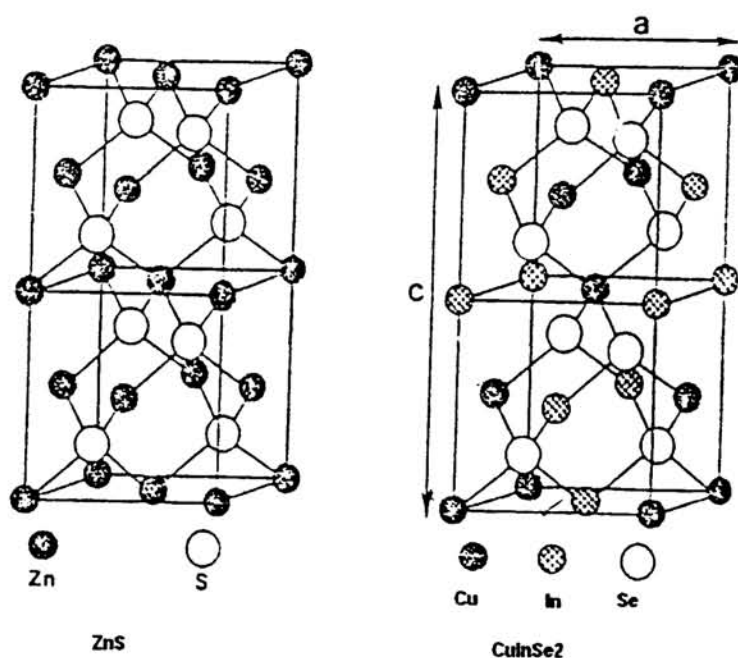


Fig. 2.7 Crystal structure of CuInSe_2 .

2.7 X-ray photoelectron spectroscopy

XPS analysis of the samples provides a powerful means for studying the chemical environment of various elements in the compound thus enabling the interpretation of

chemical states, bond energy variations etc., which may often affect the measured binding energy of elements, the percentage composition of various elements in the compound etc.

For the present analysis, the XPS spectra have been recorded on an ESCA machine of VSW scientific instruments make with a Mg and Al twin anode X-ray gun as the source. In the analysis Al $K\alpha$ (1486.6 eV) has been used as the source radiation. Detector used is a hemispherical analyzer working in FAT mode. A ‘Collect W’ software has been employed for recording the XPS data with C-1s peak as the standard for the calibration of the photoelectron spectrometer. The experimental set up is described in section.1.2.2.2.

The plots in Fig. 2.8 represent the full scan XPS spectra of the Cu-rich and In-rich samples before etching. In the spectra, in addition to peaks corresponding to Cu 2p, In 3d and Se 3d, some auger peaks and very small peaks indicating oxygen and carbon contamination on the surface of samples are also present. Here the Se 3d peaks are found to be subdued due to contamination on the surface of samples. The silver peaks are from the silver applied at an end of the film for conduction purpose. The spectra after the samples are given Argon etching for 30 minutes are shown in Fig.2.9. In the etched films the peaks for Cu, In and Se are found to be increased in intensity, while the oxygen and carbon peaks are subdued.

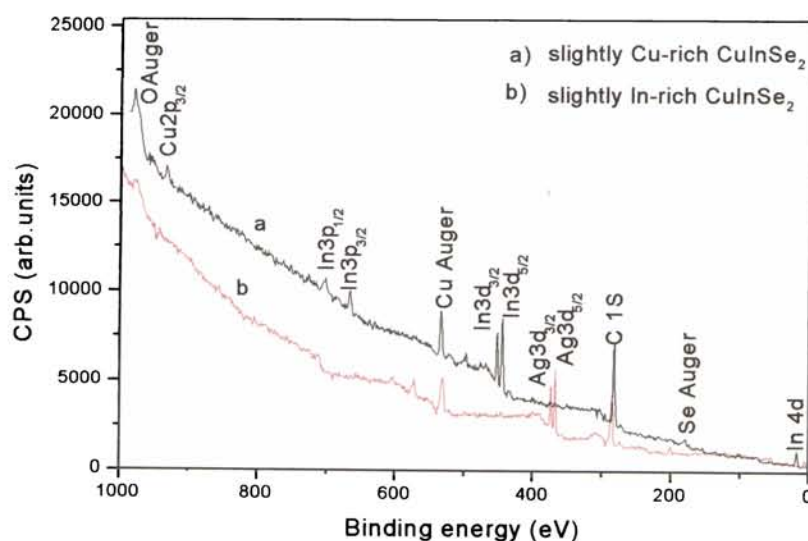


Fig.2.8 XPS spectra on $CuInSe_2$ films before Ar etching.

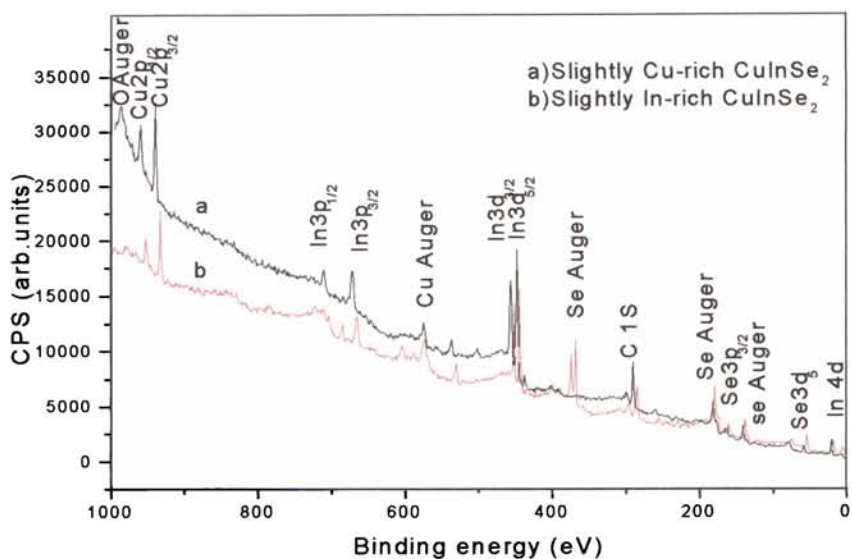


Fig.2.9 XPS spectra on $CuInSe_2$ films after Ar etching

The detailed scans of the $Cu2p_{3/2}$, $In3d_{5/2}$ and $Se3d_{5/2}$ in enlarged mode are given in Fig.2.10a-c. A comparison in the binding energy for $Cu2p$, $In3d$ and $Se3d$ obtained in the present investigation with those found in literature is given in Table. 2.6.

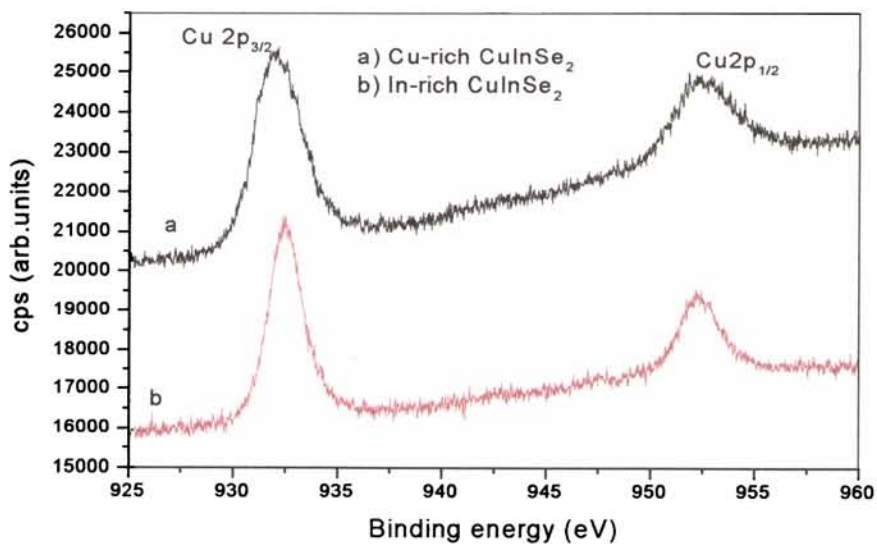


Fig.10.a Detailed spectra of $Cu 2p$ in $CuInSe_2$.

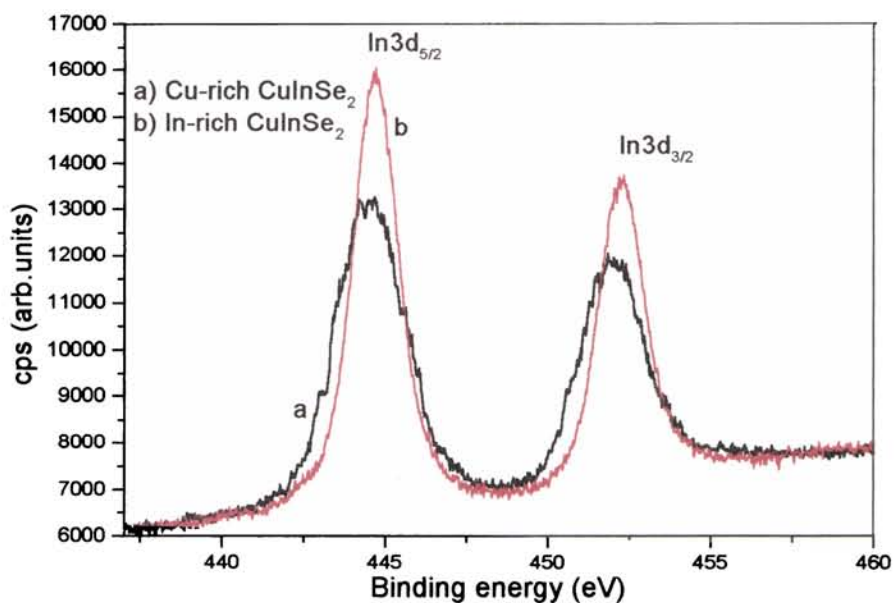


Fig.2.10b Detailed spectra of In 3d in CuInSe_2

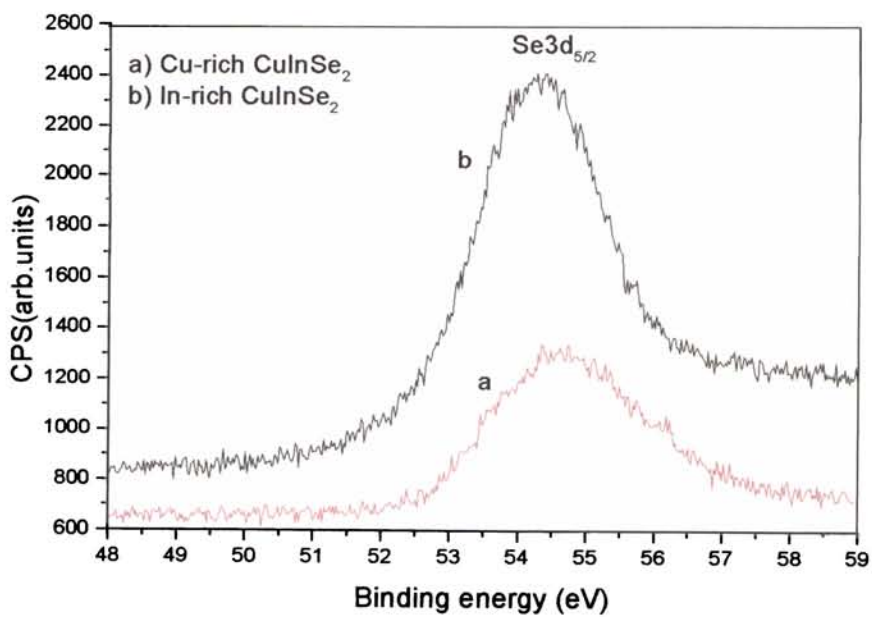


Fig.2.10c Detailed spectra of Se 3d in CuInSe_2 .

Film type	Cu2p _{3/2}	In3d _{5/2}	Se3d _{5/2}	Reference
Slightly Cu-rich CuInSe ₂	931.9 eV	444.4 eV	54.4 eV	Present study
Slightly In-rich CuInSe ₂	932.4eV	444.7 eV	54.2eV	Present study
CuInSe ₂	931.9 eV	444.7 eV	54 eV	[19]
CuInSe ₂	931.6 eV	443.9 eV	[20]
CuInSe ₂	931.9 eV	444.1 eV	53.8 eV	[21]

Table.2.6 Peak positions of Cu2p, In3d and Se3d in the X-ray photoelectron spectra of CuInSe₂.

The spectral analysis shows that the peak position of Se3d_{5/2} in In-rich CIS is 54.2 eV, very close to the standard reported binding energy value for Se3d_{5/2} in CuInSe₂ compounds (where as if the binary phase In₂Se₃ were prevalent, then Se in In₂Se₃ would have occurred at 54.8eV). In the Cu-rich CIS there is a slight shift in binding energy of Se towards the higher binding energy side, may be due to presence of Cu₂Se (54.5eV) on the surface of films [22]. The reported binding energy of In3d_{5/2} in CuInSe₂ is found to vary from 444.1 eV to 444.7 eV in literature [19-21]. As evident from the Fig.2.11b the binding energy peaks for In3d_{5/2} for the samples studied here lies in this range and is found to have a minimum for Cu rich CIS. The shift in In3d_{5/2} peak position to the higher energy side in In-rich compounds relative to Cu-rich suggest a strong bonding energy for In in the In-rich compounds. The assumption is in concordance with the bond length measurements (Table.2.4) in these films which indicate that there is a slight decrease in In-Se bond length for the In rich compounds when compared to that in Cu-rich CIS. In the same way, the display of slight shift in Cu2p_{3/2} peak towards higher binding energy side in the In-rich CIS (932.4 eV) relative to that in Cu-rich CIS (931.9 eV) is suggestive of the higher bonding energy of Cu-Se

bonds in the former [6]. It is also evident that Cu is in a monovalent state in CuInSe₂ compounds.

2.8 X-ray Reflectivity

Grazing incidence X-ray reflectivity (GIXR) is a highly penetrating and non-destructive technique for probing buried interfaces, for doing surface roughness and layer thickness studies, for determining mean electron density and mass density of the prepared samples. In the present investigation the technique is used to get an estimate of the mean mass density of the samples.

The reflectivity measurements are performed using a high resolution Siemens D 5000 X-ray diffractometer which uses a Cu K α source of 8000eV energy. The incident and reflected beams are collimated with slits of 0.05mm in width and the reflection intensity is measured by a scintillation counter. The specular reflectivity curves are recorded with a θ vs 2θ scan. For each sample, reflectivity scans, rocking scans and detector scans have been performed. The experimental data has been corrected for background scattering by offset scans. Fig. 2.11 shows a typical X-ray reflectivity curve obtained on a CuInSe₂ thin film of approximately 0.4 μ m thickness. The intensity oscillations are not present in the plot since the thickness of the films are too high for observing such oscillations. The fit to the reflectivity data has been done using the Parratt algorithm (Parratt 32). The critical angle of total external reflection of the layer α_c has been obtained from the X-ray reflectivity fit and is used to calculate the mean electron density $\langle\rho_{el}\rangle$ using the equation

$$\langle\rho_{el}\rangle = (\alpha_c^2 \pi) / (\lambda^2 r_{el}) \quad 2.18$$

where r_{el} is the classical radius of electron and $\lambda=1.54 \text{ \AA}$ is the wavelength of X-rays used. The mean mass density $\langle\rho_m\rangle$ is computed using mass number $\langle A \rangle$ and the atomic number $\langle Z \rangle$ of the samples according to their composition as

$$\langle\rho_m\rangle = (\langle\rho_{el}\rangle\langle A \rangle) / (N_A\langle Z \rangle) \quad 2.19$$

The mean electron density and the mass density of the samples experimentally determined are given in Table.2.7 along with the theoretical mass density

$$\rho_{m \text{ theory}} = (nM)/(a^2cN_A) \quad 2.20$$

calculated using the number of molecules per unit cell (n) , molar mass (M) and the lattice constants a and c for the sample.

Type	αc	$\langle \rho_{el} \rangle$	$\langle \rho_m \rangle$	$\rho_{m \text{ theory}}$
CuInSe ₂	0.00398	0.7471	2.858	2.87
		/Å ³	g/cm ³	g/cm ³

Table. 2.7 *The mean electron density and mass density from XRR.*

It is found that in the CuInSe₂ samples, the mass density from experiment and theory agrees very well, indicating that the number of vacancies or other defects is probably very less in these thin film samples.

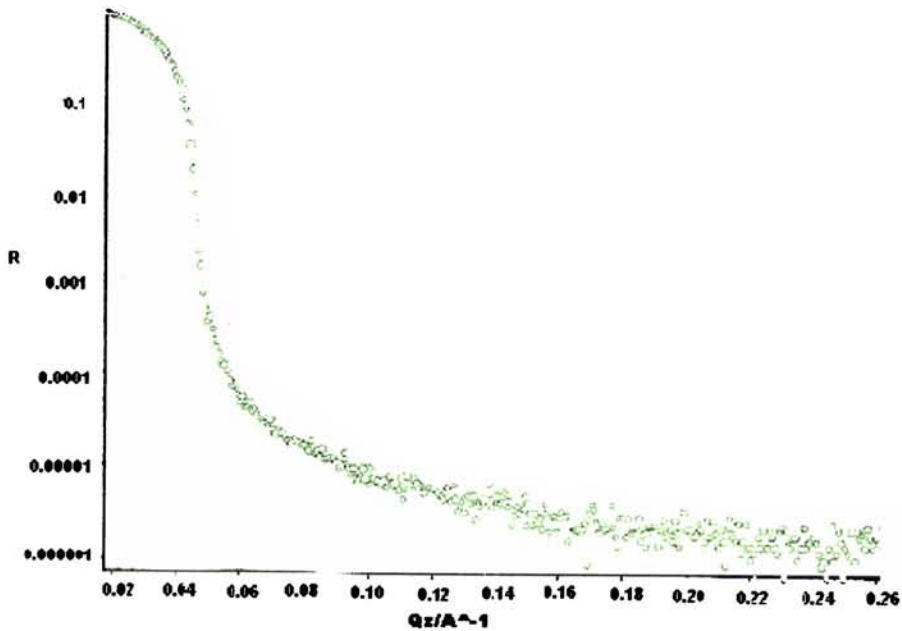


Fig.2.11. *Reflectivity plot on CuInSe₂.*

2.9 Conclusions

This chapter gives a detailed account of the compositional, morphological and structural characterization of CuInSe₂ films prepared by vacuum co-evaporation method. The films have been characterized into Cu-rich and In-rich CuInSe₂ based on their slight deviations from the Cu: In: Se = 25: 25: 50 atomic composition determined using EDAX. Morphological studies indicated that the roughness parameter as well as grain size is greater in Cu-rich CuInSe₂ films while compared to that of In-rich films.

The lattice constants as well as the tetragonal deformation in the films evaluated based on the XRD peak positions, indicated that the parameters are depending on the strain in the films. The anion-cation bond lengths are found to be almost conserved in all the films, with the Cu-Se bond length slightly lesser than In-Se bond length. XPS studies suggest slight increase in the bonding energies for In-rich CuInSe₂ relative to that in Cu-rich films. The density calculation using XRR indicates that the theoretical and experimental mass densities are almost equal, which shows that very few unaccounted vacancies or other defects are present in the samples.

References

- [1] J.E. Jaffe and A. Zunger. Phys. Rev. B. 29 (1984) 1882.
- [2] A.R.Verma and O.N.Srivastava, Crystallography for solid state physics, Wiley Eastern Limited, New Delhi, 1982, pp 174.
- [3] J.E. Jaffe and A. Zunger. Phys. Rev. B, 27 (1983) 5176.
- [4] K.G.Gunther, The use of thin films in physical investigations, J.C.Anderson (Ed), Academic press, London,1966; pp.213.
- [5] R.Glang, Hand book of Thin Film Technology, L.I. Maissel and R.Glang (Eds.), Mc Graw Hill, New York, 1970, pp.1.
- [6] S.B. Zhang; S.H.Weï and A. Zunger. Phys.Rev.B. 57 (1998) 9642.
- [7] N.Khare, G.Razzini, L.P. Bicelli, Thin Solid Films 186 (1990)113.
- [8] R.W.Berry, P.M.Hall and M.T.Harris. Thin Film Technology, Van Nostrand Reinhold Company, N.Y. 1968, p.171.
- [9] R.Swanepoel, J.Phys.E.Sci.Instrum. 16 (1983) 1214.
- [10] B.D. Cullity, Elements of X-ray diffraction, Addison-Wesley Publishing Company, U S A, 1956, pp.320.
- [11] J. Parkes, R. D. Tomlinson, M. J. Hampshire, J. Appl. Crystallogr. 6 (1973) 414.
- [12] H.W.Spiess, U.Haeberlin, G.Brandt, A.Rauber and J.Schneider, Phys.Status Solidi B 62 (1974) 183.
- [13] G.Zahn and P.Paufler, Cryst.Res.Technol. 23 (1988) 499.
- [14] K.S.Knight, Mater.Res.Bull.27 (1992) 161.
- [15] J.M.Merino, J.L.M.de Vidales, S. Mahanty, R.Diaz, and F.Rueda, J.Appl.Phys.80 (1996) 5610.
- [16] F.Frolow, L.Chernyak, D.Cahen, H.Hallak, J.Gabboun, A.Kvick and H.Graafama,Inst.Phys.Conf.Ser.152 (1998) 67.
- [17] G.K.Williamson and W.H.Hall, Acta Metall.1 (1953) 22.
- [18] S.C.Abrahams and J.L. Bernstein, J.Chem.Phys.59 (1973) 5415.
- [19] J. F. Moulder, W.F. Stickle, P. E. Sobol and K. D Bombin, Hand book of X-ray photoelectron spectroscopy, Perkin-Elmer Co, Eden Prairie MN (1992).

- [20] D. Cahen, P. J. Ireland, L. L. Kazmerski, F. A. Thiel, *J. Appl. Phys.* 57 (1985) 4761.
- [21] R. Hesse, Unfit for windows, Universal program for XPS peak fitting and spectra analysis, V-2003
- [22] L. L. Kazmerski, O. Jamjoun, P. J. Ireland and S. K. Ded, *J. Vac. Sci. Technol.*, 19 (1981) 467.

3.1 Introduction

The I-III-VI₂ chalcopyrite semiconductor compound CuInSe_2 is one of the most promising materials for thin film solar cells due to its band gap of about 1eV and the high absorption coefficient (10^4 - 10^5 cm^{-1}) for visible light. Thin film cells based on CuInSe_2 have reached energy conversion efficiencies of up to 18.8 % [1-3] for small area cells though large area solar cells of these materials, as would be the case for industrial production, show a lower efficiency, mainly due to the large presence of defects. In addition to the photovoltaic applications of this material, this ternary compound finds applications in many important fields like nonlinear optics, optoelectronic devices etc. In this context, a clear and accurate knowledge of the optical properties of the compound is very essential.

It is also a matter of great importance that in this compound, tailoring of band gap to suit our applications is possible by changing the composition of the film. Also due to the fact that both low resistivity and high resistivity CIS are needed for the fabrication of solar cells, the measurement of their band gap as well as photosensitivity properties are important. Hence in this chapter, we study the changes in band gap, photosensitivity etc. with composition variation, taking absorption spectra, transmission spectra, steady state and transient photoconductivity as well as spectral response spectra. We have used the spectral response studies to obtain information regarding the various defects present in the samples as well.

3.2 Optical transmission and absorption studies.

3.2.1 Absorption spectra and Energy band gap.

No material is fully transparent in all optical frequencies and hence there will always be some absorption in some region of the spectra. Absorption of light by different materials can induce various types of transitions such as band to band, between sub

bands, between impurity levels and bands, interactions with free carriers within a band, resonance due to vibrational state of lattice and impurities etc. These lead to the appearance of bands or absorption peaks in the absorption spectra. Hence the spectral positions of bands determine the types of transitions occurring during the process. Thus optical method provides a simple way of finding the band gap as compared to the electric method using the thermal excitation, which is less reliable because of the fact that the effective mass of electrons and holes also influence most of the electrical parameters. Optical method is less ambiguous.

The optical absorption spectra of Cu-rich as well as In-rich samples, structurally, compositionally and morphologically well characterized as explained in chapter 2, are taken using a Hitachi U-3410 UV-Vis- NIR spectrophotometer at room temperature. Two typical spectra are given in Fig.3.1

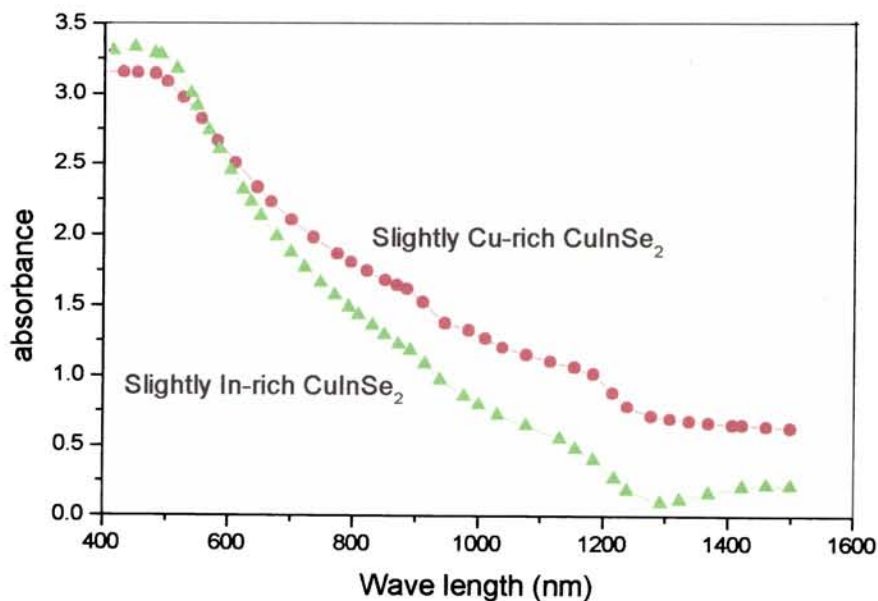


Fig.3.1 *Optical absorbance spectra of typical samples from Cu-rich side and In-rich side.*

The optical absorption coefficient α is calculated directly from the absorption spectrum using the relations [4]

$$\begin{aligned} T &= (1-R)^2 \exp(-A) \\ &= (1-R)^2 \exp(-\alpha d) \end{aligned} \quad 3.1$$

where A is the absorbance, d is the film thickness ($0.4\mu\text{m}$), R is the reflectance and T is the transmittance of the films. If $\text{Ln}(\alpha)$ or α versus $h\nu$ graphs are plotted, different regions of absorption are observed which on careful analysis has helped in the elucidation of the splitting of the top most valence band in these compounds. Postponing the discussion on splitting to a later chapter where samples giving more pronounced additive absorption features are used, here we determine the band gap both in Cu-rich and In-rich CuInSe_2 using the equation [4]

$$\alpha(\nu) = A_c (h\nu - E_g)^n / h\nu \quad 3.2$$

where $n = 1/2, 3/2$ or 2 for allowed direct, forbidden direct or indirect transitions respectively, A_c a constant and E_g the optical band gap. Analysis confirmed that the transitions that are observed in these compounds are all direct allowed transitions with $n=1/2$.

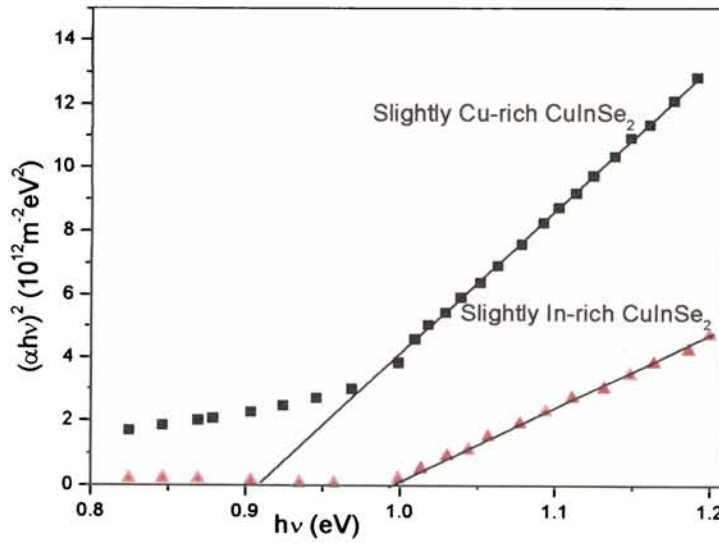


Fig.3.2 $(\alpha h\nu)^2$ versus $h\nu$ graphs on CuInSe_2 films from Cu-rich and In-rich side.

The band gaps are determined by taking the y-axis intercept of the $(\alpha h\nu)^2$ versus $h\nu$ graphs in the energy region 0.9 eV to 1.2 eV. The plots are given in Fig.3.2. It is seen that there is a shift in band gap from 0.91 eV to 0.99 eV as the [In/Cu] atomic percentage ratio changed from about 0.8 to 1.1. Such increase in band gap with increase in In concentration has been observed by various investigators [5,6]. Firoz et al reported energy gaps 0.947 eV, 0.967eV and 0.978 eV for films with In/Cu ratio 0.6, 1.04 and 1.7 respectively and attributed the variation to antisite defect formation, where In atoms of larger size occupied Cu sites as In concentration increased, resulting in increase in band gap [6]. But the explanation of increase in band gap with increase in In concentration has a simple molecular orbital interpretation in analogy with the interpretation given by Jaffe et al [7] for band gap anomaly in ternaries compared to their binary analogues. Accordingly, in ternary chalcopyrites like CuInSe_2 where the cation supports valence d-states, the five fold degenerate Cu d state splits into the threefold degenerate $\Gamma_{15}(d)$ (with the orbital lobes pointing and overlapping with the nearest-neighbour anions) and the two fold degenerate $\Gamma_{12}(d)$ (with the lobes pointing between the nearest -neighbour anions, towards the next nearest shell) in the non-cubic field of the ternary compound. The three fold degenerate $\Gamma_{15}(p)$ state of the anion interact with the $\Gamma_{15}(d)$ state of the cation of the same symmetry, with a repulsive interaction which is directly proportional to the p-d coupling matrix element $|\langle p|v|d \rangle|^2$ and inversely proportional to the energy separation $\Delta \epsilon_{pd}$ between anion p and cation d in accordance with the perturbation theory. The interaction forms a lower bonding state weighted more by the lower energy $\Gamma_{15}(d)$ state and an upper antibonding state weighted more by the higher energy $\Gamma_{15}(p)$ state. As the Cu content decreases in In-rich CuInSe_2 films compared to that in Cu-rich films, the energy separation $\Delta \epsilon_{pd}$ tends to increase in the former resulting in a reduction in the p-d repulsion. This in turn depresses the antibonding state which forms the valence band maximum (VBM) and opens up the band gap for the In-rich films. Hence decrease in Cu content in CIS produces a corresponding increase in band gap. The explanation is applicable in the case of ordered vacancy compounds and is illustrated in chapter6 on OVC's.

Thus the optical absorption studies show that with proper control of the composition, it is possible to tailor the band gaps of CuInSe_2 films according to the need. Since the absorption coefficient and band gap are of special interest in modeling the quantum efficiencies of solar cells, the study helps in fixing the composition of the films according to the requirement.

3.2.2 Transmission spectra and refractive index

Several authors have discussed different methods for the determination of the optical constants like index of refraction (n), the extinction coefficient (k), the absorption coefficient (α) as well as the thickness of the films by relating transmittance, reflectance, absorbance etc. of the films [8-10]. In the present study Swanepoel's [10] method has been used to evaluate the optical constants from the transmission spectra. The transmission spectrum of the film that is recorded in the wavelength range 2600 nm to cutoff is shown in Fig.3.3.

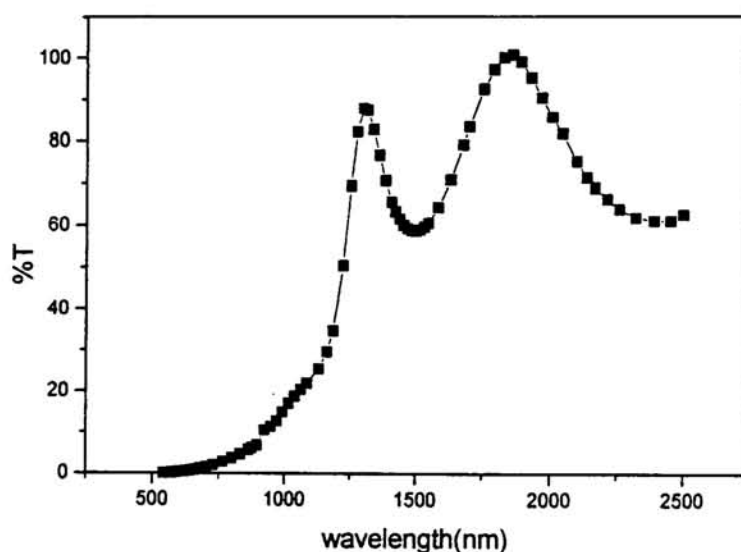


Fig.3.3 Transmission spectrum of a typical CuInSe_2 film.

The spectrum presents two well defined interference fringes, in which the overlaps of maxima and minima are drawn to obtain the values of T_M and T_m in the equation for calculating the refractive index (n) of the material

$$n = [N + (N^2 - s^2)^{1/2}]^{1/2} \quad 3.3$$

where $N = (2s (T_M - T_m) / T_M T_m) + ((s^2 + 1) / 2)$ with $s = 1.5$, the refractive index of glass substrates that are used. The refractive index that is determined for all the CuInSe_2 films is found to be in the range 2.69 to 2.7. The value is found to be a constant at all the wavelengths in the mentioned range. This value is in close agreement with $n = 2.9$ that is determined for CIS films by Tuttle et al [5].

The index of refraction (η) is actually constituted of two parts, a real and imaginary part given by $\eta = n - ik$, for an absorbing film on a transparent substrate. The extinction coefficient k is related to the absorption coefficient α by the relation

$$\alpha = 4\pi k / \lambda \quad 3.4$$

where λ is the wavelength of light that is used. Separately considering the strong absorption region and medium absorption region of the transmission spectra in Fig.3.3 and using the Swanepoel's method that is given in detail in chapter 1 the absorption coefficient is calculated. The absorption coefficient versus photon energy in the entire range of measurement of transmission spectrum is given in Fig.3.4. Different regions of absorption are observable in this graph also. The extinction constant k that is determined using eqt.3.4 is found to vary from 10^{-1} to 10^{-3} with increase in wavelength. Thus the measurements of optical constants of the films of CuInSe_2 yield almost a constant value of refractive index ($2.7 \geq n \geq 2.67$) at all wavelengths while there is a decrease in extinction coefficient with wavelength increase in the measured wavelength range.

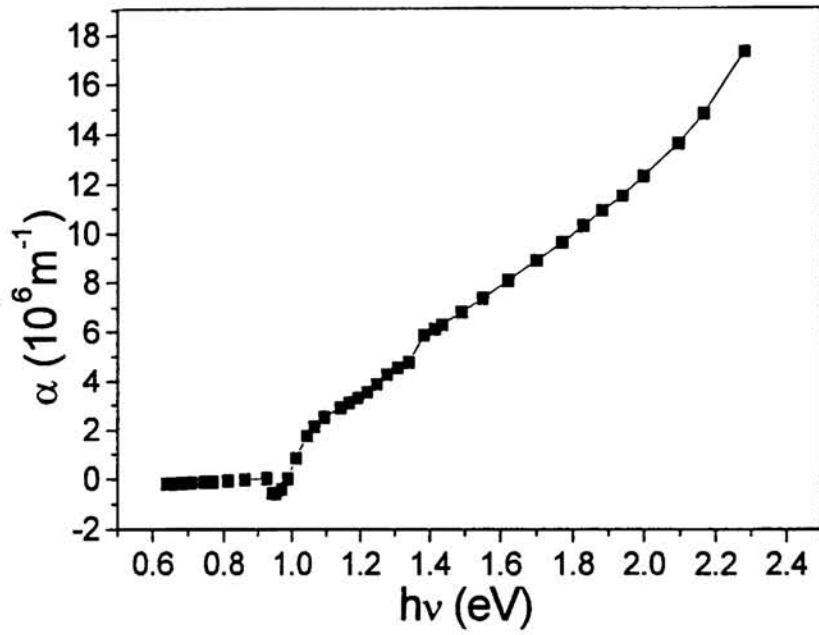


Fig.3.4 Variation of absorption coefficient with photon energy.

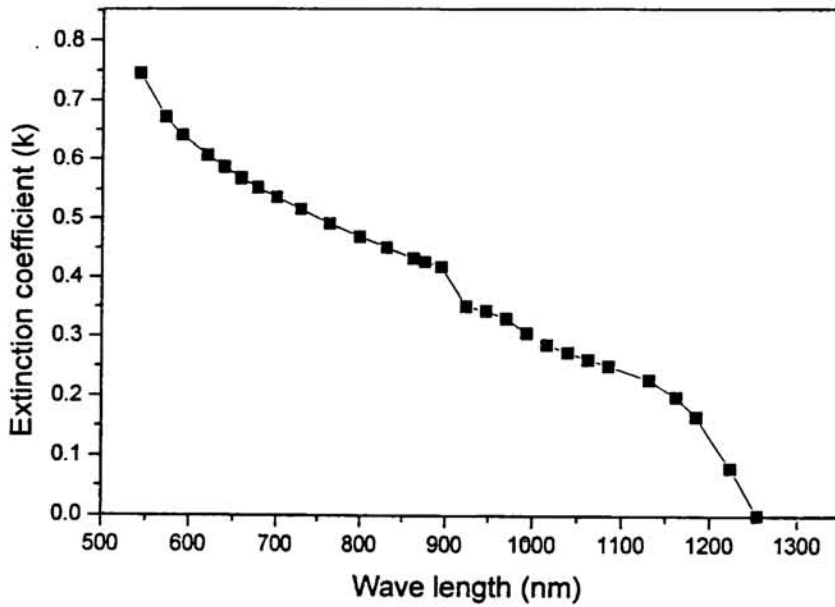


Fig.3.5 Variation of extinction coefficient with wavelength.

3.3 Photo conductivity studies in CuInSe₂ films

3.3.1 Transient photoconductivity

Transient methods of photoelectronic analysis focus on the rise or decay of photoinduced or electrical injection induced imperfection occupancies as they return to their thermal equilibrium values. From the transient photoconductivity methods, one can deduce the life time of the carriers, the capture cross section, the density of traps etc.

In the present investigation, transient photoconductivity measurements have been taken at different illumination intensities from 50mW/cm² to 110mW/cm², by varying the distance between the sample and the source after noting the illumination intensity at various positions with a photometer, to check for any photoconductivity saturation effect. After ensuring a linear variation of photoconductivity in the illuminated range, the experiments are done at an intensity of illumination of 100mW/cm². Photoconductivity measurements are done loading the sample in a CIT cryostat and cooling down to 10K initially. Silver electrodes of uniform thickness are applied at the ends of the samples with a spacing of 0.3 cm between them for illumination. The ohmic character of the electrode contacts has been tested by taking I-V measurements. The response being linear in the voltage range 5V to 30V, the current measurements at a d.c voltage of 25V are taken for calculations.

When the photoconductivity measurements are conducted on Cu-rich samples, a sudden decrease in current has been observed on illumination of the sample as in Fig.3.6 when the samples are very Cu-rich (Cu/In~1.6 to 1.4). Such a decrease in the conductivity to a value lower than that of the thermal equilibrium dark conductivity is called negative photoconductivity. In semi conductors such effects have been reported to exist due to the effect of sensitizing centers in the material, provided the levels of the sensitizing imperfections lie above the dark level so that they are empty in the dark and that the recombination imperfections compete favorably with the sensitizing imperfections for photo excited holes and also that the rate of thermal re-excitation of electrons from the sensitizing levels to the conduction band is less than the rate of capture of electrons from the conduction band by the recombination imperfections [11]. But since in these samples, some unusual phenomena like metallic

behaviour during dark conductivity measurements have also been observed (explained in chapter.4), etching studies have been performed.

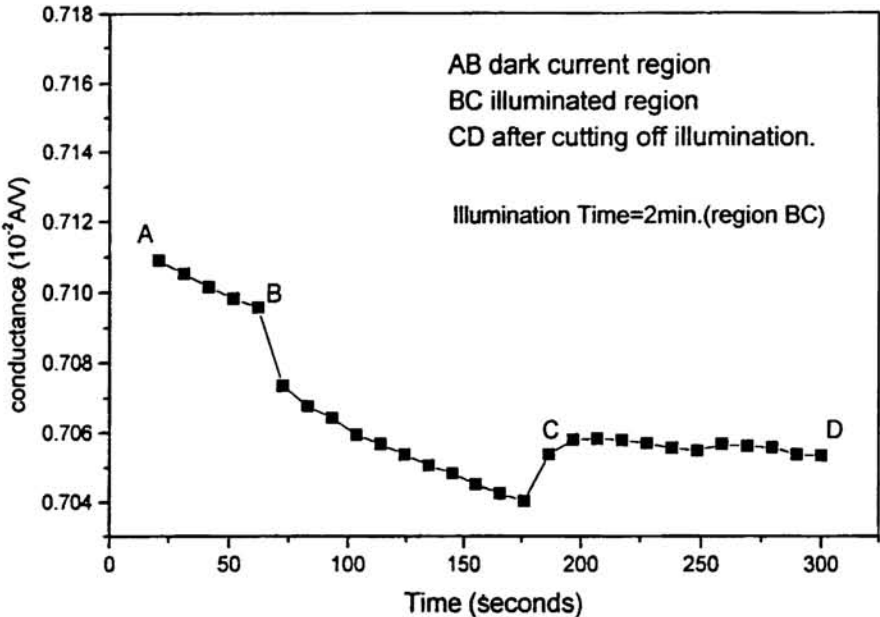


Fig.3.6 Transient photoconductivity on a Cu-rich CuInSe₂ at room temperature.

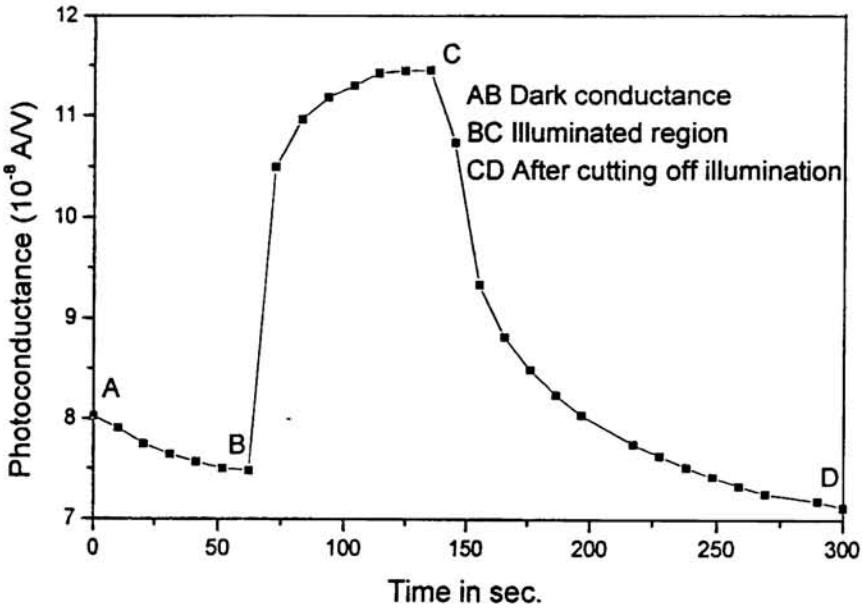


Fig.3.7 Transient photoconductivity after etching the Cu-rich CuInSe₂ sample surface.

A 5 wt % KCN aqueous solution has been used to etch the samples and the samples have been dipped for 30s. Fig.3.7 shows the photoconductivity of the sample after etching of the surface. It is observed that etching of the sample surface has reversed the photoconductivity effect. An examination of the composition from EDAX that is taken before and after etching on a typical film has shown that the composition of the film has changed from 31.3:19.4:49.3 to 22.1:25.4:52.5. This suggests that some segregates of Cu or Cu-binary compounds on the surface of the films has been the reason for the peculiar behaviour of negative photoconductivity in the very Cu-rich films. More studies on this are given in Chapter 4. This leads to the conclusion that in Cu-rich compounds, often the etching of the samples can produce an increased conductivity, implying the suitability of etched samples for forming junctions in solar cells. However the etching that is done on the In-rich samples haven't showed any change in behaviour of the films.

The transient photoconductivity behaviour of a typical CuInSe_2 film (slightly In-rich) at an illumination intensity of 100mW/cm^2 at different temperatures between 10K and 300K is represented in fig.3.8. It is seen that the initial rise and decay of the photocurrent on illumination is fast and is followed by a slow decay process (Fig.3.9). The sudden rise in conductivity on illumination may be related to the potential barrier height reduction on illumination similar to that noted from the analysis of steady state photoconductivity given in sec.3.3.2. The decay process can be assigned with two different phenomena-the fast decay that is determined by fast inter-grain barrier recovery as the photogenerated hole flux arriving to the inter-grain region suddenly ceases and the slow decay that is due to some additional time dependent processes such as trap emptying. Such long-term decay mechanism often observed in different materials has been explained as due to the involvement of deep level traps by different researchers [12]. Since the samples that are used here are slightly In-rich, (since the slightly In-rich samples show better response to light) one possibility of the trap is a deep level defect In_{Cu} . The spectral response profile that is given in section.3.3.3 also indicates the possibility of occurrence of In_{Cu} defect in these samples. It is possible that the variation of potential barrier height on illumination also modifies the emission and

capture cross sections of the traps thus influencing the rise and decay of currents on illumination and after cutting off illumination.

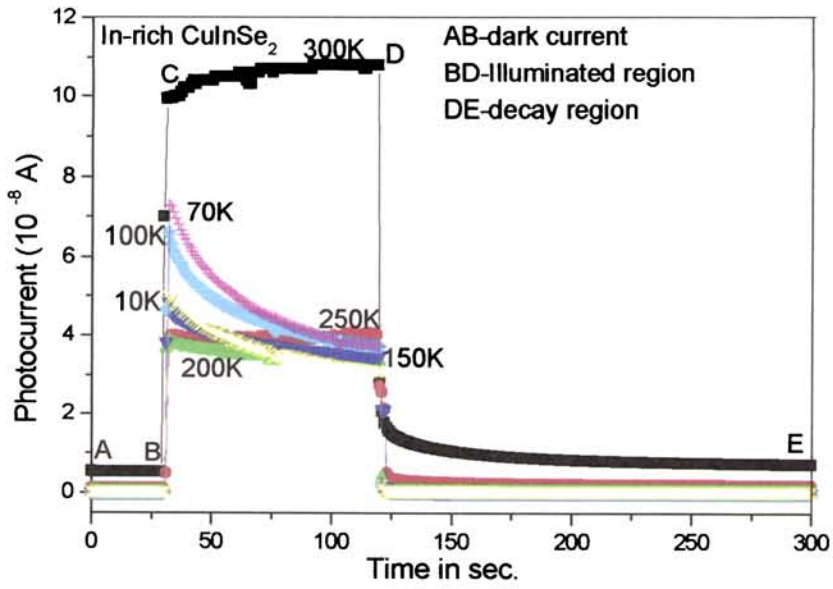


Fig.3.8 Transient photoconductivity on slightly In-rich CuInSe_2 .

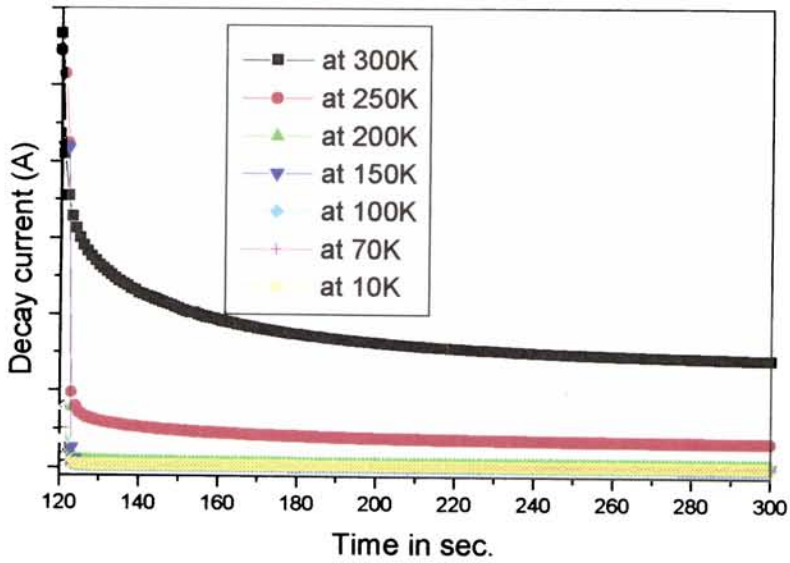


Fig.3.9 Decay part of the transient photoconductivity curves.

Analysis of the slow decay process shows that the decay curve in this region cannot be fitted with a simple exponential function. Using the differential life-time concept as suggested by Fuhs et al [13] the non-exponential decay process is analysed. The life-time τ_d given by

$$\tau_d = -[1/I_{ph*}(dI_{ph}/dt)]^{-1} \tag{3.5}$$

where I_{ph*} is the maximum photocurrent at $t=0$ for a given applied voltage, is found to vary with time

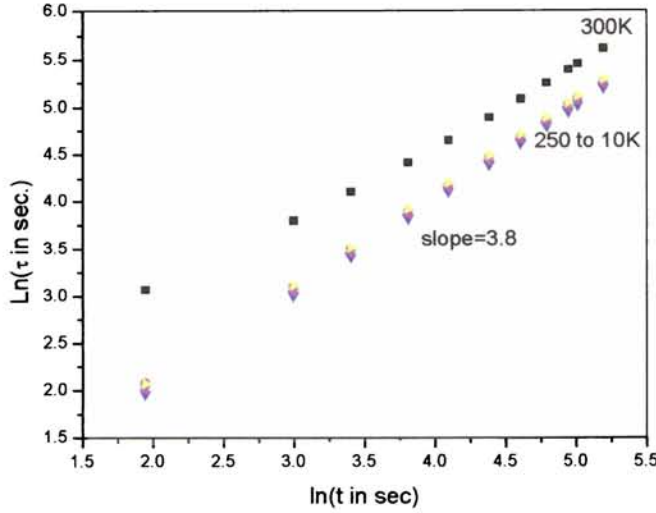


Fig.3.10 Variation of $Ln(\tau)$ with $Ln(t)$ at different temperatures.

The dependence of τ_d on time (t) is represented in the $ln(\tau_d)$ versus $ln(t)$ plot as in Fig.3.10.

It is observed from Table3.1 and Fig.3.10 that, if any particular time after cutting off illumination is considered, the decay constant continuously decreases down to the temperature 150K, while below that, the variation of decay constant is irregular. This type of temperature independent decay is attributed to the localized-localized recombination process for which no thermal activation is necessary [14]. It would be interesting to note that a similar behavioural change at low temperatures is observed and studied (chapter4) in dark conductivity measurements as a result of the hopping conduction of localized carriers in these samples.

Time ↓	→300K τ ↓	250K	200K	150K	100K	70K	10K
7 s	21.5	8	7.9	7.13	7.78	7.44	7.95
30s	60.4	33.09	32.77	30.38	32.88	31.65	33.74
60s	104.3	65.2	64.8	60.6	65.23	63.15	66.95
100s	161.2	107.8	107.4	100.87	108.1	105.04	110.9
120s	189.5	129.05	128.67	120.99	129.5	125.9	132.86
150s	232.3	160.89	160.6	151.2	161.5	157.4	165.77
180s	273.6	191.8	191.5	180.4	192.5	187.8	197.34

Table.3.1 gives the variation in values of decay constants with time at diff. temperatures.

3.3.2 Steady state photoconductivity

The experimental set up for the steady state photoconductivity measurements are same as in transient conductivity explained in sec.3.3.1. The sample has been cooled to 10K initially and the photocurrent measurements are performed in the heating cycle keeping the temperature steady at the required, pre-determined value using the temperature controller. The steady state photoconductivity (SPC) spectra of a typical (n-type) sample as a function of temperature at an illumination (ϕ) of 100mW/cm² is shown in Fig.3.11.

The sample being polycrystalline, the nature of the conductivity graph is explained by studying the effects of illumination in a polycrystalline material. A polycrystalline material is made up of grains with different orientations. The grain boundaries between these grains are characterized by interface states leading to a potential barrier between the grains. In a polycrystalline thin film sample like this, photo excitation can affect transport properties across the grain boundaries in different ways. Photo excitation may a) increase the density of free carriers through out the material b) decrease the intergrain barrier height by changing the charge in the intergrain states and (c) increase the possibility for tunneling through the intergrain barriers by decreasing the depletion layer widths in the adjacent grains [11].

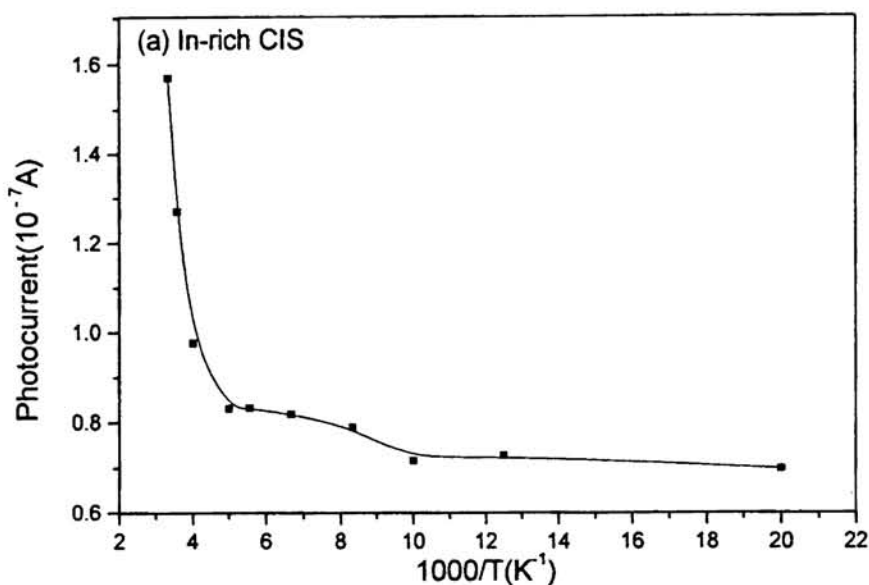


Fig.3.11 *Steady state photocurrent variation with temperature.*

Fig. 3.12 shows an energy band diagram of an intergrain barrier in an n-type polycrystalline material. Without an applied voltage electrons flow in both directions across the barrier and produce no net current. If a voltage difference is applied across the grain boundary, a net current begins to flow in a particular direction due to modification of effective barrier height. When the film is illuminated by appropriate incident radiation, electron-hole pairs will be created in the film, which will modulate the electrical conductivity through an increase in carrier concentration or decrease in barrier height.

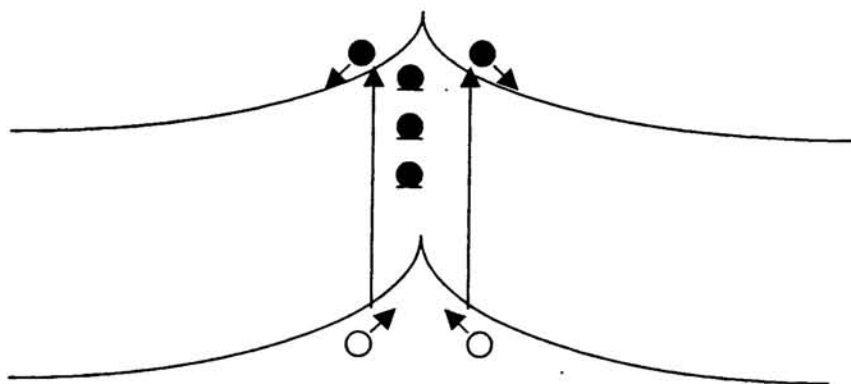


Fig.3.12 *Energy band diagram for an interparticle grain barrier in an n-type polycrystalline material.*

Thus, in general, the manifestation of the photoeffect in a polycrystalline material will be reflected in the production of additional minority carriers in the material along with a reduction ($\Delta E_{b\phi}$) of the intercrystalline barrier height (E_b) due to the exposure to the incident radiation of intensity ϕ , so that the change in conductivity can be expressed as

$$\Delta\sigma = \sigma_{\phi} - \sigma_d = \Delta\sigma_n + \Delta\sigma_{Eb} \quad 3.6$$

where σ_{ϕ} is conductivity on illumination, σ_d is dark conductivity $\Delta\sigma_n$ represents the change in conductivity due to additional carriers created and $\Delta\sigma_{Eb}$ corresponds to the change in conductivity due to change in the barrier potential $\Delta E_{b\phi}$ [12,15].

Now eqn. 3.6 may be written as

$$\Delta\sigma = q\mu_0(n+\Delta n) \exp(-E_b/kT) \exp(\Delta E_{b\phi}/kT) - q\mu_0 n \exp(-E_b/kT)$$

$$\Delta\sigma = q\mu_0 \exp(-E_b/kT) [\{ \exp(\Delta E_{b\phi}/kT) \} (n+\Delta n) - n] \quad 3.7$$

so that

$$\Delta\sigma_n = q\mu_0 \Delta n \exp(-E_b/kT) \quad 3.8$$

and

$$\Delta\sigma_{Eb} = q\mu_0 n [\exp(\Delta E_{b\phi}/kT) - 1] \exp(-E_b/kT)$$

$$\Delta\sigma_{Eb} = \sigma_d [\exp(\Delta E_{b\phi}/kT) - 1] \quad 3.9$$

If the effect of change in majority carriers can be considered insignificant, the electrical conductivity on illumination is given by

$$\sigma_{\phi} = (q^2 L n) / (2\pi m_e^* kT)^{1/2} \exp\{-E_{b\phi} / kT\} \quad 3.10$$

where $E_{b\phi}$ is the potential barrier height on illumination, T is the absolute temperature, n is the carrier concentration and L is the grain width.

In the present case, the $\ln(\sigma_{\phi} T^{1/2})$ versus $1000/T$ graph (Fig.3.13) that is plotted using eqn.(3.10) is found to have two linear regions above and below 200K, from the slope of which the barrier height is evaluated to be 0.073eV in the region above 200K, that is

much reduced from the barrier height $\sim 0.127\text{eV}$ that is calculated for the same sample from the dark conductivity (Fig.3.14) data.

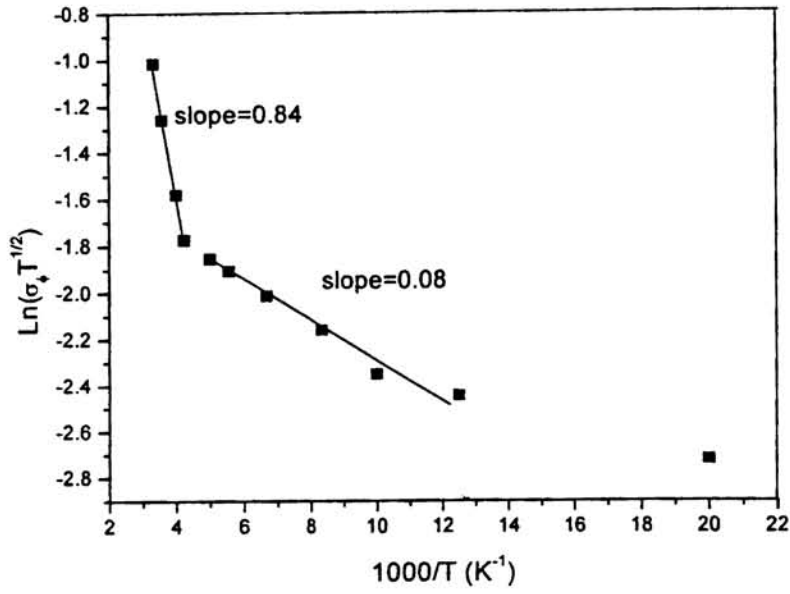


Fig.3.13 $\text{Ln}(\sigma_{\phi} T^{1/2})$ versus $1000/T$ graph on illumination.

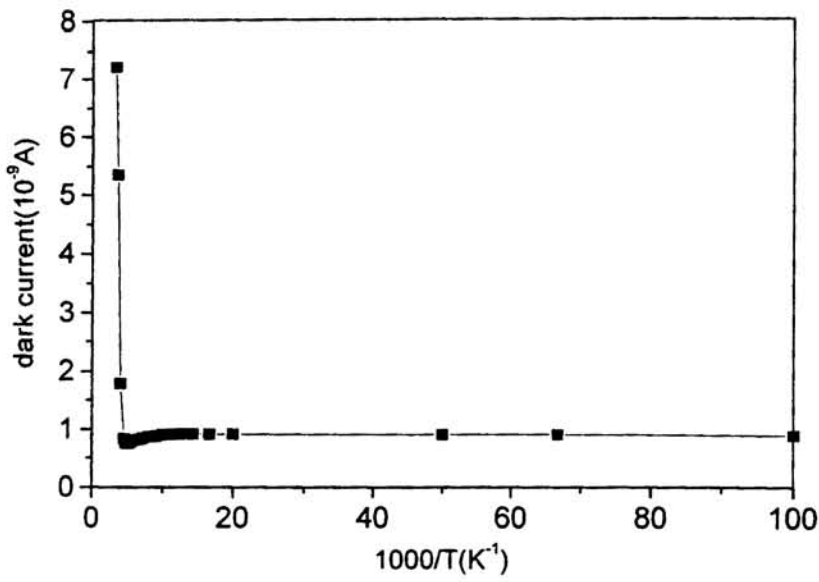


Fig.3.14 Dark current variation with temperature of the In-rich CIS film.

The barrier height on illumination below 200K is determined as ~ 0.007 eV which is very much reduced than the barrier height in dark. This indicates barrier potential reduction as a significant factor for increased conductivity on illumination. On illumination the reduction in grain boundary barrier height results in an increased probability for tunneling through the barrier. Holes that are generated by photoexcitation near the grain boundaries may get trapped at the grain boundaries decreasing the barrier height and width. The decrease in barrier width increases the tunneling probability of electrons through the barrier, the effect being predominant at low temperatures resulting in increased photosensitivity at low temperatures.

The variation in photosensitivity ($\Delta I_{ph}/I_d$) with change in temperature is shown in Fig.3.15. It is observed that photosensitivity of the samples steadily increases with decrease in temperature till 180K where as below that the change is slow but greater than the room temperature photosensitivity. This is similar to the trend that is observed in transient conductivity.

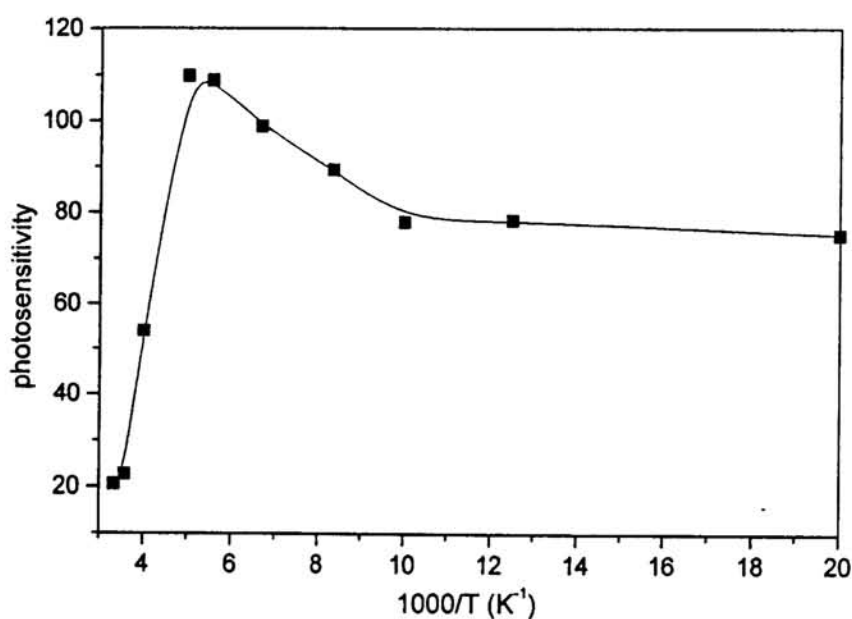


Fig.3.15 Variation in photosensitivity with temperature.

3.3.3 Spectral response in CuInSe_2

The experimental set up for spectral response is same as that of transient photoconductivity except for the fact that the source has been coupled with an Oriel 7240 grating monochromator for varying the incident energy in the required range. The measurement is taken at room temperature 300K.

The spectral response on a slightly In-rich sample with [In/Cu] ratio 1.15 is shown in Fig.3.16. The response curve is analysed in comparison with the optical absorption data taken on the same sample. On comparison, the photoactive transition bands around 1.04 eV and 0.88 eV can be assumed to be due to the transitions from the valence band to the conduction band and between defect levels respectively. The fact that there are no peaks corresponding to any binary phases or any peak like the 110 peak characteristic of the OVC's in the XRD of the sample as well as the observation that there is no significant change in the properties on etching, suggests that both the transitions that are observed belong to the CuInSe_2 phase itself.

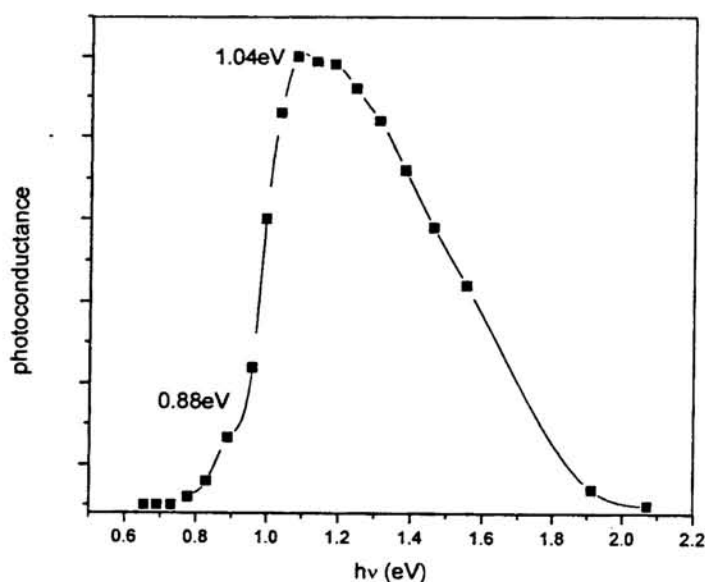


Fig.3.16 Spectral response of CuInSe_2 at room temperature.

The CuInSe_2 compounds used for the studies here are slightly In-rich and hence the expected defects are In_{Cu} or In interstitials and V_{Cu} . Of the former two In_{Cu} has lower formation energy of about 1.4eV [16]. In CuInSe_2 compounds In_{Cu} has a defect level between 0.12 to 0.16eV and two deep levels at ~ 0.25 eV and ~ 0.34 eV below the conduction band [17]. V_{Cu} usually forms an acceptor level 10-50meV above the valence band [17]. Then considering the band gap of about 1.04 eV in CIS, the defect transition observed at 0.88eV with a deficit of 160meV can be associated with a photoactive transition between a donor defect level due to In_{Cu} and a V_{Cu} acceptor level. The fact that the In -rich compounds observed are n-type corroborates the suggestion. The observance of photoactive bands in spectral photoconductivity due to such D-A pair transition has been reported earlier in CIS [18]. An activation energy of 0.16eV is observed in the dark conductivity measurements (chapter.4) on In-rich samples which also indicates the presence of In_{Cu} defect. Fig.3.18 represents the spectral response of an extremely in- rich film. Additional photoactive bands probably due to defect transitions are observed here.

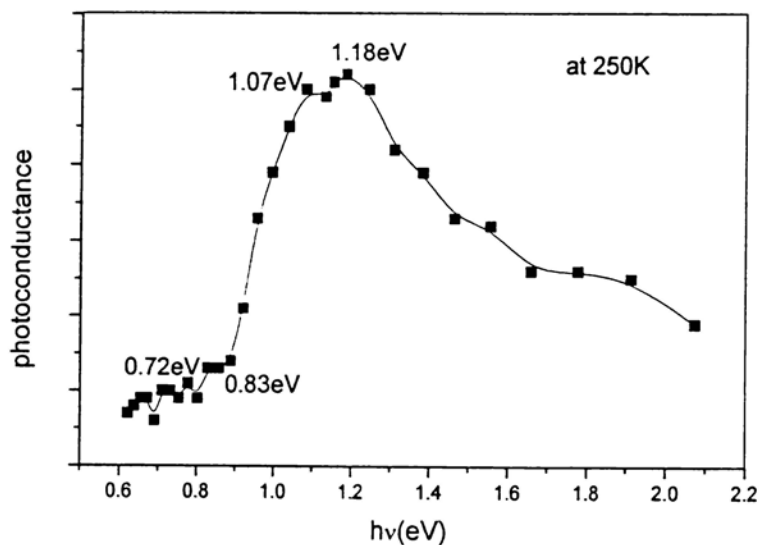


Fig.3.18 spectral response curve on an In-rich film with $\text{Cu:In:Se}=20:30:50$.

3.4 Conclusions

In this chapter, the optical properties of CuInSe_2 are studied based on optical absorption, transmission, transient and steady state photoconductivity and Spectral response. The band gap that is determined using absorbance studies reflects a shift towards the higher energy side with increase in In-content. The real part of the refractive index that is measured from transmittance spectra is found to be almost a constant while the extinction constant shows a slight decrease with increase in wavelength. The transient photoconductivity measurements showed a negative photoconductivity on Cu-rich samples while the In-rich samples are found to show very good positive response to light. The etching of the samples with KCN solution reversed the photo response nature of the former to positive photoconductivity along with reduction in Cu atomic concentration in the films while etching produced no noticeable changes on In-rich samples. The decay constants are calculated from the decay part of the transients. Steady state conductivity studies has shown reduction in potential barrier height on illumination as one significant factor contributing to increase in photoconductivity on illumination. Spectral response curves show photoactive transitions between defect levels and bands. The study indicates that while tailoring of band gap is possible in CuInSe_2 by varying the composition, the In-rich compounds are more photosensitive than the Cu-rich.

References

- [1] M.A.Green, K.Emery, K.Bucher and D.L.King, Prog.Photovoltaics 4 (1996) 59.
- [2] L.Stolt, in Proceedings of the 9th International Photovoltaic Science and Engineering Conference (Miyazaki, Japan, Nov.11-15,1996) pp.135.
- [3] M.A. Contreras, B.Egaas, K.Ramanathan, J.Hiltner, A.Swartzlander, F.Hasoon, R.Noufi, Prog Photovoltaics, 7 (1999) 311.
- [4] R.R. Philip and B. Pradeep. Thin Solid Films, 472/1-2 (2004)136-143.
- [5] J.R.Tuttle, D.Albin,R.J.Matson and R.Noufi, J.Appl.Phys.66(1989) 4408.
- [6] S.M.Firoz Hassan, M.A.Subhan, Kb.M.Mannan, Optical Materials, 14 (2000) 329.
- [7] J.E.Jaffe and A.Zunger, Phys.Rev.B, 29(1984) 1882.
- [8] O.S.Heavens, Optical Properties of Thin Solid Films (Butterworth, London, 1955)
- [9] R.E.Denton, R.D.Campbell and S.G.Tomlin, J.Phys.D 5 (1972) 852,
- [10] R.Swanepoel, J.Phys.E 17 (1984) 896
- [11] R.H.Bube. Photoelectronic Properties of semi conductors, Cambridge university press, Cambridge, NY 1992.
- [12] Pal R, Chattopadhyay K.K, Chaudhuri S and Pal A.K, Solar energy materials and solar cells 33 (1994) 241
- [13] Fuhs W and Stuke J Phys.Stat.Sol. (A) 24 (1968) 271.
- [14] Lal M and Goyal N Thin Solid Films 227 (1993)177
- [15] Roy S, Bhattacharjee B, Kundu S.N Chaudhuri S and A.K pal Materials Chemistry and Physics 77 (2003) 365.
- [16] Rincon C and Bellabarba C Phys.Rev.B 33 (1986) 7160.
- [17] Rincon C, Marquez R J.Phy.and Chem.of Solids 60 (1999) 1865
- [18] G.A.Medvedkin and M.a.Magomedov, J.Appl.Phys. 82 (1997) 4013.

Electrical characterization of CuInSe₂

4.1 Introduction

One of the basic interests of the researchers in CuInSe₂ compounds is that they can be doped p-type and n-type merely by the introduction of native defects. Development of solar cells based on p-CIS absorber layers and n-type CIS related ordered vacancy compounds is gaining rapid progress, not to mention various other combinations of p-CIS/ n-CdS/ZnO, p-CIS/CdS/ZnO:Al etc. [1- 3]

The electrical properties of CuInSe₂ films are largely influenced by various intrinsic defects such as vacancies and interstitials resulting from deviations from stoichiometric composition. In polycrystalline films, in addition to the intrinsic defects, the energy barriers that exist between adjacent grains can introduce an additional conductivity process [4]. Hence, it is of interest to investigate the electrical properties of CIS thin films of various compositions.

In the present chapter, we give an account of the electrical properties of CuInSe₂ of various compositions and discuss in detail the transport mechanisms in the films in different ranges of temperature. For the discussion of the results various models such as Arrhenius, Seto's as well as Mott's variable range hopping conduction model are used [5]. The transport properties of the films before and after etching are investigated. Hot probe method as well as room temperature Hall measurements are done to get information regarding the type of the samples as well as carrier concentration, sheet resistance etc. The etching experiments have given an insight in to the phenomenon of metal-type behaviour shown by the Cu-rich films.

4.2 Electrical conductivity in CuInSe₂ films

In 1984, Noufi et al [6] presented a qualitative observation on the dependence of electrical properties of CuInSe₂ on composition based on the experimental data they

obtained, in which they used films with the Se composition greater than the sum of Cu and In concentration as well as lesser than the sum. The resistivity ρ as well as the type of the films has been found to be different for the two categories as given in section 1.1. Through their experimental observation, they have shown that the control of electrical properties of the CIS films requires an extremely tight control of stoichiometry. They suggested that Cu vacancies in CIS are primarily responsible for the increase in p-type conductivity whereas in earlier speculations by Neumann et al [7] vacancies of In were pointed out as the responsible factors for p-type conductivity.

In our experiments on CuInSe_2 , the Se composition has been fixed at an atomic percentage composition of $50 \pm 1\%$ (according to EDAX) whereas In and Cu composition has been varied. The type of the samples, compositionally and structurally characterized are then determined using hot probe method. There after the electrical conductivity measurements have been conducted.

4.2.1 Conductivity type

The hot probe method is a simple and convenient technique to test the type of carriers in semi conducting films and utilizes the basic thermoelectric principle in determination of the carrier type. One end of the electrometer probe is heated and touched to one end of the sample. When the hot probe heats that end of the sample, the electrons at that point gain velocity and drifts to the colder end. This produces a disturbance in the equilibrium distribution of the carriers and sets up an electric field, which opposes the flow of carriers. This electric field will be positive with respect to the cold end if the carriers are electrons and negative if the carriers are holes.

The hot probe measurement that has been done on the various samples indicated that all the Cu-rich CIS samples that are prepared in our lab are p-type while the In-rich samples are n-type.

4.2.2 Electrical conductivity of CIS films

Samples of around 0.4 cm in length and 0.2 cm width have been used for conductivity measurements. Silver contacts are given on the two ends of the film and the ohmic nature of the contacts have been verified by V-I measurements at room temperature. Then the samples are loaded in the cryostat and are initially cooled to 80K. The experimental set up is explained in section.1.3.5.

4.2.2.1 Electrical conductivity in Cu-rich films.

When electrical conductivity of the samples were measured, it was surprising to see that the resistivity of the Cu-rich samples which were detected p-type by hot probe method, showed an increase in resistivity with increase in temperature. Fig.4.1 shows the resistivity variation of fresh Cu-rich CIS (composition given in Table.4.1) with temperature variation.

The metal-like behaviour shown by the Cu-rich films means either a cation disorder with the substitution of the In^{3+} cation by Cu^{1+} cation in the lattice or the formation of a conducting path through the formation of a dominating secondary phase like Cu_{2-x}Se showing metallic conduction as suggested by Niki et al [8]. Since the optical band gap has been found to be reduced with increase in Cu concentration in CuInSe_2 as explained in the previous chapter, the former possibility is considered first. Accordingly, in ternary chalcopyrites like CuInSe_2 , the interaction between the three fold degenerate $\Gamma_{15}(\text{p})$ state of the anion and the $\Gamma_{15}(\text{d})$ state of the cation of the same symmetry, forms a lower bonding state weighted more by the $\Gamma_{15}(\text{d})$ state and an upper antibonding state weighted more by the $\Gamma_{15}(\text{p})$ state. So increase in Cu content could be viewed as increasing the spread of Cu 3d orbitals thus increasing the probability of Se 3p-Cu3d interaction. This of course could be a possible explanation for increase in conductivity of films with more Cu content. But the explanation is not feasible to account for the metallic behaviour of the films for the reason below. If in an extreme case we assume that the antibonding state would be pushed high so that there would be no distinction between the valence and conduction bands (band gap \sim 0), then electrons could travel through the lattice as in a metal, but the band gap measurement has made it clear that such an overlapping is not happening. Although a decrease in band gap of Cu-rich while compared to that of In-rich is observed as depicted in chapter3, the transition to metallic behaviour can not be explained by this since optical analysis by taking the absorption spectrum has shown that even for the samples showing metallic behaviour, the lowest optical band gap is about 0.9eV. This suggested that a speculation as above can not be adopted for explaining the metallic behaviour of Cu rich films. So we investigated the 2nd probability, that is the presence of Cu . Se secondary layer on the surface of CIS as reported [8,9]. For this, we etched the samples in a 5 wt % KCN

aqueous solution giving a dipping time of 30s and conducted the conductivity studies. Fig.4.2 shows the conductivity that is measured on the films after etching.

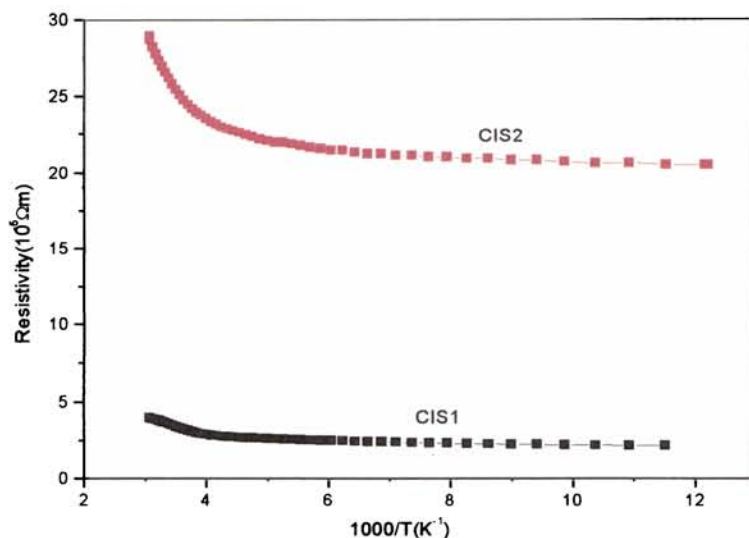


Fig.4.1 Resistivity variation of Cu-rich CIS films.

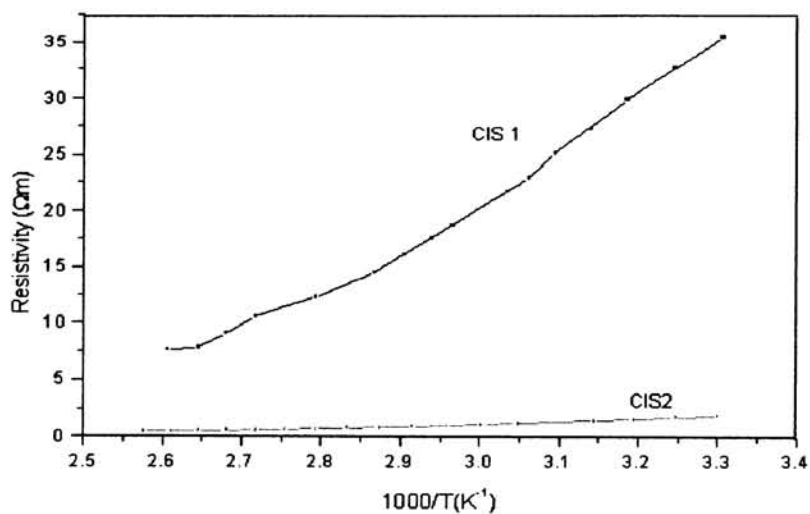


Fig.4.2 Resistivity versus $1000/T$ graphs for the etched Cu-rich films showing semi-conducting behaviour

It is observed that, the etching of the surface layer has changed the film behaviour drastically. The conductivity at room temperature has decreased in about three orders of magnitude. The film behaviour as depicted in Fig.4.2 is entirely that of a semi conducting film since the conductivity of the etched films steadily increase with temperature. Hall conductivity measurements as described in section 4.2.3 show that there is a drastic drop in the density of carriers also showing that etching has removed a number of free carriers on the surface making it certain that the conducting path has been formed on the surface of the samples in the unetched Cu-rich samples. The EDAX taken on the etched samples show that Cu composition had been decreased on etching. The changed composition on etching is better represented by the two parameters $\epsilon = \text{Cu}/\text{In}$ and $\kappa = 2\text{Se}/[\text{Cu}+3\text{In}]$ in table.4.1. The results establish beyond doubt that the metallic behaviour in the Cu rich films is due to conducting paths being formed and not due to any intrinsic behaviour of CIS. Now, looking at the composition and the electrical type of the behaviour of the etched films, we can assign them to type 2, that is p-type and intermediate ρ , according to the classification done by Noufi et al [6] as given in chapter 1. The photoconducting behaviour of the fresh and etched films is given in chapter 3.

Type of CIS film	CIS	$\epsilon = \text{Cu}/\text{In}$	$\kappa = 2\text{Se}/[\text{Cu}+3\text{In}]$	Room temperature ρ
Fresh	CIS1	1.6	1.1	$3 \cdot 10^{-5} (\Omega\text{m})$
Cu-rich	CIS2	1.4	0.9	$3 \cdot 10^{-4} (\Omega\text{m})$
Etched Film	CIS1	0.9	1.06	37 (Ωm)
	CIS2	0.8	1.3	2 (Ωm)

Table.4.1 Room temperature resistivity (ρ) and atomic% composition of CIS films.

4.2.2.2 Electrical conductivity in In-rich CIS films

Fig.4.3 shows the resistivity variation with temperature of a typical slightly In-rich CIS film with Cu: In: Se = 24: 27: 49. The resistivity versus inverse temperature plot shows a slow decrease in resistivity with increase in temperature in the temperature range 80K to 200K and a rather sharper decrease in resistivity with temperature above 200 K. The conductivity mechanisms in the two regions are identified as Mott's variable range hopping in the low temperature region and thermally activated conduction in the near room temperature region. In the thermally activated temperature range >200K, the conductivity is found to follow two types of dependences on temperature for the In rich CuInSe_2 and they are analysed in detail. It has been observed that above 270K the samples exhibited a thermally activated electrical conductivity (σ) described by Arrhenious and that in the temperature range 200K to 270K Seto's classical grain boundary effect [4,10,11] could explain the conductivity mechanism. Now the resistivity variation in different temperature ranges is considered separately.

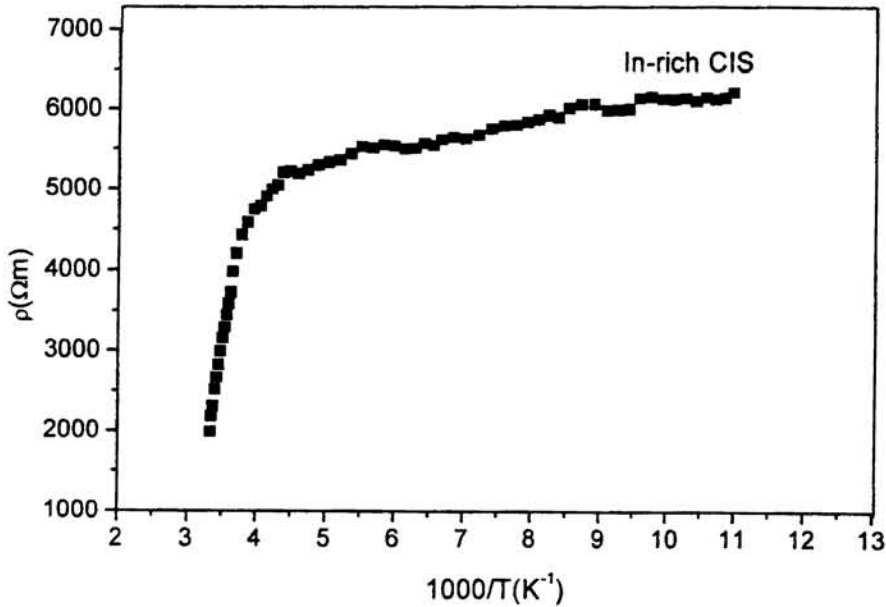


Fig.4.3 Resistivity variation of an In-rich CIS film with temperature.

Temperature Range above 270K

Analysis of the resistivity versus temperature plot shows that above 270K the samples exhibit a thermally activated electrical conductivity (σ) described by the Arrhenius relation of the type

$$\sigma = \sigma_{0a} \exp(-E_a/k_B T) \quad 4.1$$

where σ_{0a} is a pre-exponential constant, E_a is the activation energy and k_B is the Boltzmann's constant [12]. The conductivity in this range varies from $10^{-4} \Omega^{-1} \text{m}^{-1}$ to $10^{-2} \Omega^{-1} \text{m}^{-1}$. In this temperature range, two straight line regions are obtained from $\text{Ln}(\sigma)$ Vs $1000/T$ plots as shown in Fig.4.4 and Fig.4.5. The activation energies obtained are 0.5 eV when the temperature is raised above room temperature 300K and 0.16 eV between 270 and 300K. The 0.5eV activation energy indicates that in the high temperature region, the Fermi level shifts almost to the middle of the energy gap and that intrinsic conduction is taking place. In CIS, intrinsic defect levels between 120-160 meV are detected both in n and p-type materials from various experimental methods. In n-type CIS, the level usually corresponds to donor levels like V_{Se}^+ or In_{Cu}^+ [13].

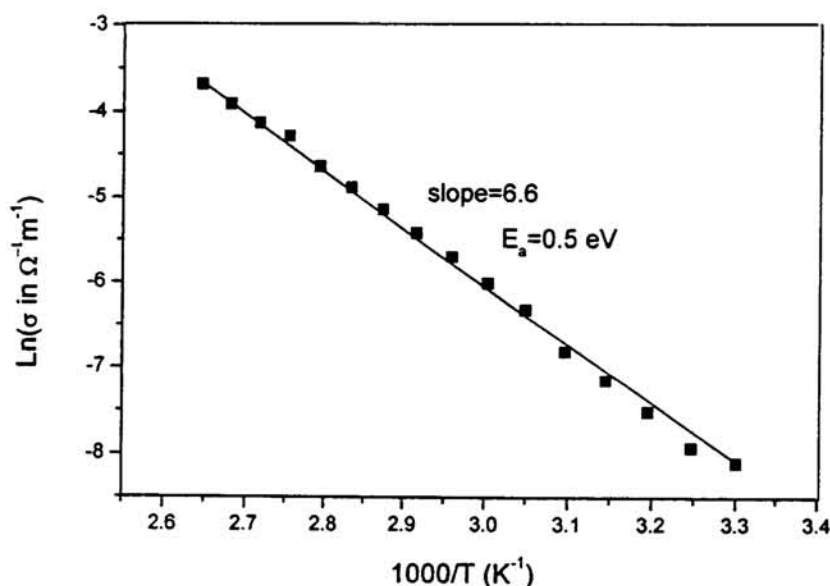


Fig.4.4 Arrhenius plot of conductivity in the high temperature range.

Accordingly, the activation energy 0.16 eV determined for the slightly In rich CuInSe_2 in the temperature range 270K to 300K can be assigned to single donor defect levels V_{Se}^+ or In_{Cu}^+ [13]. EDAX data suggests the possibility of both defects in the sample but taking the formation energy of these defects into consideration ($\sim 2.4\text{eV}$ for V_{Se} and $\sim 1.4\text{eV}$ for In_{Cu}), the possibility of formation of In_{Cu}^+ defect is more in these slightly In-rich samples [14]. The In_{Cu} defect in In-rich samples is suggested from spectral response measurements also as given in chapter 3.

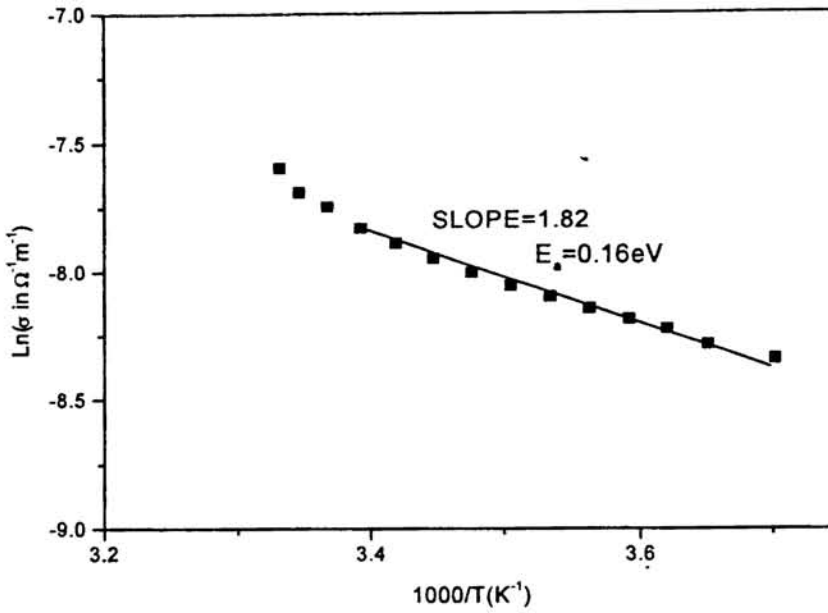


Fig.4.5 Arrhenius plot in the temperature range 270K to 300K.

In the temperature range between 200K and 270K

It has been noted that Arrhenius type of conductivity could not explain the conductivity mechanism in the temperature range 200K to 270K. Modeling shows that, in this range the conductivity mechanism can be explained using Seto's grain boundary model. The classical grain boundary trapping theory assumes the presence of trapping states at the grain boundaries, which capture free carriers. These charged states at grain boundaries

create depleted regions and potential barriers, which provide a resistance to the passage of carriers from a grain to a neighbouring one. Following the basic grain boundary model of Seto [10,11], the conductivity σ behaves as

$$\sigma T^{1/2} = \sigma_0 \exp(-q\phi_b/k_B T) \quad 4.2$$

where k_B is the Boltzmann's constant and ϕ_b is the barrier height. Even with more refined grain boundary models the same exponential dependence is obtained [15]. In these models, the current density is due to thermionic emission across the grain boundaries such as

$$J = A^* T^2 \exp(-q\epsilon/kT) \exp(-qV_{gb}/kT) \times [1 - \exp(-qV_d/kT)] \quad 4.3$$

where A^* is the effective Richardson constant, kT/q the thermal energy, $q\epsilon$ the fermi level position within the grain: $q\epsilon = E_C - E_F = kT \ln(N_C/n)$, N_C =effective density of states, n =carriers density, V_{gb} = barrier potential at the grain boundary, and V_d = bias voltage.

The grain boundary height (ϕ_B) calculated from the linear fit obtained for the $\ln(\sigma T^{1/2})$ Vs $1000/T$ curve (Fig.4.6) for the In-rich CIS in the mentioned region is found to be $\sim 0.02\text{eV}$.

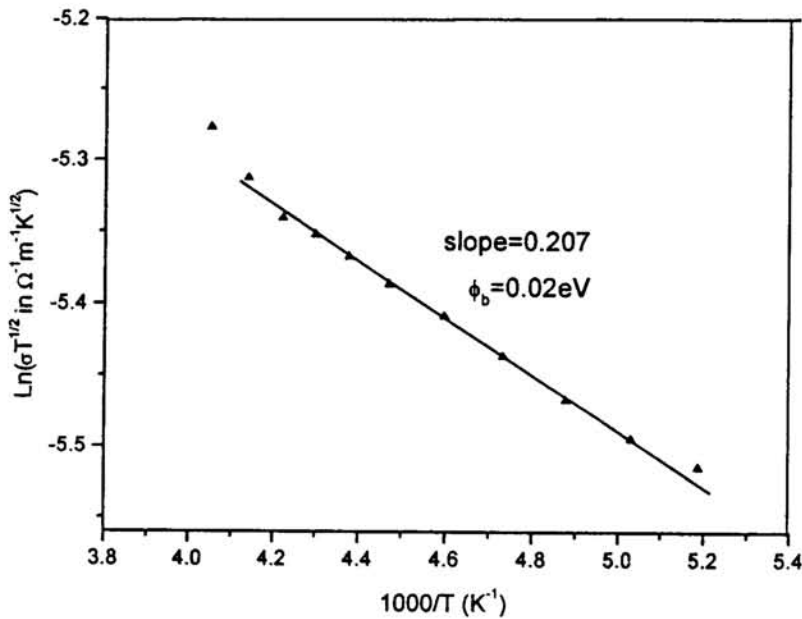


Fig.4.6 $\ln(\sigma T^{1/2})$ vs $1000/T$ Plots according to Seto's model in the temperature range between 200K and 270K.

The grain boundary height that has been determined for a sample with slightly more In concentration is given in section 3.3.2 of chapter 3. The barrier height determined from dark conductivity data $\sim 0.127\text{eV}$ for the In-rich sample is found to be greater than the barrier height determined here. The reason might be that as indium content of the films increases, the grain size becomes smaller which raises the grain boundary barrier potential.

Conductivity in the temperature range below 200K

In the low temperature region $<200\text{K}$, the prevailing mechanism of conduction followed a transition from thermally activated conductivity to Mott's variable range hopping conduction of the charge carriers in the localized states near the Fermi level [16,17], following the equation

$$\sigma = \sigma_0 T^{-1/2} \exp[-(B/T)^{1/4}] \quad 4.4$$

where B is related to the degree of disorder of the semiconductor. The hopping conduction is attributed to tunneling between states, which are close in energy but not necessarily close in space. When the temperature is low enough so that carriers cannot be excited into one of the allowed bands, the dominant conduction takes place via hopping, in which carriers hop from occupied to unoccupied sites, which are located within the band gap. Such a hopping mechanism may occur when the density of localized states is high enough to allow a non-negligible overlap of the individual wave functions. σ_0 in eqn.4.4 is related to the density of localized states $N(E_F)$ as

$$\sigma_0^2 = [N(E_F) / 2\pi\alpha k] \times (3e^4 v^2 \phi_0 / 2) \quad 4.5$$

and

$$B = 18\alpha^3 / kN(E_F) \quad 4.6$$

where α is the inverse of the localization length or the coefficient of exponential decay of the localized states wave function assumed to be 0.124\AA^{-1} , v is the typical phonon frequency approximately 10^{13}s^{-1} and ϕ_0 an overlap integral which is of the order of unity [18].

The $\text{Ln}(\sigma_{\text{hop}}T^{1/2})$ Vs $T^{1/4}$ plot for a typical CIS film ($\text{In}/\text{Cu}=1.1$) is shown in Fig. 4.7 and the Mott's parameters determined for the slightly In-rich CIS sample is given in Table. 4.2.

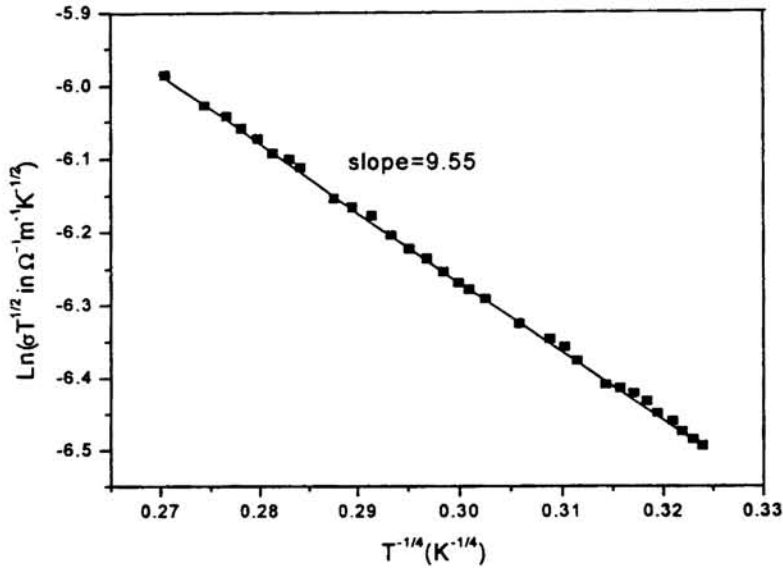


Fig.4.7 $\text{Ln}(\sigma T^{1/2})$ vs $T^{1/4}$ variation of the In rich film in the low temperature region.

Composition [In/Cu]	$B \cdot 10^4$ (K)	$\sigma_0 \cdot 10^{-6}$	$N(E_F) \cdot 10^{22}$ ($\text{cm}^{-3} \text{eV}^{-1}$)	$R \cdot 10^{-7}$ (cm) at 120K	W (eV) at 120K
1.1	0.84	3.61	4.76	0.87	0.0075
1.3	0.047	15.2	83.7	0.42	0.0036

Table.4.2 Mott's parameters from $\text{Ln}(\sigma T^{1/2})$ vs $T^{1/4}$ plot (temperature below 200K)

Mott's parameters determined for CuInSe_2 are found to be in good agreement with the values reported for polycrystalline CuInSe_2 by different investigators [4]. Mott's hopping parameters like hopping distance R for the hopping of the charge carriers among the localized states and the average hopping energy W are also calculated at a

particular temperature $T=120\text{K}$ using the estimated values of $N(E_F)$ in the In-rich CIS film. The Mott's parameters calculated on another film of In/Cu ratio 1.3 is also given in the Table.4.2. It is found that as the sample becomes more In-rich the grain size decreases and B value decreases, the observation is similar to that by Guillen and Herrero [4] who observed that the B value increased with annealing of the samples, which increased the grain size.

Thus a detailed analysis of the conduction mechanisms in different temperature ranges done for CuInSe_2 film shows that at high temperatures, the thermal activation is dominant which can be explained by Arrhenius and Seto's model where as at low temperatures hopping conduction prevails where Mott's variable range hopping conduction model is used to evaluate the associated constants as depicted in Table.4.2.

4.3.Hall measurements

The room temperature Hall coefficient measurements are done to get an estimate of the concentration and mobility of the carriers to study their influence on resistivity of semi conducting films. The Hall set up is given in section.1.3.5.2.

After loading the sample of 1sq.cm area on the sample holder with thermal grease, linearity check has been done to confirm the uniformity and ohmic behaviour of the contact. The measurements on mobility, density of carriers, Hall coefficient and type of carriers has been done. The result of the measurements on Cu-rich samples before and after etching and on In-rich samples are shown in the Table.4.3.

It is observed that the p-type Cu-rich samples showing metallic behaviour during resistivity measurements have a carrier concentration near $10^{20}/\text{cm}^3$, very near to that expected in a metal while the In-rich are having lower carrier concentrations. The room temperature resistivity is greater and carrier concentration is lesser for the In-rich CuInSe_2 samples and is found to be in good agreement with those reported in literature [19-24].

Type	CIS	CIS	n cm ⁻³	μ cm ² /Vs	ρ Ω cm	Carrier type	S Ω /cm ²	H cm ³ /C
Cu Rich Films	Fresh	CuInSe ₂ -1	8E18	10	6E-2	Holes	8E2	0.76
		CuInSe ₂ -2	1.9E20	4.77	6.7E-3	Holes	135	0.049
	Etched	CuInSe ₂ -1	2E13	3.4E2	884	Holes	2.9E7	3E5
		CuInSe ₂ -2	3E16	6.8	30	Holes	1E6	2E2
In- rich	Slightly In-rich		8E14	6.4E1	113	e-s	1E6	-7.3E3
	In-rich		3E12	5E1	3.5E4	e-s	4E8	-1.8E6

Table.4.3 Carrier Concentration (n), Carrier mobility (μ), resistivity (ρ), Sheet resistance S , Hall coefficient H and type of carriers from Hall measurement.

The KCN etched Cu-rich samples show a drastic drop in the density of carriers showing that etching has removed a number of free carriers on the surface making it certain that the conducting path as explained in sec.4.2.2.1 is formed on the surface of the samples in the unetched Cu-rich samples. The moderate hole concentration $\sim 10^{16}$ cm⁻³ with a mobility ~ 7 cm²/V-s obtained for the etched sample CIS2, implied that proper etching could enhance the suitability of these p-type films for solar cell applications.

The In-rich samples are found to be n-type and in them the resistivity increase with increase in In-content. This is in conformity with the electrical conductivity measurements, which indicates an increase in intergrain barrier potential with, increase in In-content probably due to reduction in grain size.

4.3 Conclusion

The electrical conductivity measurements and the Hall measurements on Cu-rich and In-rich samples show that the p-type Cu-rich samples are more conducting than the n-

type In-rich CIS thin films. The Cu-rich samples show the tendency of forming additional conducting paths on the surface, which accounts for the metal-like behaviour often exhibited by the samples on electrical conductivity measurements. The surface etching of the samples by KCN clearly indicated the validity of the additional-conducting path formation on the surface of Cu-rich samples. The Hall studies showed that there is a decrease in the number of carriers on etching but the majority carrier type does not change. However, the n-type In-rich samples do not show any change in the electrical conductivity on etching. Thus, it is found that the various intrinsic defects resulting from deviations in stoichiometry act like dopants producing n-type and p-type CIS films, of variable resistivity, that help in the production of suitable layers for solar cell devices.

References

- [1] D.Schmid; M.Reukh; F.Greenwald and H.W.Schock. J.Appl.phys. 73 (1993) 2902-2909.
- [2] S.N.Qiu, W.W.Lam, C.X. Qiu, I.Shih Applied Surface Science, 113/114 (1997) 761.
- [3] I.M.Dharmadasa, N.B.Chaure, J.Young, A.P.Samantilleke and T.Desol, Semicond. Sci.Technol. 18 (2003) 813.
- [4] C.Guillen and J.Herrero, J.Appl.Phys. 71(1992) 5479.
- [5] Rachel Reena Philip, B.Pradeep, G.S.Okram and V.Ganesan, Semicond. Sci. Technol, 19 (2004) 798.
- [6] R.Noufi, R.Axton, C. Herrington and S.K.Deb, Appl.Phys.Lett.45 (1984) 668.
- [7] H.Neumann, E.Nowak and G.Kuhn, Cryst. Res.Technol.16 (1981) 1369.
- [8] Niki S, Fons P J, Yamada A, Lacroix Y, Shibata H, Oyanagi H, Appl.Phys.Lett.74 (1999)1630
- [9] Schon J H, Alberts V, Bucher E , J.Appl.Phys. 81 (1997) 2799.
- [10] Seto J W J.Appl.Physics 46 (1975)115
- [11] Seto J W J.Appl.Physics 49(1984) 5365
- [12] Hassan S M F, Subhan M A, Mannan K M Optical Materials 14 (2000) 329
- [13] Rincon C, Marquez R J.Phy.and Chem.of Solids 60 (1999) 1865
- [14] C.Rincon and C.Bellabarba, Phys.Rev.B, 33(1986) 7160
- [15] S.Marsillac, T.B.Wahiba. C.El.Moctar, J.C.Bernede, A.Khelil, Solar energy materials and Solar cells 71(2002) 425.
- [16] Wasim S M, Rincon C, Marin G Phys.Stat.Sol. (a) 194 (2002) 244
- [17] Mott N F, Philos.Mag. 19 (1969) 835.
- [18] A.H.Moharram, M.M.Hafiz, A.Salem, Applied Surface Science 172 (2001) 61
- [19] Xiao H Z ,Yang L C, Rockett A 1994 J. Appl.Phys.76 1503
- [20] Pal R, Chattopadhyay K K. Chaudhuri S, Pal A K 1994 Solar Energy Materials and Solar Cells 33 241
- [21] Wang H P, Shih I, Champness C H 2000 Thin Solid Films 361 494

- [22] Wasim S M, Rincon C, Marin G 2002 Phys.Stat.Sol. (a) 194 244
- [23] Hernandez.E, Duran L, Rincon C A D, Aranguren G, Guerrero C, Naranjo J 2002 Cryst.Res.Technol. 37 1227
- [24] Ariswan, Moussa G E, Abdelali M, Guastavino F, Llinares C 2002 Solid State Communications 124 391

Preparation and Structural characterization of OVC's

5.1 Introduction

Photovoltaic devices based on CuInSe_2 and related ordered vacancy compounds (OVC) have developed rapidly in the last few years, achieving high active area efficiencies 18.8% in small device [1,2]. With the realization of the prominent role of OVC's in junction formation for efficient solar cell fabrication, the structural tolerance of the I-III-VI compounds to a large range of anion-to cation off stoichiometry which on the extreme limit is manifested by the existence of a series of compounds like CuIn_3Se_5 , CuIn_5Se_8 , $\text{Cu}_2\text{In}_4\text{Se}_7$, $\text{Cu}_3\text{In}_5\text{Se}_9$, $\text{CuIn}_7\text{Se}_{12}$, $\text{Cu}_4\text{In}_9\text{Se}_{16}$ etc. with different Cu/In/Se ratios is taken up as an interesting field of investigation [3 -5]. Zhang et al [3] proposed an OVC structure model based on the first principles total energy calculations. Their model suggested that the OVC's like CuIn_5Se_8 , CuIn_3Se_5 etc. are stabilized by the formation of $(2V_{\text{Cu}}+\text{In}_{\text{Cu}})$ defect pairs respectively in every 4, 5 etc. units of CuInSe_2 while the off-tie-line compounds like $\text{CuIn}_7\text{Se}_{12}$, $\text{Cu}_4\text{In}_9\text{Se}_{16}$ etc are formed by the introduction of 2, 1 Cu vacancies per molecule respectively in the on-tie-line compounds $\text{Cu}_3\text{In}_7\text{Se}_{12}$, $\text{Cu}_5\text{In}_9\text{Se}_{16}$. Our studies are centered on the preparation and characterization of three of the OVC's like CuIn_5Se_8 , CuIn_3Se_5 and $\text{CuIn}_7\text{Se}_{12}$.

Palatnik and Rogacheva [6] first reported CuIn_3Se_5 compound and assigned the crystal structure to space group of either $I\bar{4}$ or $I\bar{4}2m$ based on the observed extinction rule from X-ray diffraction data. Later, a refined structure solution was given by Honle et al [7] using single crystal x-ray diffraction data. They determined the space group $p\bar{4}2c$ and proposed the name, P-chalcopyrite, for this phase. Xiao et al [5] studied the epitaxial CuIn_3Se_5 thin film by transmission electron microscope and constructed a structure model by introducing ordered point defects into chalcopyrite CuInSe_2 structure to account for the extra diffraction spots. Normura and Endo [8] also constructed a structure model for CuIn_3Se_5 from the same principle. Hanada et al [9] investigated the crystal structure of CuIn_3Se_5 by combination of electron and x-ray diffraction. They limited the space group to $I\bar{4}$ or $I\bar{4}2m$ based on the observed

extinction rule followed by powder x-ray data. They further confirmed the space group to be $I\bar{4}2m$ from a convergent electron diffraction pattern along the [001] zone axis. Merino et al [10] refined the CuIn_3Se_5 structure using the structure models proposed by Honle et al [7] and Hanada et al [9] based on their x-ray diffraction data and proposed the model by Honle et al based on the argument that more realistic interatomic distances could be derived from the Rietveld refinement. The widely accepted structure for this OVC is the one given by Zhang et al [3] where as explained earlier it is explained as derived from CIS through ordered arrangement of defect complex.

The CuIn_5Se_8 compound is referred to exist in two different phases, the tetragonal α structure and the layered β phase, according to literature [11,12]. Manolikas et al [11] observed that the tetragonal α phase was having a tetragonal structure with $c \approx 2a$, with a super structure based on the Zinc blende structure. According to them, one of the sub-lattices was occupied by Se atoms and the ordering of the cation and of the vacancies on a sublattice of tetrahedral interstices caused the doubling of the unit cell along the c-axis. They arrived at the conclusion that this phase was having a thioallite -like structure. At higher temperatures, there are reports on existence of a disordered zinc-blende γ phase. The electron diffraction combined with high resolution electron microscopic studies showed that the layered phase of CuIn_5Se_8 was having a hexagonal structure with lattice parameters $a=0.72\text{nm}$ and $c=3.4\text{ nm}$, the main difference between the α and β phases being in the stacking of the close- packed anion layers. A 5-layer stacking periodicity was reported for the β structure by Frangis et al [12] while later both Folmer et al [13] and Tseng et al [14] reported a 7- and 14-layer stacking periodicity for this layered compound. Merino et al [10] assigned all the reflections obtained in the powder diffraction pattern of this compound to two structures named trigonal γ and other hexagonal γ_H . Kohara et al [15] reported the successful preparation of both hexagonal and tetragonal CuIn_5Se_8 by physical vapor deposition. The hexagonal film had a layered structure with a five-fold close- packed stacking of Se while the tetragonal film had a columnar structure with a lattice spacing of 3.3 \AA , corresponding to the cubic close- packed stacking of Se. Tham et al studied the structure of the layered compound by means of electron diffraction and high-resolution electron spectroscopy [16]. Studies of the optical properties of layered

CuIn₅Se₈ are done by Mahanty et al [17] from reflectance, Bacewicz et al [18] from optical absorption studies and Rincon et al [19] from absorption technique. In spite of all the reports on the layered CuIn₅Se₈, very few reports on the structure, optical properties and electrical properties of the tetragonal CuIn₅Se₈ are seen in literature. Zhang et al [3] explained the tetragonal CuIn₅Se₈ to have a chalcopyrite tetragonal structure, which is derived from CuInSe₂ by the introduction of 1 unit of the defect complex (2V_{Cu}+In_{Cu}) in every 4 units of CuInSe₂. Our study is on the structural, optical and electrical properties of the tetragonal chalcopyrite CuIn₅Se₈.

No reports other than Zhang et al's [3] reference to the compound as an off-tie-line compound with 1 unit of the defect complex (2V_{Cu}+In_{Cu}) and 2 neutral Cu vacancies in every 6 units of CuInSe₂ are available on CuIn₇Se₁₂ in literature, to the best of our knowledge.

In this chapter, the studies on the preparation and structural characterization of the OVC's CuIn₅Se₈, CuIn₃Se₅ and CuIn₇Se₁₂ are given. The compositional and morphological characterizations are done by EDAX, SEM and AFM where as phase and structure identification has been done by XRD. Binding energy calculations are done by XPS measurements. The bond length determination has been done by the 'CTB plus $\eta = \eta_{\text{expt}}$ ' rule.

5.2 Preparation of thin films of CuIn₅Se₈, CuIn₃Se₅ and CuIn₇Se₁₂.

The preparation technique used is same as that in the case of CuInSe₂ (given in section.2. 2) and is described in detail in section1.2.1. Here also the same vacuum coating unit as in the case of deposition of CIS is used taking all the preliminary measures as substrate cleaning, cleaning of boats, maintenance of vacuum, control of substrate and source temperatures etc. as described in section.1.2.1 for obtaining good quality films. But for the preparation of OVC's the source temperatures are so adjusted that In flux greatly exceeds that of Cu flux. Even then, since the reaction rate at the substrate often varies, the different OVC films are selected for further studies only after ensuring their composition by EDAX and their structure by XRD

5.3 Compositional analysis and Morphological Characterization

Energy dispersive X-ray analysis has been done for determining the composition of the films. But along with that, X-ray diffraction techniques has been used to ensure that

there was no secondary phase formation and that the films are giving chalcopyrite characteristic reflections. Very often, the films are found to have a very small percentage of sodium content, which has been diffused from the soda-lime glass substrates used. Since the Na diffusion is found to affect the properties of the films especially the electrical conductivity of the films to a certain extent, they have been sorted separately.

As in the case of CuInSe_2 , the morphological characterization of the films is done using scanning electron microscopy and atomic force microscopy. All the films appear to be uniform to the naked eye.

5.3.1 EDAX spectra

The experimental set up for the compositional analysis are as given in section.2.4.1. The EDAX spectra obtained on the different films are shown in fig.5.1 a-c. Considering the monovalency of Cu, triple valency of In and divalency of Se usually observed in CuInSe_2 compounds, the electrical neutrality of the compounds is well explained. The valency of the elements in the compound has been verified by ESCA studies also.

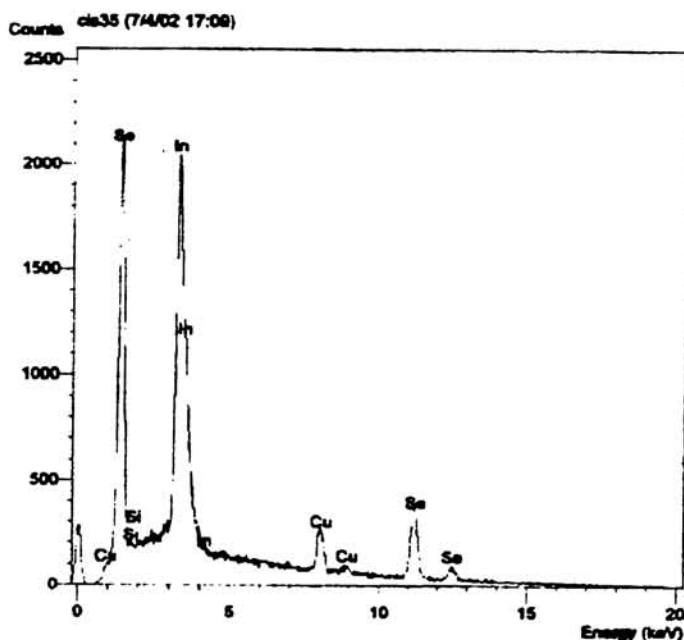


Fig.5.1a EDAX spectrum of CuIn_3Se_5 thin film with $\text{Cu:In:Se} = 11:34:55$

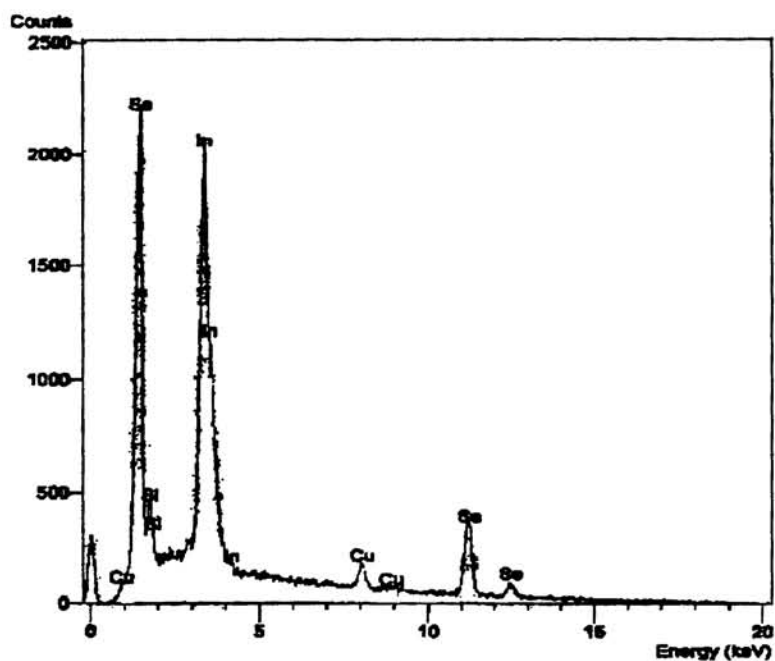


Fig.5.1b EDAX spectrum of $CuIn_5Se_8$ thin film with $Cu:In:Se = 7:36:57$

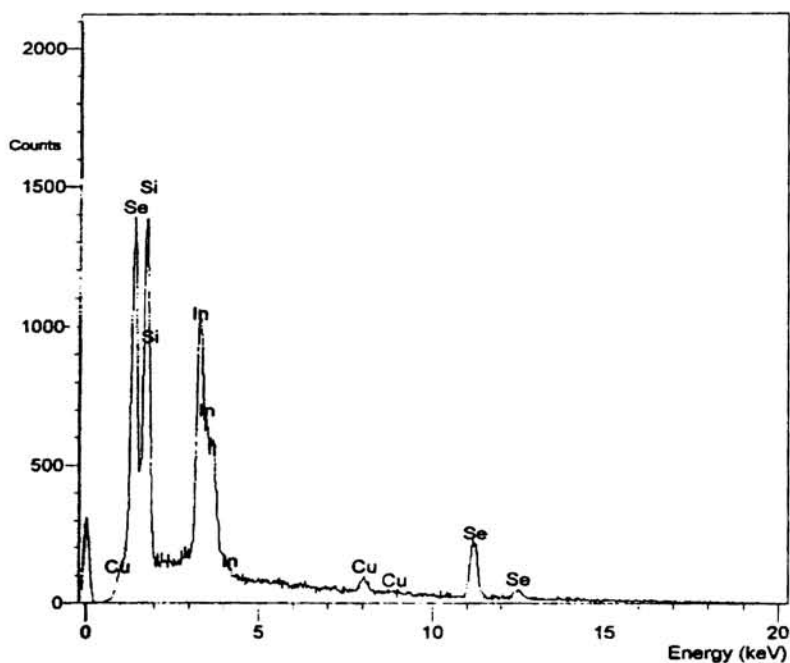


Fig.5.1c EDAX spectrum on a $CuIn_7Se_{12}$ thin film with $Cu:In:Se = 5:36:59$

All the spectra are normalized and the percentage composition is given. In some spectrum the Si peak appears from the substrate. Even while allowing for the 2%

experimental error, the different films are found to have the expected atomic % composition for the OVC's CuIn_3Se_5 , CuIn_5Se_8 and $\text{CuIn}_7\text{Se}_{12}$.

5.3.2 Scanning Electron Micrographs

The SEM images on three different films are shown in Fig.5.2a-c.

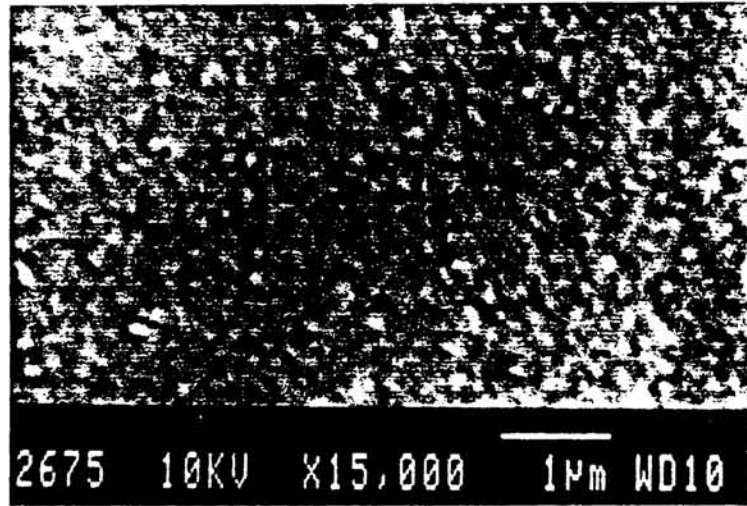


Fig.5.2a SEM image on CuIn_3Se_5 thin film

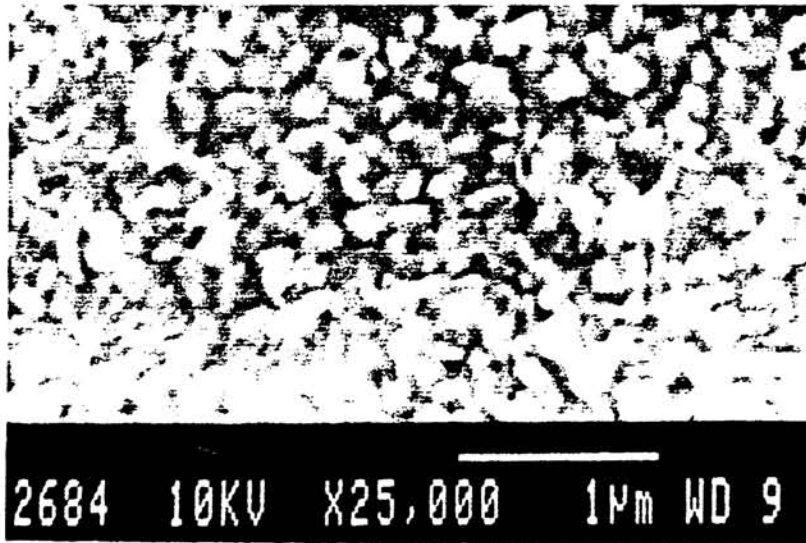


Fig.5.2.2 SEM image on CuIn_5Se_8 thin film.

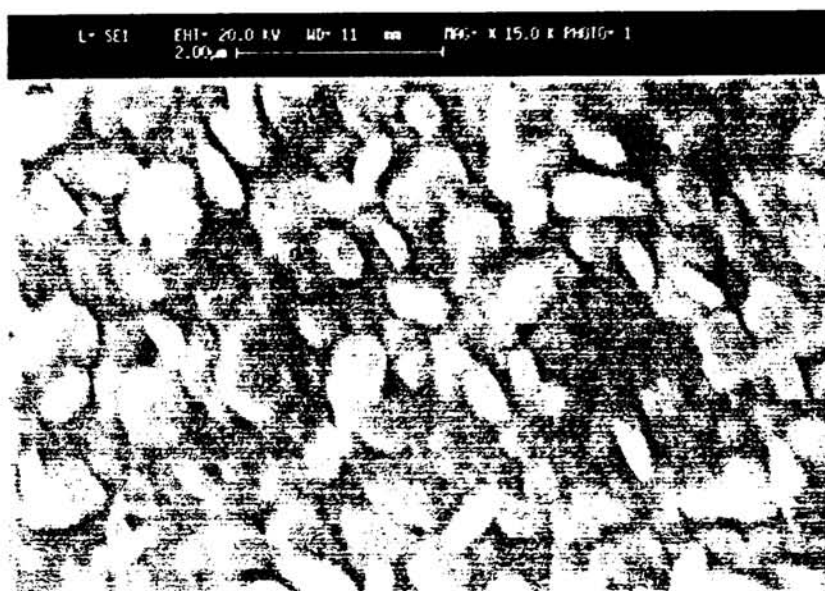
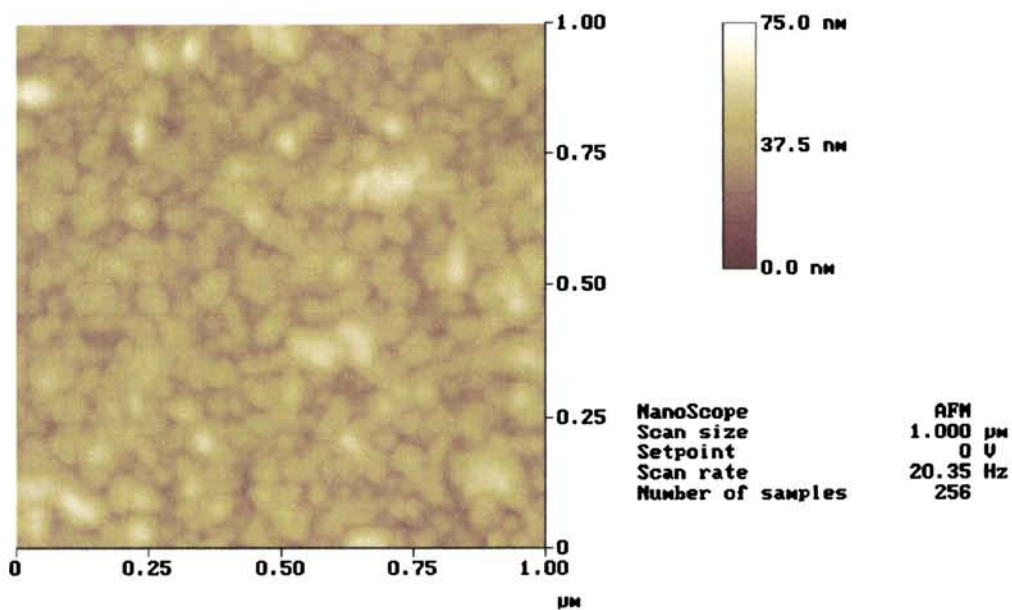


Fig.5.2c SEM Image on $\text{CuIn}_7\text{Se}_{12}$ thin film.

Since the grain size is very small, the grain size calculation from the images seems not dependable. More over though it is not clear from the SEM, it is seen from the AFM that each grain observed is an agglomeration of particles. But the SEM images clearly indicate the polycrystalline nature of the films with well-defined boundaries for the grains. If the grain size is roughly estimated, it is seen that it is much greater than that calculated from XRD, which is the expected outcome of the clustering of particles.

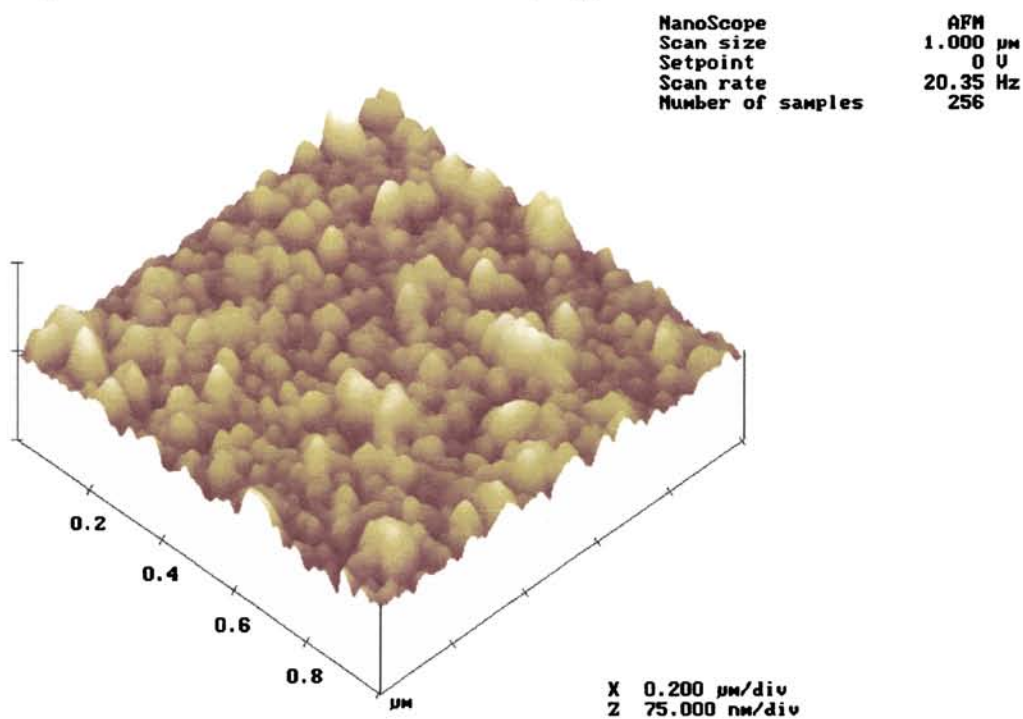
5.3.3 Atomic Force Microscopy

The same arrangement as explained in Chapter 2 for AFM measurements is used here also. The “in contact mode AFM” has been used to image the surface features of the thin film samples, employing an AFM Nanoscope E, Digital Instruments, with a silicon nitride cantilever to probe different portions of the film surface. The root mean square values of the surface roughness parameter as well as the grain sizes are noted from the atomic force micrographs. The 2-d micrographs for CuIn_5Se_8 , CuIn_3Se_5 and $\text{CuIn}_7\text{Se}_{12}$ are given in Fig.5.3 a-g and the 3-d micrographs in Fig.5.4a-g. The micrographs give evidence to the fact that the growth pattern of the films often varies when slight changes in composition are made. The agglomeration of the particles is very clear in the 2-d micrographs, which clarify the fact that grain size measurements



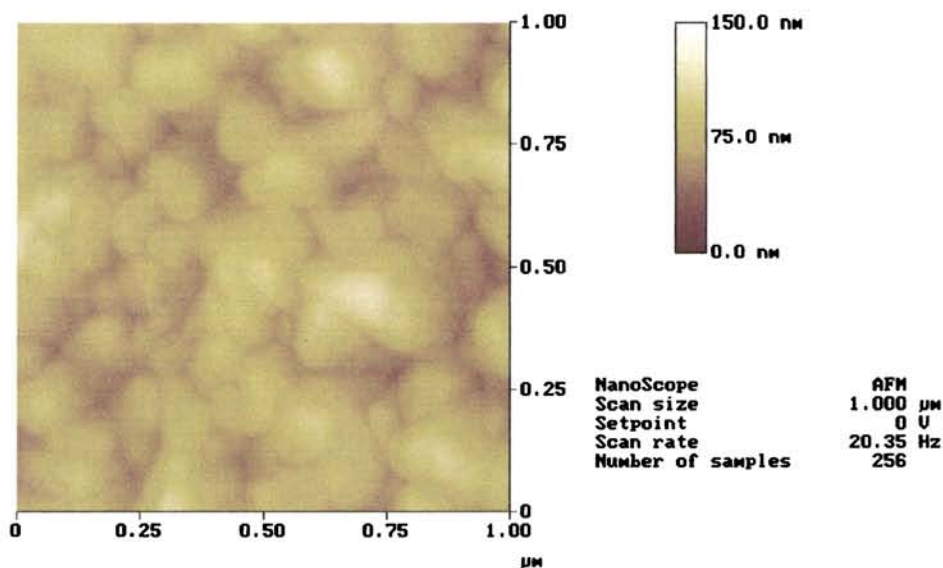
cis-45.008

Fig.5.3a Two dimensional AFM on $CuIn_3Se_5$ film with $Cu:In:Se = 10.8:33.2:56$



cis-45.008

Fig.5.4a Three dimensional AFM on $CuIn_3Se_5$ film with $Cu:In:Se = 10.8:33.2:56$



cis-51.003

Fig.5.3b Two dimensional AFM on CuIn_5Se_8 film with $\text{Cu}:\text{In}:\text{Se} = 7:36:57$.

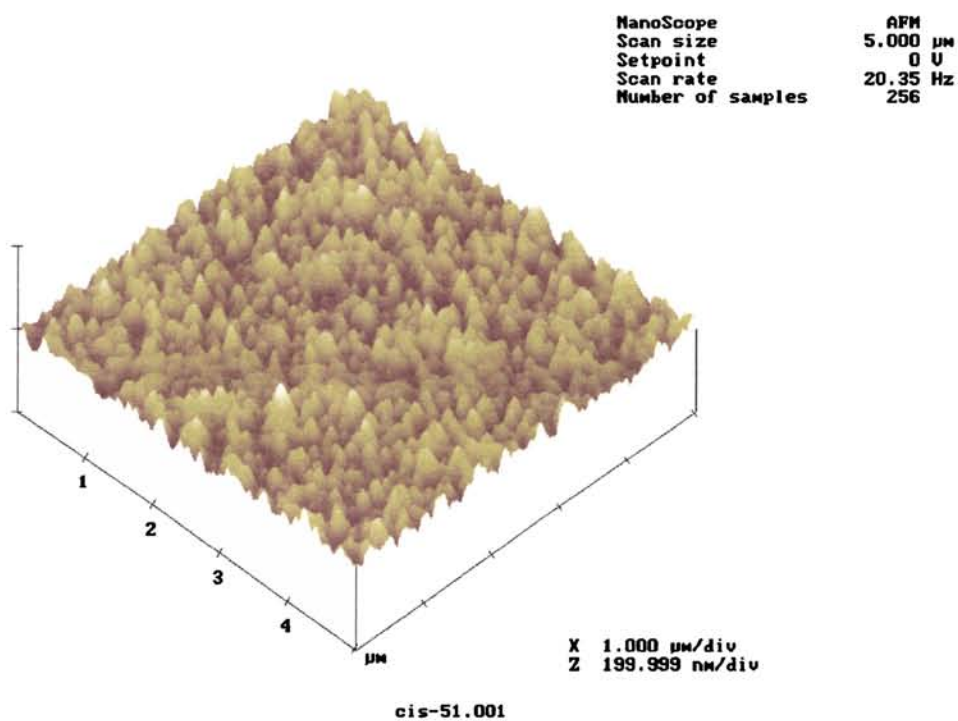
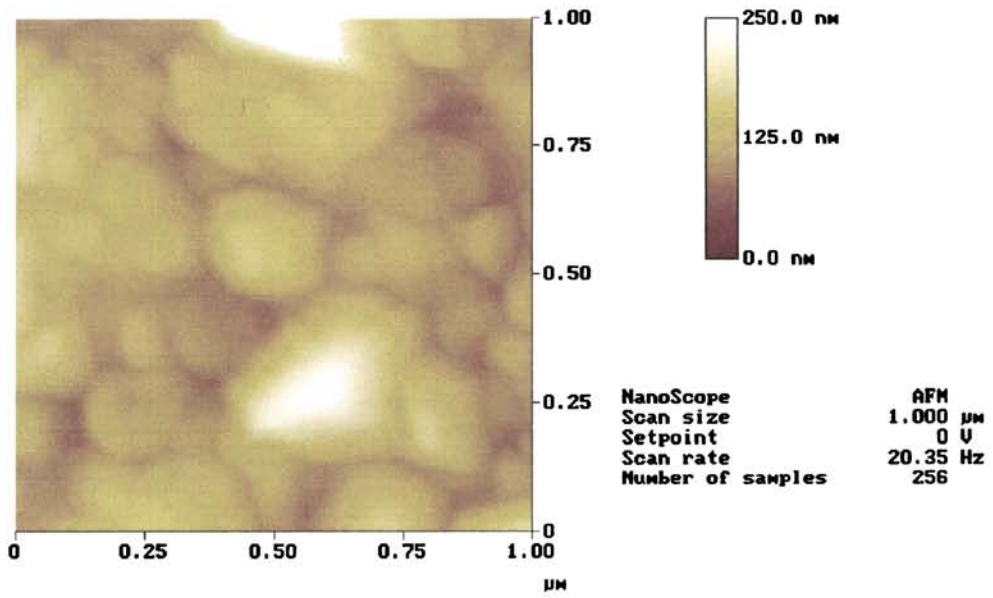


Fig.5.4b Three dimensional AFM on CuIn_5Se_8 film with $\text{Cu}:\text{In}:\text{Se} = 7:36:57$.



cis-49.008

Fig.5.3c Two dimensional AFM on $\text{CuIn}_7\text{Se}_{12}$ film with $\text{Cu}:\text{In}:\text{Se}=5:36:59$

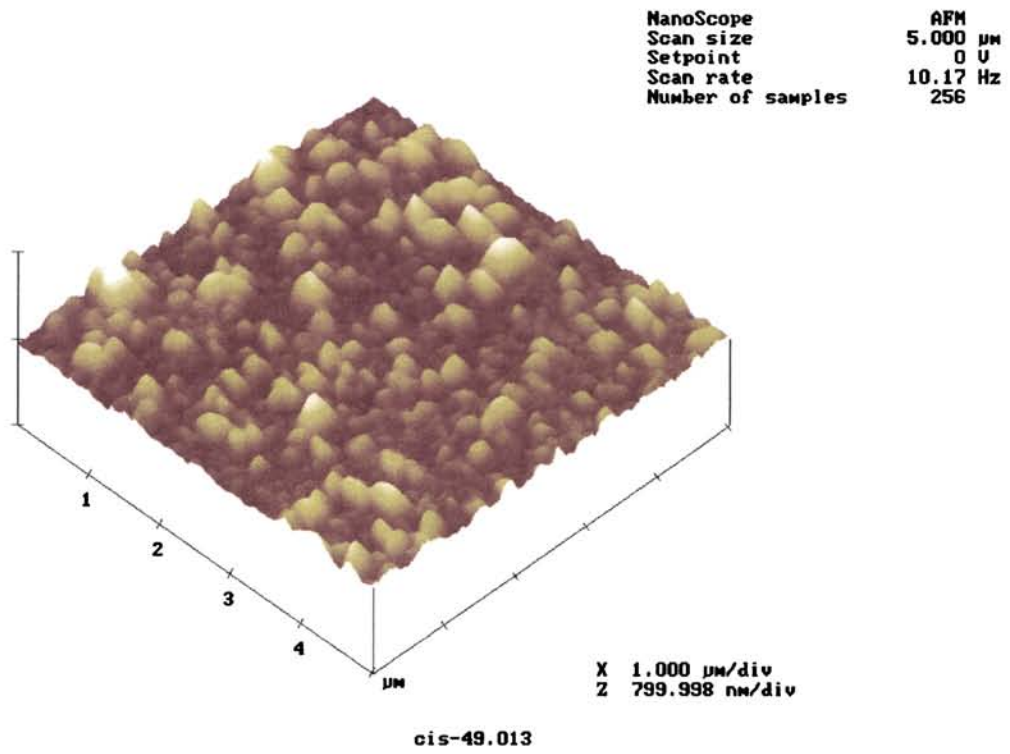


Fig.5.4c Three dimensional AFM on $\text{CuIn}_7\text{Se}_{12}$ film with $\text{Cu}:\text{In}:\text{Se}=5:36:59$

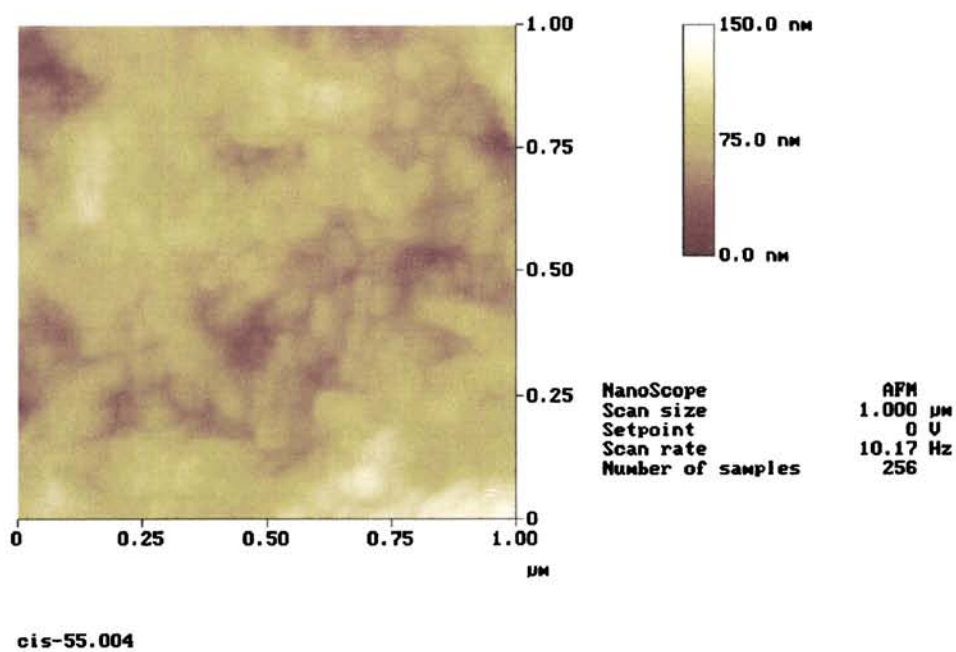


Fig.5.3d Two dimensional AFM on $\text{CuIn}_9\text{Se}_{14}$ film with $\text{Cu}:\text{In}:\text{Se} = 4.1:38.5:57.4$

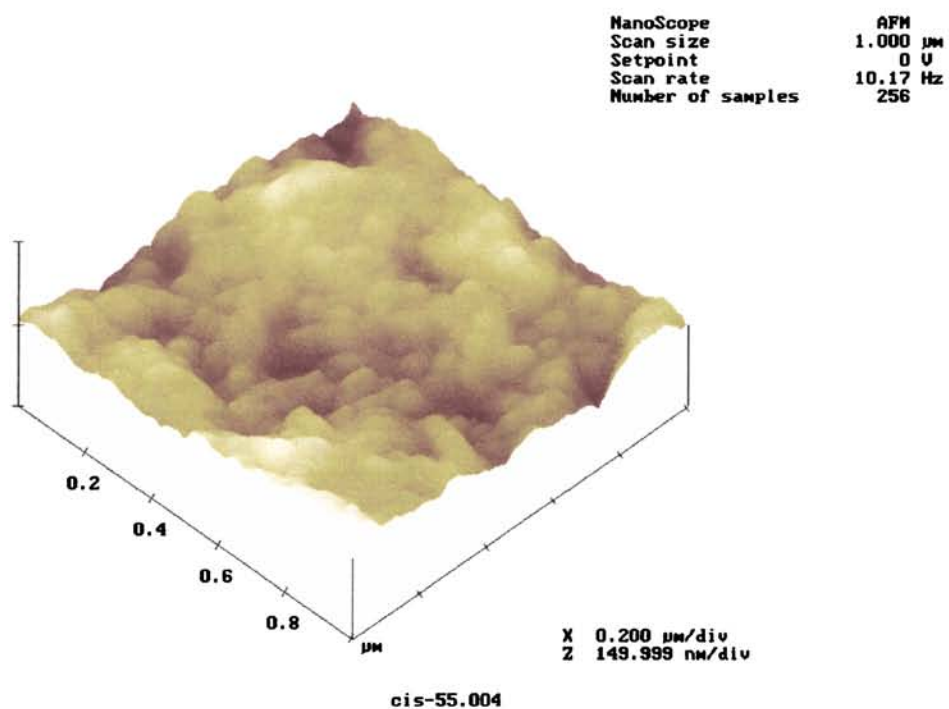


Fig.5.4d Three dimensional AFM on $\text{CuIn}_9\text{Se}_{14}$ film with $\text{Cu}:\text{In}:\text{Se} = 4.1:38.5:57.4$

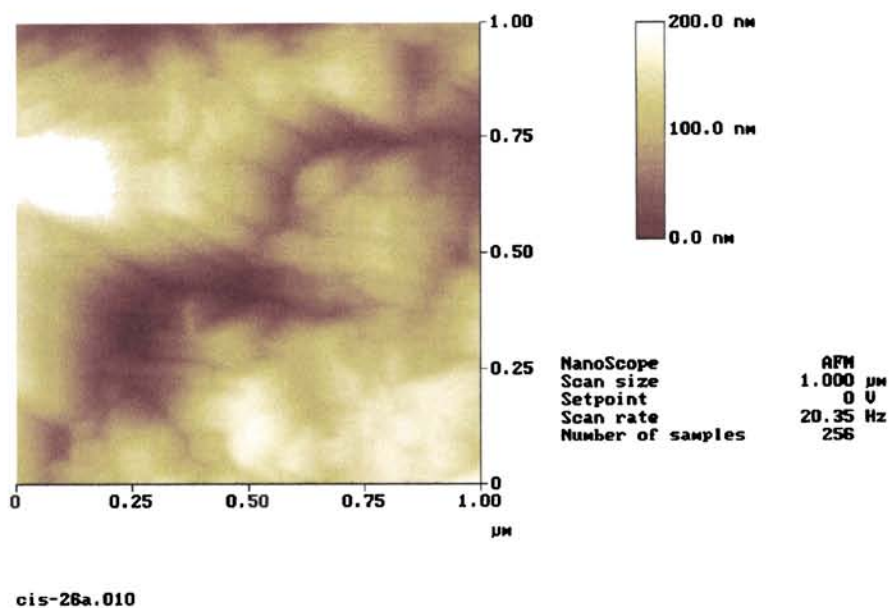


Fig.5.3e Two dimensional AFM on CuIn_3Se_5 film with $\text{Cu}:\text{In}:\text{Se} = 10:32:54.9$ and $N_a = 3.1\%$

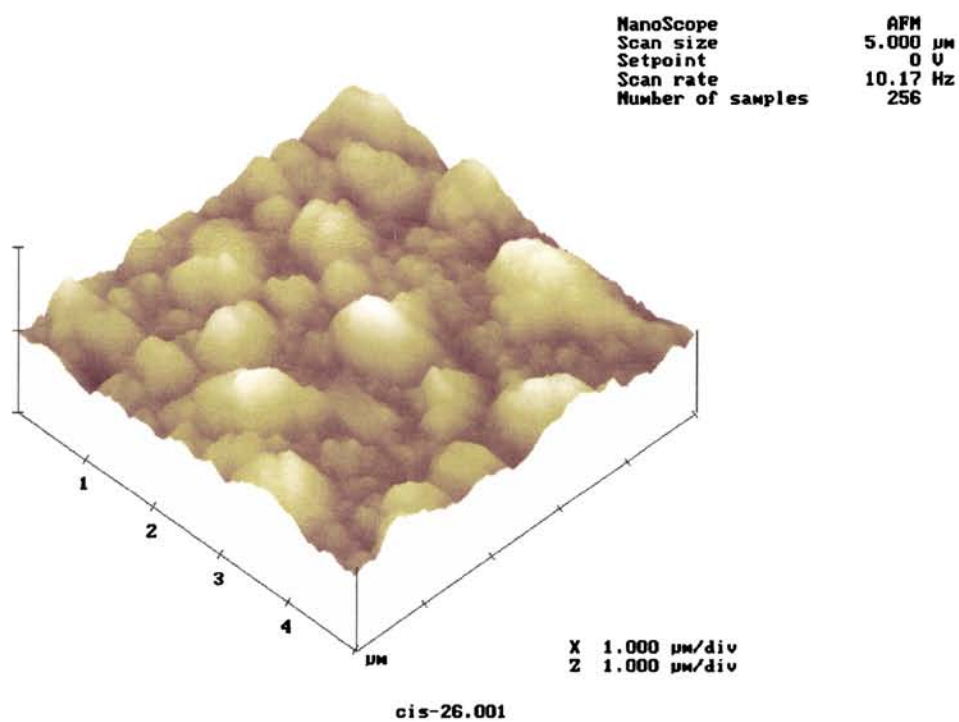


Fig.5.4e Three dimensional AFM on CuIn_3Se_5 film with $\text{Cu}:\text{In}:\text{Se} = 10:32:54.9$ and $N_a = 3.1\%$

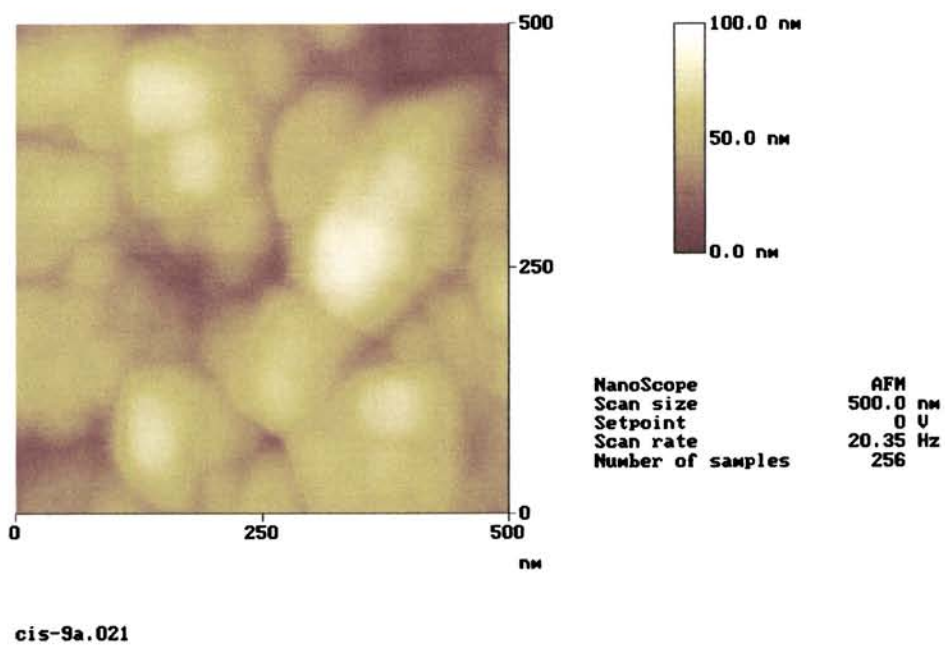


Fig.5.3f Two dimensional AFM on CuIn_5Se_8 film with $\text{Cu}:\text{In}:\text{Se} = 6.8:36.2:54.4$ and $N_a = 2.6\%$

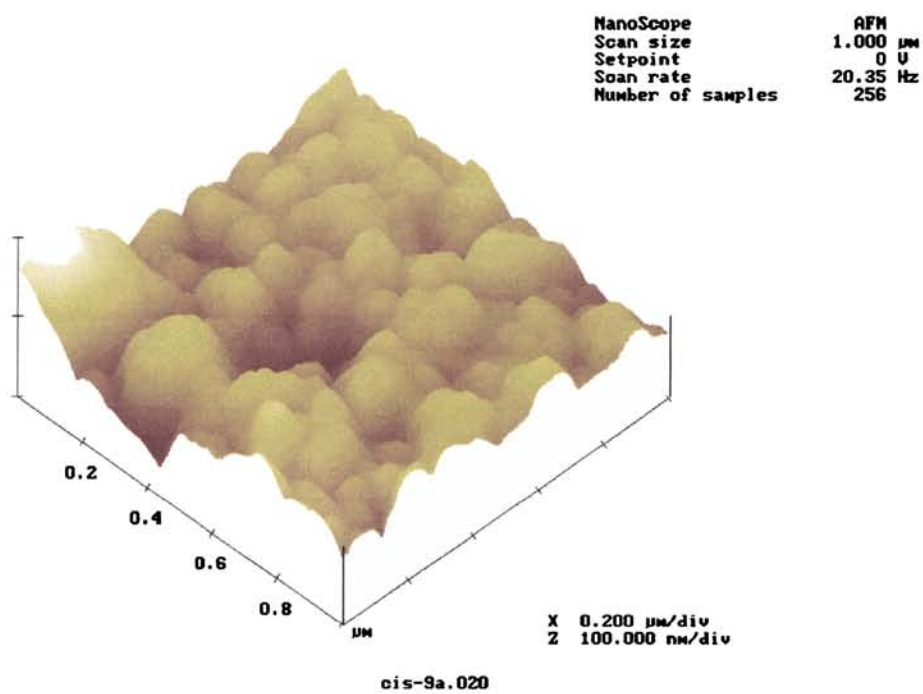


Fig.5.4f Three dimensional AFM on CuIn_5Se_8 film with $\text{Cu}:\text{In}:\text{Se} = 6.8:36.2:54.4$ and $N_a = 2.6\%$

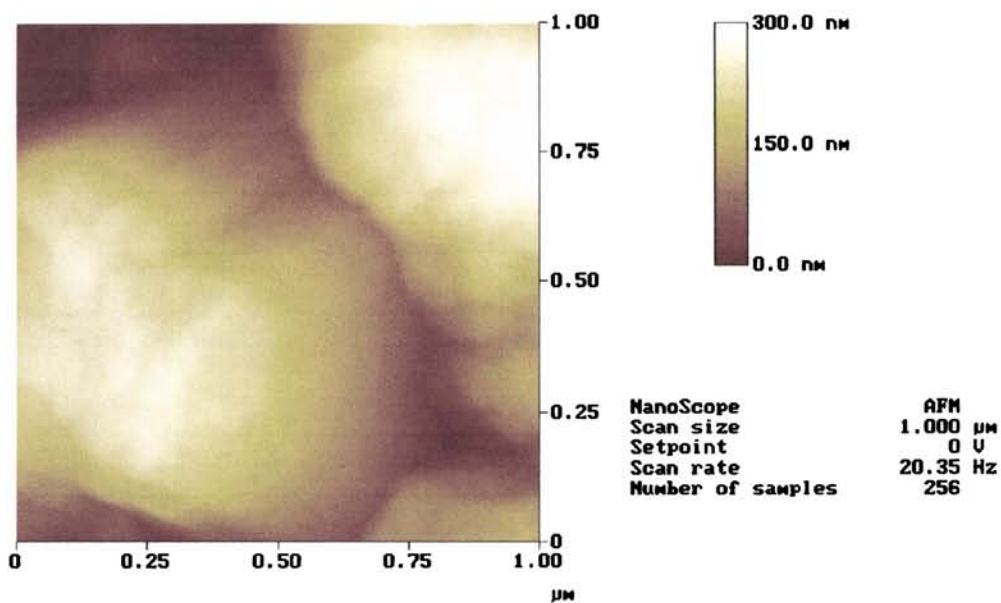


Fig.5.3g Two dimensional AFM on a thin film with Cu:In:Se= 13.5:40.4:46.1

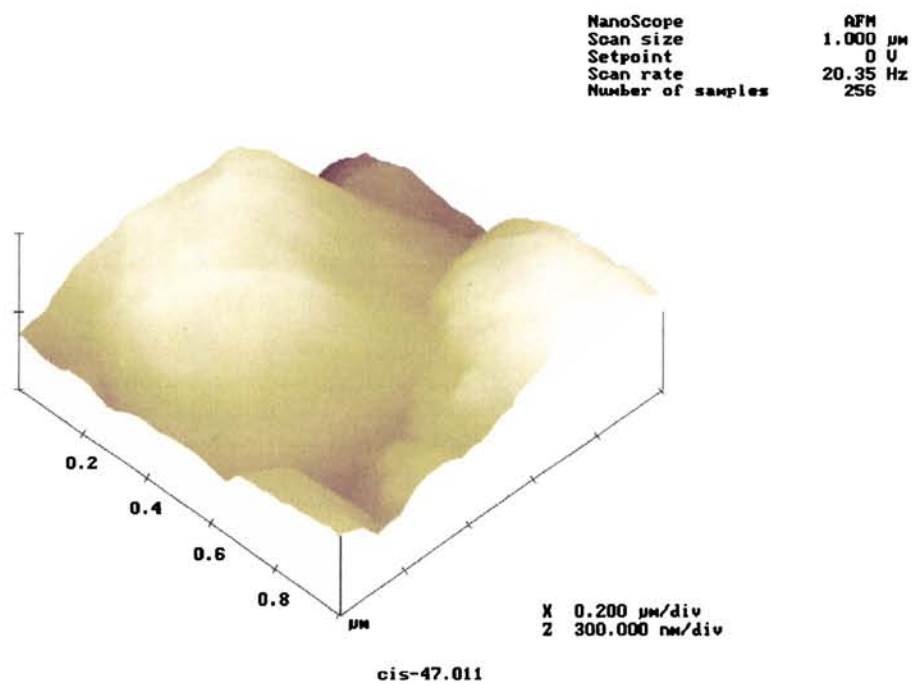


fig.5.4g Three dimensional AFM on a thin film with Cu:In:Se= 13.5:40.4:46.1

from these will of course lead to values greater than the particle sizes measured from the XRD. The roughness parameter and the grain sizes calculated from the films are given in Table.5.1. It is observed that in the films where sodium has diffused, the surface roughness is greater.

Type and number	r.m.s value of Roughness (nm)	Grain size (nm)
CuIn ₃ Se ₅ No: 45	7	25
CuIn ₅ Se ₈ No: 51	13	90
CuIn ₇ Se ₁₂ No: 49	32	104
CuIn ₉ Se ₁₄ No: 55	17	57
CuIn ₃ Se ₅ No: 26 (with Na)	43	25
CuIn ₅ Se ₈ No: 9 (with Na)	34	108
CuIn _{2.99} Se _{3.4} No: 47	77	188

Table.5.1 Grain Size and root mean square values of the surface roughness of the films from.AFM.

5.4 Structural characterization

Here also X-ray diffraction (XRD) is used for studying the structure of films. The XRD data on the OVC'S CuIn₅Se₈, CuIn₃Se₅ and CuIn₇Se₁₂ are used for obtaining the lattice parameters, the bond lengths, the distortion of the unit cell and the non-ideal anion displacement. The strain in the films as well as the particle sizes is also calculated.

5.4.1 X-ray diffraction

XRD profiles on typical OVC samples CuIn₅Se₈, CuIn₃Se₅ and CuIn₇Se₁₂ taken at ambient temperature at a scan speed of 1° per minute employing a Regaku D MaxC X-ray diffractometer with CuK α 1 as source radiation are shown in Fig. 5.5 a -c.

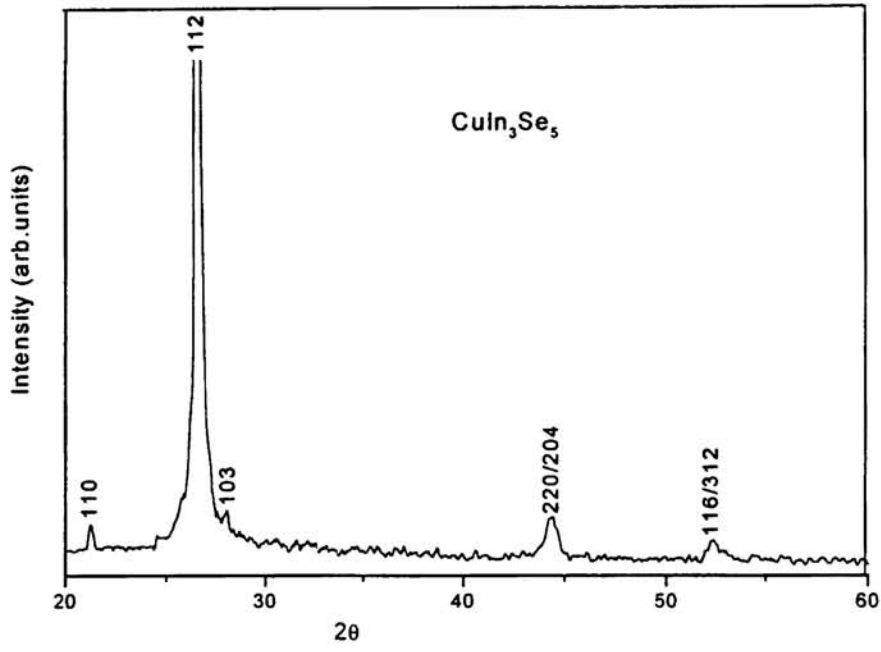


Fig.5.5a XRD profile on a typical CuIn_3Se_5 film.

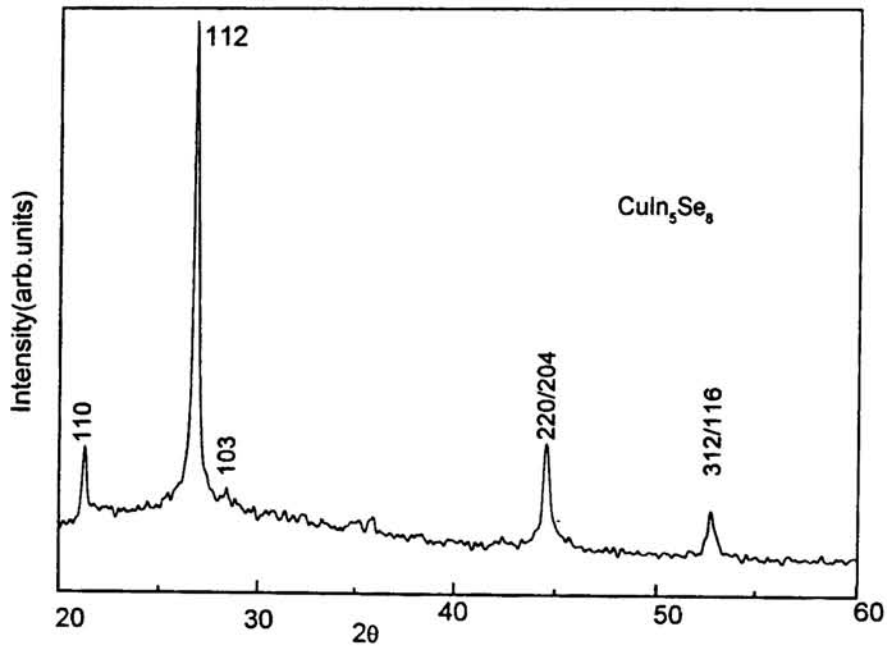


Fig.5.5b XRD profile on a typical CuIn_5Se_8 film.

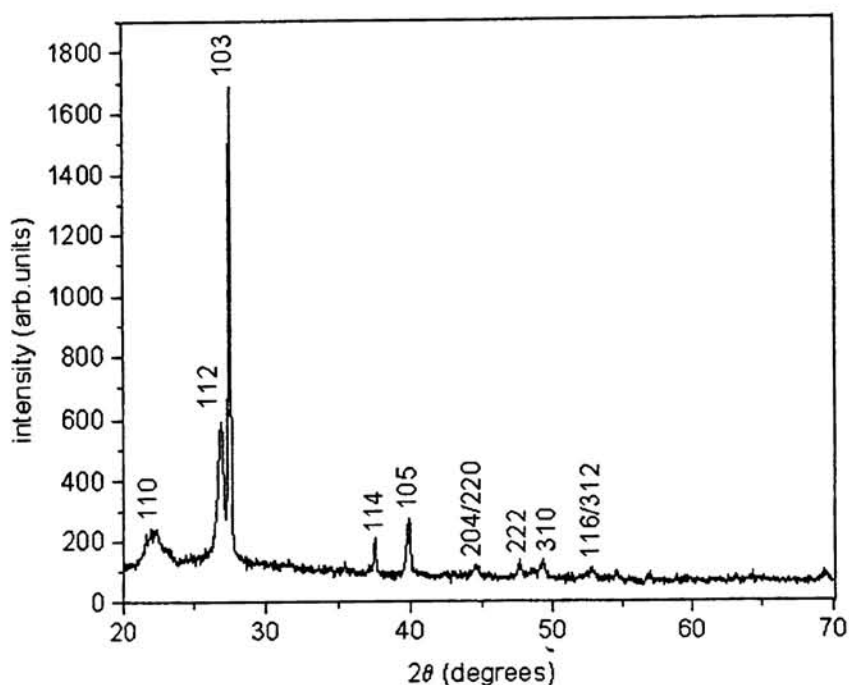


Fig.5.5c XRD profile on a typical $\text{CuIn}_7\text{Se}_{12}$ film.

A comparison with peak positions for the OVC's reported in literature shows that the prominent peaks in CuIn_3Se_5 and CuIn_5Se_8 correspond to reflections from 112 planes. (Here in the figures, the peaks corresponding to 112 reflection is cut so as to make the other peaks clearly visible.) The other significant peaks are 220/204 and 116/312, the chalcopyrite characteristic peak 103 and the 110 peak which is present only in OVC's and never in CuInSe_2 . But in $\text{CuIn}_7\text{Se}_{12}$ the reflection from the chalcopyrite characteristic peak 103 is found to be the most prominent.

It is found that there is an emergence of (110) reflection peak in the x-ray diffraction pattern of OVC's while it is never present in the diffraction pattern of nearly stoichiometric CuInSe_2 films. This could be accounted for by the x-ray structure factor calculation. For x-ray structure factor calculation, we have to assume the atomic positions. The positions of the 8 atoms in CuInSe_2 are given in table 2.5. Here u represents the anion displacement, which in the present calculations are taken to be about 0.24, from the experimental value of deformation parameter. However small

variations in u value makes no appreciable effect on structure factors $|F|$ determined using the equation [20]

$$|F| = \sum_{n \rightarrow 1}^8 f_n \exp 2\pi i(hu_n + kv_n + lw_n) \quad 5.1$$

the summation extending over all the 8 atoms of the unit cell with atomic positions denoted by u_n , v_n and w_n as shown in the table.2.5 and h , k and l are the reflecting planes from the XRD. The values of f_n are obtained by plotting graphs as in fig.5.6 [20] and by noting the value of f_n from the graphs corresponding to the experimental $\sin\theta/\lambda$ in the diffraction pattern. $|F|^2$ obtained by multiplication of $|F|$ with its complex conjugate ought to be proportional to the relative intensities of the diffracted beams. The calculated values of $|F|^2$ are given in table 5.2 and are found to be in good stead with the observed relative intensities, provided the preferential growth of the polycrystalline films along the (112) plane is taken into consideration. In the case of polycrystalline thin films, the relative intensity of reflection depends to a great extent on the preferred orientation of grains in the film with respect to the substrate surface and hence we are not attempting a comparison in observed and calculated relative intensities but only noting whether a reflection is possible or not by comparing with structure factors. To make intensity calculations taking into consideration the multiplicity factors and Lorentz-polarization factor, the crystals ought to be randomly oriented in the film which here is not applicable. On doing the structure analysis as above, it is observed that 110 reflection has $|F| = 0$ for CuInSe_2 which means that according to the suggested atomic positions a reflection from (110) cannot be present in stoichiometric or nearly stoichiometric CuInSe_2 and this theoretical observation is confirmed by the experiment. However if there is an absence of one atom in the usual position (a vacancy) or a substitution of an atom in the place of another (like In_{Cu}) and if the defects are ordered throughout, then we may observe a 110 reflection in the XRD since then, the structure factor can take a non zero value. In the In rich- Cu deficient OVC's, Cu vacancies and In on Cu sites are orderly arranged as... $\text{Cu-V}_{\text{Cu}}\text{-In}_{\text{Cu}}\text{-V}_{\text{Cu}}\text{-Cu}$along a superlattice and this explains the emergence of (110) reflection peak in the XRD of only ordered vacancy compounds. Thus looking at the structure factor calculation, it is clear why the 110 peak is characteristic of OVC's.

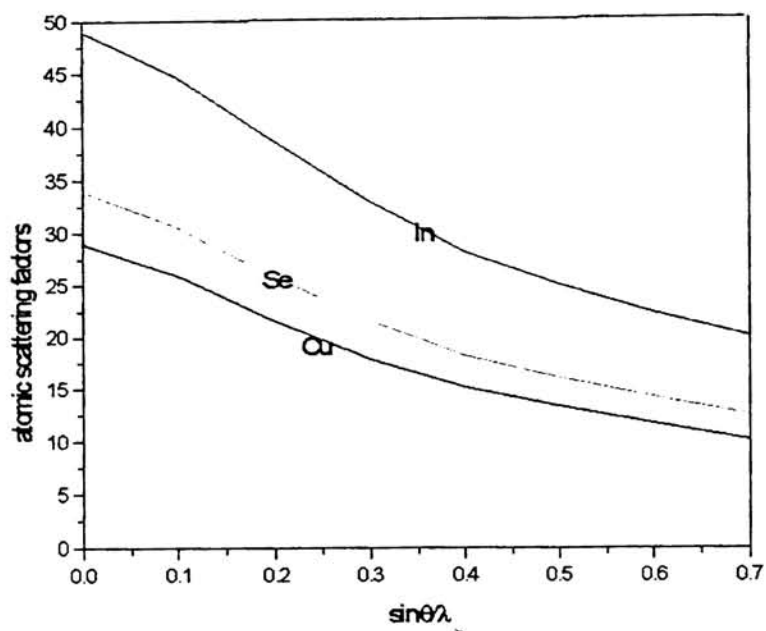


Fig.5.6 $\sin\theta/\lambda$ Vs atomic scattering factors for Cu, In and Se.

In CuInSe_2						In OVC		
2θ	d(A)	hkl	$\sin\theta/\lambda$	$ F ^2$	Observed I/I_0	2θ	d(A)	Observed I/I_0
-	-	110	-	-	none	21.250	4.178	Medium
26.4	3.37	112	0.15	17,138	strong	26.800	3.324	strong
27.45	3.247	103	0.16	918	weak	27.360	3.257	weak
44.05	2.0541	204	0.24	12,544	strong	44.550	2.032	strong
52.15	1.7525	224	0.28	37,960	medium	52.850	1.7309	medium

Table.5.2 Structure factor and observed reflections in CIS and the OVC CuIn_5Se_8

5.4.2 Lattice parameters

Here also the determination of lattice parameters is used for assessing the bond lengths and the non-ideal anion displacement in the compounds and are calculated using the Nelson-Riley method for lattice parameter determination [21].

The method of calculation is described in detail in section.2.6.2.1. The approximate values, a_1 and c_1 for the lattice parameters from the positions of the two highest angle lines are calculated first. The approximate axial ratio c_1/a_1 is then calculated and used in Eqn. below

$$a = (\lambda/2\sin\theta) \{(h^2+k^2)+(l^2/(c/a)^2)\}^{1/2} \quad 5.2$$

to determine an a value for each high-angle line on the pattern. These values of a are then extrapolated against $((\cos^2\theta/\sin\theta)+(\cos^2\theta/\theta))$ to find a more accurate value of a which is then used in the calculation of c using Eq.(5.3).

$$c = (\lambda/2\sin\theta)\{(c/a)^2(h^2+k^2)+l^2\}^{1/2} \quad 5.3$$

The c values thus obtained are extrapolated against $((\cos^2\theta/\sin\theta)+(\cos^2\theta/\theta))$ to obtain an accurate value of c . Two successive extrapolations are done for obtaining the lattice parameters in the present case.

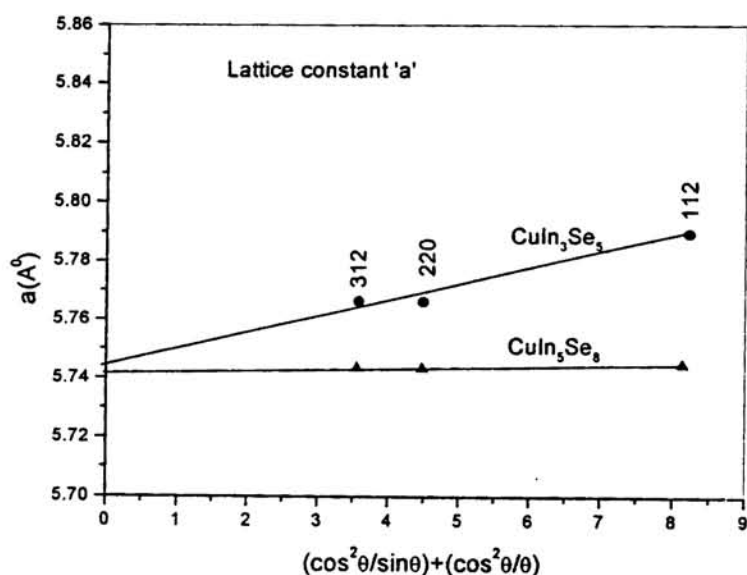


Fig.5.7 Nelson-Riley plot for lattice constant 'a' in $CuIn_3Se_5$ and $CuIn_5Se_8$.

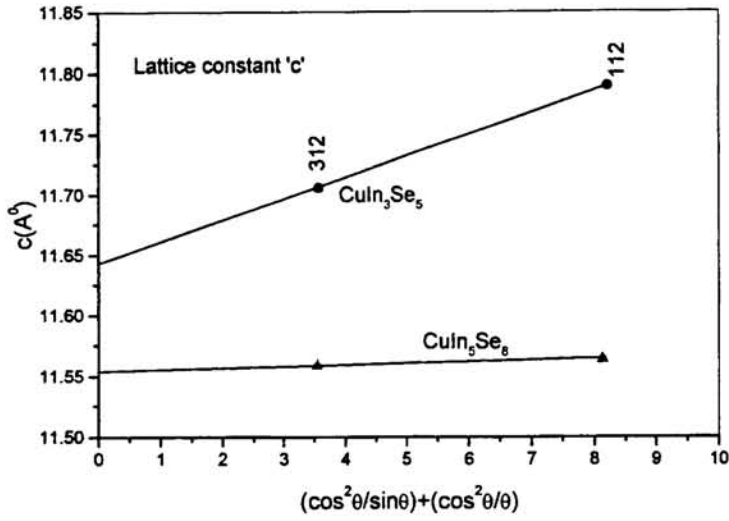


Fig.5.8 Nelson-Riley plot for lattice constant 'c' in CuIn_3Se_5 and CuIn_5Se_8 .

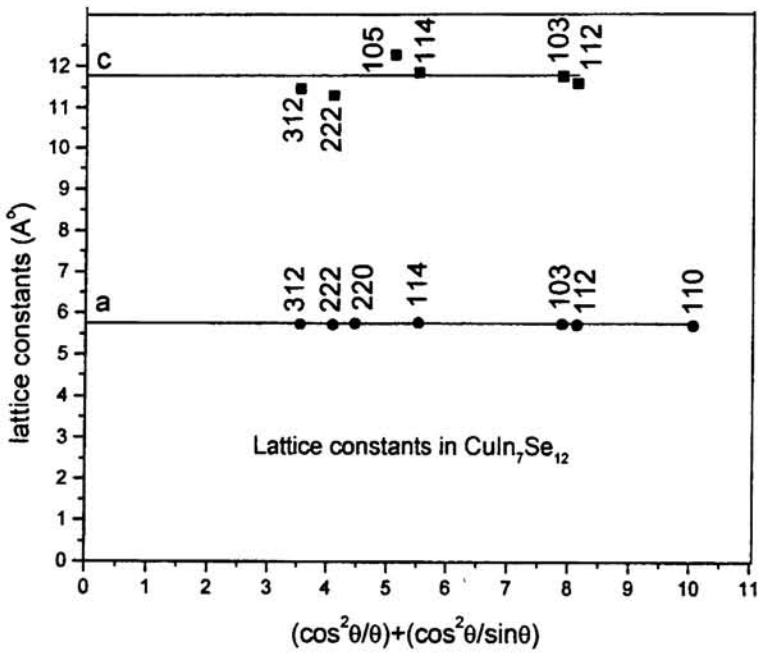


Fig.5.9 Nelson-Riley plot for lattice constant 'a' & 'c' in $\text{CuIn}_7\text{Se}_{12}$.

The lattice constants a_0 and c_0 obtained for the OVC's are given in table.5.2.

Type of samples	Lattice constant (a_0) \AA	Lattice constant (c_0) \AA
CuIn_3Se_5	5.744	11.637
CuIn_5Se_8	5.7415	11.552
$\text{CuIn}_7\text{Se}_{12}$	5.746	11.779

Table.5.2 Lattice parameters of OVC's.

The lattice parameters determined for the OVC's are found to be in agreement with that calculated by different investigators [10,15]. Merino et al [10] reported $a=5.755 \text{\AA}$ and $c=11.53 \text{\AA}$ for CuIn_3Se_5 where as N.Kohara et al [15] reported $a=5.73 \text{\AA}$ and $c=11.44 \text{\AA}$ for CuIn_5Se_8 . Reports are not available on $\text{CuIn}_7\text{Se}_{12}$ for comparison of lattice parameters. However slight differences in a and c parameters are observed in the compounds. The strain in the films is determined to get an insight into many of the characteristic properties exhibited by the films.

5.4.3 Grain size and strain in the films

Assuming the total reflection width of the XRD peaks as

$$\beta_{hkl} = \beta_{\text{size}} + \beta_{\text{strain}} = (0.9\lambda / (D \cos\theta)) + (4\epsilon \tan\theta_{hkl}) \quad 5.4$$

where ϵ is the microstrain in the sample and D is the crystallite size and by constructing Williamson-Hall plots taking full-width at half maximum of the XRD peaks* $\cos\theta$ on the y-axis and $4\sin\theta$ along the x-axis, the strain parameter and particle size are estimated. Fig. 5.10 gives the W.H plots for the OVC's. The strain is determined to be $6.1 \cdot 10^{-3}$, $3.2 \cdot 10^{-3}$ and $6.3 \cdot 10^{-3}$ respectively for CuIn_3Se_5 , CuIn_5Se_8 and $\text{CuIn}_7\text{Se}_{12}$ films from the plots shown in Fig. 5.10.

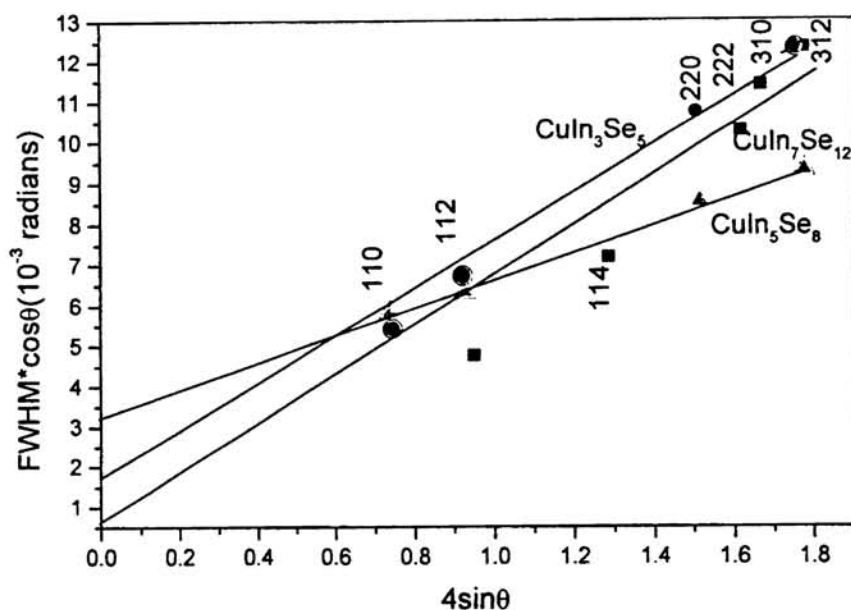


Fig.5.10 *W.H.plots on the OVC's.*

The particle sizes determined from Scherrer formula are found to be around 18-20nm, 16-19 nm and 23-25 nm respectively in the case of CuIn_3Se_5 , CuIn_5Se_8 and $\text{CuIn}_7\text{Se}_{12}$ films. But the strain in the films is depending on various parameters like type of substrate, mode of construction etc. and hence cannot be expected to remain a constant with the films. But a knowledge of these will help in discussion of the deformation of the tetragonal lattice which follows.

5.4.4 Tetragonal deformation, non-ideal anion displacement and bond lengths.

In the case of all the OVC films, the determination of lattice constants indicates that the unit cell is tetragonally distorted, with a dialation along the c-axis yielding a deformation parameter $\eta=c/2a \neq 1$. The anion C which has two A and two B cations as nearest neighbours, adopts an equilibrium position closer to one pair of cations than to the other, that is $R_{AC} \neq R_{BC}$ as in the case of stoichiometric CIS described in section.2.6.2.3. According to the most widely accepted structure proposed by Zhang et al [3] the difference in structure of the OVC's CuIn_5Se_8 , CuIn_3Se_5 from that of CIS is the introduction of the defect complex $(2V_{\text{Cu}} + \text{In}_{\text{Cu}})$ respectively in every 4, 5 units of CuInSe_2 while the off-tie-line compound $\text{CuIn}_7\text{Se}_{12}$ is formed by the introduction of one

defect pair ($2V_{Cu}+In_{Cu}$) and 2 neutral Cu vacancies in 6 units of CIS. The anion displacement and the bond lengths are determined here from the experimental value of η using the simple rule termed by Jaffe et al [22,23] as ‘CTB plus $\eta = \eta_{expt}$ ’ rule, which is basically related to Bragg’s classical principle of transferability and conservation of elementary bonds in different compounds. The method is described in detail in section 2.6.2.3. The deformation parameter, the non-ideal anion displacement and the bond lengths determined for the OVC’s are given in Table.5.3.

Type of films	η	u	$R_{AC} (A^0)$	$R_{BC} (A^0)$	Bond length mismatch
$CuIn_3Se_5$	1.013	0.23635	2.47058	2.5613	-.4563
$CuIn_5Se_8$	1.006	0.2364	2.4705	2.5612	-.4563
$CuIn_7Se_{12}$	1.025	0.2364	2.4657	2.5543	-.4447

Table.5.3 *Structural parameters anion displacement and bond lengths in the OVC’s using ‘CTB plus $\eta = \eta_{expt}$ ’ rule.*

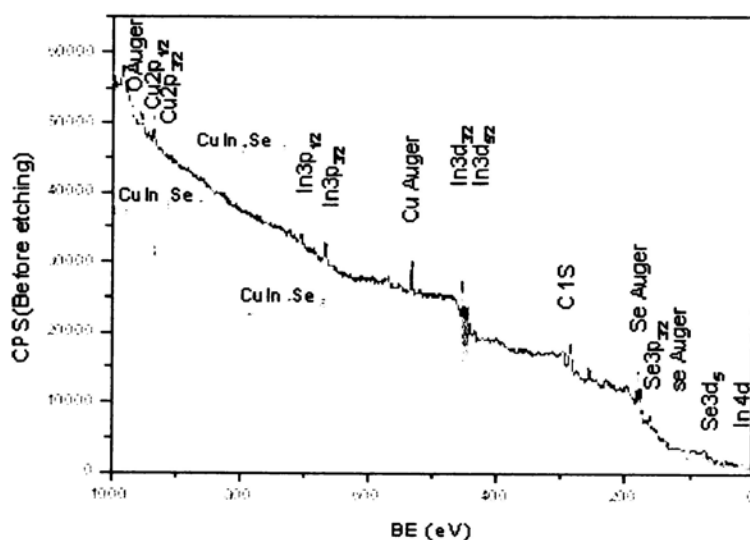
It is observed that the bond-lengths remain almost constant in the case of on-tie line OVC’s where as they deviate slightly in the case of the off-tie line compound. The observation is in agreement with that of Chang et al [4], where they calculated the equilibrium bond lengths in various OVC’s from EXAFS and observed that the Cu-Se bond lengths in all the on-tie line OVC’s are independent of the stoichiometry and atomic configurations where as they found that the averaged In-Se bond lengths decreases slightly as Cu occupation decreases. Such a decrease is observable for the In-Se bond lengths in the present calculations depicted in Table.5.3 also. The Cu-Se bond length is lesser than the In-Se bond length, which means the anion, is slightly displaced towards the cation Cu in OVC’s too. The tetragonal deformation is measured to be greatest for the $CuIn_7Se_{12}$ lattice and least for $CuIn_5Se_8$. An examination of the strain

parameter (section 5.4.3) indicates that the tetragonal deformation is related to the strain measured in the films, which is also largest for $\text{CuIn}_7\text{Se}_{12}$ and least for CuIn_5Se_8 .

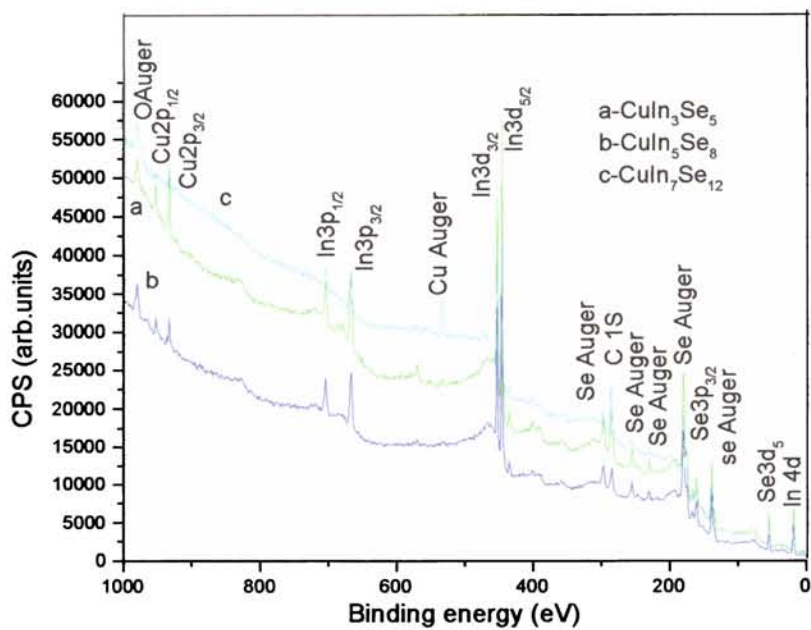
5.5 X-ray photoelectron spectroscopy

The XPS analysis of the OVC's has been used to ascertain the chemical state of the elements in the compound and also to observe whether there is any change in binding energy of the elements due to changes in chemical bonding.

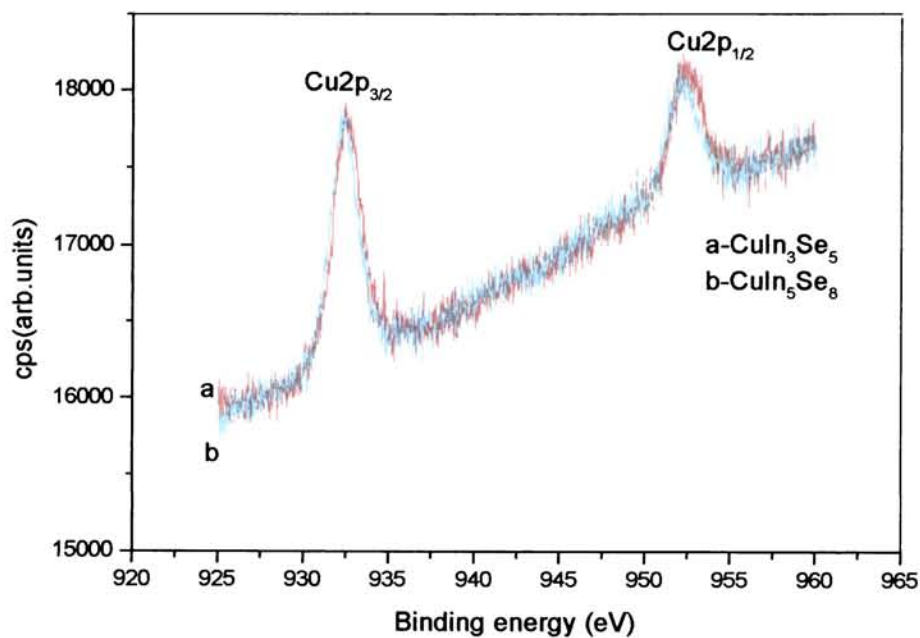
The experimental arrangements are described in section 2.7. The full scan spectra of the OVC's before and after etching are represented in Fig.5.11 a-b. In the spectra of the OVC's, in addition to peaks corresponding to Cu 2p, In 3d and Se 3d, some auger peaks and very small peaks indicating oxygen and carbon contamination on the surface of samples are also present. After Ar etching for 20-30 min. the peaks for Cu, In and Se are found to be increased in intensity in the full scan spectra. The detailed scans of the $\text{Cu}2p_{3/2}$, $\text{In}3d_{5/2}$ and $\text{Se}3d_{5/2}$ in enlarged mode are given in Fig.5.12 a-c. The positions of Cu 2p, In 3d and Se 3d determined from the detailed scan are given in Table.5.4.



5.11a XPS spectra on OVC's before etching.



5.11b XPS spectra on OVC's after Ar etching.



5.12a Detailed spectra of Cu 2p in OVC's.

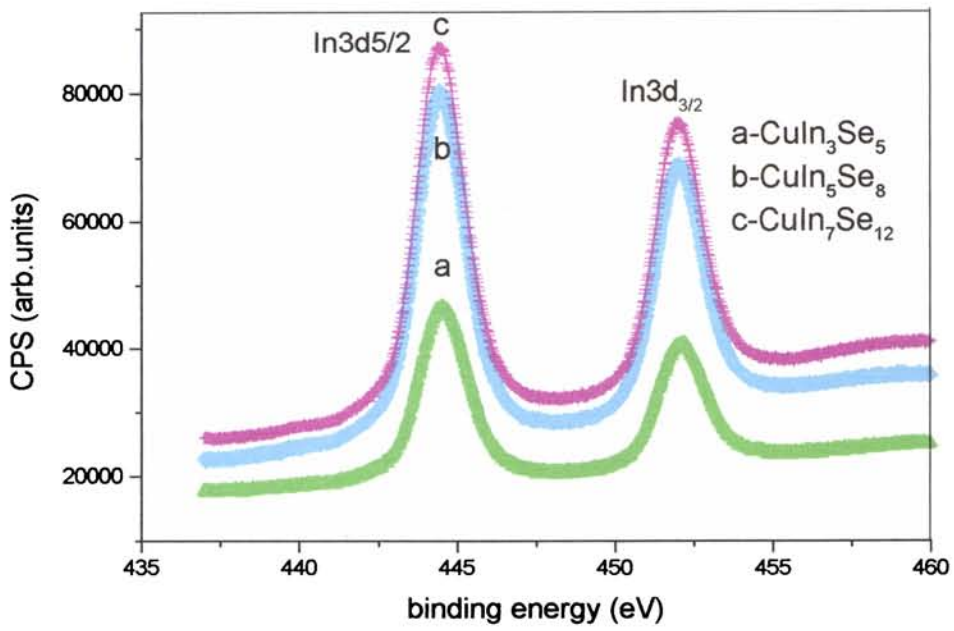


Fig.12b Detailed spectra of In3d on OVC's.

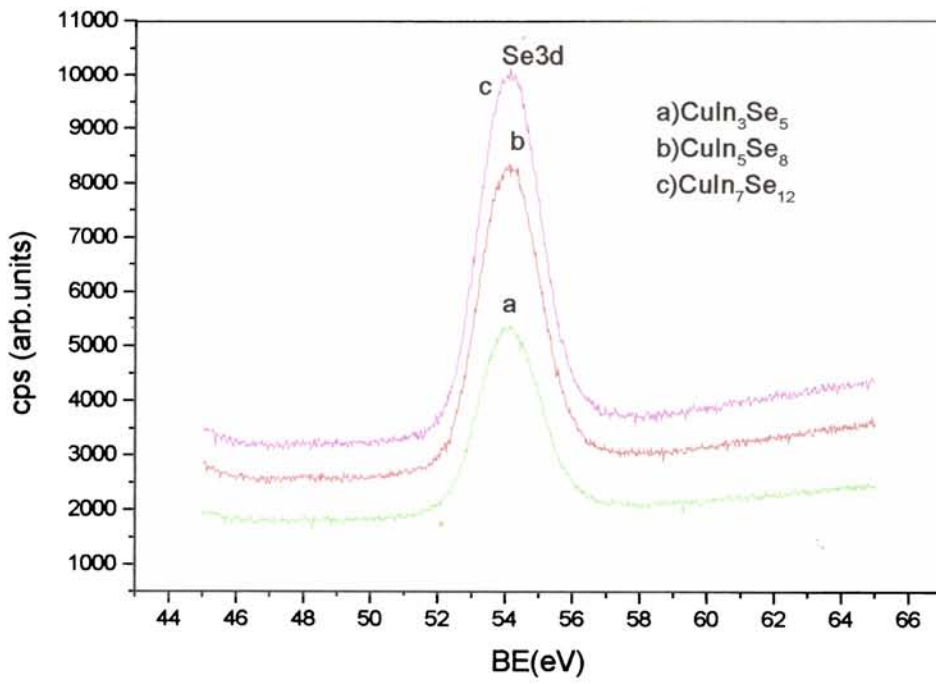


Fig.12.c Detailed spectra of Se3d on OVC's.

Film type	Cu2p _{3/2}	In3d _{5/2}	Se3d _{5/2}
CuIn ₃ Se ₅	932.3 eV	444.5eV	54 eV
CuIn ₅ Se ₈	932.2 eV	444.6 eV	54 eV
CuIn ₇ Se ₁₂	932.3 eV	444.4 eV	54 eV

Table.5.4 Peak positions of Cu2p, In3d and Se3d in the X-ray photoelectron spectra of OVC's.

Within the limits of resolution, the position of the observed Se emission peak in the OVC's correspond to ~54eV which is same as the position of Se peak in CuInSe₂ [24]. Comparison of the peak positions given in Table.5.4 with values reported for CuInSe₂ (as given in Table.2.6) by Moulder et al [24] shows a slight shift to higher binding energy side for Cu peak, a slight shift to lower binding energy side for In peak while the Se peak is exactly at the same position as that in CuInSe₂. But on comparison with the binding energies reported by Cahen et al [25] for CuInSe₂ and Hesse et al [26] as shown in table.2.6, both Cu and In peaks are found to have shifts towards higher binding energy side. A possibility for the shifts observed is the vacancy related mechanism that results in higher bonding energy for Cu-Se bonds in the defect compounds [3]. A slight decrease in the bond-length of In-Se bonds as the Cu occupation decreases in the OVC's has been reported by Chang et al [4], which could be pointed out as the reason for slight increase in binding energy of In in CuIn₅Se₈ compared to that in CuIn₃Se₅. XPS shows that Cu is in a monovalent state in all the OVC compounds. Further, though the films are In-rich, the presence of any binary phase like In₂Se₃ in the film is eliminated, since if In₂Se₃ is present as a binary phase in the film, then the position of Se3d_{5/2} peak should have shown a shift towards 54.8 eV, which is the reported [24] peak position for Se3d_{5/2} in In₂Se₃.

5.6 X-ray Reflectivity

In the case of OVC's the technique is used to get an estimate of the mean mass density of the samples so that it can be compared with the theoretical mass density to see whether there is introduction of unintended defects and vacancies.

The experimental set up is the same as given in section.2.8. Here also the intensity oscillations are not present in the X-ray reflectivity curve of the OVC films shown in Fig.13 a-c, since the thickness of the films are too high for observing such oscillations. The critical angle of total external reflection of the layer α_c has been obtained from the X-ray reflectivity fit using the Parratt algorithm and is used to calculate the mean electron density $\langle\rho_{el}\rangle$. The method of calculating the mean electron density $\langle\rho_{el}\rangle$, the mass density $\langle\rho_m\rangle$ and the theoretical mass density $\rho_{m\ theory}$ are given in section.2.8. The values calculated for the OVC films are given in Table.5.5. It is observed that the measured mean mass density is only slightly lesser than the theoretical mass density, which indicates that the unintended defects are very few in these samples. The mass density is least for the OVC $\text{CuIn}_7\text{Se}_{12}$ which has the maximum number of ordered defects like $(2V_{\text{Cu}}+\text{In}_{\text{Cu}})$ and two neutral Cu vacancies.

Type	α_c	$\langle\rho_{el}\rangle$	$\langle\rho_m\rangle$	$\rho_{m\ theory}$
CuIn_3Se_5	0.00529	$1.32/\text{\AA}^3$	2.5g/cm^3	2.75g/cm^3
CuIn_5Se_8	.00445	$0.932/\text{\AA}^3$	2.18g/cm^3	2.78g/cm^3
$\text{CuIn}_7\text{Se}_{12}$.00447	$0.9423/\text{\AA}^3$	1.82g/cm^3	1.88g/cm^3

Table.5.5 *The mean electron density and mass density from XRR.*

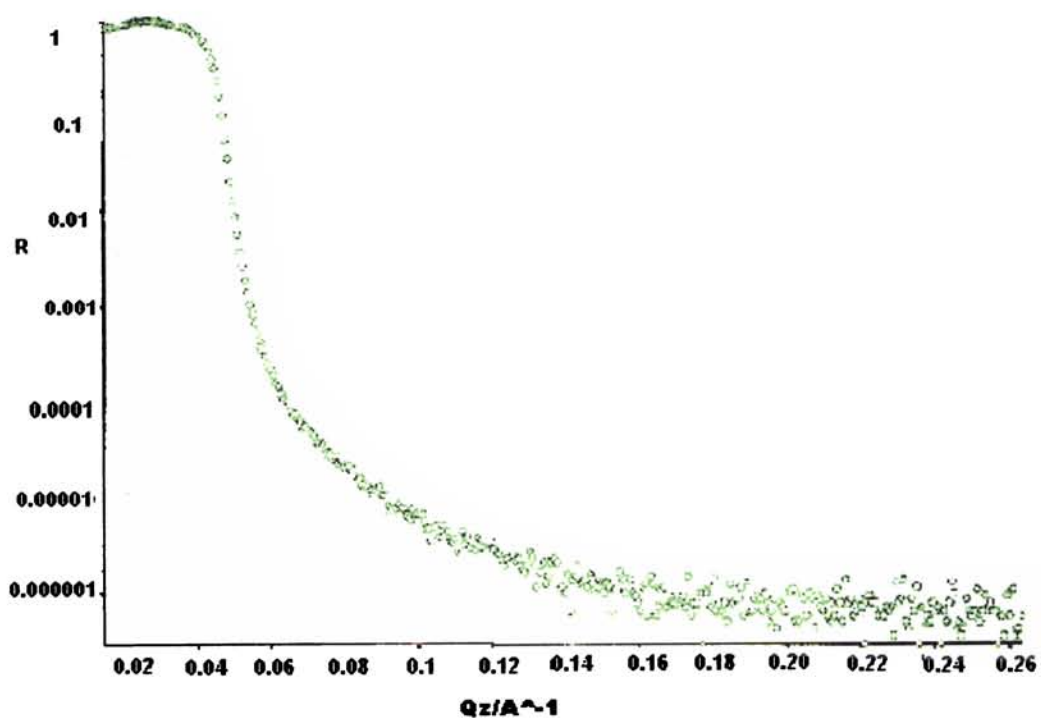


Fig.5.13a Reflectivity plot on CuIn_3Se_5 .

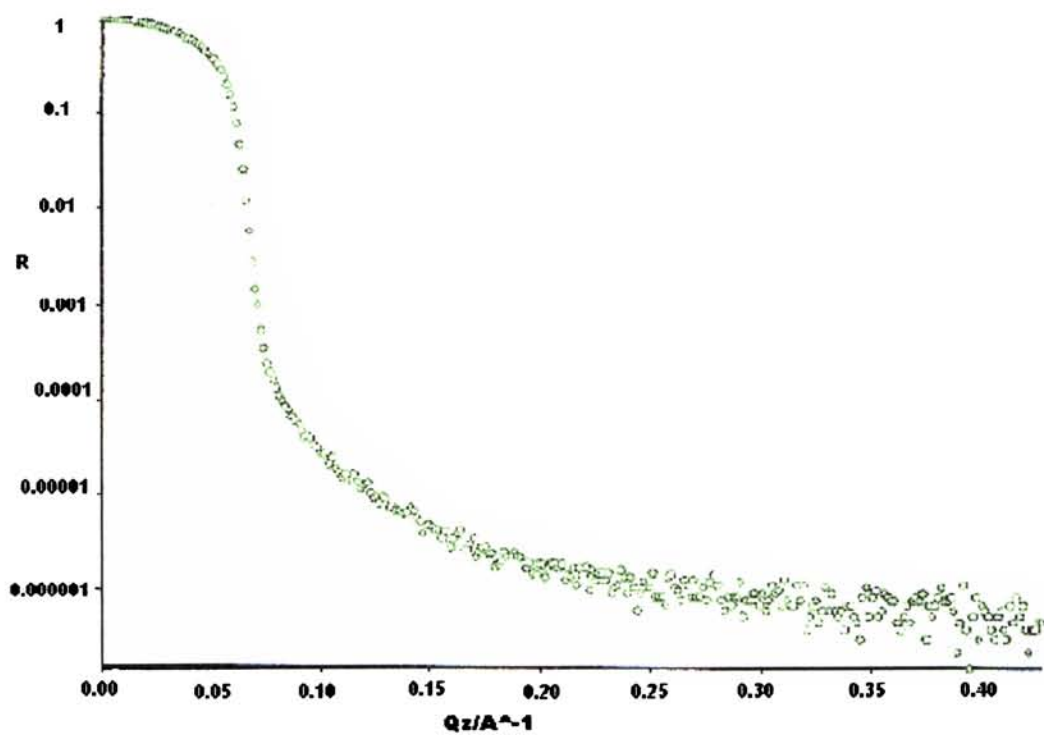


Fig.5.13b Reflectivity plot on CuIn_5Se_8 .

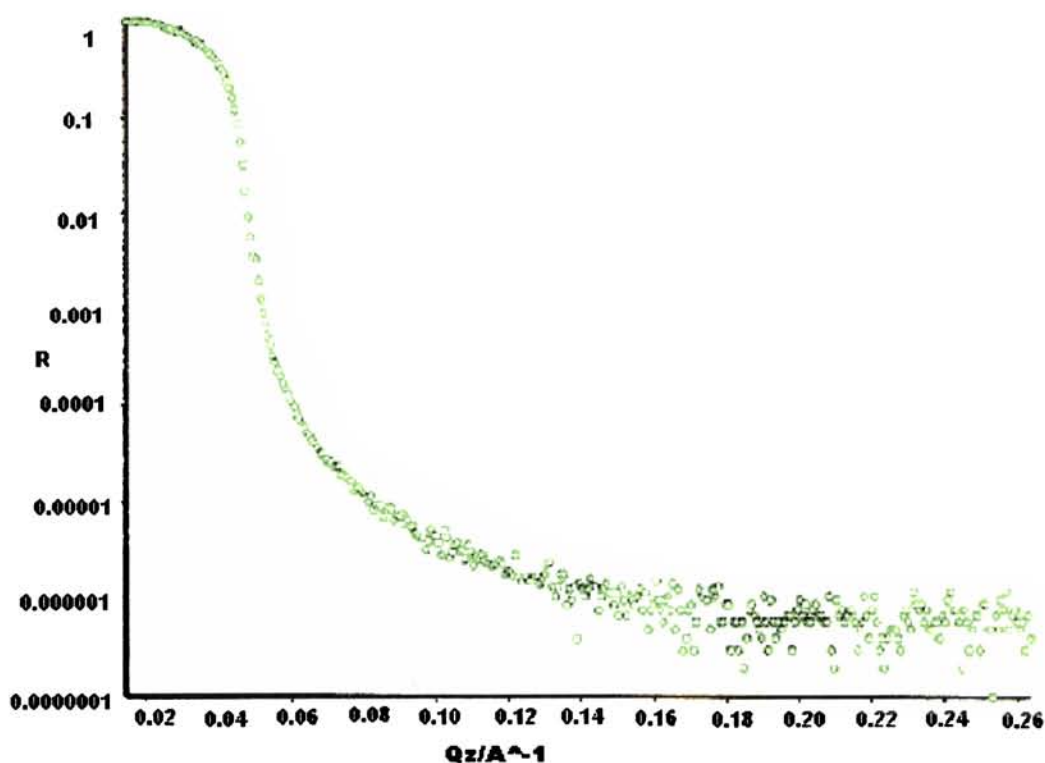


Fig.5.13c Reflectivity on $\text{CuIn}_7\text{Se}_{12}$

5.7 Conclusion

A detailed account of the compositional, morphological and structural characterization of the OVC's CuIn_3Se_5 , CuIn_5Se_8 and $\text{CuIn}_7\text{Se}_{12}$ prepared by multisource co-evaporation is given in this chapter. The derivative structure of the OVC's from CuInSe_2 by the introduction of defect complexes in on-tie line compounds and additional neutral Cu vacancies in off-tie line compounds are considered here and the bond lengths are determined using 'CTB plus $\eta = \eta_{\text{expt}}$ ' rule. The bond lengths are found to be almost conserved in the case of CuIn_3Se_5 and CuIn_5Se_8 , while slightly different in the case of the off-tie line compound $\text{CuIn}_7\text{Se}_{12}$. The tetragonal deformation is found to be greatest in the case of films with greatest strain. XPS measurements confirm that the films are devoid of any binary phase formation. XRR indicates that unintended defects are very few in the films.

References

- [1] M.Contreras, B.egaas, K.Ramanathan, J.Hiltner, A.Swarzlander, F.Hasoon and R.Noufi, Prog.Photovoltaics 7 (1999) 311.
- [2] D.Schmid, M.Ruekh, F.Grunwald and H.W.Schock, J.Appl.Phys. 73 (1992) 2902.
- [3] S.B. Zhang; S.H.Wei and A. Zunger. Phys.Rev.B. 57 (1998) 9642 .
- [4] Chang C.H, Wei S.H, Johnson J.W, Zhang S.B, Leyarovska N, Bunker G and Anderson T.J Phy Rev B 68 (2003) 054108.
- [5] H.Z.Xiao, L.C. Yang and A.Rockett, J.Appl.Phys.76 (1994) 1503.
- [6] L.S.Palatnik and E.J.Rgacheva, Dokl. Akad. Nauk SSSR, 174 (1967) 80.
- [7] W.Honle, G.Kuhn and U.C.Boehnke, Cryst.Res.Technol. 23 (1988) 1347.
- [8] S.Normura and S.Endo, Trans.MRS Jpn 20 (1996) 755.
- [9] T.Hanada, A.Yamana, Y.Nakamura, O.Nittono and T.Wada, Jpn.J.Appl.Phys.36 (1997) L1494.
- [10] J.M.Merino, S.Mahanty, M.Leon, R.Diaz, F. Rueda, J.L.Martin de Vidales, Thin Solid Films 361(2000) 70.
- [11] C.Manolikas, J.V. Landuyt, R. De Ridder and S.Amelinckx, Phys. Stat. Sol. (a) 55 (1979) 709.
- [12] N.Frangis, G.Van Tendeloo, C. Manolikas, J. Van Landuyt and S. Amelinckx., Phys. Stat.sol. 96 (1986) 53.
- [13] J.C.W. Folmer, J.A.Turner, R.Noufi and D. Cahen, J.Electrochem.Soc.132 (1985) 2281.
- [14] B.H.Tseng and C.A Wert, J.Appl.Phys. 65 (1989) 2254.
- [15] N. Kohara, S. Nishiawaki, T.Negami and T.Wada, Jpn.J.Appl.Phys.39 (2000) 6316.
- [16] A.T.Tham, D.S.Su, W.Neumann, P.S.Bischof, C.BeilHarz and K.W.Benz, Cryst. Res. Technol. 36 (2001) 303.
- [17] S.Mahanty, J.M. Merino, R.Diaz, F.Rueda, J.L.Martin de V., and M.Leon, Inst. Phys.Conf.Ser. 152 (1998) 499.

- [18] R.Bacewicz, J.Filipowicz and A.Wolska, *Inst. Phys.Conf.Ser.*152 (1998) 507.
- [19] C.Rincon, S.M.wasim, G.marin, R.Marquez, L.Nieves and G.S. Perez, *J.Appl.Phys.* 90 (2001) 4423.
- [20] B.D.Cullity, *Elements of x-ray diffraction*, Addison-Wesley publishing company Inc, U.S.A, 1956.
- [21] J.B.Nelson, D.P.Riley, *Proc.Phys.Soc.*, 57 (1945) 160.
- [22] J.E. Jaffe, A. Zunger, *Phys. Rev. B* 29 (1984) 1882.
- [23] J.E. Jaffe, A. Zunger, *Phys. Rev. B* 27 (1983) 5176.
- [24] Moulder J.F, Stickle W.F, Sobol P.E and Bombin K.D *Hand book of x-ray photoelectron spectroscopy* 1992 Perkin-Elmer Co, Eden Praire MN.
- [25] D. Cahen, P. J. Ireland, L. L. Kazmerski, F. A. Thiel, *J. Appl.Phys.*57 (1985) 4761.
- [26] R.Hesse, *Unfit for windows, Universal program for XPS peak fitting and spectra analysis*, V-2003.

Chapter 6

Optical studies on the OVC films

6.1 Introduction

The significance of the ordered vacancy compounds (OVC) is that though structurally they are very much like the stoichiometric CuInSe_2 , their band gaps are much different from that of stoichiometric CIS. The OVC's usually have a wider band gap than CIS – one reason that it is used in forming homojunctions with the p-type Cu-rich CIS in the fabrication of solar cells.

Zhang et al [1] reported the corrected LDA band gaps for tetragonal CuIn_3Se_5 and CuIn_5Se_8 as 1.26eV and 1.34 eV respectively, larger than the 1.04 eV gap of CIS. Xiao et al [2] reported a band gap ≥ 1.18 eV for chalcopyrite CuIn_3Se_5 films. Ariswan et al [3] observed a band gap 1.23 eV in the tetragonal CuIn_3Se_5 thin films fabricated by flash evaporation. Rincon et al [4] determined a band gap equal to 1.23eV from absorption spectra for hexagonal CuIn_5Se_8 crystals.

In spite of all these investigations, reports of optical studies on tetragonal CuIn_5Se_8 are very few and that on $\text{CuIn}_7\text{Se}_{12}$ are practically none. In this chapter, the optical absorption as well as photoconductivity studies on tetragonal CuIn_3Se_5 , CuIn_5Se_8 and $\text{CuIn}_7\text{Se}_{12}$ are depicted and the effect of p-d hybridization on band gap has been considered in explaining the band gap variation. Spectral response and photoluminescence measurements have been used to obtain information regarding defects in the ordered vacancy compounds.

6.2 Optical Absorption studies

The optical absorption spectra of the OVC samples are taken using a Hitachi U-3410 UV-Vis- NIR spectrophotometer at room temperature and the graphs are analysed to determine the absorption coefficient and the optical band gap of the OVC films.

The absorption spectra on typical films of CuIn_3Se_5 , CuIn_5Se_8 and $\text{CuIn}_7\text{Se}_{12}$ are given in Fig.6.1.

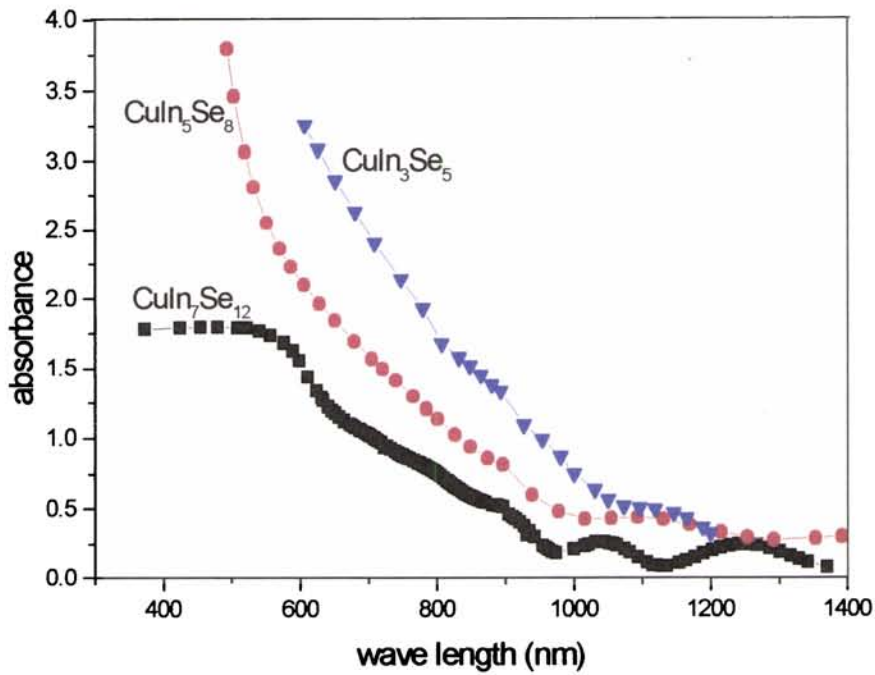


Fig.6.1 Optical absorbance spectra of typical samples of CuIn_3Se_5 , CuIn_5Se_8 and $\text{CuIn}_7\text{Se}_{12}$.

The optical absorption coefficient α for the different films are calculated directly from the absorption spectrum using the relations as given in section 3.2.1, that is

$$\begin{aligned}
 T &= (1-R)^2 \exp(-A) \\
 &= (1-R)^2 \exp(-\alpha d)
 \end{aligned}
 \tag{6.1}$$

where A is the absorbance, d is the film thickness ($0.3\text{-}0.4\mu\text{m}$), R is the reflectance and T is the transmittance of the films. On analysis using the equation

$$\alpha(\nu) = A_c (\hbar\nu - E_g)^n / \hbar\nu
 \tag{6.2}$$

where $n = 1/2, 3/2$ or 2 for allowed direct, forbidden direct or indirect transitions respectively, A_c is a constant defined as $4\pi\sigma/nCE$ where C represents the speed of light, σ is the extrapolated dc conductivity at $T = \infty$, E is the measure of the extent of band tailing, n is the refractive index and E_g is the optical band gap. The transitions are found

to be direct allowed transitions and the optical band gap in the case of the three compound films are obtained by the extrapolation of the straight line regions of the $(\alpha h\nu)^2$ versus $h\nu$ graphs to the x-axis with $y=0$. The plots are given in Fig.6.2a-c.

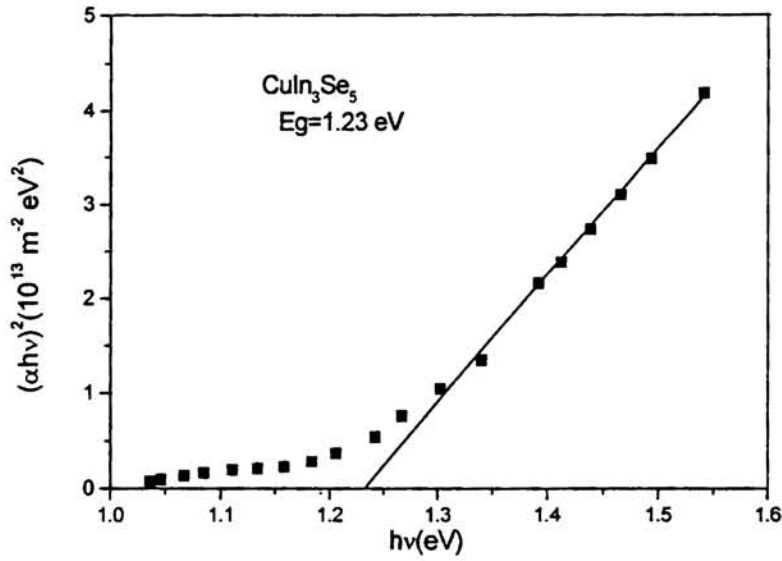


Fig.6.2a $(\alpha h\nu)^2$ versus $h\nu$ graph on CuIn_3Se_5 film.

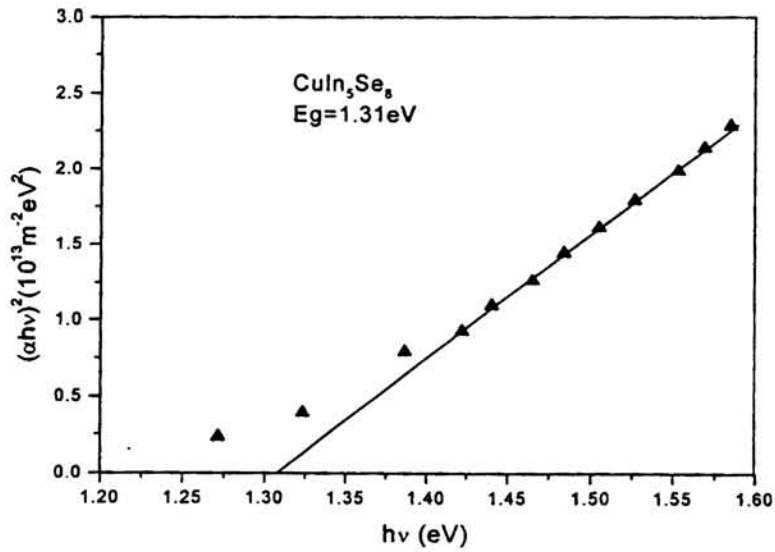


Fig.6.2b $(\alpha h\nu)^2$ versus $h\nu$ graph on CuIn_5Se_8 film.

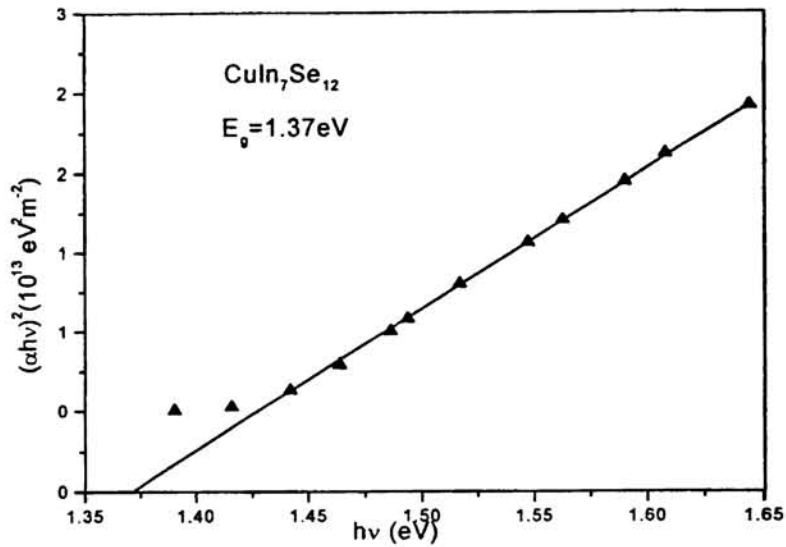


Fig.6.2c $(\alpha hv)^2$ versus $h\nu$ graph on $CuIn_7Se_{12}$ film.

The band gaps that are obtained for $CuIn_3Se_5$, $CuIn_5Se_8$ and $CuIn_7Se_{12}$ are 1.23eV, 1.31eV and 1.37eV respectively and are found to be in agreement with the earlier reported values [1,3] in the case of the first two, where as for $CuIn_7Se_{12}$ no reports are available for comparison. The increase in band gap with decrease in Cu content has a suitable explanation on the basis of molecular orbital theory. As explained in section.3.2.1, in ternary chalcopyrites like Cu-In-Se compounds where the cation supports valence d-states, the five fold degenerate Cu d state splits into the threefold degenerate $\Gamma_{15}(d)$ and the two fold degenerate $\Gamma_{12}(d)$ in the tetragonal field of the ternary compound. Many investigators have pointed out the large p-d repulsions in the ternaries as the reason for decrease in the energy gap of the ternary chalcopyrites relative to their binary analogues [5,6]. The reason being, when p-d interaction occurs and bonding and antibonding states are formed, the antibonding state is pushed high up due to the repulsive interaction between $\Gamma_{15}(p)$ and $\Gamma_{15}(d)$, in turn causing a reduction in band gap in the ternaries relative to their binary analogues. That is, the three fold degenerate $\Gamma_{15}(p)$ state of the anion interact with the $\Gamma_{15}(d)$ state of the cation of the same symmetry, with a repulsive interaction which is directly proportional to the p-d

coupling matrix element $\langle p|v|d \rangle^2$ and inversely proportional to the energy separation $\Delta \varepsilon_{pd}$ between anion p and cation d in accordance with the perturbation theory [7]. The interaction forms a lower bonding state weighted more by the $\Gamma_{15}(d)$ state and an upper antibonding state weighted more by the $\Gamma_{15}(p)$ state. Due to the pushing up of the antibonding states in the ternaries, the band gap is much reduced in them when compared to that in the binary analogues, where no such pushing up of states happens. Now, transferring the trend to OVC's, we assume that the strength of the interaction determines the extent of downward shift of the antibonding state, thus regulating the band gap variations in the ordered vacancy compounds. The bonding and antibonding states in CuInSe_2 as well as in the OVC's are represented in Fig.6.3. Here the solid lines represent CuInSe_2 states and dashed lines the OVC states. q and q' represent the separation between $\text{Se}\Gamma_{15}(p)$ and $\text{Cu}\Gamma_{15}(d)$ in CuInSe_2 and OVC's respectively. As the Cu content is very much reduced in Cu deficient defect compounds when compared to that in CuInSe_2 , the energy separation $\Delta \varepsilon_{pd}$ tends to increase in the former resulting in a reduction in the p-d repulsion. This in turn depresses the antibonding state which forms the valence band maximum (VBM) and opens up the band gap for the OVC films. Thus the p-d repulsion is very much reduced in defect compounds due to diminished d-character with periodic Cu vacancies leading to a large band gap in them [1]. This is the possible reason for observing a larger band gap in all the Cu-deficient OVC compounds of CIS when compared with the band gap of CIS itself.

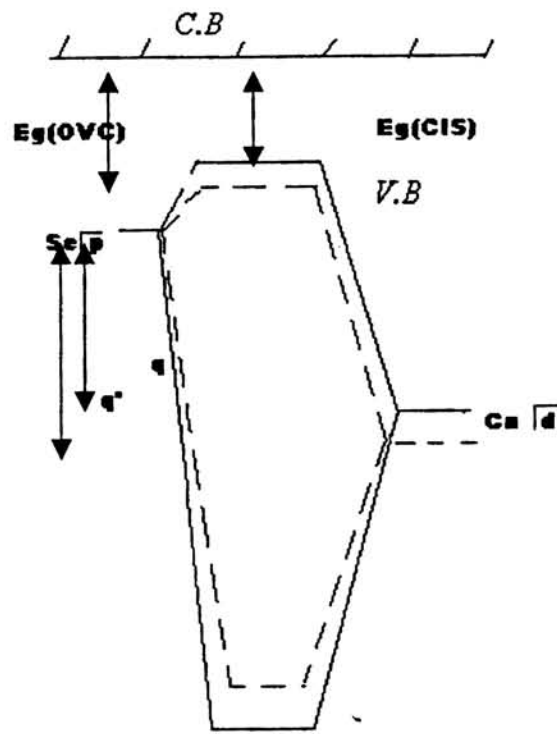


Fig.6.3 The schematic diagram showing p-d repulsion between $Se\Gamma_{15}(p)$ and $Cu\Gamma_{15}(d)$ resulting in variations in band gap.

The transmission spectrum of the film that is recorded in the wavelength range 2600 nm to cutoff is shown in Fig.6.4. It is seen that there is a shift to the shorter wavelength side for the OVC's in the order $CuIn_3Se_5$, $CuIn_5Se_8$ and $CuIn_7Se_{12}$. This is in agreement with the band gaps determined from the absorbance spectrum, where it is observed that the band gaps change from 1.23eV in $CuIn_3Se_5$ to 1.37eV in $CuIn_7Se_{12}$.

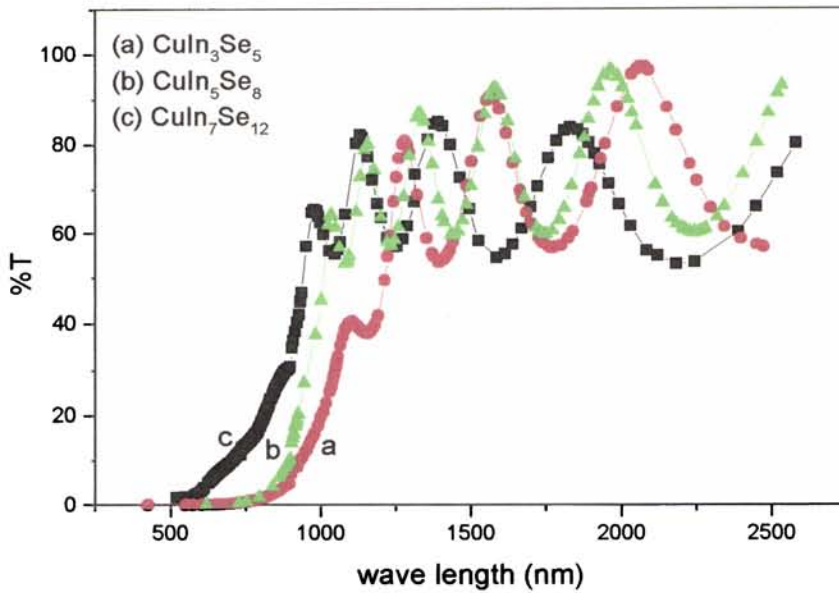


Fig.6.4 Transmission spectra of the OVC films.

The refractive index of the films, which is determined by Swanepoels' method [8] as described in section.3.2.2 is found to vary from 2.69 to 2.73 in CuIn_3Se_5 , from 2.54 to 2.65 in CuIn_5Se_8 and from 2.4 to 2.66 in $\text{CuIn}_7\text{Se}_{12}$ in the wave length range 1050 to 2000 nm. The extinction constant k that is determined using equation

$$\alpha = 4\pi k / \lambda \quad 6.3$$

where λ is the wavelength of light that is used and α is the absorption coefficient, is found to vary from 10^{-1} to 10^{-3} with increase in wavelength. Thus the refractive index for all the films lies roughly in the range $2.72 \geq n \geq 2.4$.

6.3 Photo conductivity studies in OVC films

The photoconductivity studies include measurement of transient photoconductivity, steady state photoconductivity and spectral response studies. Transient photoconductivity is used in determining the decay constants, the steady state measurements are used for determining the process taking place during excitation like the barrier height reduction observed here and the spectral response studies help in detection of defects present in the films.

6.3.1 Transient photoconductivity

Here also as done in the case of CIS (section.3.3.1) the photocurrent at different illumination intensities from 50mW/cm^2 to 110mW/cm^2 , by varying the distance between the sample and the source after noting the illumination intensity at various positions with a photometer has been taken, to check for any photoconductivity saturation effect. After ensuring a linear variation of photoconductivity in the illuminated range, the experiments are done at an intensity of illumination of 100mW/cm^2 . Photoconductivity measurements are done loading the sample in a CIT cryostat and cooling down to 10K initially. Silver electrodes of uniform thickness are applied at the ends of the samples with a spacing of 0.3 cm between them for illumination. By taking I-V measurements, the ohmic character of the electrode contacts has been tested. The response being linear in the voltage range 5V to 30V, the current measurements at a d.c voltage of 10V or 25V are taken for calculations.

The transient photoconductivity behaviour of typical OVC films at an illumination intensity of 100mW/cm^2 at different temperatures between 10K and 300K is represented in Fig.6.5a-c. The sudden rise in conductivity on illumination may be related to the potential barrier height reduction on illumination which make the conducting grains electrically “better connected” among them, similar to that noted from the analysis of steady state photoconductivity given in the next sec. The decay process can be assigned with two different phenomena-a fast decay that is determined by the fast inter-grain barrier recovery as the photogenerated hole flux arriving to the inter-grain region suddenly ceases and the slow decay that is due to some additional time dependent processes such as trap emptying (Fig.6.6a-c) [9-11]. The slow decay region is analysed with the purpose of obtaining the decay time constants in different films. Analysis shows that the decay curves in this region cannot be fitted with a simple exponential function but is time dependent indicating the involvement of sustained trap emptying processes. A possible origin of such a trap in the OVC films is the donor defect In_{Cu} , the occurrence of which is in conformity with the structural and compositional studies. Using the differential life- time concept as suggested by Fuhs et al [12] the non- exponential decay process is analysed. The life- time τ_d is calculated using the eqn.

$$\tau_d = -[1/I_{ph*}(dI_{ph}/dt)]^{-1} \quad 6.4$$

where I_{ph*} is the maximum photocurrent at $t=0$ for a given applied voltage.

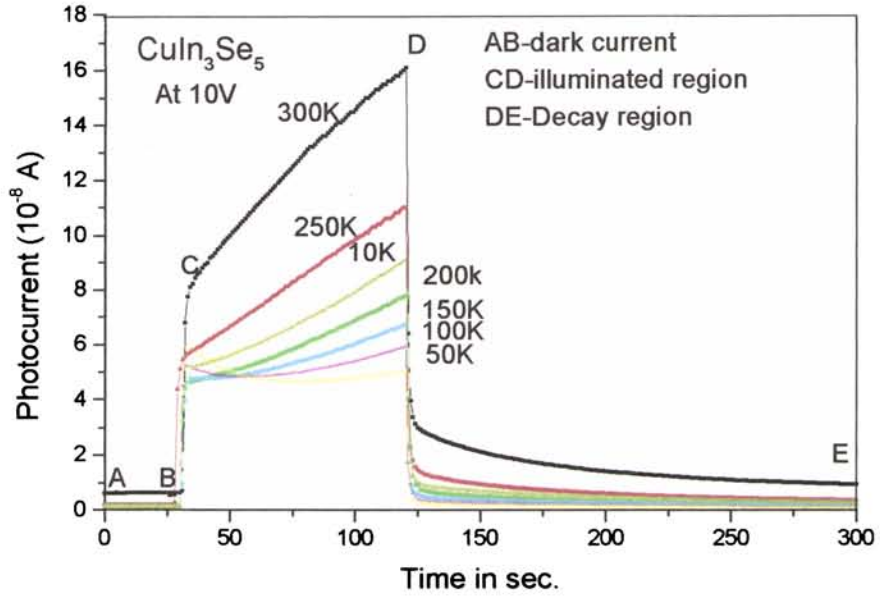


Fig.6.5a Transient photoconductivity on a $CuIn_3Se_5$ film.

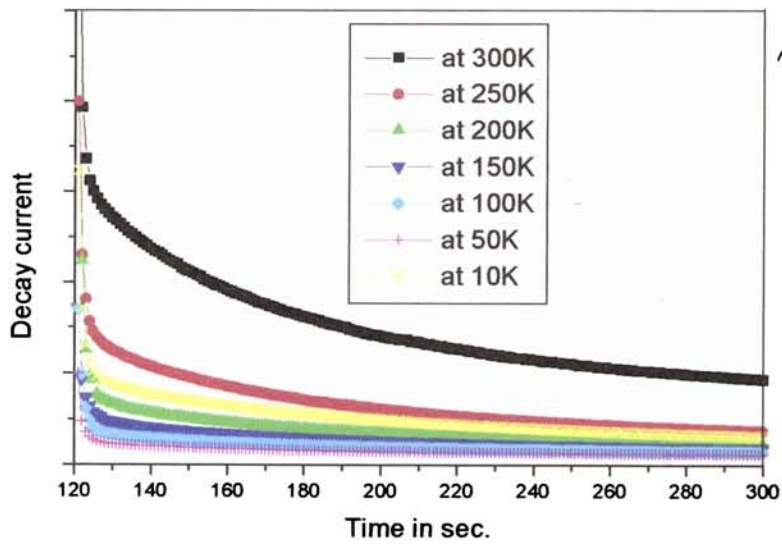


Fig.6.6a Decay part of the transient photoconductivity curve on $CuIn_3Se_5$ film .

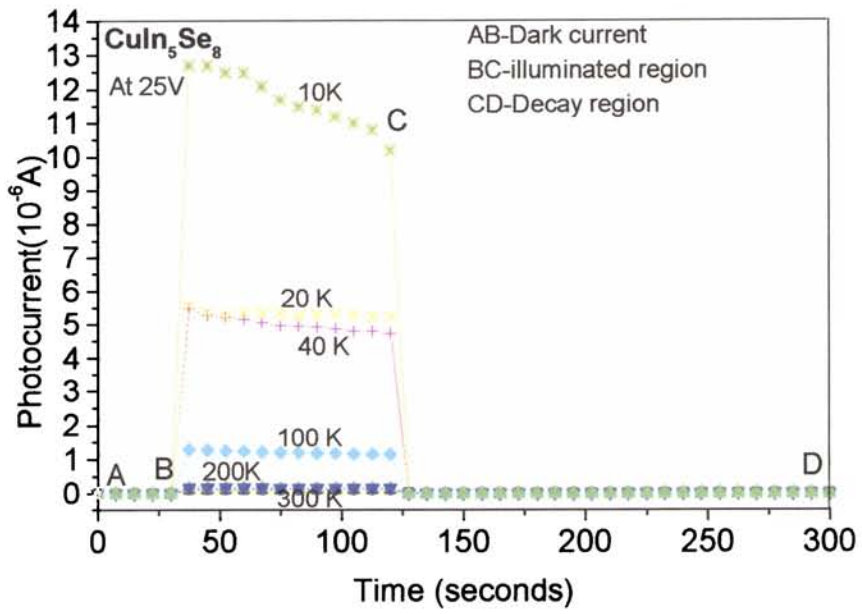


Fig.6.5b Transient photoconductivity on a CuIn₅Se₈ film.

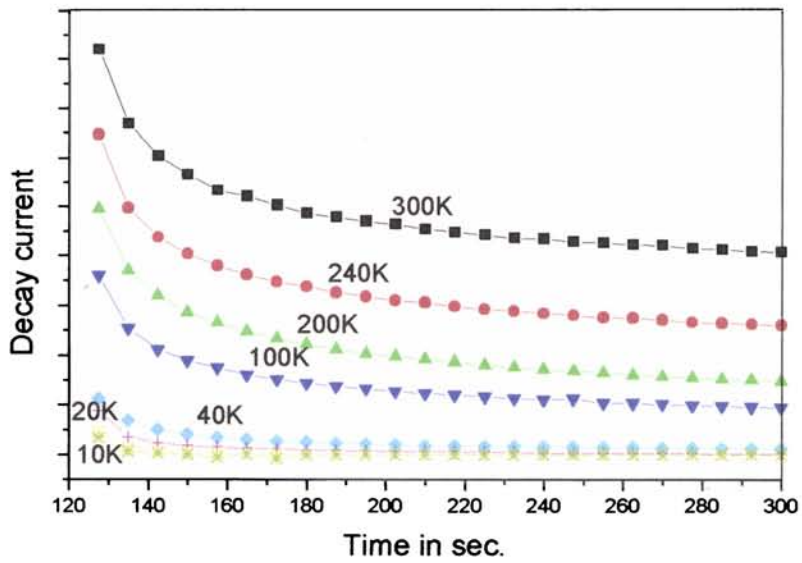


Fig.6.6b Decay part of the transient photoconductivity curve on CuIn₅Se₈ film .

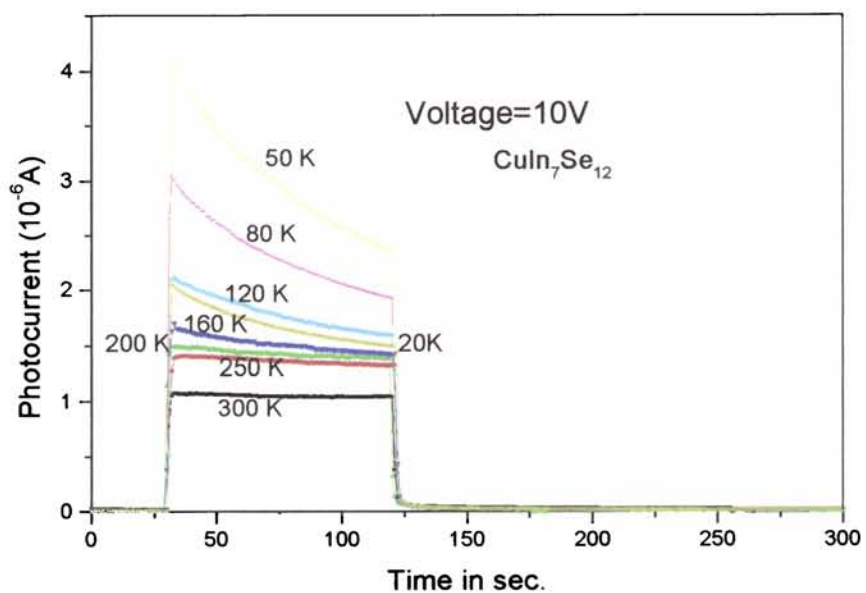


Fig.6.5c Transient photoconductivity on a CuIn₇Se₁₂ film.

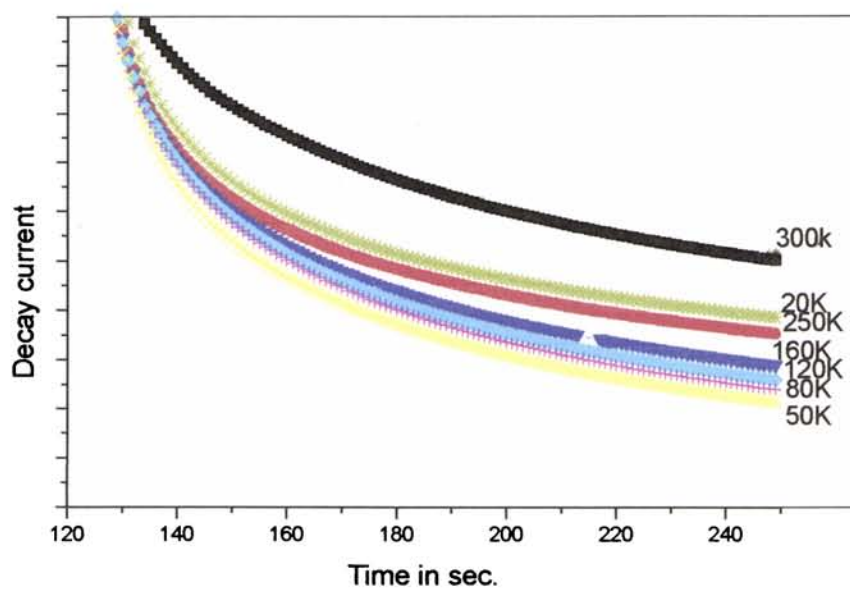


Fig.6.6c Decay part of the transient photoconductivity curve on CuIn₇Se₁₂ film.

The life-time from the decay curve is found to vary with time for all the OVC's and the dependence of τ_d on time (t) is represented in the $\ln(\tau_d)$ versus $\ln(t)$ plot as in Fig.6.7a-c.

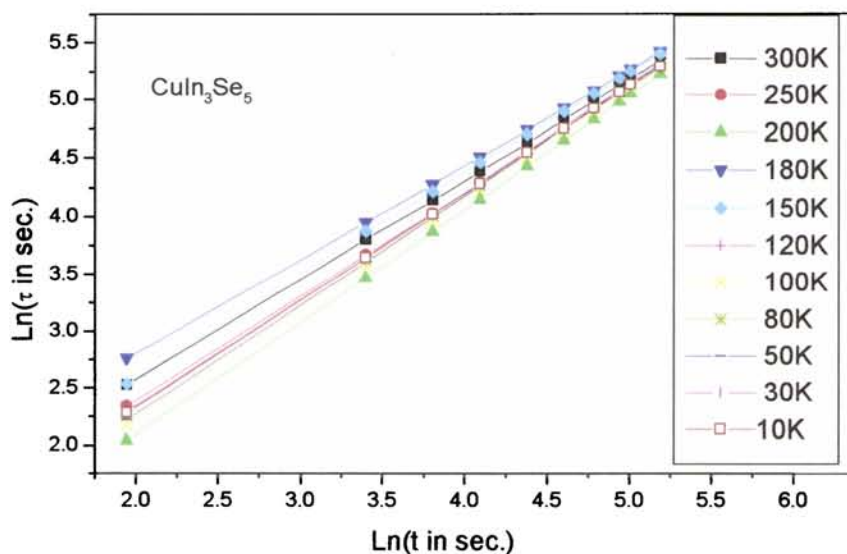


Fig.6.7a Variation of $\ln(\tau)$ with $\ln(t)$ at different temperatures on CuIn_3Se_5 film.

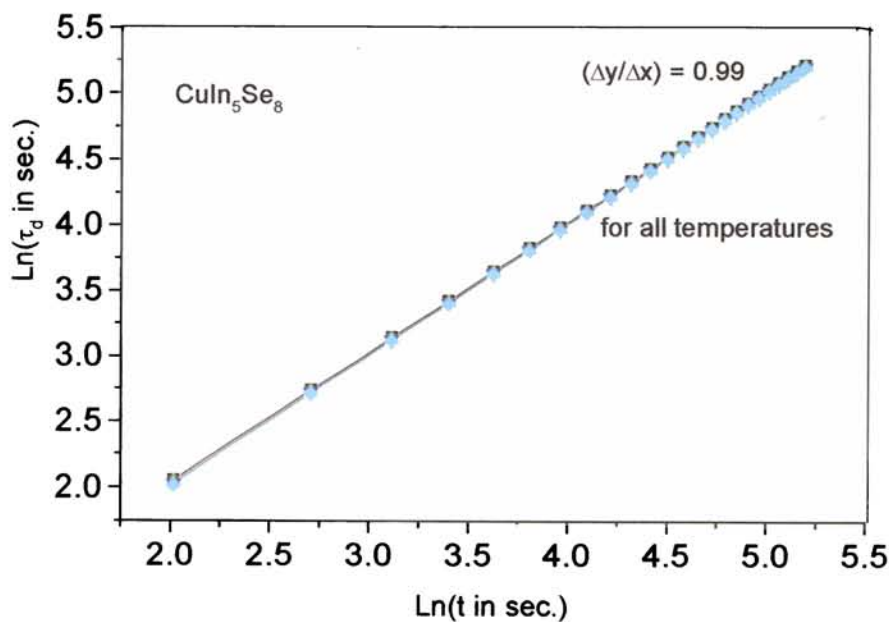


Fig.6.7b Variation of $\ln(\tau)$ with $\ln(t)$ at different temperatures on CuIn_5Se_8 film.

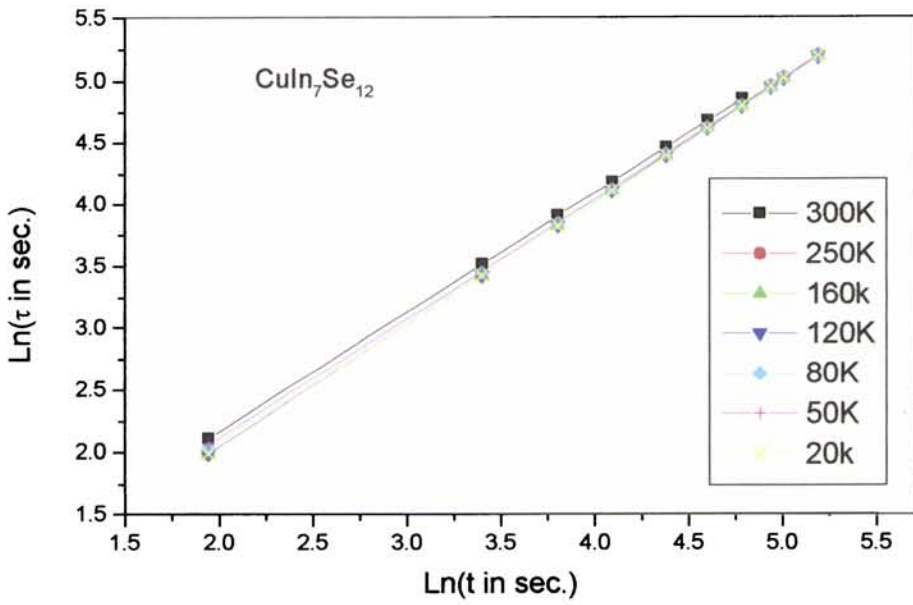


Fig.6.7c Variation of $\ln(\tau)$ with $\ln(t)$ at different temperatures on $\text{CuIn}_7\text{Se}_{12}$ film.

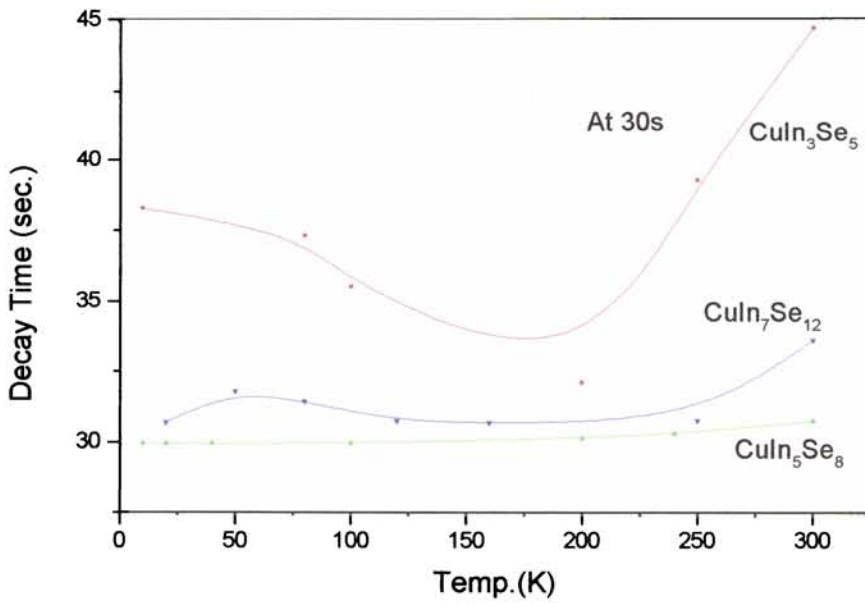


Fig.6.8a Variation in decay time with temperature in the films at time 30s after cutting off illumination.

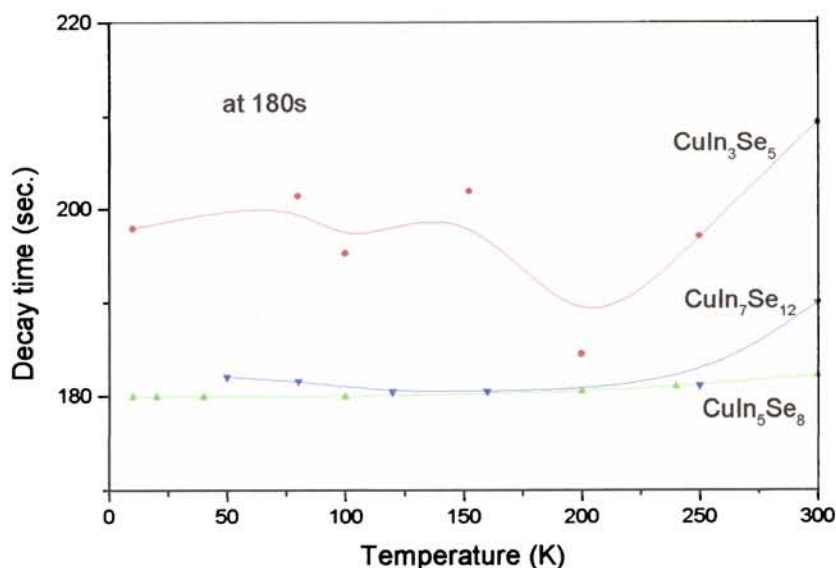


Fig.6.8b Variation in decay time with temperature in the films at time 180s after cutting off illumination.

The variation of lifetime with temperature at definite time intervals for all the films at 30s and 180s after cutting off the illumination is represented in Fig.6.8a-b. In all the OVC films that are studied, the lifetime (in the slow decay region) is found to decrease with decrease in temperature up to around 180K while below that the decay behaviour in the films does not show a particular dependence on temperature. We assume that as in the case of CuInSe₂ discussed in section.3.3.1 the temperature independent decay at low temperatures is due to localized- localized recombination process for which no thermal activation is necessary [13]. Thus unlike in the case of Cu-rich CuInSe₂, all the In-rich films such as In-rich CuInSe₂ and the OVC's studied here are highly photoconducting and show a rapid increase in conductivity on illumination. But the photoconducting effect is found to be temperature dependent also except at very low temperatures as indicated by the variation of decay constant with temperature in Fig.6.8.

6.3.2 Steady State Photoconductivity

The experimental set up is same as that explained in section.3.3.2. Here also the photocurrent has been measured during the heating cycle and at an illumination

intensity of 100mW/cm^2 . The steady state photocurrent measured on the OVC films are shown in Fig. 6.9a-c. The dark current measured on the OVC films are given in Fig.6.10a-c. It is observed that in CuIn_3Se_5 photocurrent increases with increase in temperature while in the other two OVC's the photocurrent decreases with increase in temperature, in the temperature range above 100K. The same trend is observed in transient photoconductivity also.

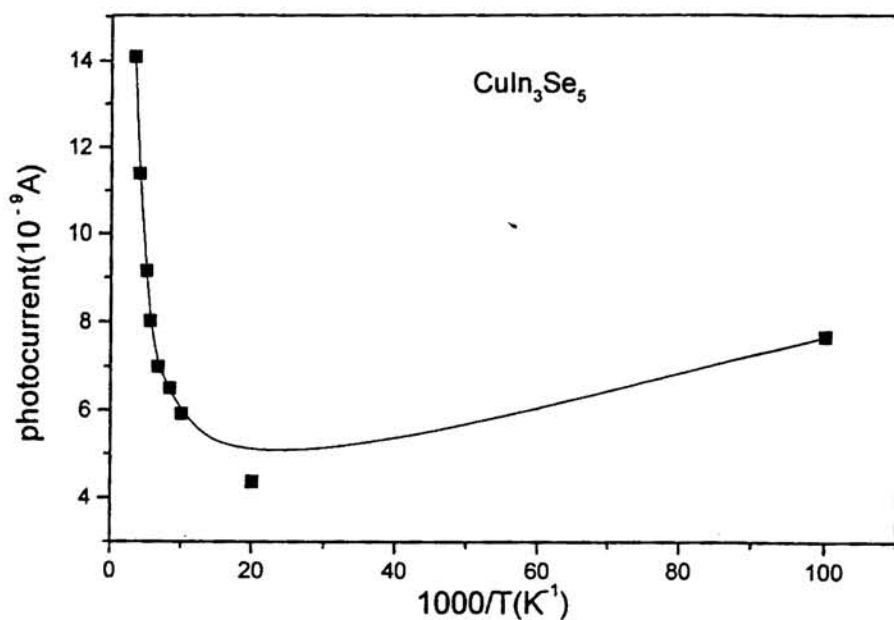


Fig.6.9a Variation of steady state photocurrent with temperature in CuIn_3Se_5 film.

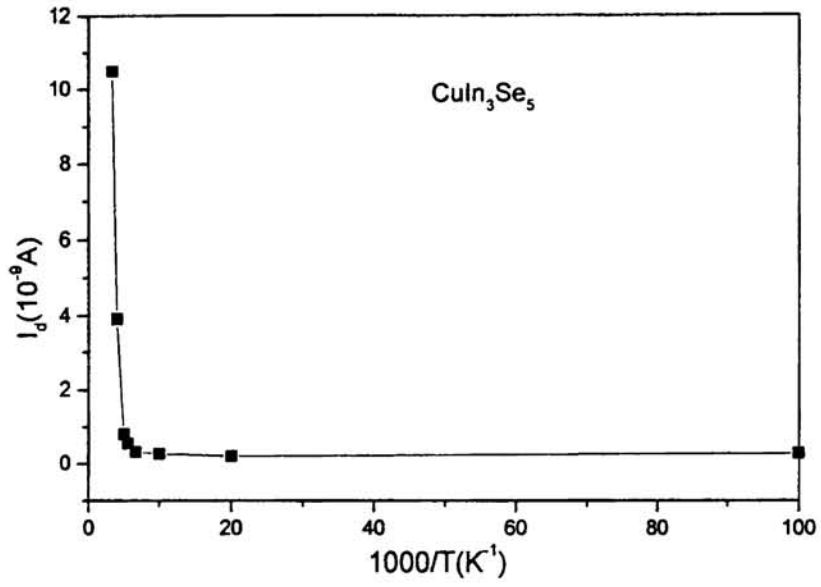


Fig.6.10a Dark current variation with temperature in $CuIn_3Se_5$ film.

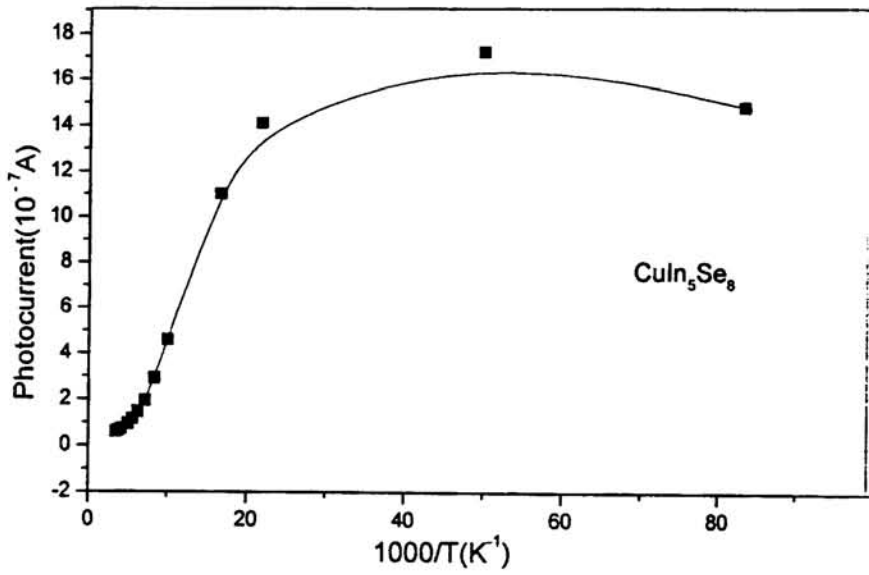


Fig.6.9b Variation of steady state photocurrent with temperature in $CuIn_5Se_8$ film.

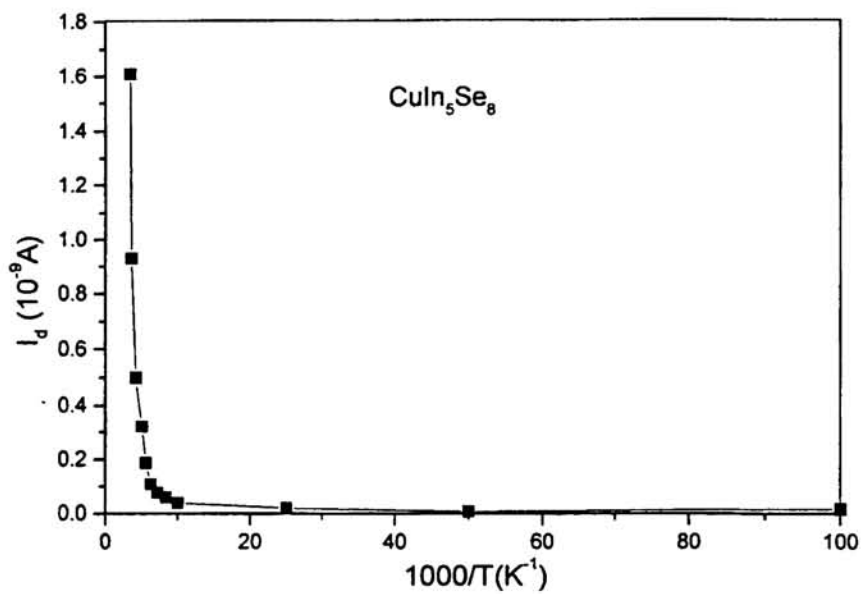


Fig.6.10b Dark current variation with temperature in $CuIn_5Se_8$ film..

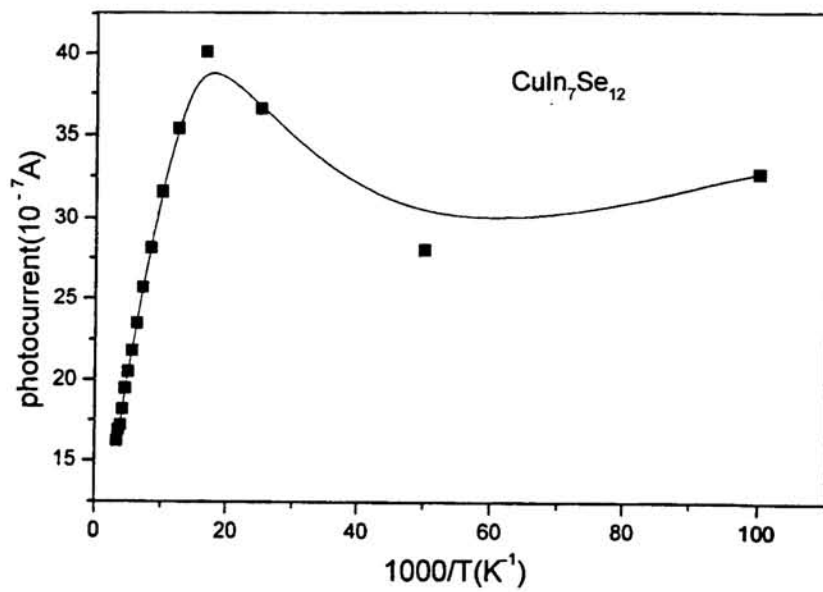


Fig.6.9c Variation of steady state photocurrent with temperature in $CuIn_7Se_{12}$ film.

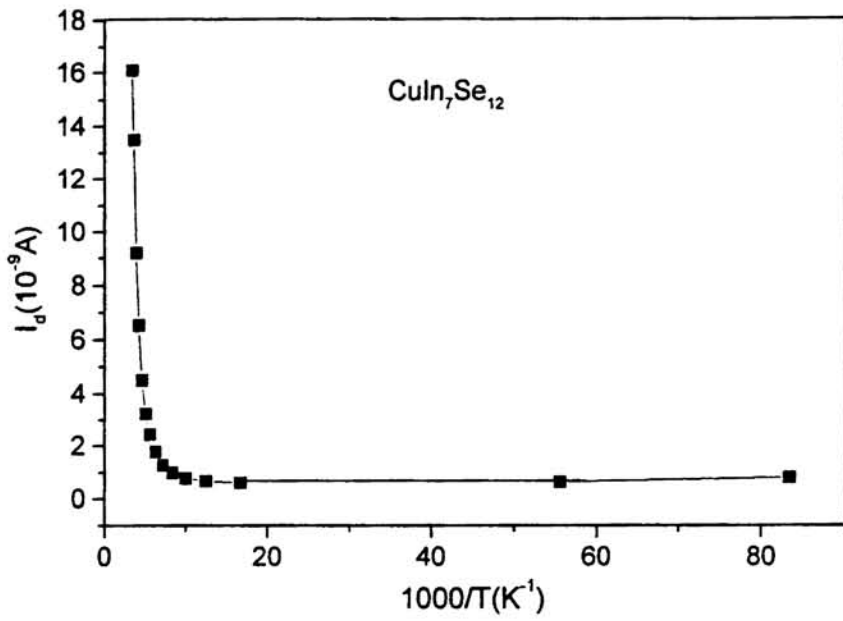


Fig.6.10c Dark current variation with temperature in $\text{CuIn}_7\text{Se}_{12}$ film.

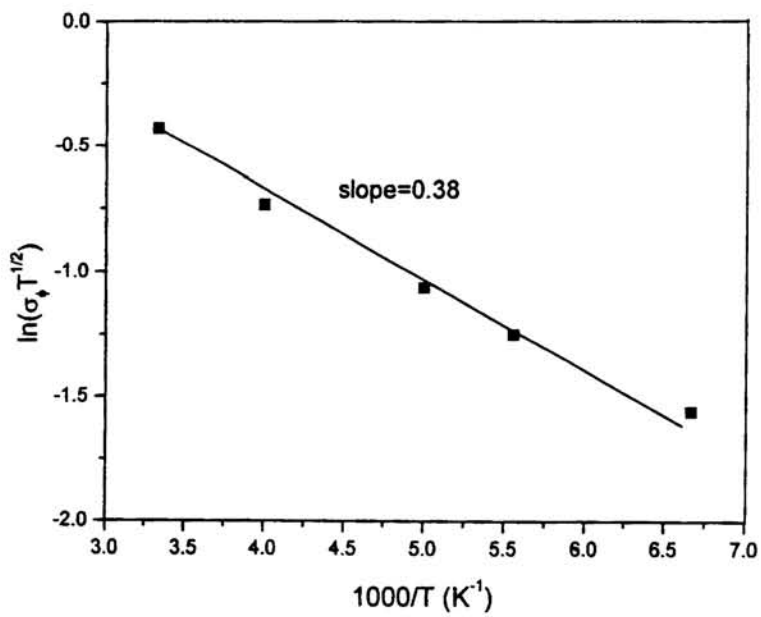


Fig.6.11a $\ln(\sigma_\phi T^{1/2})$ versus $1000/T$ graph for barrier height determination on illumination in CuIn_3Se_5 film .

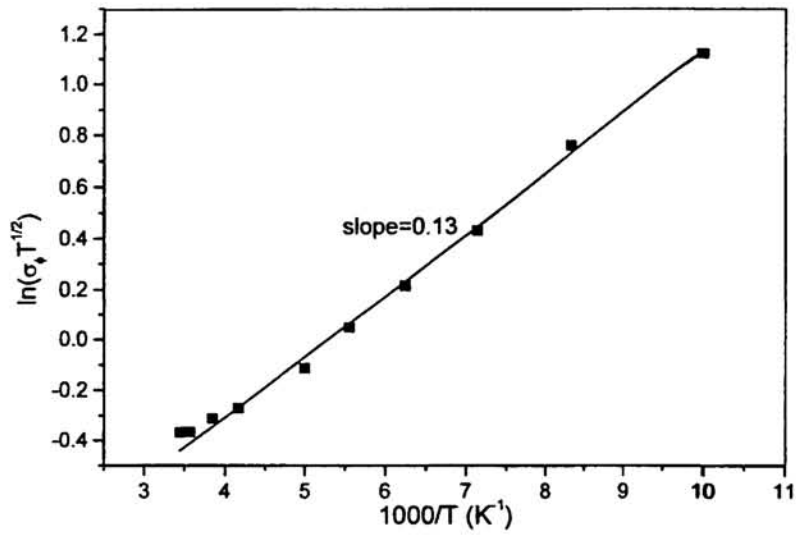


Fig.6.11b $\ln(\sigma_{\phi} T^{1/2})$ versus $1000/T$ graph for barrier height determination on illumination in $CuIn_5Se_8$ film .

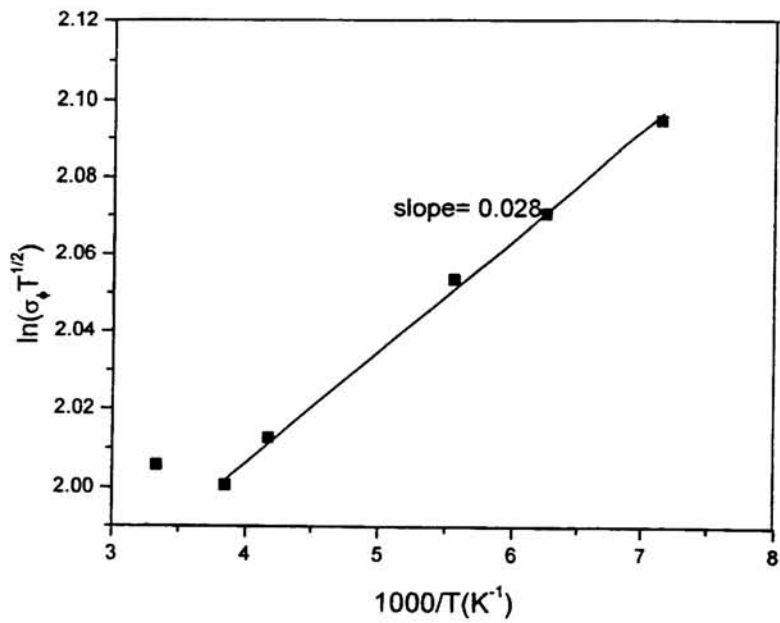


Fig.6.11c $\ln(\sigma_{\phi} T^{1/2})$ versus $1000/T$ graph for barrier height determination on illumination in $CuIn_7Se_{12}$ film .

As in the case of CuInSe_2 polycrystalline films, in the OVC films also the grain boundary effect might be significant. To determine the grain boundary effect, the barrier height before and after illumination has been calculated by plotting $\ln(\sigma_{\phi} T^{1/2})$ versus $1000/T$ graph (fig.6.11a-c). The theory is explained in detail in section.3.3.2. Calculations show that there is a sudden decrease in barrier height in the films on illumination, probably due to the trapping of photoexcited holes at the grain boundaries leading to reduction in barrier height and width. The decrease in barrier height usually increases the probability of tunneling across the barriers, thus increasing the conductivity of the films. This effect is usually predominant at low temperatures and hence may be contributing significantly towards the increased conductivity on illumination at low temperatures. Since presence of defects has been identified from spectral response studies (section 6.3.3) and from the nature of decay shown by the transients, variation of potential barrier height on illumination due to modifications in the emission and capture cross sections of the traps on illumination can also be another reason for the increase in photoconductivity on illumination.

The barrier heights calculated before and after illumination are given in Table.6.1.

Type of film	Barrier height in dark	Barrier height on illumination
CuIn_3Se_5	0.13 eV	0.03 eV
CuIn_5Se_8	0.07 eV	0.01 eV
$\text{CuIn}_7\text{Se}_{12}$	0.09 eV	0.0024 eV

Table.6.1 *Barrier heights determined before and after illumination from $\ln(\sigma_{\phi} T^{1/2})$ versus $1000/T$ graph.*

The variation in photosensitivity ($\Delta I_{ph}/I_d$) with change in temperature are shown in Fig.6.12a-c.

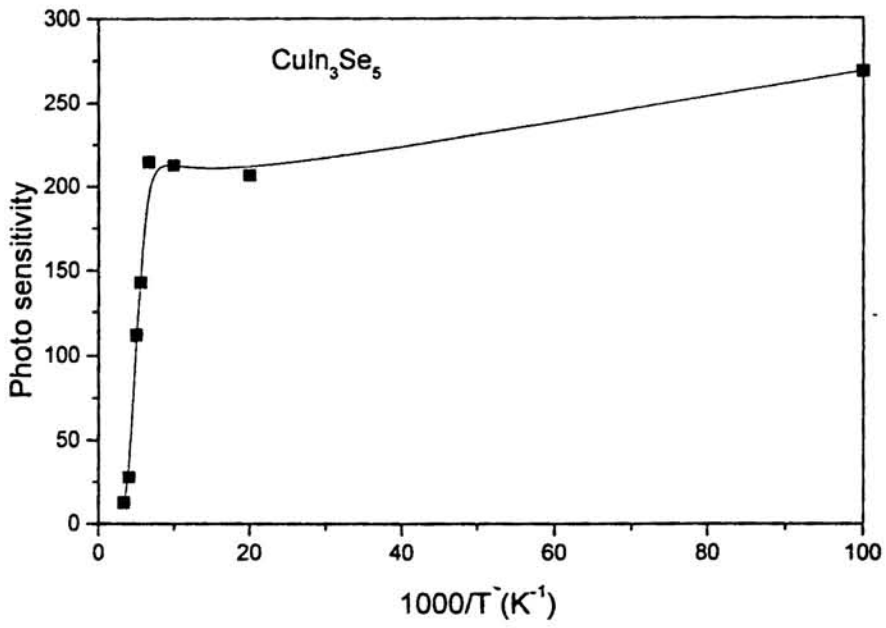


Fig.6.12a Variation of photosensitivity with temperature in CuIn_3Se_5 .

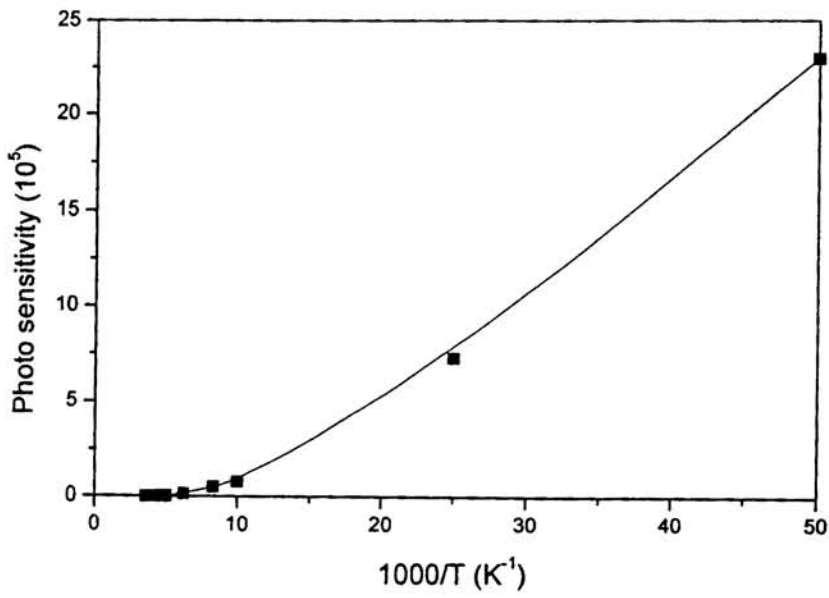


Fig.6.12b Variation of photosensitivity with temperature in CuIn_5Se_8 .

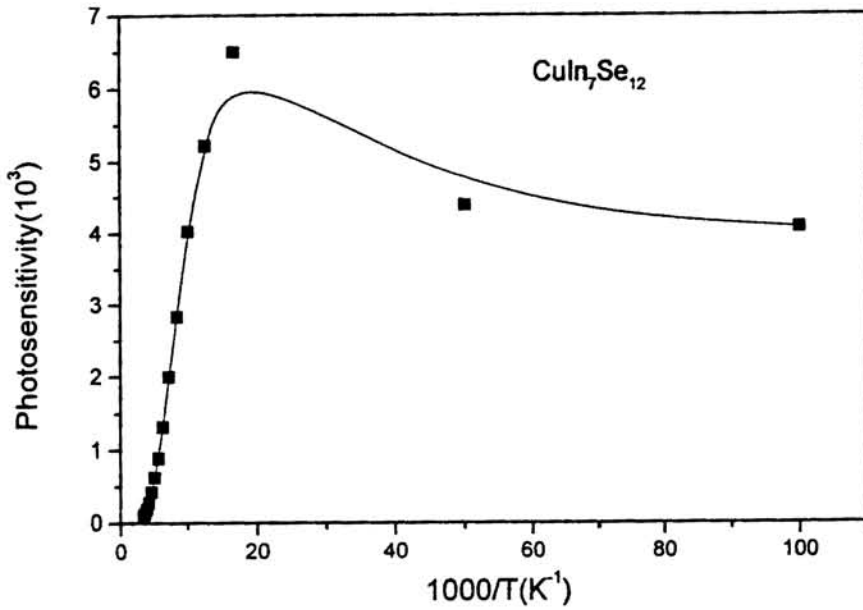


Fig.6.12c Variation of photosensitivity with temperature in $CuIn_7Se_{12}$.

Photosensitivity is found to increase with decrease in temperature down to around 100K while below that the behaviour is not predictable. This could be because temperature independent processes are active in the low temperature region as suggested in section 6.3.1.

6.3.3 Spectral Response Studies.

The experimental arrangement for spectral response studies is same as given in section 3.3.3. The measurements are done in the wavelength range 2000nm to 600nm using a Halogen lamp coupled with an Oriel 7240 grating monochromator as the source. The sample has been cooled to 10K in the cryostat initially and the photocurrent measurements are done varying the incident energy, keeping the temperature of the sample constant using the temperature controller.

The spectral response curves at different temperatures on $CuIn_3Se_5$ are given in Fig.6.13a-b, on $CuIn_5Se_8$ in Fig.6.14a-c and on $CuIn_7Se_{12}$ in Fig.6.15a-b. The figures depict more than one photoactive transitions in all the films. There are different methods for determining the gap energy associated with the observed transitions

[3,14,15]. Ariswan et al [3] used a method following the theory proposed by DeVore [11] where $(I_{ph}hv)^2$ is plotted against (hv) and then extrapolating the straight line graph to the X-axis at $y=0$ to obtain the band gap corresponding to a transition. But this method is not practical in the case where a number of peaks and shoulders are present in the spectral response curve. Marcano et al [14] and A.Serpi [15] discussed the origin of the photoactive transitions in relation to the peak positions observed in the response curve while some authors discuss it with respect to the threshold energies of the photoactive transition curve [16]. In the present case since more than one peak is observable in each curve, the discussion is done with respect to the peak positions. Here since the peaks obtained are broad, the attempt is only to relate the photoactive band positions to the possible cause of its origin and not to determine the exact band gap or the positions of defect levels in the film.

Examination of the spectral response curves at 300K obtained on $CuIn_3Se_5$, $CuIn_5Se_8$ and $CuIn_7Se_{12}$ (Fig.6.13a) shows the most dominant peaks around 1.28eV, 1.3eV and 1.35eV respectively. In comparison with absorption spectrum where the room temperature band gaps of $CuIn_3Se_5$, $CuIn_5Se_8$ and $CuIn_7Se_{12}$ are obtained as 1.23eV, 1.31eV and 1.37eV respectively, the prominent photoactive transition peaks could be related to the band-to-band transition in the compounds. Here the threshold energy of the transition at 1.1eV also has some significance when compared with the photoluminescence data depicted in section.6.4 where peaks at 1.1eV are observable in the PL curve on all the three samples. Postponing the discussion on the 1.1eV curve to the next session, the photoactive transition around 0.88eV is considered. Since a transition around 0.88-0.89 eV is observable in all the three OVC's studied (Fig.13a-^{6.139} 6.15a), its origin could be from a defect common in all the OVC's. As it is discussed in the earlier chapter, all these compounds have an ordered arrangement of 1 unit of the defect complex $(2V_{Cu}+In_{Cu})$ in every 4,5 or 7 units of $CuInSe_2$, which means there is possibility of In_{Cu} and V_{Cu} defects in all these OVC compounds. A study of defect states in CIS compounds shows that In_{Cu} has two deep levels at ~ 0.25 eV and ~ 0.34 eV and V_{Cu} has a shallow acceptor level between 0.01 to 0.05 eV [17]. Hence the broad band near 0.88 eV might be related to a D- A transition between a donor defect In_{Cu} at a deep level ~ 0.34 eV below the conduction band edge and a shallow acceptor defect

$V_{Cu} \sim -0.05$ above the valence band edge in all the three OVC's. This transition is found to be broad with the energy range varying from around 0.75eV to 0.9eV in the compounds.

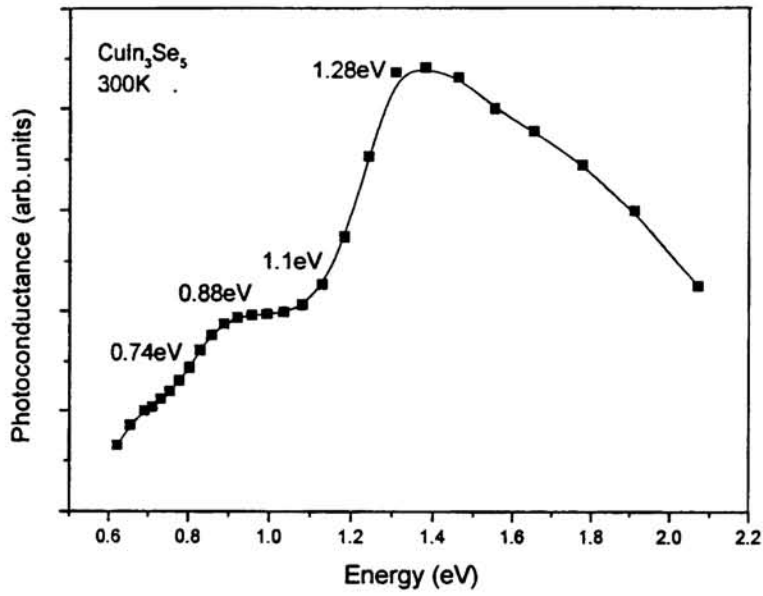


Fig.6.13a Spectral response on $CuIn_3Se_5$ at 300K.

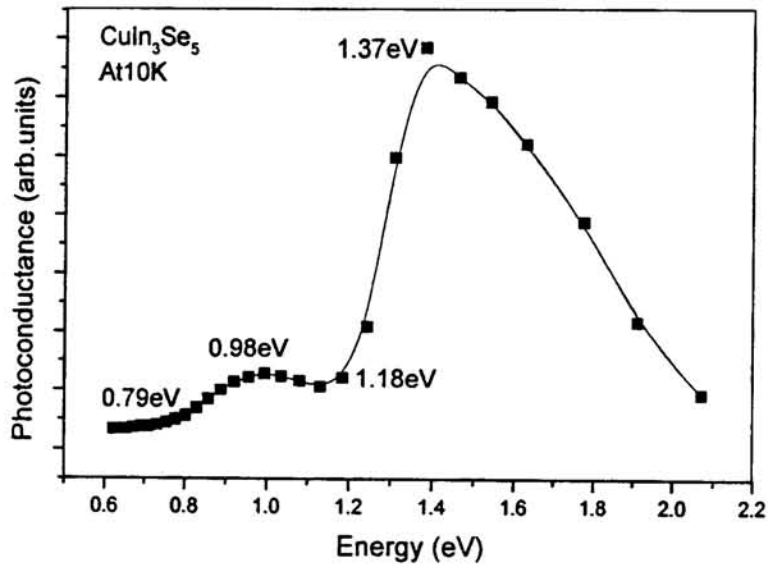


Fig.6.13b Spectral response on $CuIn_3Se_5$ at 10K.

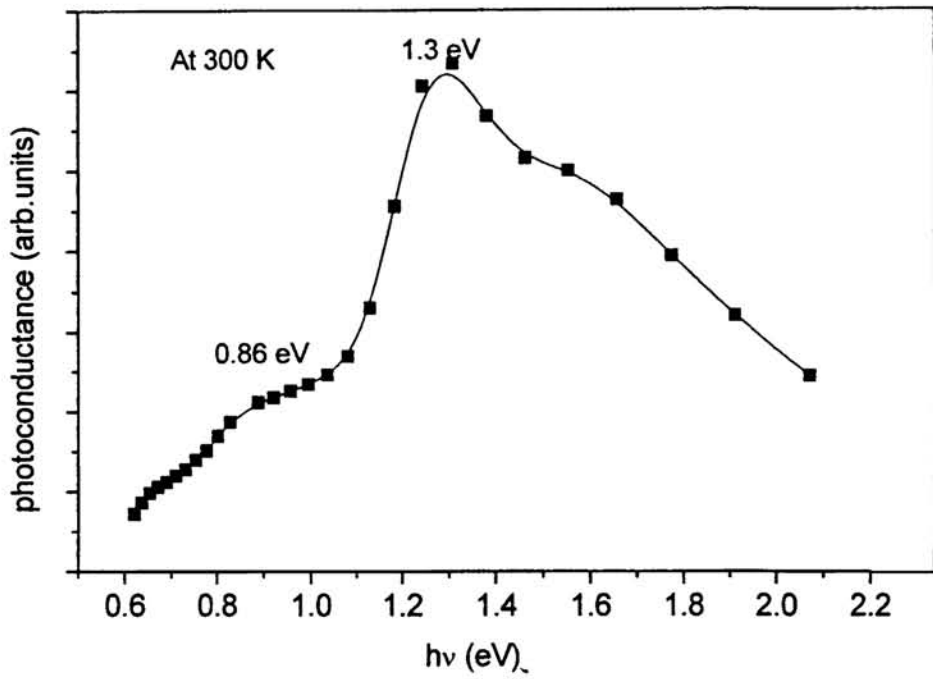


Fig.6.14a Spectral response on CuIn_5Se_8 at 300K.

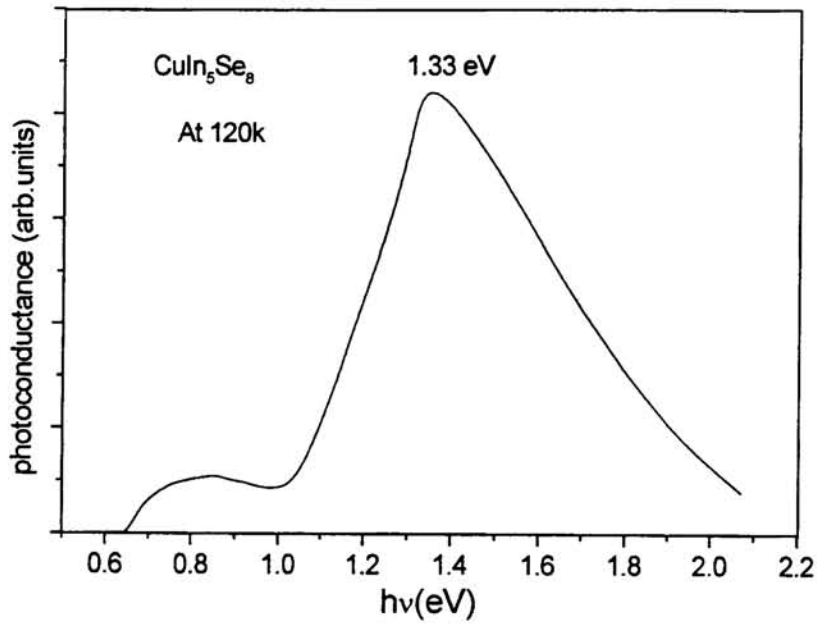


Fig.6.14b Spectral response on CuIn_5Se_8 at 120K.

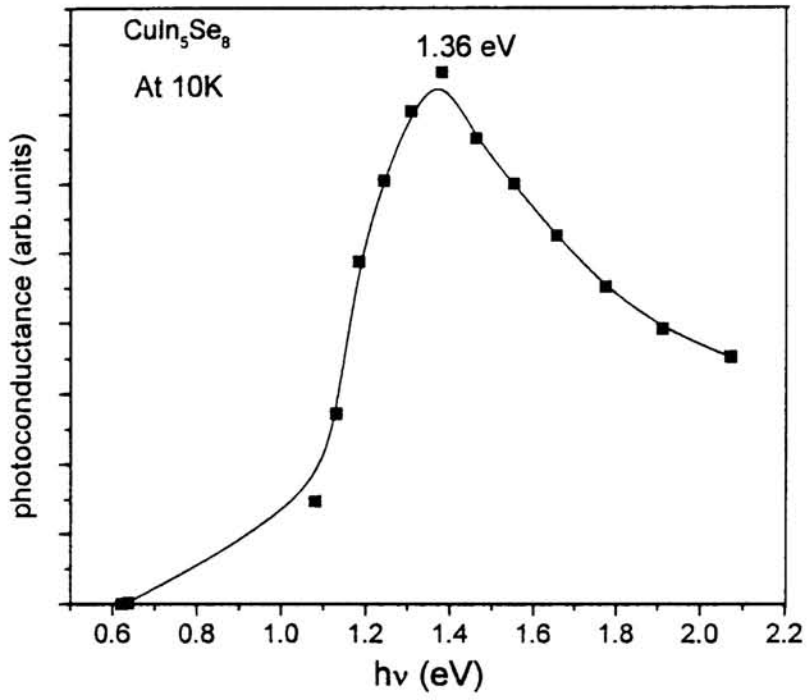


Fig.6.14c Spectral response on CuIn₅Se₈ at 10K.

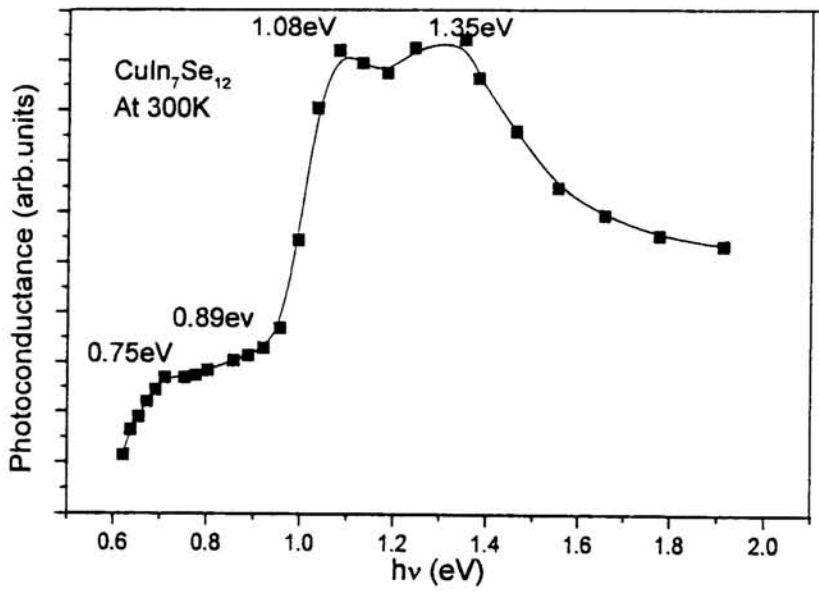


Fig.6.15a Spectral response on CuIn₇Se₁₂ at 300K.

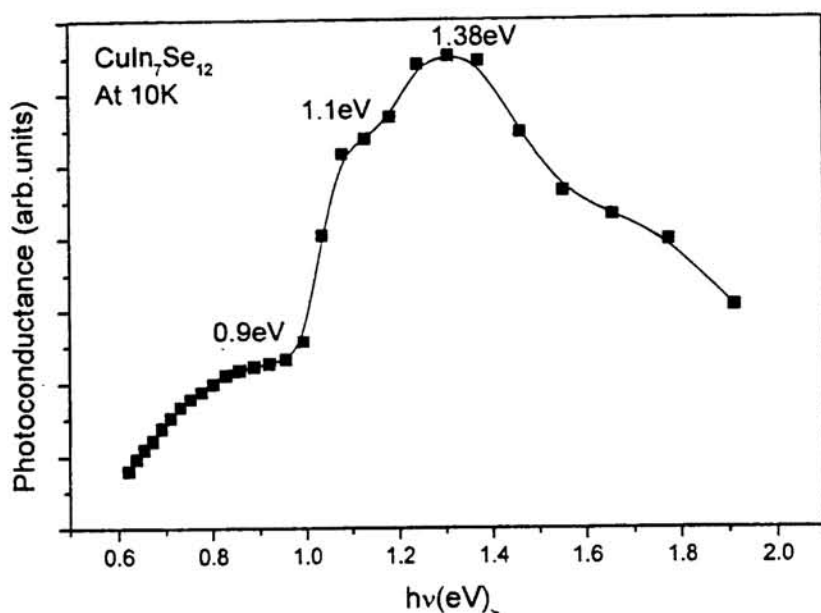


Fig.6.15b Spectral response on CuIn₇Se₁₂ at 10K.

In all the OVC's the peak positions are found to be shifted towards the lower energy side with increase in temperature, possibly due to the sum of the effects of electron phonon interaction and thermal expansion, of which former has been reported to be the most dominant [4,18].

6.4 Photoluminescence studies on the OVC's.

The experimental set up for photoluminescence measurements is given in section.1.3.4.3. The PL spectra obtained on CuIn₃Se₅, CuIn₅Se₈ and CuIn₇Se₁₂ films are shown in Fig.6.16a-c. In all the three compounds, the luminescence shows two sharp peaks one around 1.1eV and the other around 0.75eV. In CuIn₃Se₅, the spectrum is dominated by a peak of 4 meV full width at half maximum (FWHM) at 1.103eV and a sharp peak of 2meV FWHM at 0.75eV. In CuIn₅Se₈, the spectrum has a peak of 6meV FWHM at 1.111eV and another of 3meV at 0.754eV. In CuIn₇Se₁₂, a peak of 5 meV FWHM at 1.113eV and another sharp peak of 3meV FWHM at 0.755 eV are seen in

the spectrum. Keeping in mind that the band gaps estimated for the compounds CuIn_3Se_5 , CuIn_5Se_8 and $\text{CuIn}_7\text{Se}_{12}$ are 1.23eV, 1.31eV and 1.37eV, the emissions in the PL spectra on these compounds can be considered to have common origins. The emission near 1.1eV with difference of 127meV, 199meV and 257meV respectively in CuIn_3Se_5 , CuIn_5Se_8 and $\text{CuIn}_7\text{Se}_{12}$ from the band to band energy gap can all be considered to have their origin from a radiative D-A pair recombination between the donor defect state In_{Cu}^+ which is assumed to have activation energies 120-160 meV as well as around 250meV and the acceptor state V_{Cu}^- verified by different investigators to have an activation energy ranging from 10-50meV [17]. For instance, if in CuIn_3Se_5 , the donor level due to In_{Cu}^+ is at 120meV and the acceptor level V_{Cu}^- is at 10meV, then the gap between the two defect states is 1.1eV, which exactly coincides with the position of the PL peak assigned to be due to the D-A pair recombination in the compound. Selenium vacancies also have the donor levels at the same position but transition from In_{Cu} has more probability in the OVC samples where the ordered arrangement of defect In_{Cu} and V_{Cu} is always expected. Further the samples are slightly In-rich which adds to the possibility of presence of the defect In_{Cu} having a lower formation energy ~ 1.4 eV compared to the formation energy 2.4 eV for V_{Se} , in the OVC's. [19]. The result is in good agreement with the spectral photoconductivity studies where the photoactive transition peak around 1.1eV clearly observed in CuIn_5Se_8 and $\text{CuIn}_7\text{Se}_{12}$ films can be said to involve the same defect states In_{Cu} and V_{Cu} . It is a difficult task to assign the deep level emission near 0.75eV to a particular transition unambiguously, since the difference in energy of this peak with the band to band gap energy which is estimated to be in the range 0.48 to 0.6eV is comparable only with the activation energy 0.56 ± 0.14 eV reported by various measurements on CuInSe_2 corresponding to the donor defect In_i^{+++} [17]. Hence one possibility for the occurrence of the peak at 0.75eV is a radiative transition from the donor defect state In_i^{+++} to the valence band. For instance, if some excess In happen to occupy the interstitial positions in CuIn_3Se_5 and form a donor level at 0.48eV below CBM, then we can assume that a transition from this level to the valence band gives rise to the 0.75eV PL peak in the compound. In spectral response (PC) studies, especially at low temperatures a broad photoactive band is observed in the energy range $\sim 0.75\text{eV}$ to 0.9eV, and a comparison of the PL and PC

gives rise to the speculation that the defect states involved behind the PL peak observed near 0.75eV at room temperature might be the same as that behind the broad band transition observed in the PC. There is a possibility that at room temperature, the PL transitions have been influenced by phonon vibrations thus shifting it to the lower energy range edge, that is 0.75eV which further leads to the assumption that the PL peak at 0.75 eV may be due to a D-A pair recombination between a donor defect In_{Cu} at a deep level ~ 0.34 eV below the conduction band edge and a shallow acceptor defect $\text{V}_{\text{Cu}} \sim 0.05$ above the valence band edge in all the three OVC's. There is a possibility that as the OVC's are becoming more In-rich and more deficient in Cu, the donor and acceptor levels may be becoming more spread out than in CuInSe_2 for which the levels are usually observed at 0.34 eV and 10-50meV, so that a D-A transition between the two levels can give a PL peak at 0.75eV. It seems more reasonable to assume the pair recombination in the OVC's rather than a radiative transition from defect states formed by In interstitials, once the OVC structure is studied and here we adopt the former explanation.

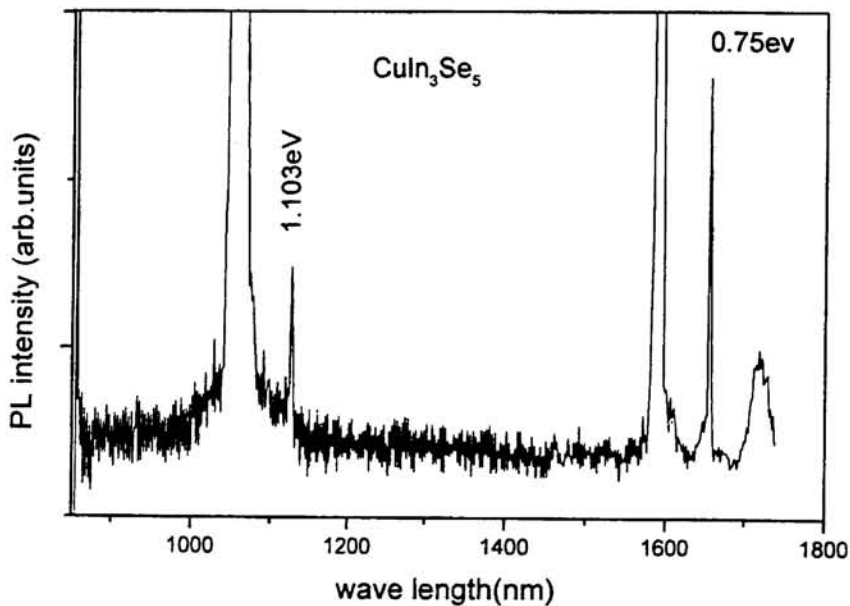


Fig.6.16a PL spectrum on CuIn_3Se_5 at room temperature.

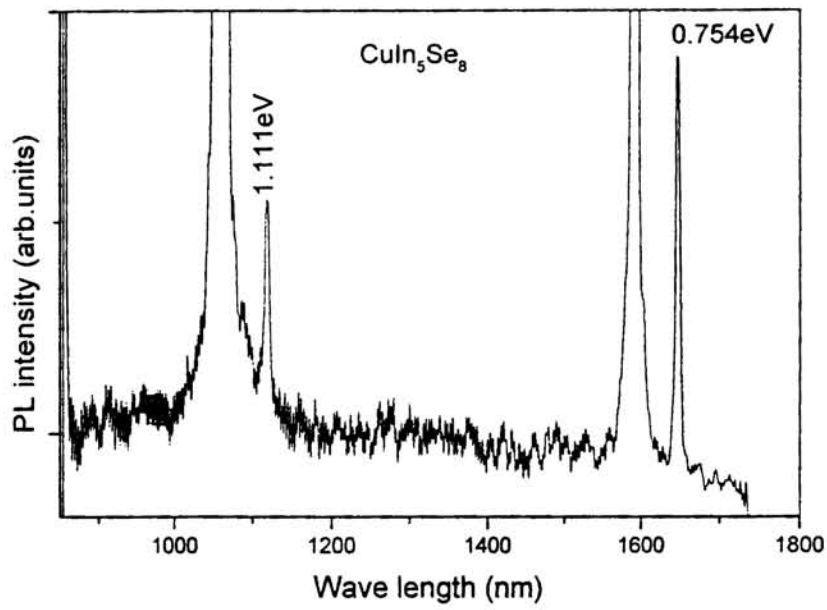


Fig.6.16b PL spectrum on CuIn_5Se_8 at room temperature.

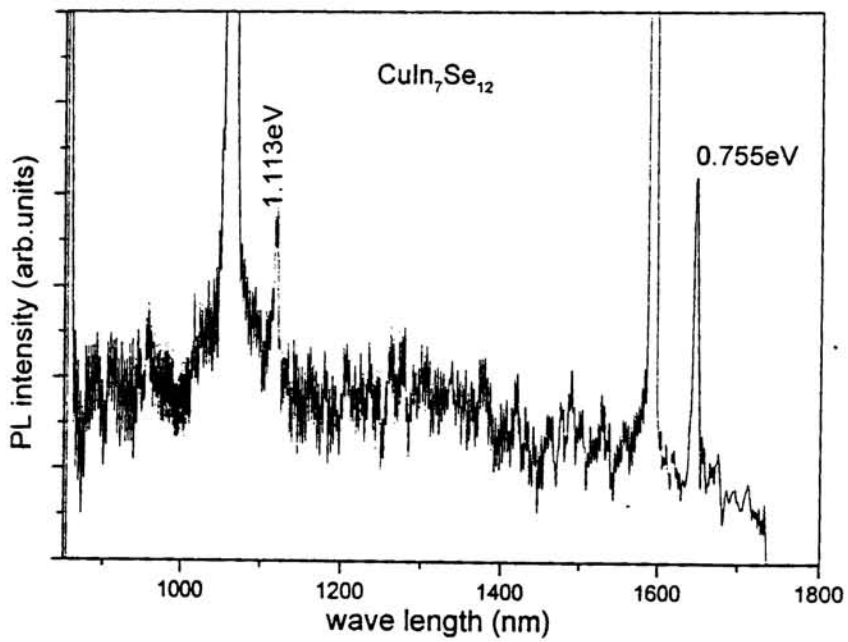


Fig.6.16c PL spectrum on $\text{CuIn}_7\text{Se}_{12}$ at room temperature.

6.5 Conclusion

In this chapter, the optical band gaps and the optical constants like absorption coefficients, refractive index and extinction coefficient of the OVC compounds are studied from the absorption and transmission spectra. The increase in the band gaps of the OVC's relative to that of CuInSe_2 is explained using p-d repulsion effects. Transient and steady state photoconductivity measurements have been used to determine the decay constants and the barrier height variation on illumination respectively. Spectral response studies of the OVC films at room temperature and at low temperatures have been used for determining the defect states present in the compounds. PL at room temperature has also been used to detect the defect states in the compound.

References

- [1] S.B. Zhang, S.H. Wei and A. Zunger. *Phys.Rev.B.* 57 (1998) 9642 .
- [2] H.Z.Xiao, L.C. Yang and A.Rockett, *J.Appl.Phys.*76 (1994) 1503.
- [3] Ariswan, G.E.Moussa, M.Abdelali, F.Guastavino, C.Llinares, *Solid state communication* 124 (2002) 391.
- [4] C.Rincon, S.M.Wasim, G.Marin, R.Marquez, L.Nieves and G.Sanchez Perez, *J.Appl.Phys.* 90(2001) 4423.
- [5] J.E. Jaffe and A. Zunger. *Phys. Rev. B.* 29(1984)1882 .
- [6] J.L.Shay; B.Tell; H.M.Kasper and L.M.Schiavone. *Phys. Rev. B.* 5(1972) 5003.
- [7] A Miller, A. Mac Kinnon, D. Weaire, in: *Solid state physics*, Ed. H. Ehrenreich, F. Seitz, D. Turnbull, Academic, New york, 36 (1981).
- [8] R.Swanepoel, *J.Phys.E* 17 (1984) 896.
- [9] S.Roy; B.Bhattacharjee, S.N.Kundu, S.Chaudhuri and A.K.pal, *Materials Chem. Physics.* 77 (2003) 365.
- [10] M.S. Kamboj, G.Kaur and R.Thangaraj. *Thin Solid Films*, 420(2002) 350.
- [11] H.B.Devore. *Phys.Rev.* 102(1956) 86.
- [12] W. Fuhs and J.Stuke, *Phys.Stat.Sol. (A)* 24 (1968) 271.
- [13] M. Lal and N.Goyal. *Thin Solid Films.* 227(1993) 177.
- [14] Marcano et al, *Journal of Applied physics*, vol. 90, (2001)1847.
- [15] A.Serpi, *J.Phys.D: Appl.Phys.*, Vol.9, (1976) 1881.
- [16] R.H.Bube. *Photoelectronic Properties of semi conductors*, Cambridge university press, Cambridge, NY 1992.
- [17] Rincon C and Marquez R. *J.Phys.chem. Solids* 60 (1999)1865.
- [18] Rincon C, Wasim S.M. Marin G, Molina I, *J. Appl. Phys.* 93 (2003) 780.
- [19] Rincon C and Bellabarba C, *Phys.Rev.B* 33 (1986)7160

Electrical characterization of the OVC's.**7.1 Introduction**

With the development of a new model for CuInSe_2 based heterojunctions by Schmid et al [1], where the active pn junction is formed between the chalcopyrite CIS and the OVC CuIn_3Se_5 , the investigations of these technologically important OVC's have attracted rapid interest. In spite of the fact that many studies have been done on the transport properties of both p-type and n-type CIS, only very few reports of such studies made on OVC's are seen in literature [2,3]. In the present chapter, we combine the low temperature as well as near room temperature conductivity measurements and Hall measurements to study the transport properties of the OVC compounds CuIn_3Se_5 , CuIn_5Se_8 and $\text{CuIn}_7\text{Se}_{12}$. As done in the case of CIS films (explained in chapter 4), in OVC's also the transport mechanisms in the films in different ranges of temperature are discussed in detail using various models such as Arrhenius, Seto's as well as Mott's variable range hopping conduction model. The type of the samples has been determined by Hot probe method and Hall measurements. The latter has been used to get further information regarding the carrier concentration, sheet resistance etc.

7.2 Electrical conductivity in the OVC's.

All the OVC samples prepared here are determined to be n-type by Hot probe method. The method is described in section.4.2.1. For electrical conductivity measurements, samples of around 0.4 cm in length and 0.2 cm width have been used with Silver contacts on the two ends of the film. After verifying the ohmic nature of the contacts by V-I measurements at room temperature, the samples are loaded in the cryostat and are initially cooled to 80K. As done in the case of CIS films, low temperature conductivity measurements are done during the heating cycle employing Keithley 617 programmable electrometer for resistance measurement and Lakeshore DRC-93 CA controller for temperature control. The pressure inside the cryo has been kept of the order of 10^{-6} Torr.

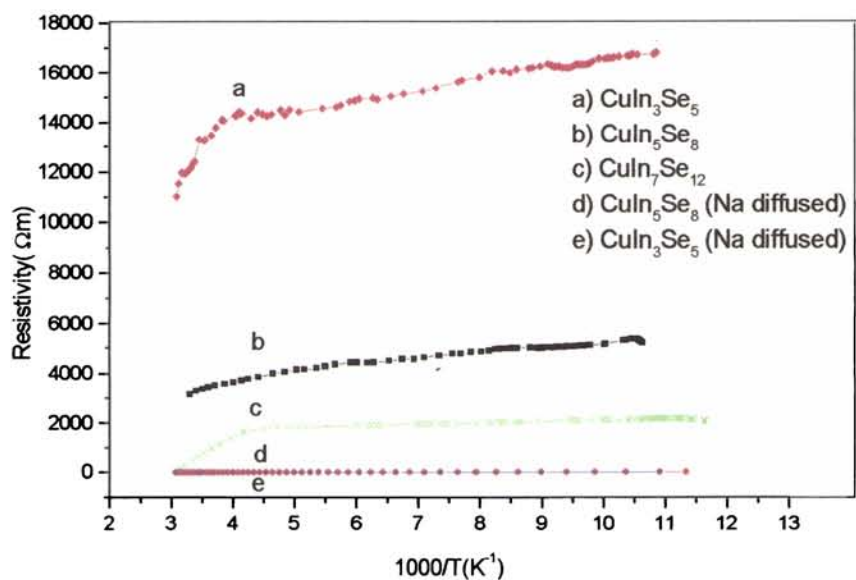


Fig.7.1 Resistivity versus reciprocal of temperature in the OVC's.

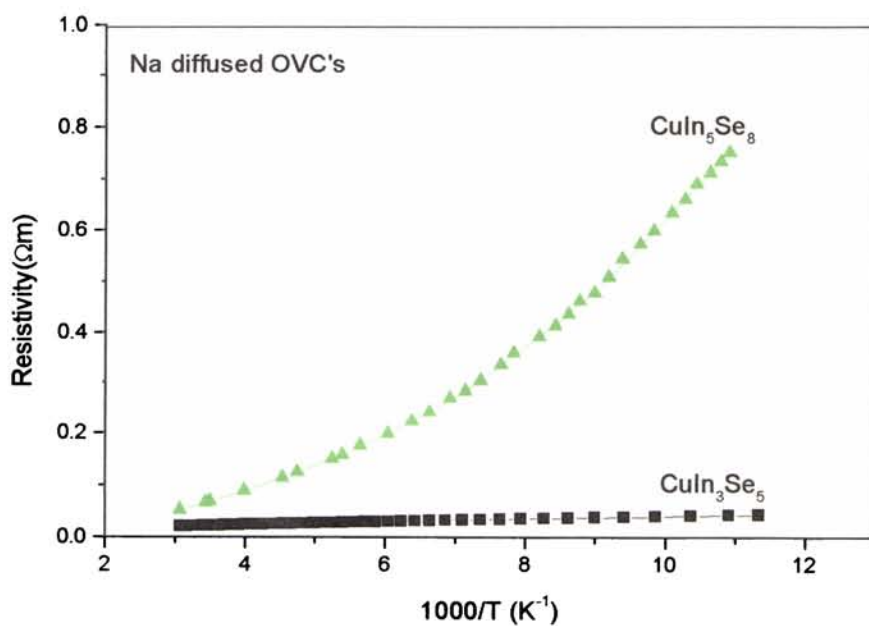


Fig.7.2 Resistivity versus reciprocal temperature on the Na diffused OVC's.

Fig.7.1 represents the variation in resistivity of the samples with temperature variation. It is observed that presence of sodium increases the conductivity of even the OVC films as in the case of Na diffused CuIn_5Se_8 and CuIn_3Se_5 with 2 to 3 at% sodium respectively. Since their representation as d and e in Fig.7.1 is overlapping, a more distinguishable representation is given in Fig.7.2. On the other hand CuIn_3Se_5 , CuIn_5Se_8 and $\text{CuIn}_7\text{Se}_{12}$ shows high resistivity as represented in Fig.7.1 by the representative samples a, b and c.

The resistivity versus inverse temperature plots in Fig.7.1 for the OVC films show a decrease in resistivity with increase in temperature characteristic of semiconducting films in the entire temperature range from 80 K to 300 K with a rather sharper decrease in resistivity in the temperature range above 200 K. The conductivity mechanisms in the two regions are identified as Mott's variable range hopping in the low temperature region and thermally activated conduction in the near room temperature region. In the thermally activated temperature range >200 K, the conductivity is found to follow two types of dependences on temperature as in the case of the In rich CuInSe_2 explained in chapter 4.

Temperature range above 255K

It is observed that above 255 K the samples exhibit a thermally activated electrical conductivity (σ) described by the Arrhenious relation of the type

$$\sigma = \sigma_{0a} \exp(-E_a/k_B T) \quad 7.1$$

where σ_{0a} is a pre-exponential constant, E_a is the activation energy and k_B is the Boltzmann's constant [4]. In this specified temperature range linear plots are obtained (Fig.7.3) when $\text{Ln}(\sigma)$ values are plotted against $1000/T$ for CuIn_3Se_5 and CuIn_5Se_8 samples. But the slope of $\text{Ln}(\sigma)$ Vs $1000/T$ graph (Fig.7.4) is found to be continuously varying in the case of OVC $\text{CuIn}_7\text{Se}_{12}$ so that the data could not be fitted to the Arrhenius equation in the specified temperature range for this compound.

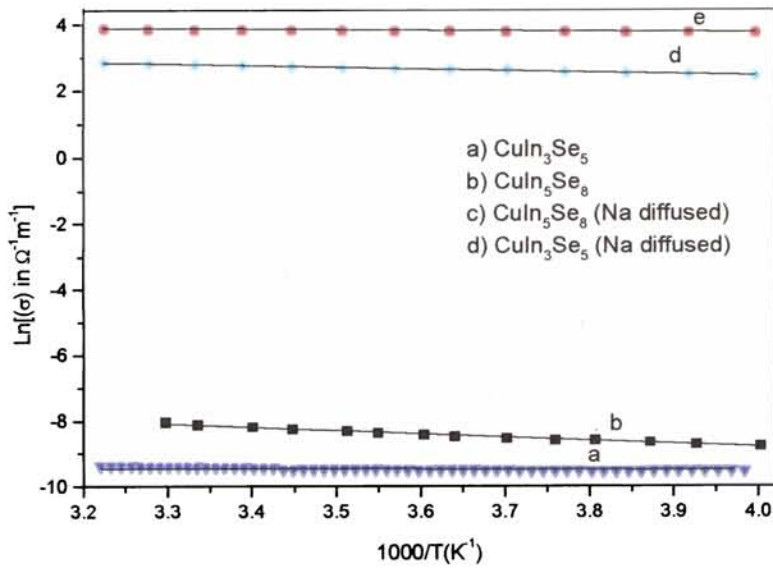


Fig.7.3 Arrhenius plot for CuIn_3Se_5 and CuIn_5Se_8 films.

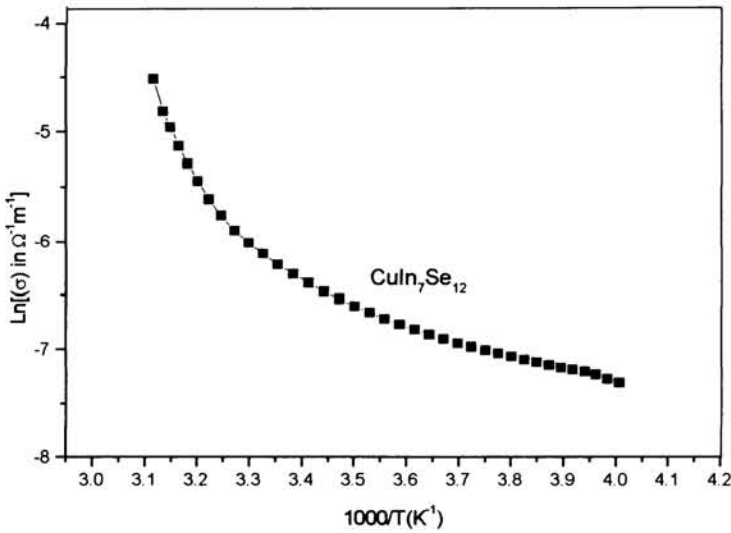


Fig.7.4 Arrhenius plot for $\text{CuIn}_7\text{Se}_{12}$.

From the slope of the graphs in Fig.7.3, the activation energies for the OVC's CuIn_3Se_5 and CuIn_5Se_8 are determined and the possible levels from which the electrical excitation is activated are noted in Table.7.1. For all the OVC's (except CuIn_5Se_8 - Na diffused) an activation energy in the range 0.013 to 0.029 eV is obtained as depicted in

Table.7.1. Rincon and Marquez [5] attributed activation energies in the range $\sim 0.01\text{eV}$ to $\sim 0.02\text{eV}$ measured by different researchers to double donor levels $\text{In}_{\text{Cu}}^{++}$ or $\text{V}_{\text{Se}}^{++}$ and explained the variations observed in terms of screening effects. Accordingly the activation energies that are obtained in the case of OVC's CuIn_3Se_5 and CuIn_5Se_8 can be assigned to the activation from $\text{In}_{\text{Cu}}^{++}$ defect levels in these compounds.

Arrhenius plot (in the temp.range $>255\text{ K}$)		
Film	E_a (eV)	Identified defect
CuIn_5Se_8	0.02	$\text{In}_{\text{Cu}}^{++}$
CuIn_3Se_5	0.029	$\text{In}_{\text{Cu}}^{++}$
$\text{CuIn}_7\text{Se}_{12}$	-	Mixed
CuIn_5Se_8 (Na diffused)	0.05	In_i^{+++}
CuIn_3Se_5 (Na diffused)	0.013	$\text{In}_{\text{Cu}}^{++}$

Table.7.1 Activation energies calculated from Arrhenius plot in the temperature range 200K-300K.

The In_{Cu} defect in these samples is consistent with the PL and PC studies (in chapter 6) and with the EDAX analysis that shows the presence of an extra amount of indium. The activation energy 0.05eV in Na diffused CuIn_5Se_8 may be due to the presence of In_i^{+++} or due to the Na impurity in the sample [5,6]. There is possibility of occurrence of both these levels in the sample since in it the In content is slightly greater than the expected ratio for CuIn_5Se_8 and Na is also found to be diffused. But activation from Na level is not observed in the sodium diffused CuIn_3Se_5 where Na content is more, and so here more probability is given to the activation from In_i^{+++} level that is usually reported to occupy a donor level $0.046 \pm 0.012\text{ eV}$ below the CBM.

Between 200K and 255K

It has been observed that a new conductivity mechanism that could not be explained by Arrhenius model is coming into play in the temperature range below

255K. Analysis showed that the conductivity process in the specified range could be explained by Seto's model for the OVC's CuIn_3Se_5 and CuIn_5Se_8 . It has been explained in chapter 4 that the grain boundary model of Seto [7,8] gives the conductivity σ as

$$\sigma T^{1/2} = \sigma_0 \exp(-q\phi_b/k_B T) \quad 7.2$$

where k_B is the Boltzmann's constant and ϕ_b is the barrier height.

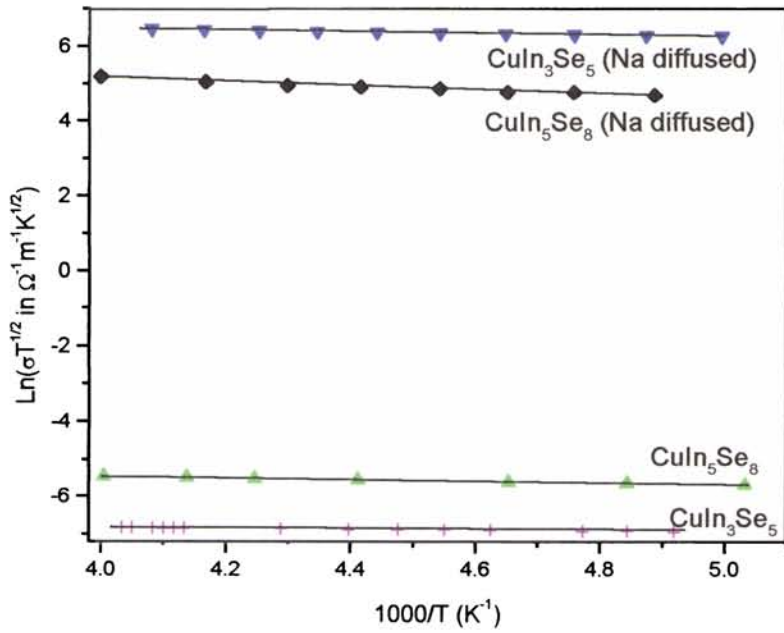


Fig.7.5 Seto's plots for the OVC's.

The grain boundary height (ϕ_B) calculated from the linear fit obtained for the $\text{Ln}(\sigma T^{1/2})$ Vs $1000/T$ curve (Fig.7.5) for the OVC's are given in Table.7.2.

Seto's plot (in temp.range ~200 to 255K)		
Film	ϕ_B	Cause
CuIn ₅ Se ₈	0.018	Grain boundary effect
CuIn ₃ Se ₅	0.019	Grain boundary effect
CuIn ₅ Se ₈ (Na diffused)	0.04	Grain boundary
CuIn ₃ Se ₅ (Na diffused)	0.019	Grain boundary

Table.7.2 Seto's plot for the OVC's.

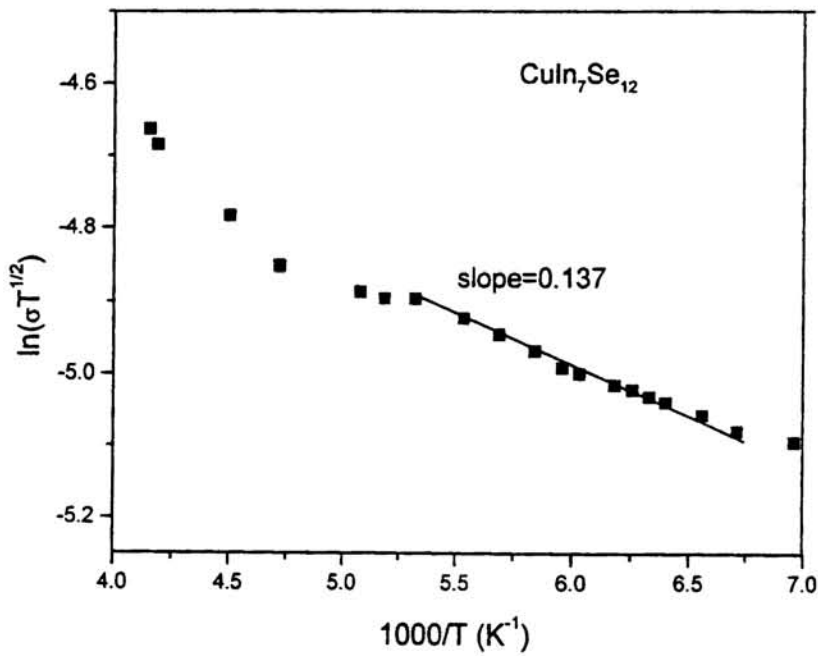


Fig.7.6 Seto's plot for CuIn₇Se₁₂.

It is observed from Fig.7.6 that in the OVC's with composition CuIn₇Se₁₂, the slope of $\ln(\sigma T^{1/2})$ Vs $1000/T$ graphs is continuously varying in the temperature

range 200 to 250K and hence the data could not be fitted to the Seto model. The attempt to model it by introducing potential fluctuations at the grain boundaries [9] with the fluctuating barrier $\varphi_B = V_{gb} + \xi$ (considering V_{gb} as the barrier potential at the grain boundary and ξ denoting the Fermi level position within the grain) introducing a Gaussian distribution $P(\varphi_B)$

$$P(\varphi_B) = (1/\sigma_\varphi\sqrt{2\pi})\exp\{-((\bar{\varphi}_B - \varphi_B)^2 / 2\sigma_\varphi^2)\} \quad 7.3$$

$\bar{\varphi}_B$ being the mean barrier height and σ_φ being the standard deviation (as usually done for such curves with varying slopes) has also failed for this defect compound in the mentioned temperature range. In the off-tie-line polycrystalline OVC $\text{CuIn}_7\text{Se}_{12}$, in addition to intrinsic and grain boundary effects, a large number of defects like Cu vacancies, In_{Cu} sites and neutral Cu vacancies [10] that are assumed to be present in them also contribute to conduction on thermal agitation. The defects could be of migratory nature due to jumping of carriers from one defect to another. The conduction being of a mixed nature might be the reason the curve could not be explained by a single model. But as the temperature is lowered it is observed that the Seto's model could be fitted to the data in the range 190K to 150K (Fig.7.6) and the grain boundary height that is calculated from the plot is around 0.0118eV.

Below 200K

In the low temperature region <200 K, the prevailing mechanism of conduction followed a transition from thermally activated conductivity to Mott's variable range hopping conduction of localized carriers [2,11], following the equation

$$\sigma = \sigma_0 T^{-1/2} \exp\{- (B/T)^{1/4}\} \quad 7.4$$

where B is related to the degree of disorder of the semiconductor. The calculated values of B from the $\text{Ln}(\sigma T^{1/2})$ Vs $T^{-1/4}$ plots (Fig.7.7) are given in Table.7.3. The theory behind the hopping process is given in detail in chapter 4. The density of states $N(E_F)$, the prefactor σ_0 and the Mott's hopping parameters like the hopping distance R for the hopping of the charge carriers among the localized states and the average hopping

energy W that are calculated at a particular temperature $T=120K$ are listed in Table.7.3. The degree of disorder is found to be maximum in the Na diffused samples. This may be because the substitution of Na in the lattice of the OVC's could be causing more disorder in the structure. The fact that only limited variations are observed in the ordering of other samples could be attributed to the reason that all of them are polycrystalline samples that are prepared under the same substrate temperature and therefore only controlled variations in ordering due to changes in grain sizes and introduction of defects would be present.

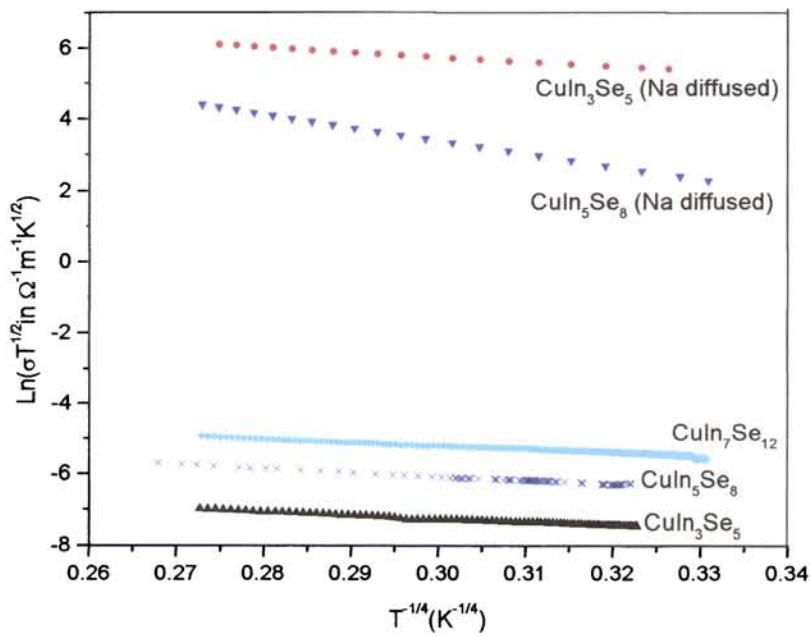


Fig. 7.7 $\text{Ln}(\sigma T^{1/2})$ vs $T^{1/4}$ variation of the OVC films in the low temperature region.

Mott's parameters from $\ln(\sigma T^{1/2})$ vs $T^{-1/4}$ plot (temperature below 200K)					
Film	$B \cdot 10^4$ (K)	$\sigma_0 \cdot 10^{-6}$	$N(E_F) \cdot 10^{22}$ ($\text{cm}^{-3} \text{eV}^{-1}$)	$R \cdot 10^{-7}$ (cm) at 120K	W (eV) at 120K
CuIn_5Se_8	1.59	2.6	2.5	1.03	0.0088
CuIn_3Se_5	0.86	3.56	4.63	0.88	0.0076
$\text{CuIn}_7\text{Se}_{12}$	0.78	3.73	5.09	0.86	0.0074
CuIn_5Se_8 (Na diffused)	191	2.38	0.021	3.4	0.029
CuIn_3Se_5 (Na diffused)	4.7	1.52	0.847	1.35	0.012

Table.7.3 Mott's parameters for the OVC's.

Thus a detailed analysis of the conduction mechanisms in different temperature ranges done for OVC films show that at high temperatures, the thermal activation is dominant which can be explained by Arrhenius and Seto's model where as at low temperatures hopping conduction prevails where Mott's variable range hopping conduction model is used to evaluate the associated constants as depicted in Table.7.3.

7.3 Hall measurements

As in the case of CuInSe_2 , the room temperature Hall coefficient measurements have been done to get an estimate of the concentration and mobility of the carriers in the OVC films. Hall Van Der Pauw controller together with a programmable power supply and programmable temperature controller have been used for the Hall experiments on the samples.

As explained in chapter 4, each sample of 1sq.cm area has been loaded on the sample holder with thermal grease and linearity check has been done to confirm the uniformity and ohmic behaviour of the contact. The measurements on mobility, density of carriers, Hall coefficient and type of carriers has been done and are given in Table.7.4.

Type	n cm ⁻³	μ cm ² /Vs	ρ Ω cm	Carrier type	S Ω /cm ²	H cm ³ /C
CuIn ₃ Se ₅	8E10	2.5E2	3E5	electrons	5E9	-7.6E7
CuIn ₅ Se ₈	7.9E9	2.3E3	3.4E5	electrons	5.59E9	-7.9E8
CuIn ₇ Se ₁₂	2E13	1E2	2E3	electrons	6E7	-2.5E5
CuIn ₃ Se ₅ (Na diffused)	7E17	3.4	2.5	electrons	6E4	-2.07E1
CuIn ₅ Se ₈ (Na diffused)	6E16	7.1	1.3E1	electrons	1.6E5	-9.25E1

Table.7.4 Carrier Concentration (n), Carrier mobility (μ), resistivity (ρ), Sheet resistance (S), Hall coefficient (H) and type of carriers from Hall measurement.

The carrier concentration is found to be much greater in the Na diffused samples but the mobility of the carriers is lesser for the same. The increased conductivity of the Na diffused samples may be due to the very large carrier density in them. In all the samples the type of carriers are found to be electrons which supports the Hot probe measurement that demonstrated n-type nature of the OVC samples studied. The resistivity measurements show that Na diffusion in the OVC samples could be made beneficial in their applications in devices where greater conductivity is required.

7.4 Conclusion

Analysis of the electrical conduction in CuInSe₂ related ordered vacancy compounds are done based on different available models. The diffusion of Na is found to be increasing the conductivity of even the OVC films, the property can be manipulated while making solar cells with these n-type OVC films as n-junctions. In the low temperature region the conductivity in all the compounds are dominated by Mott's variable range hopping while above 200K the contribution from both grain boundaries and defect levels are found to be predominant in CuIn₃Se₅ and CuIn₅Se₈. Though

variable range hopping could explain the conductivity in low temperature region for $\text{CuIn}_7\text{Se}_{12}$, a particular model could not explain the conductivity process in the near room temperature range (especially above 200K), the reason being attributed to the mixed nature of conductivity in these samples.

References

- [1] D. Schmid, M.Reukh, F.Grunwald, H.W.Schock, J.Appl.Phys. 73 (1993) 2902.
- [2] S.M.Wasim, C.Rincon and G.Marin, phys.stat.sol.(a) 194, (2002) 244.
- [3] E.Hernandez, L.Duran, C.A.D. Rincon, G.Aranguren, C.Guerrero and J. Naranjo, Cryst.Res.Technol. 37 (2002) 1227.
- [4] S. M. F. Hassan, .M. A. Subhan and K. M. Mannan Optical Materials 14 (2000) 329.
- [5] C. Rincon and R.Marquez, J.Phy.and Chem.of Solids 60 (1999) 1865.
- [6] I .Dirnstorfer, M. T. Wagner, D. N. Hofmann, M.D. Lampert, F .Karg and B.K. Meyer Phys.Stat.Sol. 168 (1998) 163.
- [7] J. W. Seto J.Appl.Physics 46 (1975)115.
- [8] J. W. Seto J.Appl.Physics 49(1984) 5365.
- [9] J. H Werner, Solid State Phenom. 37-38 (1994) 213.
- [10] S. B. Zhang, S. H. Wei, A. Zunger Phy.Rev.B 57 (1998) 9642.
- [11] N. F. Mott, Philos.Mag. 19 (1969) 835.

Valence band splitting in Cu-In-Se compounds**8.1 Introduction**

The lifting of degeneracy of the top most valence band of the I-III-VI compounds due to the combined effect of the spin orbit and crystal field interaction has been a matter of great interest to the researchers on these compounds, ever since the observation of three transitions from the three closely spaced split levels of the uppermost valence band to a single conduction band by shay et al [1]. Investigation showed that there is a direct correlation between the structure of the compounds and the splitting phenomena observed in these compounds. Different methods such as electroreflectance studies [1] and optical absorbance measurements [2-4] have been used for the elucidation of the splitting parameters in the compounds. Theoretical studies have been done to put forward different models to determine and explain the splitting phenomena. The p-d hybridization observed in these compounds has also been found to affect the splitting parameters in the compounds.

In this chapter, we initiate the study of splitting in the CuInSe_2 related ordered vacancy compounds CuIn_3Se_5 , CuIn_5Se_8 and $\text{CuIn}_7\text{Se}_{12}$ in thin film form along with the studies on Cu-rich/In-rich compounds based on optical absorbance spectra and investigate the various factors contributing to the splitting in these compounds. Hopfield's quasicubic model [5] has been used for the evaluation of the valence band splitting parameters in the compounds from the optical absorbance spectra. Linear hybridization model [3,4,6,7] is employed for determining the percentage contribution of Cu-d and Se p-orbitals to hybridization which is found to influence the variation observed in spin orbit splitting in the various Cu-In-Se compounds.

8.2 A brief review of investigations on the valence band splitting in chalcopyrites

The quasi cubic model, developed by Hopfield [5] to explain the properties of Wurtzite crystals was extended to ternary chalcopyrite crystals by Rowe et al [8] to explain the valence band structure of the chalcopyrites. In their study on $ZnSiAs_2$ and $CdSnP_2$, the compression of the chalcopyrite lattice along the optic axis was proposed as the dominating factor determining the ordering of valence bands. Later Shay et al [1] investigated the electronic structure of $AgInSe_2$ and $CuInSe_2$ by electroreflectance and photoluminescence studies and determined the valence band splitting parameters at 77K as crystal field splitting (ΔCF)=0.006eV and spin orbit splitting (ΔSO) =0.233eV in $CuInSe_2$ and $\Delta CF=-0.143eV$ and $\Delta SO=0.298eV$ in $AgInSe_2$. They observed that the spin-orbit splitting was considerably less than expected for p-levels and attributed it to 17% hybridization of Ag 4d levels and ~34% hybridization of Cu 3d levels with the p-orbitals of the anion. They suggested that crystal field splitting of the VBM of II-IV-V₂ compounds varied as $(3/2)b(2-(c/a))$ where b was the deformation potential and that the sign and magnitude of ΔCF in I-III-VI₂ compounds were also dominated by the built in lattice distortion [9].

Jaffe et al [10] reported $\Delta CF = -0.03eV$ for $CuInSe_2$ (with tetragonal distortion $\eta \sim 1.004$) and observed that the singly degenerate $\Gamma 4v^2$ was raised above doubly degenerate $\Gamma 5v^2$ in all the I-III-VI chalcopyrites they studied except in $CuInS_2$. Further, they noticed that for the Cu-based ternary chalcopyrites, the crystal field splitting ΔCF did not scale linearly with $(\eta-1)$ contrary to the observation by Shay et al [9] for group II chalcopyrites. They observed that in the compounds, a further splitting of $\Gamma 5v^2$ state into $\Gamma 6v + \Gamma 7v$ due to spin-orbit interaction could also occur. Jaffe et al [11] further analyzed the band gap anomaly in I-III-VI₂ chalcopyrites relative to their binary analogues and pointed out that the anomaly had not only a d-character contribution ΔE_g^d but also a cation electronegativity contribution ΔE_g^{CE} and a structural contribution ΔE_g^s to it. Calculation of $CuInSe_2$ (CIS) band structure as a function of η indicated that there was no significant band gap variation when η was changed but that

ΔCF changed almost linearly with η . They also observed [11] that valence band states drop in energy and conduction band states rise in energy with increasing anion displacement u in the chalcopyrite compounds, leading to an increase in ΔE_g^s part of the band gap anomaly with increase in u . They further gave a simple molecular-orbital interpretation to p-d hybridization.

Yoodee et al [6] calculated the mixing and repulsion of the p and d bands leading to pd hybridization in I-III-VI₂ compounds by the method of matrices. The crystal field interaction was taken into account in the calculations but they neglected the effect of structure component discussed by Jaffe et al [11]. In their method for determination of spin-orbit splittings of the p-orbitals, the spin-orbit splittings for the (I), (III) and (VI) atoms that constitute the compound were all included.

Artus et al [7] considered the disadvantage of taking the spin-orbit splitting of the metal p-orbitals in the calculation of the spin-orbit splitting of the p-orbitals of the compound (as done by Yoodee et al [6]) pointing out the fact that metal p-orbitals do not occur inside the valence band of the compound. They proposed a model where the spin-orbit splitting of the p-orbitals was determined taking only the splitting in III and VI compounds.

Wei et al [12] calculated the spin-orbit splitting and crystal field splitting in a series of chalcopyrites and found that for all the chalcopyrites they studied, the crystal field splitting ΔCF was negative. The negative value was found to be increasing as the tetragonal distortion $1-\eta$ of the compound increased. The spin-orbit splitting and crystal field splitting obtained by them for CIS were 0.184 eV and -0.02 eV respectively. The ΔCF in CIS was also calculated by Rodriguez et al [31] and they observed that there was an increase in ΔCF from -0.016 eV to -0.09 eV with increase in tetragonal distortion. According to their calculations, the top of the valence band was found to be a singlet Γ_4^2 and the next band a doublet Γ_5^2 .

8.3 Investigations on the Valence band Splitting in thin films of CuInSe_2 and the OVC's CuIn_3Se_5 , CuIn_5Se_8 and $\text{CuIn}_7\text{Se}_{12}$.

All the above references study the splitting observed in the valence band of chalcopyrites of the type ABC_2 . Our experimental observations indicated that there is the possibility of splitting in the CuInSe_2 related OVC's like CuIn_3Se_5 , CuIn_5Se_8 and $\text{CuIn}_7\text{Se}_{12}$ also. Among the structurally, morphologically and compositionally characterized samples, those exhibiting additive absorption regions or humps in their fundamental absorption region in the optical absorption spectra were selected for the splitting studies.

The plots marked 'experimental' in Fig.8.1 (a-e) respectively show the spectra in the fundamental absorption region of Cu-rich CuInSe_2 , In-rich CuInSe_2 , CuIn_3Se_5 , CuIn_5Se_8 and $\text{CuIn}_7\text{Se}_{12}$ thin films that are obtained from optical absorbance experiments at room temperature.

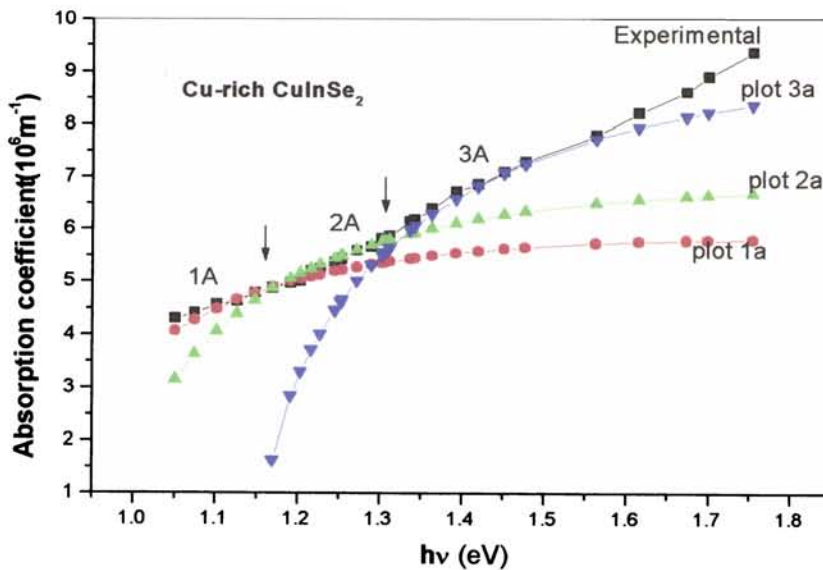


Fig. 8.1(a): Absorption spectra in the fundamental absorption gap of a Cu-rich sample.

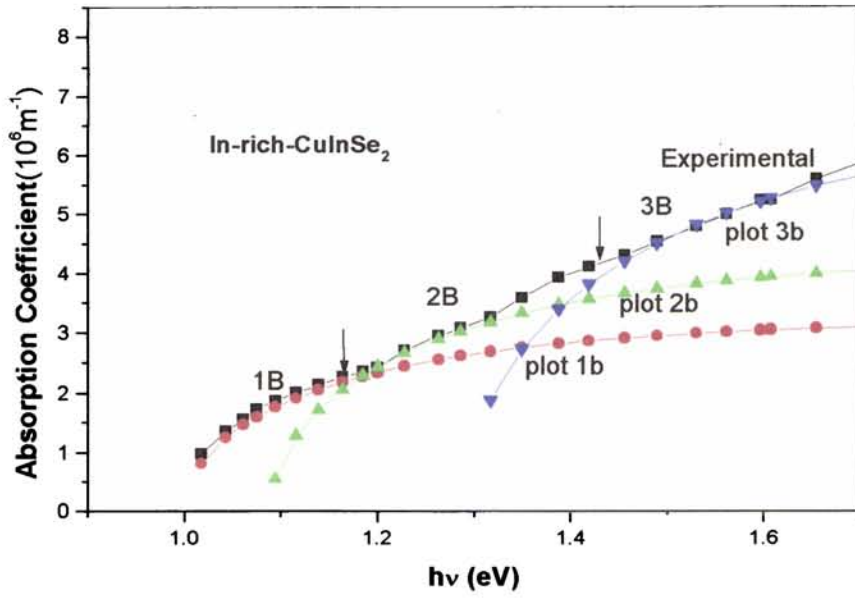


Figure 8.1(b): *Absorption spectra in the fundamental absorption gap of an In-rich sample.*

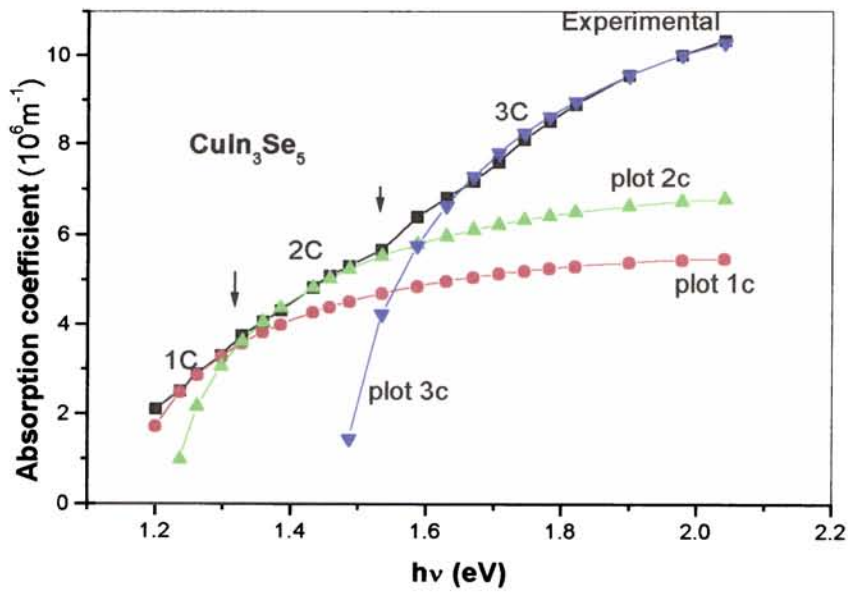


Figure.8.1(c): *Absorption spectra in the fundamental absorption gap of CuIn_3Se_5 film.*

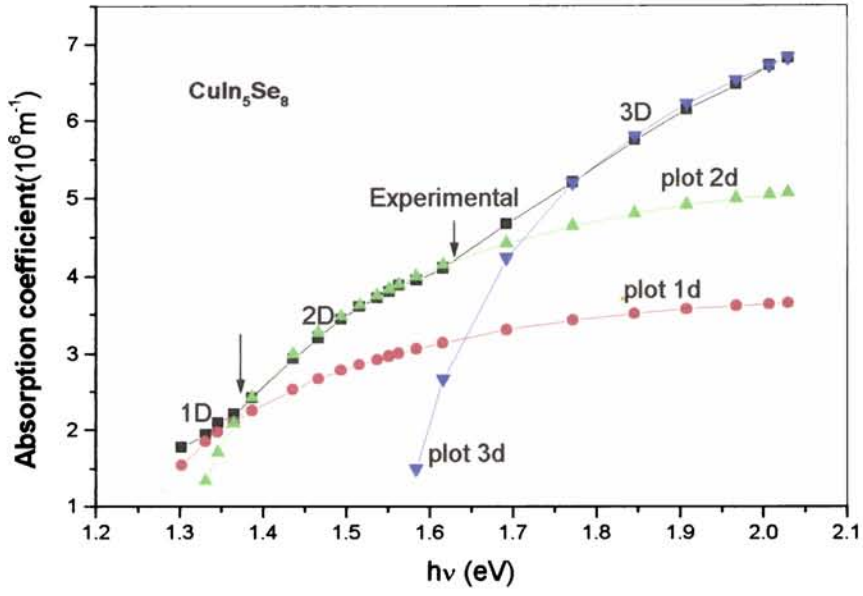


Figure.8.1(d): Absorption spectra in the fundamental absorption gap of CuIn_5Se_8 film.

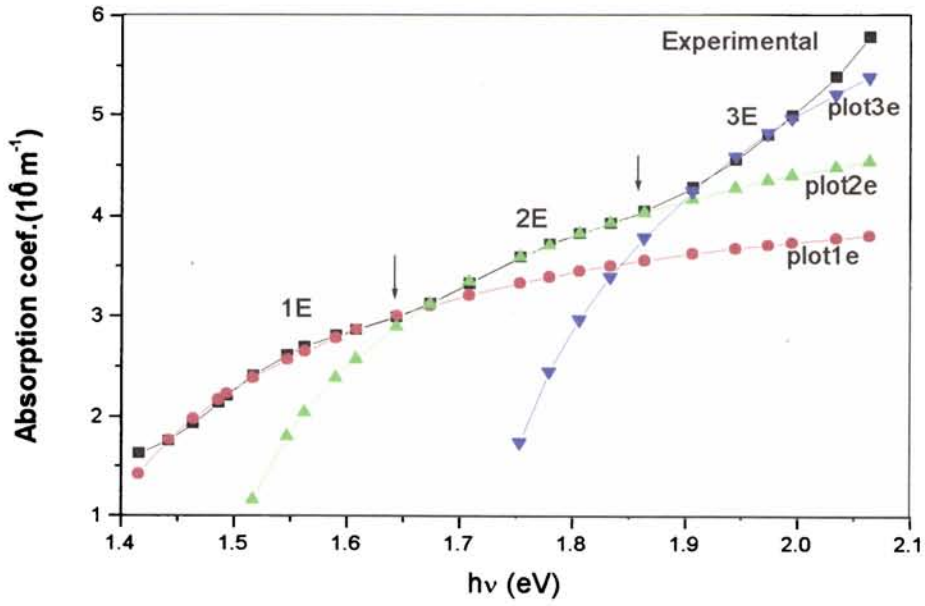


Figure.8.1(e): Absorption spectra in the fundamental absorption gap of $\text{CuIn}_7\text{Se}_{12}$ film.

The analysis of the absorption data using the equation

$$\alpha_{(v)} = A_c (h\nu - E_{gc})^n / h\nu \quad (8.1)$$

where $\alpha_{(v)}$ is the absorption coefficient at energy $h\nu$, $n = 1/2, 3/2$ or 2 for allowed direct, forbidden direct or indirect transitions respectively, A_c is a constant and E_{gc} is the optical band gap. [14,15] confirms that the transitions for all the films are direct allowed. Now the spectra of the compounds are analysed giving considerable attention to the three-fold absorption region in the fundamental absorption gap. When the band gap E_{g1} that is obtained from the $(\alpha h\nu)^2$ versus $h\nu$ plots as represented in the Figures.8.2(a,b and g) and the corresponding constant A_1 (Table.8.1) calculated using equation (8.1) for each film, are utilized to determine the absorption coefficient α_{cal} , the calculated absorption coefficients (α_{cal}) values are found to agree with the experimental α_{exp} values only in the photon energy range marked '1(A-E)' in the Figures.8.1(a-e) while it is found to be much lesser than the experimental α above this region, as shown by plots 1(a-e) in Fig.1(a-e). The considerable difference in the experimental and calculated α values indicates the possibility of additive absorptions above this range. The repetition of the analyses, taking the differences in to consideration yield a second direct band gap E_{g2} as shown in Fig.8.2 (c,d and g) and constant A_2 for each film which when used to draw the plots 2a-e in Fig.8.1 indicate a third additional absorption region '3(A-E)' where the transition could be fitted with a third band gap E_{g3} (Fig.8.2 (e,f and g)) for each film. Thus the analysis of the additive absorption region yield three direct allowed band gaps in the fundamental absorption region of each film indicating that the observation could be linked with interband transitions arising from three split levels of the upper valence band.

The band gaps E_{g1} , E_{g2} and E_{g3} for each film and the corresponding constants A_1 , A_2 and A_3 are given in Table. 8.1 .

Type of film	Band gap (E _{g1}) eV	Band gap (E _{g2}) eV	Band gap (E _{g3}) eV	Constant A ₁	Constant A ₂	Constant A ₃
Cu rich-CuInSe ₂	0.90	0.99	1.16	1.1*10 ⁷	1.35*10 ⁷	1.9*10 ⁷
In rich-CuInSe ₂	1.00	1.09	1.29	6.27*10 ⁶	8.78*10 ⁶	1.5*10 ⁷
CuIn ₃ Se ₅	1.17	1.23	1.48	1.2*10 ⁷	1.5*10 ⁷	2.8*10 ⁷
CuIn ₅ Se ₈	1.25	1.31	1.57	8.3*10 ⁶	1.21*10 ⁷	2*10 ⁷
CuIn ₇ Se ₁₂	1.37	1.49	1.73	9.43*10 ⁶	1.24*10 ⁷	1.91*10 ⁷

Table.8.1. *The band gaps and the corresponding constants in each film.*

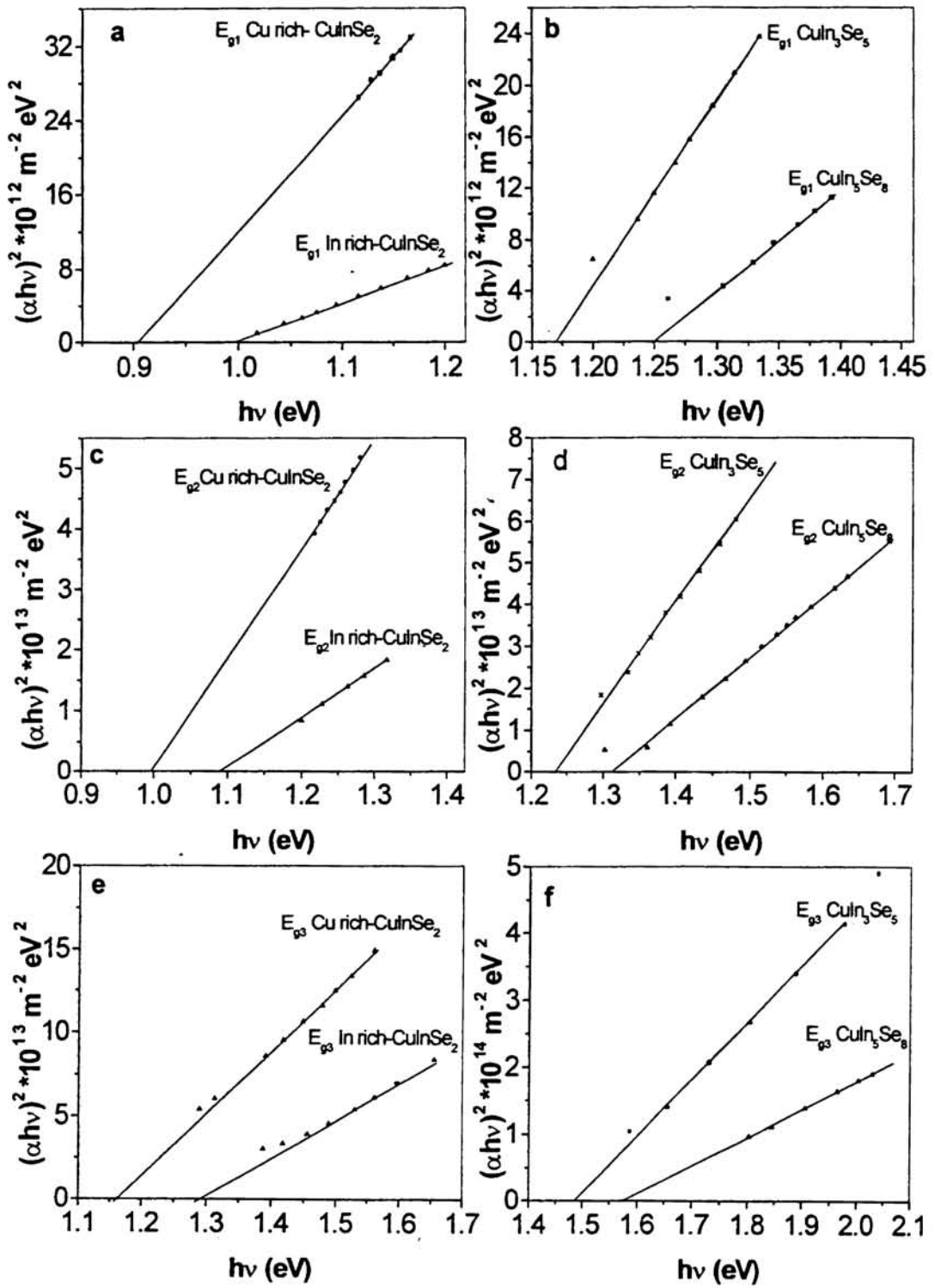


Fig.8.2. $(\alpha h\nu)^2$ versus $h\nu$ plots for p-type/n-type CuInSe₂, CuIn₃Se₅ and CuIn₅Se₈.

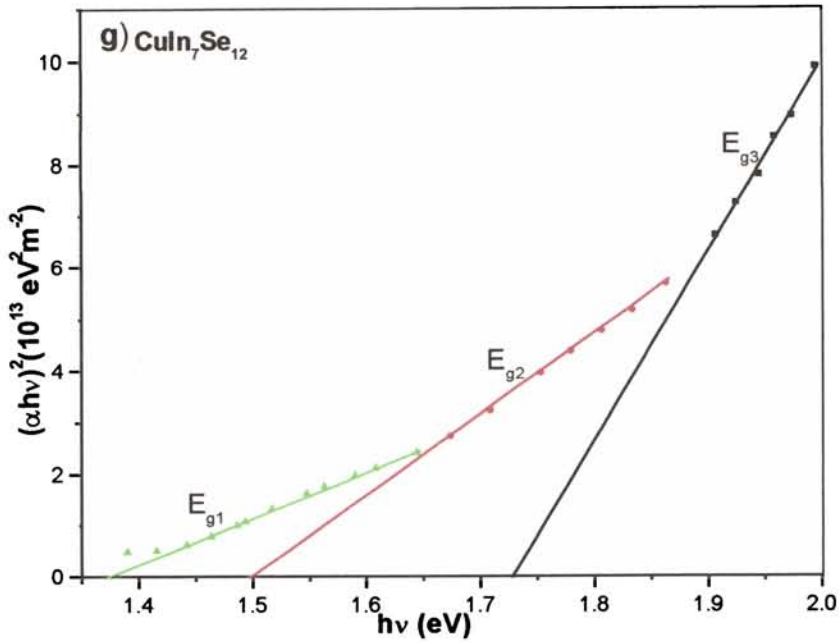


Fig.8.2 cont. $(\alpha hv)^2$ versus hv plot for $\text{CuIn}_7\text{Se}_{12}$ film giving E_{g1}, E_{g2} and E_{g3} .

In chalcopyrite compounds, due to the existence of a tetragonal crystal field, the triple degeneracy of the top most valence band level Γ_{15} is lifted such that a singlet level Γ_4 lies above a doubly degenerate level Γ_5 [7]. Due to the additional spin orbit interaction, the doublet Γ_5 further splits into Γ_6^5 and Γ_7^5 while Γ_4 convert to Γ_7^4 and Γ_1 to Γ_6^1 . The transitions from the three levels in the upper valence band to the conduction band minimum Γ_6^1 are conveniently labeled as A, B and C as in Fig.8.3 which correspond to Γ_{7v}^4 to Γ_{6c}^1 , Γ_{6v}^5 to Γ_{6c}^1 and Γ_{7v}^5 to Γ_{6c}^1 transitions, the upper index indicating the single group representation from which the state originates. Thus a complete lifting of degeneracy of the top most valence band level due to the combined effect of a non-cubic crystalline field and spin-orbit interaction is observable in chalcopyrite compounds. Analysis showed that the three direct transitions observed in the fundamental absorption region of the Cu-In-Se films are also associated with the

transitions from the three split levels produced by the lifting of the threefold degeneracy of the top-most Γ_{15} level in the valence band of these compounds.

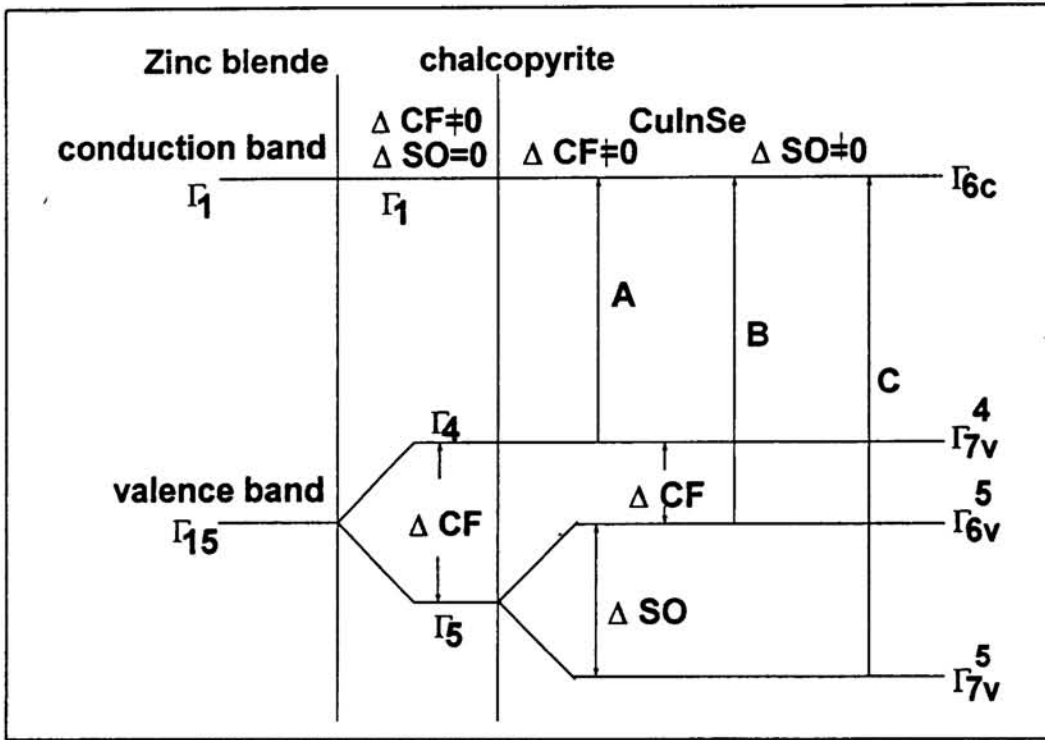


Fig.8.3. Valence band splitting in the Cu-In-Se compounds showing A, B and C transitions in the case when Δ_{CF} and Δ_{SO} are not negligible and in chalcopyrites where only Δ_{CF} has value.

As done by most of the investigators, we too employed Hopfield's quasi-cubic model adapted to chalcopyrites [5,8], for the evaluation of the valence band split parameters in each of the Cu-In-Se compounds. Within this model, the energies of the two Γ_7 levels relative to the Γ_6 level in the valence band of a chalcopyrite crystal are given by

$$E_{1,2} = -\frac{1}{2} (\Delta_{CF} + \Delta_{SO}) \pm \frac{1}{2} \left[(\Delta_{CF} + \Delta_{SO})^2 - \frac{8}{3} \Delta_{CF} \Delta_{SO} \right]^{1/2} \quad 8.2$$

where Δ_{SO} is the splitting of valence band due to spin-orbit interaction and Δ_{CF} is the splitting due to the tetragonal crystalline field interaction in the valence band of the compounds. The crystal field splitting (CFS) and the spin-orbit splitting parameters thus determined from the difference of E_{g1} and E_{g3} relative to E_{g2} for the various compounds using equation 8.2 are given in Table.8.2.

Type of Film	Δ_{CF} (eV)	Δ_{SO} (eV)
Cu rich- CuInSe_2	-0.11	0.20
In rich- CuInSe_2	-0.11	0.23
CuIn_3Se_5	-0.08	0.27
CuIn_5Se_8	-0.08	0.28
$\text{CuIn}_7\text{Se}_{12}$	-0.16	0.27

Table.8.2. *Crystal field split (Δ_{CF}) and spin orbit split (Δ_{SO}) parameters.*

An examination of the split parameters shows that the spin orbit splitting parameters of CuInSe_2 are in good agreement with the values reported for it earlier by different investigators in this field and that it is much reduced from the Δ_{SO} that is calculated by Artus et al's [7] method where p-d hybridization effects are not taken in to consideration. The ordered vacancy compounds show an enhancement in their Δ_{SO} relative to that in CuInSe_2 . To explain the variation in crystal field splitting for the films depicted in Table.8.2, knowledge of the structural parameters of the compounds when taken in thin film form is necessary since, basically CFS is represented as due to the effect of three factors (1) existence of two distinct cations $A \neq B$, (2) tetragonal deformation $\eta \neq 1$, and (3) anion displacement $u \neq 1/4$ in the chalcopyrites.

First we discuss the crystal field splitting observed in these compounds relating it with the structural constants like η , u and anion-cation bond length alternation that influence the tetragonal crystalline field and then move on to the discussion on spin splitting.

The structural constants calculated by the method discussed in detail in chapter.2, Section.2.6 for the films used for the study are given in Table.8.3.

Film Type	a (Å)	c (Å)	η	u	R_{AC} (Å)	R_{BC} (Å)
Cu rich- CIS	5.717	11.743	1.027	0.23623	2.4708	2.5614
In rich- CIS	5.789	11.763	1.016	0.23633	2.4706	2.5613
$CuIn_3Se_5$	5.744	11.637	1.013	0.23635	2.47058	2.5613
$CuIn_5Se_8$	5.7415	11.552	1.006	0.2364	2.4705	2.5612
$CuIn_7Se_{12}$	5.746	11.779	1.025	0.23645	2.4657	2.5543

Table.8.3. Structural constants like lattice parameters (a and c), tetragonal distortion (η), anion displacement(u) and bond lengths (R_{AC} and R_{BC}).

Examination of the CFS values depicted in Table.8.2 in relation to the structural constants given in Table.8.3 suggests that there is an increase in CFS with increase in tetragonal distortion parameter. In the films where $\eta \sim 1.006$ the CFS is observed to be equivalent to that in CIS films of the same distortion studied by Rodriguez et al [13]. But it is clear on comparison between the structural parameters and the CFS values for the various compounds that distortion is not the only factor deciding the crystal field splitting. For instant though distortion in the Cu-rich film and $CuIn_7Se_{12}$ are found to be same, the CFS vary. The measurement of CFS in different groups of compounds like in II-IV-V and in II-VI compounds led Shay et al [9] to come to a similar conclusion that

though built-in lattice distortion has a dominant influence on CFS in II-IV-V crystals, when crystals of Wurtzite where lattice constants are nearly ideal are considered, the CFS is dominated by phenomena other than lattice distortion. Later studies [1,9-13] have recognized the influence of u values and the bond length differences on CFS. Hence it is reasonable to assume that CFS that we observe in the ternaries is influenced by a number of factors including the structural constants such as η , u etc. and even the preparation conditions and form of the crystal (such as single crystals, thin film etc) which often determines the distortion by inducing strain. This could be the reason for the different CFS values obtained by different investigators for the same ternary compound having constructional differences and slightly different structural parameters [9-13].

The variation in spin-orbit splitting in the Cu-In-Se compounds have a much better explanation based on p-d hybridization effects and the percentage contribution of the Cu and Se orbitals to hybridization in the compounds. A comparison of the spin orbit splitting of all the compounds measured experimentally; with the theoretical splitting equal to 0.51eV obtained by Artus et al [7] indicate a reduction in the experimentally ascertained values. According to Artus et al

$$\Delta p = \frac{29}{20} [0.2 \Delta p(III) + 0.8 \Delta p(VI)] \quad 8.3$$

with $In \Delta p(III) = 0.27eV$ and $Se \Delta p(VI) = 0.37 eV$ from Cardona [16]. Comparison is done with Artus et al's method since it does not involve the discrepancy occurring on inclusion of the spin orbit coupling of the metal ions of the binary analogue in the calculation of spin orbit splitting of the compound as done by Shay et al [9] or the disadvantage of including metal p orbitals in the calculations as in the method used by Yooder et al [6].

The noticeable difference in the spin-orbit splitting in $CuInSe_2$ from experiment and theoretical calculations as above suggests, the unavoidable effect of hybridization between the anion p-orbital and noble metal d-orbital in the top valence bands of these compounds on their photo-electronic properties or in other words, the profound

influence of the proximity of noble metal d-levels in the upper most valence bands of these compounds on their optical behaviour. In the tetragonal field of the chalcopyrite compounds, the five-fold degenerate d-levels split in to threefold $\Gamma_{15}(d)$ and twofold $\Gamma_{12}(d)$ with the $\Gamma_{15}(d)$ lying above the $\Gamma_{12}(d)$ level. The three fold degenerate $\Gamma_{15}(p)$ state of the anion interact with the $\Gamma_{15}(d)$ state of the cation of the same symmetry, with a repulsive interaction which is directly proportional to the p-d coupling matrix element $|\langle p|v|d \rangle|^2$ and inversely proportional to the energy separation $\Delta \varepsilon_{pd}$ between anion p and cation d in accordance with the perturbation theory [17]. The interaction forms a lower bonding state weighted more by the $\Gamma_{15}(d)$ state and an upper antibonding state weighted more by the $\Gamma_{15}(p)$ state. The strength of the interaction determines the extent of downward shift of the antibonding state, thus regulating the band gap variations in the ordered vacancy compounds as explained in Chapter 6.

The influence of p-d hybridization on the spin-orbit splitting in the compounds is also determined by the strength of interaction between the $\Gamma_{15}(p)$ and $\Gamma_{15}(d)$ orbitals of the same symmetry. To understand better, let us consider separately the spin-orbit splitting in the p and d orbitals as shown in Fig.8.4. It has been obtained [9] from the diagonalization of the L-S matrices that $\Gamma_{15}(p)$ state splits into a doublet Γ_8 above a singlet Γ_7 , whereas the $\Gamma_{15}(d)$ splits into a doublet Γ_8 below a singlet Γ_7 as shown in Fig.8.4. As shown in Fig.8.4, the splitting of d-orbitals is negative with the singlet above the doublet while the spin-orbit splitting of p-orbital is positive with the doublet above the singlet. Due to $\Gamma_{15}(p)$ - $\Gamma_{15}(d)$ interaction, the negative Δ_{SO} of the d-levels partially cancels the positive Δ_{SO} of the p-levels, which in effect leads to the observed decrease in the spin-orbit splitting of the ternary as compared to the theoretical value 0.51 eV obtained by Artus et al [7] using equation (8.3) where splitting of p-orbital alone is considered.

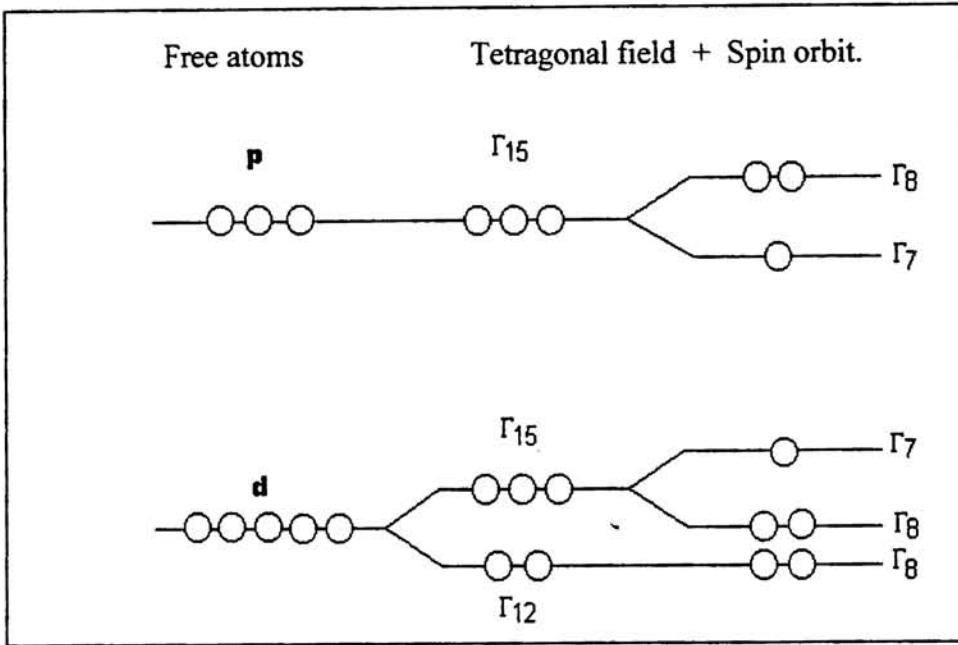


Fig.8.4. Spin-orbit splitting of p and d-orbitals in the upper valence band of CuInSe₂.

The d- splitting in CuInSe₂ with $\Delta d(I) = -0.15$ eV is calculated as

$$\Delta d = \frac{29}{20} \Delta d(I) = -0.22 \text{ eV} \quad 8.4.$$

Hence depending on the percentage contribution of the d-orbitals and p-orbitals to hybridization, the spin-orbit splitting parameters in the I-III-VI chalcopyrites is different. Transferring the trend to OVC's, where Cu concentration is lesser, the observed increase in the Δ_{SO} values in OVC's compared to that in CuInSe₂ (Table.8.2) can be attributed to the lesser contribution of Cu-d orbitals to hybridization. We use the linear hybridization of orbitals (LHO) [4,6,7] where Δ_{SO} could be written as a linear sum of the p and d orbital contribution to hybridization to determine the percentage

contributions. Unlike the Tell and Bridenbaugh model [18] where non-cubic crystal fields and p-d hybridization are not considered or Kildal's model [19] where though non-cubic crystal fields are considered p-d hybridization effects are not assumed, in LHO both aspects are taken into consideration and hence most appropriate for the present calculations. Within LHO model

$$\Delta_{so} = \beta\Delta p + (1-\beta)\Delta d \tag{8.5}$$

where β is the percentage of p orbital contribution and $(1-\beta)$ that of d orbital contribution to hybridization.

Type of Film	% Contribution to hybridization	
	from	
	Cu-d orbital $(1-\beta)$	Se-p orbital (β)
Cu rich- CuInSe_2	42%	57%
In rich- CuInSe_2	38%	62%
CuIn_3Se_5	33%	67%
CuIn_5Se_8	32%	68%
$\text{CuIn}_7\text{Se}_{12}$	33%	67%

Table.8.4. Percentage contribution to hybridization from Cu-d orbital and Se-p orbital .

It is apparent from the $(1-\beta)$ values depicted in Table. 8.4 that the Cu-d orbital contribution to hybridization is maximum in the case of Cu-rich CIS films where the spin orbital splitting is minimum while the contribution is reduced in the OVC's leading to an enhancement of Δ_{so} values in them. This is undoubtedly associated with the diminished d-character in the OVC's upon forming dense periodic Cu vacancies in

them, which is also the suggested explanation for the increase in band gap in the OVC's relative to that in CIS [20]. Thus there is a definite correlation between the spin-orbit splitting and the p-d hybridization in the different types of Cu-In-Se films investigated.

The observation of reduced contribution of Cu-d orbital to hybridization due to increased Cu vacancies in the ordered vacancy compounds agrees very well with the explanations for enhancement in band gaps in the OVC's due to reduction in the strength of p-d hybridization. This is because, if there is a reduction in the atomic percentage of Cu as in the OVC's relative to that in CIS, the repulsion between $\Gamma_{15}(p)$ and $\Gamma_{15}(d)$ decreases and the antibonding state is depressed downwards leading to an increase in band gap in the former. So we can arrive at the conclusion that the cause behind both the observations (a) the Cu-deficient OVC's have a band gap greater than that in CuInSe_2 and (b) the spin-orbit splitting is greater in OVC's compared to that in CuInSe_2 is one and the same, that is, the reduction in Cu-d orbital to p-d hybridization in the OVC's.

8.4 Conclusion

In this chapter, we discussed the valence band splitting in CuInSe compounds like Cu-rich/In-rich CuInSe_2 , CuIn_3Se_5 , CuIn_5Se_8 and $\text{CuIn}_7\text{Se}_{12}$ due to simultaneous effect of crystal field and spin-orbit interactions. It is observed that the crystal field splitting is influenced to a great extent by (i) the tetragonal distortion which often varies due to parameters like strain, constructional differences, form of the compound such as single crystalline, thin film etc. (ii) the anion displacement and (iii) bond length variations. The spin orbit splitting on the other hand is found to be acted upon by p-d hybridization effects, which also exerts its influence on optical band gap of the CuInSe compounds. The relative decrease in the experimentally determined spin orbit splitting in the ternaries is attributed to Se $\Gamma_{15}(p)$ and Cu $\Gamma_{15}(d)$ interaction. It is also observed that the lesser the contribution of Cu d orbital to hybridization, the more is the spin orbit splitting as well as the band gap. So the increase in spin orbit splitting in the ordered vacancy compounds is attributed to the reduced atomic concentration of Cu in the OVC's.

References

- [1] J.L Shay, B.Tell, H.M.Kasper and L.M.Schiavone. Phys.Rev.B. 7 (1973) 4485.
- [2] J.R. Tuttle, D.Albin, R.J. Matson, R. Noufi, J. Appl. Phys. 66 (1989) 4408.
- [3] R.R. Philip and B. Pradeep. Thin Solid Films (in press).
- [4] R.R.Philip and B.Pradeep. Semicond. Sci.Technol. 17 (2002) 1157.
- [5] J.J. Hopfield. J. Phys. Chem. solids. 15 (1960) 97.
- [6] K. Yoodee, J. Wooley and V. Sa-yakanit. Phys. Rev. B. 30 (1984) 5904.
- [7] L. Artus, Y. Bertrand and C. Ance. J. Phys. C. Solid State Phys. 19 (1986) 5937.
- [8] J.E Rowe, J.L .Shay, Phys. Rev. B 3 (1971) 451.
- [9] J.L.Shay and J.H.Wernick. Ternary chalcopyrite semiconductors: Growth, electronic properties and applications, Pergamon, Oxford,1975; 79-128.
- [10] J.E. Jaffe and A. Zunger. Phys. Rev. B. 28 (1983) 5822.
- [11] J.E. Jaffe and A. Zunger. Phys. Rev. B. 29 (1984) 1882.
- [12] S. H.Wei and A. Zunger. J. Appl. Phys. 78 (1995) 3846.
- [13] J. A.Rodriguez, L.Quiroga, A.Camacho and R. Baquero. Phys. Rev. B. 59 (1999)1555.
- [14] J.Herrero and C.Guillen. J. Appl. Phys. 69 (1991) 429.
- [15] V.F.Gremenok, R.W.Martin, I.V.Bodnar, A.E.Hill, R.D.Tomlinson, I.A.Victorov, O.V.Ermakov, C.A.Faunce, R.D.Pilkington, I.Martil, F.L.Martinez, E.P.Zoretskaya, M.V.Yakushev, W.Schmitz and K.Bente. Thin Solid Films 394 (2001) 24.
- [16] M.Cardona, Modulation spectroscopy, Solid State Phys. Academic, Suppl. 11, N. Y. 1969 pp.69.
- [17] J.E. Jaffe and A. Zunger. Phys. Rev. B. 27 (1983) 5176.
- [18] B.Tell and P.M. Bridenbaugh, Phys.Rev.B. 12 (1975) 3330.

- [19] H.Kildal, Phys.Rev.B. 10 (1974) 5082.
- [20] R.R.Philip and B.Pradeep. Semicond.Sci. Technol. 18 (2003) 768.

Scope for future research:

The study highlights the possibility of investigating further into various unexplored properties of the group of compounds and the potential in using them for various applications like photovoltaic cells, non-linear devices etc. The preparation of OVC compounds suggests the possibility for research concentrating on the preparation of a large number of stable tie-line and off-tie line ordered vacancy compounds with diverse optical and electrical properties. Very few of these technologically important compounds have been studied so far. This could form a class of compounds with various combinations of opto-electronic properties that can be suitably selected for fabricating solar cells. The proximity of d-orbital to the top of the valence band has been observed to exhibit some effects, but many more might still to be known. An investigation in that direction also seems to yield promising results. Investigation of defects in the OVC's, in which very little work has so far been done, ought to yield insight into the various transition mechanisms possible in these materials and hence an innovative field to continue researches in.

